New routes of preparation of active and stable mesoporous Ni-alumina based catalysts for methane dry reforming and CO2 methanation

Leila Karam

Sorbonne Université

Ecole doctorale de Physique et Chimie des matériaux

Laboratoire de réactivité de Surface

University of Balamand

Department of chemical engineering

New routes of preparation of active and stable mesoporous Ni-alumina based catalysts for methane dry reforming and CO_2 methanation

Par Leila KARAM

Dirigée par Mme Pascale MASSIANI et Mme Nissrine EL HASSAN

Présentée et soutenue publiquement le 4 Octobre 2019

Devant un jury composé de :

Mme Sophie Cassaignon	Professeure (SU-France)	Président
M. Axel Lofberg	Chercheur CNRS (Univ. Lille-France)	Rapporteur
M. Mohammad Ahmad	Professor (AUB-Lebanon)	Reviewer
M. Carlos Henriques	Associate Professor (IST-Portugal)	Examiner
M. Elie Chalhoub	Assistant Professor (UOB-Lebanon)	Invité
M. Julien Reboul	Chercheur CNRS (SU-France)	Invité
Mme Pascale Massiani	Chercheure CNRS (SU-France)	Supervisor
Mme Nissrine El Hassan	Associate Professor (UOB-Lebanon)	Supervisor

Acknowledgment

This work would not have been brought to life without the extensive endeavors of many people from so many parts who have been my support from the very beginning.

I would like first to thank the research council at the University of Balamand, the ecole doctorale at Sorbonne University and the European SOL-CARE project for financing my work when accomplishing my thesis.

An enormous thanks goes to my supervisors who have played the role of the engine that helped me propel through my thesis years in the smoothest possible fashion. In light of this, I would like to seize the opportunity to thank Dr. Nissrine El Hassan because she gracefully offered me the chance to apply for a PhD candidacy and paved the way for me to delve into the realm of research. She truly played the role of an authentic catalyst in accelerating my thesis work and she provided me with the full support, whether morally, emotionally, or educationally. She taught me how to cope with stress and overcome any impediment that comes along my way throughout my research years.

In parallel, I would like to thank my second supervisor Dr. Pascale Massiani for her continuous support when I was in France. She not only helped me with my research and thesis, but also made me feel at home. She also created an enriching environment which was conducive to an ever-rising drive for research and learning. Needless to say, her support encompassed all aspects: moral, emotional, and educational. She made me embrace positivity and made me strongly believe that nothing can abate me from reaching my goals. In addition, she constantly rectified my report and engaged in the exploitation of the work results.

Another series of thanks goes to both the Lebanese and French jury members who consented upon correcting my thesis in an objective and constructive ways. I would also like to specifically thank Dr. Julien Reboul for his help concerning the MOF part in this thesis. His expertise in this field provided me with a new interesting scientific knowledge. I am thankful for him also because he was always very kind and available whenever I needed him. I am grateful for Dr. Carlos Henriques who did not hesitate to host me in his lab in Portugal whereby I had the opportunity to further enrich my research work. His PhD student Carminha also imparted positivity and boosted my performance. I am indebted to Dr. Elie Chalhoub for his help and support in the kinetics measurements and modeling set-up. My appreciation goes also to Dr. Axel Lofberg, for he attended my “comité de suivi de thèse” that took place on a yearly

basis. His evaluation of the work was very beneficial and he was ready to help in any possible way.

An enormous thanks goes to Ms. Sandra Casale for her help in microscopies experiments, to Dr. Jean Marc Krafft because he taught me how to use the Raman spectroscopy and Mr. Mohamed Selman for he helped me operate upon XRD. My warmest thanks goes to Ms. Annie Mettendorff who facilitated my stay in the laboratory, and arranged all my travels and accommodations in the smoothest possible way. It was always fun and beneficial to communicate with her because she allowed me to ameliorate my French language.

I want to express my deepest gratitude for two of my favorite professors at the university, Dr. Ghassan Akkary and Dr. Zeina Jundi, who have always encouraged and believed in me. As for Dr. Zeina, it is worth mentioning that she was not only a teacher, but also an excellent mentor who always guided me on the right path and will always be a great inspiration for me.

My colleagues and friends, especially Abdallah, Antoine, Asma, Aya, Claudia, David, Deurcy, Gabriela, Ghinwa, Hala, Hagop, Jackie, Katia, Kosty, Lena, Louay, Oscar, Riad, Ricardo, Samer, Vanessa, have played a pivotal role because they have provided me with a warm shoulder to lean on whenever I needed support. They made me embark on my thesis journey in the lightest possible way and converted all my stressors into laughers.

I will also seize the great opportunity to explicitly thank my parents and my siblings for their unconditional love and support. Whenever an obstacle attempted to pull me down, my family used to push me up. Whenever an impediment put me in the deepest abyss, my family relocated me to the summit. They have truly made what is impossible possible. Therefore, I owe them my research, my work, and my thesis.

Table of content

List of abbreviations

ALD	Atomic Layer Deposition
ATR	Auto Thermal reforming
BET	Brunauer-Emmet-Teller
BP	British Petroleum
CSDRM	Combined Steam Dry Reforming of Methane
CTAB	Cetyl Trimethyl Ammonium Bromide
DRM	Dry Reforming of Methane
EDF	Equilibrium Deposition Filtration
EDX	Energy Dispersive X-ray
EIA	Energy information administration
EISA	Evaporation Induced Self-Assembly
EOR	Enhanced oil recovery
EPA	Environmental Protection Agency
FTIR	Fourier transform infrared spectroscopy
FWHM	Full Width at Half Maximum
GHG	Green House Gas
HAADF	High Angular Annular Dark Field
ICDD	International Center for Diffraction Data
IPC	Intergovernmental Panel on Climate Change
IUPAC	International Union of Pure and Applied Chemistry
IWI	Incipient Wetness Impregnation
MAR	Microactivity-reference
MOF	Metal Organic Framework
OPEC	Organization of Petroleum Exporting Countires
POM	Partial Oxidation of Methane
RWGS	Reverse Water Gas shift
SEM	Scanning Electron Microscopy
STEM	Scanning Transmission Electron Microscopy
SRM	Steam Reforming of Methane
TCD	Thermal Conductivity Detector
TGA	Thermo-gravimetric analysis

TEM	Transmission Electron Microscopy
TOF	Turn Over Frequency
TPR	Temperature Programmed Reduction
WI	Wet Impregnation
WGS	Water Gas Shift
XPS	X-ray photoelectron spectroscopy
XRD	X-Ray Diffraction
XRF	X-Ray Fluorescence

General introduction

Fossil fuels dependencies have been a serious addiction for most of the population since the middle of last century due to the need to ensure access to energy for quality of life and for economic development. Equally important, however, is the climate change problem encountered by the use of fossil fuels (non-renewable source) through the emissions of pollutants, CO_2 specifically, contributing to global warming. As an alternative energy source, hydrogen (H_2) and carbon monoxide (CO) mixture can be transformed following a specific reaction pathway to fuels, chemicals and electricity meeting everyone's need. There are several available processes to generate the required mixture of H_2 and CO from methane, like steam reforming, dry reforming, and partial oxidation reforming. In this work, the focus will be targeted toward dry reforming of methane since this reaction uses CH_4 and CO_2 as reactants, both of which are greenhouse gases. Even if CH_4 is a short-lived climate pollutant, its emission should not be underestimated. Indeed, CH_4 is not only obtained from gas production, but it is also emitted from livestock and rice paddies, ruminant animals, side products of industrial activities, landfills (biomass), and waste water treatment. CO_2 is mainly transferred to the atmosphere from combustion of fossil fuels. Thus, the conversion of both pollutants to energy will minimize fossil fuels dependency, and will contribute to reduce its disastrous climate consequences on the planet.

Dry reforming of methane process is an endothermic reaction that is still under research studies striving to find an active and stable catalyst. Although noble-metals can be active and stable, they are scarcely available and expensive which led to the development of transition metals, nickel specifically. The drawback of using Ni-based catalyst is the sintering of Ni and the formation of carbon under the harsh reaction condition. The recent approaches are targeted towards enhancing the performance of Ni supported on different oxides, mainly Al_2O_3, by 1) employing different methods of Ni deposition on the support, 2) altering the shape of the support and 3) adding a second promoter or metal. However, the preparation methods were not yet efficient enough to stabilize Ni against thermal agglomeration and carbon deposition.

In this thesis, catalysts that are highly active and stable in dry reforming of methane are synthesized inspired by different positive parameters seen in literature. Needless to say, the Al_2O_3 oxide was selected as support for Ni. The direct one-pot method that involves adding Ni within the synthesis of Al_2O_3 was adopted along with alteration in the shape of alumina to

ensure occlusion and confinement of nickel nanoparticles inside the pores or walls of structured oxide. MgO was also selected as basic dopant to prevent solid carbon accumulation.

This research work is a joint PhD between the "Laboratoire de réactivité de Surface" at Sorbonne University and the Department of chemical engineering at University of Balamand. It is also a part of a European ERANETMED project (SOL-CARE) that includes three European countries (Spain, Italy, Portugal) in addition to Lebanon.

The manuscript is divided into six main chapters. Chapter I provides a general overview on the non-renewable fossil fuels source of energy, their environmental issues, and the possible renewable alternative energy pathways involving C_1-based molecules (CO_2 and CH_4). A detailed explanation is presented on dry reforming of methane reaction, then the state of the art catalysts already used in the reaction are elaborated and analyzed to understand the challenges faced.

Chapter II is dedicated to the technical part involving the principle of all the used characterization techniques, the applied procedures on the tested materials (calcined, reduced, and spent), and the derived results from each equipment. The chapter also embraces an evaluation of the thermodynamic equilibrium of the reactions, and the experimental catalytic tests set-ups. Note however that this chapter will not introduce the conditions of preparation of the samples that will be described in the respective chapters where they will be developed.

Chapter III tackles the effectiveness of using MgO as basic dopant in mesoporous Ni-Al_2O_3 materials by one-pot synthesis. The chapter begins with a brief bibliographic recall on the existing Mg-based alumina materials. Then, the preparation methodology used in this thesis is described in details before presenting the obtained physicochemical properties, the reducibility and the catalytic performances. The focus will be on the effect of magnesium loading with a clear explanation on why its use should be optimized.

Chapter IV introduces a novel technique to occlude Ni nanoparticles inside Al_2O_3 pores following an innovative metal organic framework (MOF) route. Firstly, this chapter gives concise recalls on MOF materials, their types, and the reason behind choosing MIL-53(Al) as MOF sacrificial precursor in our study. Then, the preparation of mesoporous Ni-Al_2O_3 from MOF is described and the material obtained is compared structurally, physically and

catalytically to a second MOF-based sample prepared by impregnation and conventional Ni-Al_2O_3 material.

Chapter V applies the above-mentioned materials exhibiting good performances in dry reforming of methane to another reaction of interest in the energy domain, the CO_2 methanation that also consumes CO_2. A brief state of the art catalysts is given at the beginning of the chapter before explaining the preparation methods of the materials used and their physiochemical properties along with the catalytic tests results.

Chapter VI ends this report by treating some of the materials in a more realistic dry reforming gaseous conditions evolved from pyrolysis of biomass wastes as given by a Lebanese industry. The aim of this last pat is to investigate the efficiency of our catalysts under harsh conditions of dry reforming that contains CH_4, CO_2, H_2 and CO in the reactants feed, making more difficult to obtain the expected H_2/CO products ratios.

I. Chapter I: Literature review

I.1. Sources of energy from fossil resources

Mixtures of hydrogen (H_2) and carbon monoxide (CO), known as syngas, are important in the energy domain since they can lead to the production of fuel. Such mixtures can be obtained from methane following different reforming reactions. In this chapter, the main resources of methane are presented along with the various pathways of converting it into H_2 and CO. Through the description, an interest is highlighted on the dry reforming of methane (DRM) reaction that will be in the core of this work and where CO_2 is used as a co-reactant. A state of the art is provided to summarize the advancements achieved in the existing catalysts for this reaction. The chapter ends with an outline of the objectives and methodology of the present thesis.

I.1.1. Main resources

a) Fossil fuels

Fossil fuels were discovered over 150 years ago. They are formed from organic matter deposited over the course of million years and fabricated by natural processes deep in the earth or under the sea bed by anaerobic decomposition of buried dead organisms. The fossil fuels such as oil, coal and natural gas extracted by human operations can be further transformed and refined into petroleum products [1–3]. In other words, fossil fuels exist in different forms (solid, liquid, gas) and they have a wide range of carbon content going from products with low carbon to hydrogen ratio like methane (volatile materials) to non-volatile pure carbon as anthracite coal. Oil, coal, and natural gas are known for being described as the energy of the world due to the versatile energy supplies they can offer [3,4] playing a crucial role in the 21st century world energy market with an average rate of production of about several million barrels per day. For instance, oil is the world's primary fuel source for transportation capable of being transformed not only into fuel oil, diesel oil, kerosene, gasoline, and liquefied petroleum gas (propane, butane), but also into other products like fertilizers, plastics and pharmaceutical compounds [2,5]. Coal is mainly used to produce electricity, steel, manufacture cement and synthesize liquid fuel as well as for heating [2,6]. Nowadays, the use of natural gas has been growing in a fast pace into the sector of electric power generation (heat, electricity) with an interesting reliance in other areas (industries, residential, commercial, pipeline and distribution) [2,7].

b) Methane (CH_4)

As natural gas transport is expensive and problematically hard due to the relatively low energy content in relative to its volume, the global market of oil is much bigger and a basic requirement for energy needs. Nevertheless, and in close relationship towards the tendency of using greener energy, the natural gas consumption has increased in the last decade for it is considered as the cleanest burning petroleum based fuel, and this tendency is planned to continue with a net worldwide increase of about 2.8% annually from 2001 to 2025 [8]. It is important to mention that CH_4 properties are utilized when speaking about natural gas because it accounts about 95% of its total volume. The other components with a total of 5%, contain traces of ethane, propane, butane, pentane, nitrogen, carbon dioxide and water vapor [8]. CH_4 gas is a prominent raw material with high abundancy in remote areas distributed all around the world. According to BP statistical review and OPEC oil and gas data, Iran, Russia, Qatar and Turkmenistan have the highest natural gas reserves (Figure I-1) [9]. Methane has the ability to

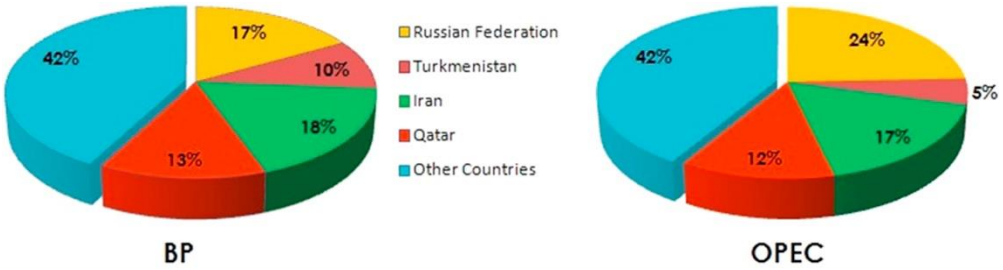

Figure I-1: Natural gas reserves distribution across the world [9]

produce more heat and light energy by mass (H/C ratio: 4/1) than other hydrocarbons and fossil fuels (oil (H/C<2/1), coal (H/C<1/1)) resulting in significantly less carbon dioxide and other pollutants that create smog and pollutes the environment. In other words, one should rely more on CH_4 and replace it for coal and oil to generate electricity and fuel transportation while contributing to environment protection.

I.1.2. Reserves, human consumption and potential depletion

There exists a dilemma about the persistence of this non-renewable source of energy (coal, oil and natural gas) and whether the existing reserves could withstand the intense consumption by the human being [1,10]. Estimations about fossil fuels reserves and availabilities differ and nobody can really have an accurate prediction on their exhaustion. Global energy consumption has increased by 2.2% (2.1 million barrels per day) in 2017 compared to an average of 1.7% for the previous 10 years (BP) [2]. The energy information

administration (EIA) has drawn a relation between the world fuel production and consumption as a function of time (Figure I-2) [11]. It is intelligible that there is an annual change in the world liquid fuels consumption with a positive (2014-2015) or negative (2017) relation between the amounts produced and consumed. EIA predicts that oil discoveries will decrease by 0.2 million b/d in 2019 making global demand outpaces production. In 2020, oil supply will increase by 0.1 million b/d.

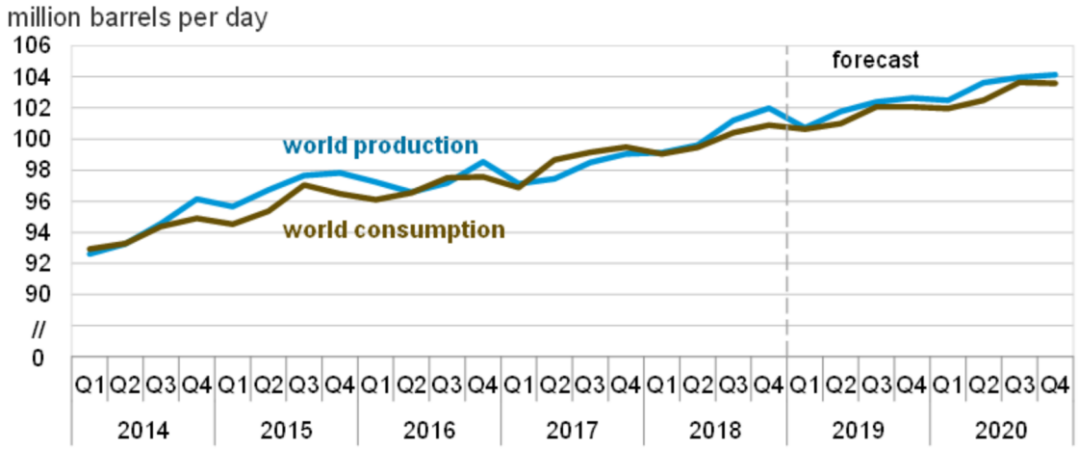

Figure I-2: World liquid fuels production and consumption balance, Source: Energy information administration [11]

On the other hand, scientists and oil companies have a consensus that oil production for the long term forecast has reached a peak (Figure I-3) and we will at a certain moment run out of oil supplies [10,12,13]. The size of oil reserves regularly discovered are getting smaller through years even if technologies (EOR: enhanced oil recovery) are highly advanced for finding new places to look for potential seams of oil. For instance, even if we take the most optimistic case scenario (4% depletion, green curve), in 2025 the world will be able to produce the same quantity of oil as in 1970. Not to mention that the world population in 2025 will be 50% more than what we had in the 1970's [10]. This means that the new discoveries and technologies have only delayed the fall and it is a must that we reduce our

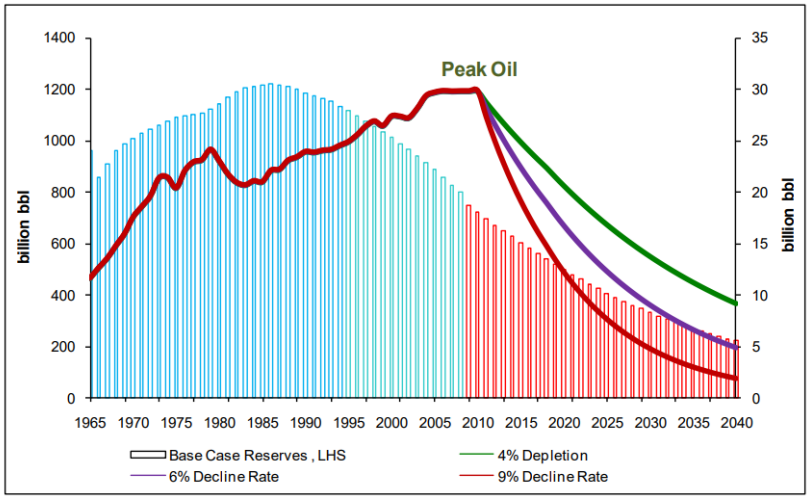

Figure I-3: Peak Oil Forecast, Source: BP statistical review of world energy 2009 [10]

dependence and adjust the falling oil supplies to avoid their depletion. In addition, shahriar Shafiee et al. calculated oil, coal and gas depletion following Klass and New model, and estimated that coal reserves will last until 2112 and it will be the single fossil fuel available after depletion of oil and gas in 2042 [1] if people continue to use them as source of energy. Concerning CH_4, no matter what is the amount of reserve available, it should not be allowed to escape into the atmosphere due to environmental reasons that will be mentioned in the following paragraph.

I.1.3. Environmental issue

I.1.3.1. CO_2 emissions

Another downstream of relying on this traditional method to produce energy, is the detrimental impact on the environment. Burning fossil fuels results in formation of carbon dioxide (CO_2) which is one of the primary greenhouse gases (GHG) responsible for global warming [7,14,15]. According to BP, the global emissions of CO_2 from energy had increased on a basis of 10-year average (2006-2016) by 1.3%. However, in 2017 only, CO_2 emitted faced a calamitous grown by 1.6% [2] which means that humans continue increasing dependencies on fossil fuels resources contributing to a calamitous effect on the environment.

The intergovernmental panel on climate change (IPCC) has summarized in the form of a graph (Figure I-4) the amount in Kg of CO_2 emitted per megawatt-hour (MWh) of energy produced from any type of fossil fuels [16]. We can see several points from this figure. For

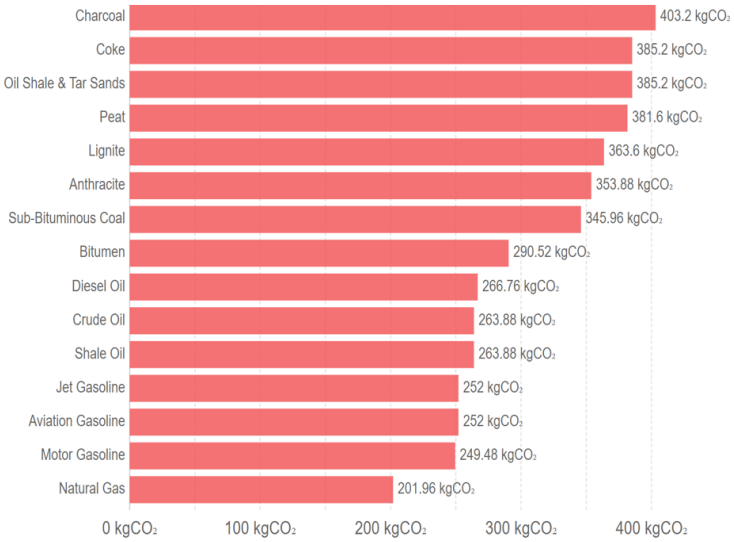

Type of fossil fuels	Amount of CO_2 emitted ($KgCO_2/MWh$)
Charcoal	403.2
Coke	385.2
Oil shale & Tar sands	385.2
Peat	381.6
Lignite	363.6
Anthracite	353.88
Sub-Bituminous coal	345.96
Bitumen	290.52
Diesel oil	266.76
Crude oil	263.88
Shale oil	263.88
Jet gasoline	252
Aviation gasoline	252
Motor gasoline	249.48
Natural gas	201.96

Figure I-4: Carbon dioxide (CO_2) emissions factor, measured in kilograms of CO_2 produced per megawatt-hour (MWh) of energy produced from a given fossil fuel source. Source: intergovernmental panel on climate change (IPCC) [16]

instance, the graph demonstrates that the combustion of coal is responsible for the highest percentage of CO_2 emissions (403.2 $KgCO_2$/MWh). The unconventional oil sources comes next such as oil shale and tar sands with 385.2 $KgCO_2$/MWh emissions. The conventional sources (diesel oil, crude oil, shale oil, and gasoline) also contribute to important CO_2 gas emissions. By comparison, natural gas (CH_4) also results in an inevitable release of CO_2 but in much less quantity than other burning hydrocarbons (201.96 $KgCO_2$/MWh). This is why it is considered as the cleanest type of fossil fuels. Moreover, its burning results in very low amount of NO_x, particulates, and almost 0 SO_2 emissions [2,8]. Hence, CH_4 presents important advantages compared to the other hydrocarbon feedstock, even if its utilization also contributes to an average of 2% increase per year of CO_2 emissions which is planned to regularly continue as illustrated by predictions made until 2050 (Figure I-5) [17].

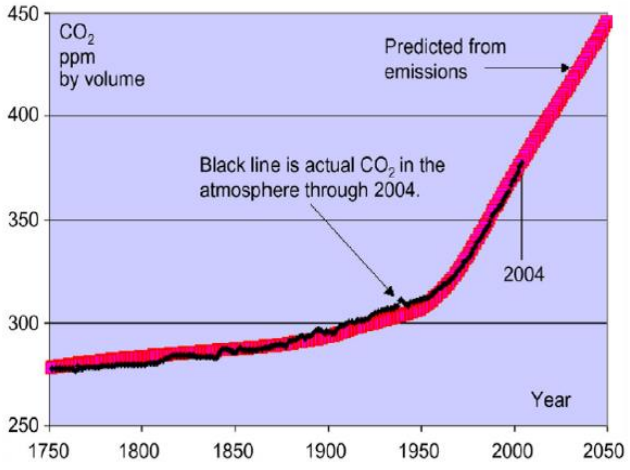

Figure I-5: Global carbon dioxide levels since the beginning of industrial revolution [17]

I.1.3.2. Diversity of deleterious impacts

An additional environmental issue related to using fossil fuels comes from the fact that people nowadays are facing difficulties in extracting oil and gas sources. They rely on fracking and the use of energy intensive methods prone to escape of more CO_2 gases and other air pollutants like sulfur dioxide from acid rain, nitrogen oxides (NO_x), mercury and carcinogenic chemicals [16,18,19].

This stark truth of CO_2 greenhouse emission in addition to the chronic gases are further boosted by scientific facts of sea levels rise, hotter temperatures, and the occurrence of storm weather patterns like tsunamis and hurricanes. They can also contribute to serious health complications in the human being such as lung malfunctioning, asthma, cancer and cardiovascular diseases. They can lead as well to the death of aquatic animals and pollution of ground water if any oil spill is triggered [20,21]. Not to mention that coal mines cause relocation and damage the vegetation, top-soil and contamination of rivers [22].

I.1.3.3. CH_4 and CO_2 as greenhouse gases

The negative consequences of burning fossil fuels and CH_4, and producing CO_2 is not the sole problem. It is significant to deem in mind that CH_4 (oxidized carbon) is also by itself a pollutant if released into the atmosphere as CO_2 gas (reduced carbon). CH_4 and CO_2 are considered as greenhouse gases because they both absorb and emit thermal infrared radiation at the range of our planet emitted wavelength, trapping the heat and making the planet warmer [7,17]. CH_4 is tougher than CO_2 as greenhouse gas with around 120 times more radiative force but it has a shorter lifetime effect with only 12.4 years average. In contrary, CO_2 is a complex molecule thermodynamically stable in the atmosphere with indefinite lifetime [23,24]. It is now well recognized that an effective way to control CH_4 and CO_2 emissions to air and reduce their negative effect in the atmosphere would be to use both as feedstock for energy production especially that there exist natural processes in which methane and CO_2 are emitted.

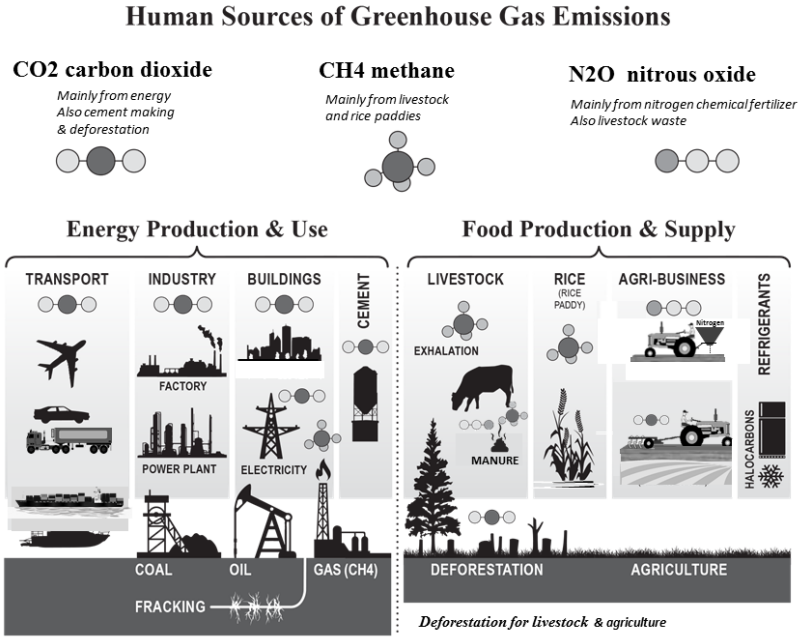

Figure I-6: Summary of human sources of greenhouse gas emissions [17]

Needless to say, Figure I-6 demonstrates that the concentrations of atmospheric greenhouse gases (CH_4 and CO_2) do not only come from burning of fossils fuels but they originate as well from different natural and human activities (biomass) sources [17,23]. Based on a balance between GHG sources and sinks (conversion of the species to different chemical compounds), the amount of GHG in addition to its residence time (RT) in the atmosphere are estimated to be 73% (RT: 150 years) for CO_2, 17% (RT: 12 years) for CH_4, and 8% (RT: 100 years) for other greenhouse gases (N_2O) [7,8,17,25,26]. In brief (Figure I-6), CH_4 is emitted

from livestock and rice paddies, and also from ruminant animals, side products of industrial activities, landfills, gas production, coal mining and waste water treatment. CO_2 is transferred to the atmosphere from production of cement, deforestation in addition to energy (combustion of fossil fuels). According to the United States environmental protection agency (EPA), CO_2 sources come mainly from burning of fossil fuels (93%) while CH_4 sources are distributed between petroleum systems (33%), landfills (20%) and enteric fermentation (22%) (Figure I-7) [27]. Landfills and enteric fermentation are included in the biomass category that can be used as a source of energy limiting reliance on fossil fuels. This strategy is one of our interest and it will be tackled in more details in chapter VI of the thesis.

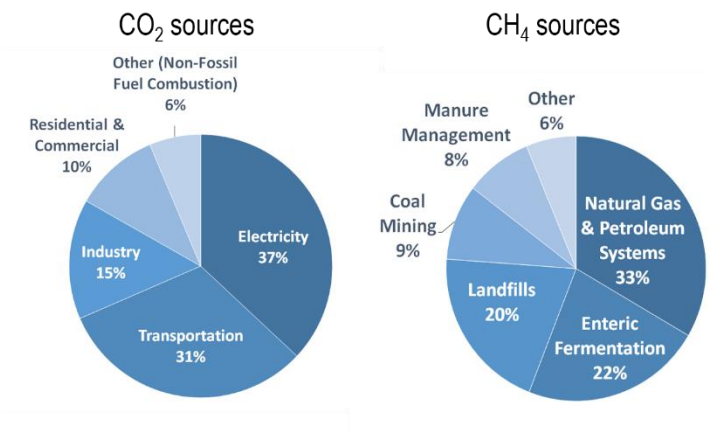

Figure I-7: Percentage of greenhouse gases sources [27]

In order to mitigate the anthropogenic emissions (CH_4 and CO_2) a forward step has been taken by scientists considering few courses of action [17,28] such as improving the efficiency of combustion engine, minimizing utilization of fossil fuels, constructing energy-efficient building, frequent usage of recycled materials, shifting to low carbon energy sources, capture and sequestration of greenhouse gases, reducing deforestation, and fertile land management. Because these pathways are somehow daunting and require deeper investigations and studies to assure their efficiency and be pursued, chemists have been more concerned recently, as mentioned earlier, in utilizing CH_4 and CO_2 either together or separately as raw compounds for the production of useful fuels and chemicals. This is what will be elaborated in the next section.

I.3 Pathways for CH_4 and CO_2 conversions

There are several ways of converting CH_4 and CO_2 gases [17,28,29] through economic pathways. For example, CH_4 and CO_2 can be each used to produce chemicals such as food & beverages, solvent for pharma, fire extinguishers, solvents, and hydrocyanic acid. However, the market potential of fuel is 15 times higher than chemicals and speaking from the structural point of view, chemicals have higher molecular complexity than fuels which are made of simple

chains as in hydrocarbons [17]. Thus, the focus of researchers is mainly towards energy production.

Methane can be used **directly** for the production of heat and power generation by combustion (severe conditions needed to break the stable C-H bond) or it can be converted (**indirect** pathway) to produce a synthesis gas (called syngas) that is a mixture of hydrogen (H_2) and carbon monoxide (CO) [7,28–30]. CO_2 can be also converted (**indirect** pathway) to syngas. Making syngas is of strong interest because it is a crucial intermediate for the production of fuels needed for transportation and energy. The ratio of the syngas produced varies and depending on this value the targeted application is altered. Figure I-8 summarizes the main existing pathways for **syngas applications** [29,31]. An important route (in red) is the use of syngas as reactant in Fischer-Tropsch synthesis for the subsequent production of fuel (gasoline,

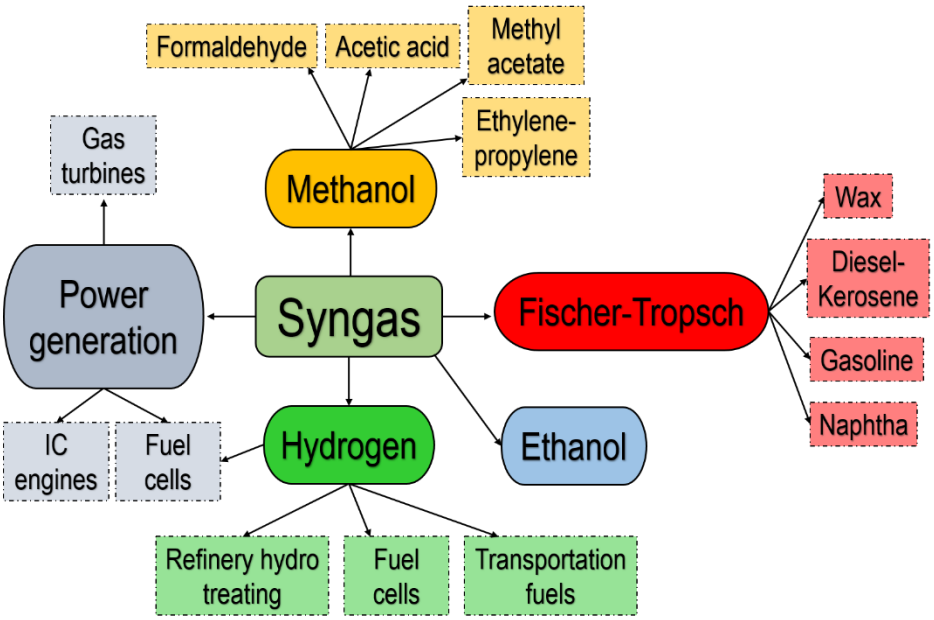

Figure I-8: Schematic with a brief summary about synthetic gas applications [29]

diesel, naphtha), another one (in grey) concerns power generation for fuel cells and gas turbines, a third one (in green) consists in using hydrogen as the source for transportation and refinery hydro treating and, finally, syngas can be converted to methanol to synthesize formaldehyde, acetic acid and ethylene propylene. In fact, in order to obtain the required syngas adapted to the targeted route, there are several reforming approaches in which methane reacts with variant oxidants (H_2O, CO_2, O_2) to synthesize H_2 and CO with different ratios.

I.3.1. Different reforming processes for syngas production

Table I-1 illustrates the six existing methane reforming processes along with their chemical reactions, their enthalpy and their resultant H_2:CO ratio [7,29,30]. Reactions 1 and 2 are widely studied in literature and industrialized in some areas. These reactions in addition to reaction 3 rely on H_2O, O_2 or the combination of H_2O and O_2 to oxidize CH_4 resulting in an H_2:CO ratio between 2 and 3. In brief:

Table I-1: Chemical reactions of CH_4 reforming processes along with their corresponding enthalpy and H_2:CO ratios

Rxn	Reforming Processes	Chemical Reactions	ΔH_{298K} (kJ.mol^{-1})	H_2:CO ratio
1	Steam reforming (SRM)	$CH_4+H_2O \rightarrow 3H_2 + CO$	+206	3:1
2	Partial oxidation (POM)	$CH_4+1/2O_2 \rightarrow 2H_2+CO$	-38	2:1
3	Auto thermal reforming (ATR)	$CH_4+x/2O_2+(1-x)H_2O \rightarrow (3-x)H_2+CO$	+206.2-241.8x	(2-3):1
4	Oxy-CO_2 reforming	$3CH_4+\mathbf{CO_2}+O_2 \rightarrow 6H_2 + 4CO$	+58	3:2
5	Dry reforming (DRM)	$CH_4+\mathbf{CO_2} \rightarrow 2H_2 + 2CO$	+247	1:1
6	Bi-reforming (CSDRM)	$3CH_4+\mathbf{CO_2}+2H_2O \rightarrow 8H_2 + 4CO$	+220	2:1

- In **steam reforming (SRM)**, CH_4 is oxidized by a steam generating a syngas with a H_2:CO ratio of 3 suitable for H_2 production. This reaction is very endothermic and its process is divided into four steps. The first reformer operates at very high temperatures (800-900 °C) with pressure around *15-30 atm* demanding high energy investment to produce the steam itself. The second reformer works at a temperature of 1000 °C and uses a mixture of H_2O and O_2 in the feed. Then, H_2/CO ratio is adapted using successive reactions of water gas shift at 400 °C and 200 °C, respectively [7,32,33].
- **Partial oxidation (POM)** operates at lower temperature than SRM between 500 and 700 °C. The syngas produced has a ratio of 2 adequate for methanol synthesis and purification of CH_4 reactant is not always required. Despite these qualities, this reaction suffers from being highly exothermic. This problem can induce hot-spots in the reactor making the process more complicated and increase the risk of explosion. Pure oxygen supplies also come with a share of technical and economic problems inquiring industries to look for alternative solutions rather than cryogenic unit to separate oxygen from air [33–35].

- **Auto thermal reforming (ATR)** combines H_2O to the process of partial oxidation to solve the economic issue raised. The bright side of adding H_2O within the feed is the ability to impact and control the H_2/CO ratio in the gas product allowing a simpler adaptation to several downstream operations such as ammonia and methanol. However, safety concerns associated with the presence of oxygen have limited their use. In addition, this reaction is more energy demanding and part of the methane fed is invested to generate heat in order to reach the appropriate operating temperature and achieve an optimal conversion of methane to syngas avoiding soot formation [29].

Since the trend nowadays is toward curtailing CO_2 amount in the atmosphere which is also our main concern in this thesis, the focus becomes more towards the 3 next methane reforming reactions that consume such gas in addition to CH_4 (Rxn 4,5,6 in Table I-1):

- **Oxy-CO_2 reforming** resembles ATR in regards to the aim and outcome. The use of a sole O_2 carrier favors the thermodynamic production of H_2 and CO mixture. But, the economic barriers made it imperative to combine CO_2 in the process. Adding CO_2 within the feed leads to H_2/CO ratio of around 6/4 suitable for further use in ammonia and methanol synthesis processes. It has also the appeal of auto thermal operations especially that the latter consumes CO_2. However, safety concerns associated with the presence of oxygen have limited their use.
- **Dry reforming of methane (DRM)** uses only carbon dioxide as an oxidizing agent reacting with CH_4 to synthesize hydrogen and carbon monoxide. This reaction is recently attracting the attention of many scientists despite owing less favorable thermodynamics than the previous mentioned reactions. But, what makes this reaction more interesting is its ability to **greenly** consume the **natural gas** reducing the carbon impact by proportionally consuming **1 mole of carbon dioxide per one mole of methane** invested. The **product** is eventually a **syngas** with an **equimolar ratio of 1** used as a feedstock for the synthesis of large chain hydrocarbons by Fischer-Tropch approach. The energy invested in the reaction may be curtailed by the use of appropriate catalytic systems which would downstream open the opportunity to dry reforming to become an economical process competing SRM that is already industrially mature. What prevents DRM from being scaled up to industrial level, is the difficulty in finding a catalyst that could withstand the high temperature required (due to thermodynamic reasons that will be explained in chapter II) and resist deactivation by sintering and carbon deposition [7,33,36,37]. **This reaction, and more specifically the question of improvement of catalysts, is our core interest in this thesis.**

- **Combined steam and dry reforming of methane (CSDRM)** is a new emerging reforming reaction combining SRM and DRM. Compared to other CO_2 consuming reactions, this chemical reaction produces a "metgas" with an H_2:CO of 2 leading to formation of higher value products particularly methanol and its derivatives. This reaction has been rarely reported in literature due to its high endothermic feature and requirement of energy [7,29,38].

I.3.2. Dry reforming of methane regarding literature

The "web of science" research engine was used as a reliable basic source to estimate the amount of papers published on DRM, SRM, and POX through the years. Statistics were performed on two bases: topic and title search. Figure I-9 illustrates the number of publications for each of these 3 reactions (graphs A to C respectively) as a function of time (year). It is clear

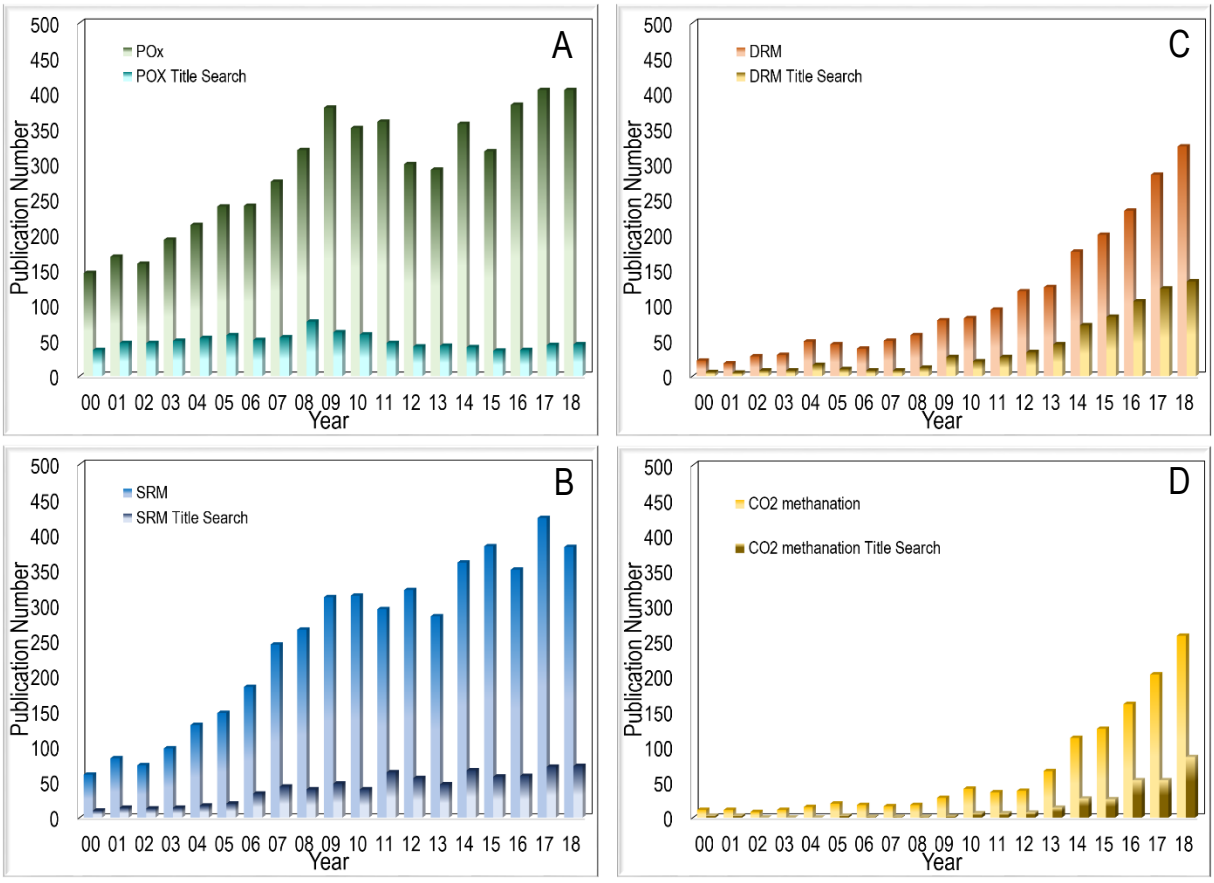

Figure I-9: Statistical histograms displaying the evolution of the publications number as a function of year for SRM, POX, DRM and CO_2 methanation reported studies. The search was evaluated between 2000 and 2018 using either the topic or title in the search engine

that the total number of publications for both SRM and POX (Figure I-9 A-B) is more numerous than DRM research papers as these reactions are more mature and already implemented in some industries. On the other hand, the number of publications available for

these two reactions does not follow any constant trend through time. A small increase is noticed for SRM and POX publications from 2003 till 2009 (200-350 papers) followed by a decrease from 2010 till 2013 (350-300 papers) and a stability in the 2014-2018 period (around 350 papers). In contrast, we can see from Figure I-9 C that the number of papers dealing with DRM reaction (CH_4 and CO_2 as reactants) exhibits a continuous increase in terms of research studies from 2000 till 2018 in response to the environmental CH_4 and CO_2 issues elaborated earlier. For example, 15 years earlier in 2004, only 50 publications were found related to DRM whereas in 2018, about 325 reports dealt with this reaction. This shows that there are so much work in this domain as will be seen in further paragraphs. The reason why we have such increment trend curve is the presence of deficient catalysts incapable of withstanding side reactions that lead to their deactivation despite the improvements made coining DRM in the research stage era. Note also that a similar trend is visible in Figure I-9 D for another reaction using CO_2 (methanation) to which we will also dedicate some interest as introduced in the next session.

I.3.3. Side reactions of catalytic dry reforming of methane

There are several side reactions that could be encountered during DRM. One should compromise his test conditions during operation of the main reaction to satisfy his needs by realizing high conversions and avoiding as much as possible the formation of side products or deactivation of the uploaded catalyst. A summary of the involved reactions are presented in Table I-2 [33,39]:

Table I-2: List of possible involved reactions in dry reforming of methane

Reactions	Equations	ΔH°_{298} (kJ/mol)	Temperature range (°C)
Main reaction			
Dry reforming of methane (DRM)	$CH_4 + CO_2 \rightarrow 2H_2 + 2CO$	247	600-1000
Side reactions with no C(s) production			
Water gas shift (WGS)	$CO + H_2O \rightarrow CO_2 + H_2$	-42.1	200-500
Reverse water gas shift (RWGS)	$CO_2 + H_2 \rightarrow CO + H_2O$	42.1	500-800
CO_2 methanation	$CO_2 + 4H_2 \rightarrow CH_4 + 2H_2O$	-165	100-500
Side reactions inducing C(s)			
CO_2 hydrogenation	$CO_2 + 2H_2 \rightarrow 2H_2O + \mathbf{C_{(s)}}$	-90	100-500
CO dehydrogenation	$CO + H_2 \rightarrow H_2O + \mathbf{C_{(s)}}$	-131	100-500
CO disproportionation	$2CO \rightarrow CO_2 + \mathbf{C_{(s)}}$	-172	100-600
CH_4 decomposition	$CH_4 \rightarrow 2H_2 + \mathbf{C_{(s)}}$	75	600-900

The main **DRM** process is a direct reaction between CH_4 and CO_2 and it is the most endothermic reaction in the series of equations because the CO_2 molecule is very stable. Hence, in order for it to act as an oxidant and interact with CH_4 a high energy is needed to activate it. **Water gas shift (WGS)** and **reverse water gas shift (RWGS)** are non-desirable side reactions that can thermodynamically occur in parallel to the main reaction. However, only the *RWGS* reaction is within the temperature range of *DRM* and thus it is more inclined to be triggered. This reaction consumes CO_2 and H_2 to produce CO and H_2O and thus reduces the ratio of H_2:CO product to less than the required value (1, section I.3.1). The presence of H_2O in the product of the RWGS reaction is also a drawback. In fact, steam could oxidize the reduced active phase during the in-situ run, decreasing catalytic activity and deactivating the catalyst.

CO_2 methanation (Sabatier reaction), seen as possible undesirable reaction in Table I-2, is not in the thermodynamic range of DRM, however, it has also gained our attention in the present work because it is a particular technique that further curtails CO_2 emissions and produces CH_4 as an energy carrier. It has also been newly developed in literature since it is seen in Figure I-9 D that the number of research studies related to this application has been recently continuously increasing through time in a manner similar to that for DRM. Details about this reaction and a literature review will be explained in details in Chapter V.

The formation of carbon should be also taken into account because it is the most limiting feature deactivating DRM catalysts in most published studies. Table I-2 encloses the chemical reactions related to solid carbon deposition in methane reforming processes. In fact, there are four reactions that produce carbon as a product. **CO_2 hydrogenation** and **CO dehydrogenation** are exothermic reactions feasible at low temperatures and therefore they are exempted from being considered in DRM side reactions. On the other hand, **CO disproportionation** (Boudouard) and **CH_4 decomposition** reactions could strike simultaneously with the main reaction producing carbon that blocks the catalyst pore and covers the active sites [7,36,39]. In this PhD, stability experiments were operated mainly at 650 °C coining the probable formation of carbon deposits to *CH_4 decomposition* only. It is important to mention also that not all carbon deposits (Cα, Cβ) are detrimental leading to catalyst deactivation (Cγ), but their continuous accumulation inside the reactor could increase pressure, plug the reactor, and cease the reaction [40].

I.4. State of the art catalysts for dry reforming of methane

Dry reforming of methane reaction needs a robust catalyst capable of withstanding the harsh operating conditions imposed by the reaction, i.e. the high temperature levels and the occurrence of possible side reactions mentioned above. Thus, researchers are trying to design a convenient catalyst using modern catalysis techniques combining several features like low cost, recyclability and environmentally benign ensuring 100% selectivity towards the desired products and good stability [41–44]. The catalytic activity, selectivity and stability per surface atom rely mainly on the type of metal adopted (active component), particle size, structure and location, reduction extent, accessibility of active metal sites, and choice of oxide support. Thus, the current section of this report tackles the type of catalysts employed in dry reforming covering the active phases, the promoters, and the supports examined in this reaction along with their corresponding catalytic activity and stability and the reason behind their deactivation if any. Note that in heterogeneous DRM catalysis, people use oxides as support for the metals and it has no direct catalytic role. In our case, we will focus on Al_2O_3-based support because it is cheap, has a high attrition resistance and high thermal stability [45] that make it industrially enticing.

I.4.1. Type of metals and supports in dry reforming of methane

a) Noble and transition metals: The active metal elements are often divided into two categories: noble metals such as Pt, Ru, Pd, Ir and Rh, and transition metals like Ni, Fe, Cu and Co. A decent number of studies have concealed experimentally and theoretically the excellent activity and stability of precious noble metals in dry reforming of methane due to their high capability of hindering carbon deposition as well as tolerance towards corrosion and oxidation [37,46]. On the other side, these metals are not economically convenient for large-scale industrial service due to their high price and scarce availability [7,43]. Thus, the number of papers embracing noble metals as a primary active phase on Al_2O_3 support has diminished through years especially in the period of 2010-2019 inspecting around 6 papers of different noble metals (Pd, Pt, Ir, Rh) as main active phase with small to moderate amount (0.5-1 wt%) [47–53]. The presence of such small amount of noble metal is not enough to cast carbon formation and increasing further the amount of noble metals added enhance the activity and stability but increase a lot the price of the catalyst. As a consequence these samples were adjusted with alkaline or alkaline earth metals. The CO_2 activation is boosted to form O species

that reacts with $C_{(s)}$ to form CO enhancing basicity of the catalyst and resistance to deactivation [48,51–53]. Other non-alkaline oxygen carriers (PrO_2, ZrO_2) were added to low amount noble metals to benefit from the transfer of oxygen to the reactants abating carbon filaments [47,50]. All the advances in drawing attention towards low-amount noble based-materials by altering them with promoters did not totally eliminate the presence of carbon, and higher loadings are still needed to avoid deactivation and ensure excellent activity and stability.

Due to the restrictions of noble metals (high cost and scarce availability), transition metals have invaded dry reforming of methane studies with nickel receiving much attention due to its vast availability, cheapness and agnate noble metals catalytic activity in DRM [54]. Nevertheless, using nickel promotes sintering and coke formation that are two major concerns in dry reforming decreasing catalytic stability [33,41,42]. Fewer attention has been given to Co-Al_2O_3 based catalysts since they are less performing in DRM [55–59]. They are sensitive to deactivation from oxidation by CO_2 perturbing its stability [55]. Thus, ***the key in dry reforming studies is to design high carbon and sintering-resistance nickel-based catalysts.*** In order to reach this goal, a design of highly active coke-resistant Ni-Al_2O_3 based catalysts can be achieved by utilizing promoters, alloying Ni with other metals, changing support characteristics and catalysts synthesis techniques.

b) Al_2O_3 as support for metal Ni: The supports are in direct physical contact with the supported active sites and affect their behavior and structure, not to mention that in some cases it could interfere in the chemical reactions. The used materials are expected to have a large surface area to efficiently disperse the metal nanoparticles, uniform size and shape morphology, strong mechanical strength, high thermal stability, high surface to volume ratio and a number of defect sites, corners, edges and kinks [43,44].

To date, there are many oxides that have been studied and investigated to support the active phase for methane dry reforming such as SiO_2, Al_2O_3, La_2O_3, MgO, ZrO_2, and CeO_2 [46,59]. Back in 2000 and 2002, studies showed that metal dispersion (Rh) increases in the order of $TiO_2 < La_2O_3 < CeO_2 < ZrO_2 < MgO < SiO_2 <$ MCM-41 $< Al_2O_3$ [60,61]. Since ***nickel is our main interest as active phase*** we checked its performance over different supports in several literatures. Ruckenstein and Hu were the first to highlight the importance of the support nature for nickel. In their study, they proved that the activity and selectivity of the catalyst were highly dependent on the nature of the support following the order of $TiO_2 < SiO_2 < Al_2O_3$. They related such behavior to the metal-support interaction since it can activate and modify the

electronic and chemical properties of the active phase [62]. For instance, TiO_x molecules covered the active sites during reduction by migrating over the surface of Ni particles curtailing the surface free energy and decreasing the catalyst activity. Several other researchers asserted such assumption in their publications [37,46]. Zhang R.J. et al. [63] conducted similar studies to show the significant influence of the support types on the state of active phase (NiO species) and their dry reforming catalytic performance. This group related again the poor performances of SiO_2, TiO_2, and ZrO_2 based catalysts to the low reduction temperature commonly associated to weak interaction with the active Ni species. On the other side, Al_2O_3 based catalyst had very high stability for more than 100 h even at high gas hourly space velocity.

Despite the fact that both silica and alumina have received much attention compared to other supports type due to the high metal dispersion they provide [43], Al_2O_3-based catalysts are still taking the most important space for DRM with almost 109 papers published between the years 2010- early 2019 compared to 55 papers for its silica counterpart (Data taken from Web of Science). In brief, these 2 supports differ chemically. Kinetics and mechanistic studies in literature stated that there is a dual function for DRM depending on the support nature. Thus, it is proved that on acidic or basic supports the CH_4 is activated on the metal and CO_2 on the carrier forming formates or oxy-carbonates. However, for inert materials like SiO_2, CH_4 and CO_2 are activated on the metal only, following a mono functional pathway so when carbon forms by dehydrogenation of methane, the activation of CO_2 and reaction with carbon will become limited resulting in catalyst deactivation [46]. All this leads to inert SiO_2 weakly interacting with the metal, less stable and active compared to mildly acidic Al_2O_3. This chemical difference was recently tackled by Xu Yan et al. [64] in a study where Ni/SiO_2 and Ni/Al_2O_3 were prepared by a same technique to elucidate the effect of the support properties on the catalytic performances. Results have indicated that Ni/SiO_2 depicts initially higher conversion, but poorer stability due to the reduction of Ni at lower temperature than that of Al_2O_3 forming very large Ni particles of 31 nm and promoting the formation of coke precursors. Ni/Al_2O_3 kept stable for 50 h time on stream due to the formation of $NiAl_xO_y$ species reducible at very high temperature stabilizing Ni nanoparticles (Figure I-10).

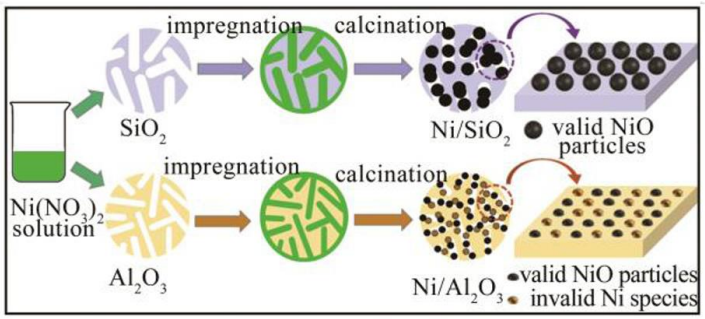

Figure I-10: Scheme representing effect of support on nickel particles [64]

Another important chemical feature that can be addressed is the hydrophobicity and hydrophilicity in both supports. Al_2O_3 is more hydrophilic so its surface is more prone to be hydrated when in contact with H_2O and therefore less available for oxidizing metallic sites and more stable [46]. A study was done by our group on the effect of Ni-based silica and Ni-based alumina catalysts on their performance in reforming. Results indicated a re-oxidation of the Ni^0 active phase in silica-based materials while alumina-based samples preserved the metallic nickel state [65].

However, even if alumina appears to be a better support than silica, Ni-supported on Al_2O_3 still faces deficiencies due to the acidic feature of the support in addition to the common problem encountered on any support that is the high reaction temperature triggering agglomeration of Ni particle that in turn develops carbon. At the present moment, efforts are being made to adjust the Ni-Al_2O_3 stability and synthesize a material that could persist the high reaction temperatures with desirable small, active and stable metal nanoparticles.

I.4.2. Recent developments in stabilization of Ni-Al_2O_3 catalysts

The unstable status of Ni is related to its low Tammann temperature ($0.5T_{melting\ point}$:590 °C) increasing the mobility of the bulk atoms and making the catalyst more susceptible to sintering [37,66]. Thus, deactivation of Ni-Al_2O_3 catalysts very often arises from nickel sintering or thermal agglomeration. Sintering induces a loss of active surface by structurally modifying the catalyst with crystalline growth of the active phase. This phenomenon is strongly favored in DRM by the elevated temperature applied (the reasons will be detailed in section II.2.1.1) and the atmosphere (H_2, O_2) in contact with the catalyst. Carbon residues developed from CH_4 decomposition side reaction, as mentioned earlier, deactivate also the catalyst by either covering the active sites and/or by blocking the pores [67]. Many researchers attributed a correlation between nickel sintering and carbon formation suggesting that large nickel particles have higher carbon deposition rate during methane decomposition [68]. There are three types of carbon classified as **Cα**, **Cβ**, and **Cγ**. **Cα** is known as the most reactive carbon species trivially eliminated by oxidation or reduction at low temperatures (300-450 °C). This type of carbon does not deactivate the catalyst and can play an intermediate role in DRM reaction to *in-situ* form CO product. **Cβ** derives from carbon nanotubes can be removed also at temperatures not exceeding 600 °C. This type of carbon does not lead to catalyst deactivation unless Ni particles become totally encapsulated within the nanotubes preventing access to the gaseous reactants. The formation of carbon nucleus detach and drive Ni nanoparticles away

from the Al_2O_3 support. If carbon nanotubes are formed in large amount they can contribute to reactor plugging and cease of reaction. **Cγ** is a graphitic crystalline carbon created from the interaction between **Cα** and **Cβ** or/and between carbons of the same type (**Cα- Cα/ Cβ- Cβ**) that gradually transform into **Cγ** with time on stream. **Cγ** is the most deleterious type of carbon demanding very high temperatures to be removed (600-850 °C) destroying catalyst stability [69,70].

Around 102 papers were published in the recent years (2010- early 2019) on the improvements made in synthesizing Ni-alumina catalyst that can resist sintering and carbon deposition. The table in the Appendix summarizes the advances done in literature during the past 10 years on Ni-Al_2O_3 preparation methods (17 publications). The table mainly comprises the type of Al_2O_3 used, the method of Ni insertion and its particle size with the test conditions applied, the CH_4/CO_2 conversions obtained, and the reasons of deactivation if any. Thus, the following paragraphs highlight on the main developments made concerning Ni-Al_2O_3 materials and their main results.

I.4.2.1. Alterations in Ni addition to Al_2O_3 support

I.4.2.1.1. Post-Ni addition to Al_2O_3

Taking a look into the Table, several researchers tested different methods of Ni deposition on *commercial Al_2O_3* to enhance its performance. For instance, some used the wet impregnation (W.I.) method to add nickel. However, this technique usually results in a weak interaction between the Ni active phase and the Al_2O_3 support forming large nickel particles that triggered filamentous carbon during DRM reaction [71–74]. Incipient wetness impregnation (I.W.I) was developed to further improve the dispersion and is quite frequently used in many reforming application. It is based on adding a metal-containing solution with volume equivalent to the catalyst support volume [64,75]. The nickel particle size could be as small as 4 nm using this method [64], however Ni generally sinters during the high reaction temperature making it vulnerable to be encapsulated and detached from the Al_2O_3 matrix by carbon, decreasing drastically CH_4 conversion from 80 to 50% as seen in the table. Other techniques applied like the equilibrium deposition filtration technique (EDF) [72], and electrospinning [76], achieved nickel particle sizes of 12 and 6.5 nm respectively. Despite being innovative routes, they do not fit the industry requirements, like the W.I. and I.W.I. that are very simple to apply, and control of many parameters are needed and expensive. Not to mention

that for the case of electrospinning synthesized catalyst, a high amount of carbon was formed after 300 minutes of DRM reaction only [76].

I.4.2.1.2. Simultaneous Ni addition to Al_2O_3

In order to further minimize the particle size and enhance its distribution, few researchers have suggested the direct incorporation of Ni metal into the Al_2O_3 framework (Table in the Appendix) [77–79]. Newnham J. et al. compared the synthesis of Ni/Al_2O_3 using W.I. and I.W.I. to the one synthesized directly in a polyethylene bottle in presence of both Ni and Al precursor [80]. The latter catalyst showed a decrease of 10% in conversion in 10 h then it was stabilized for 200 h with only 2-3% conversion loss. However, the size of the Ni crystallite was sintered after test from 11 to 15 nm contributing eventually to the formation of a lot of carbon nanotubes. Zhan L. et al. [81] developed also a 2-step hydrothermal technique where $Ni(OH)_2$ nanoparticles were synthesized by a 1st-step hydrothermal then anchored into a 2nd-step hydrothermal in presence of alumina precursor to adjust the environment and form a thermally stable catalyst. The unique leaf-like Ni/Al_2O_3 obtained offers more active sites contributing to higher catalytic activity and stability as well as carbon resistance compared to one-step hydrothermal and conventional impregnation method. In addition, the Table Appendix describes a new method to include Ni precursors within the synthesis of the support [77–79,82]. A comparison between impregnated Ni and one-pot (with Ni put in the synthesis mixture) $Ni-Al_2O_3$ shows that Ni can be trivially separated from the support when added after Al_2O_3 synthesis due to the weak interaction that forms destructive carbon in DRM (Figure I-11 b) encapsulating Ni particles by layers and increasing rate of catalyst deactivation. The "one-pot" route managed to form Ni particles in the range of 5-15 nm, with good stability but did not cast the development of carbon, for 28 % of carbon was formed on the spent catalyst compared to 64 % for its impregnated counterpart [77].

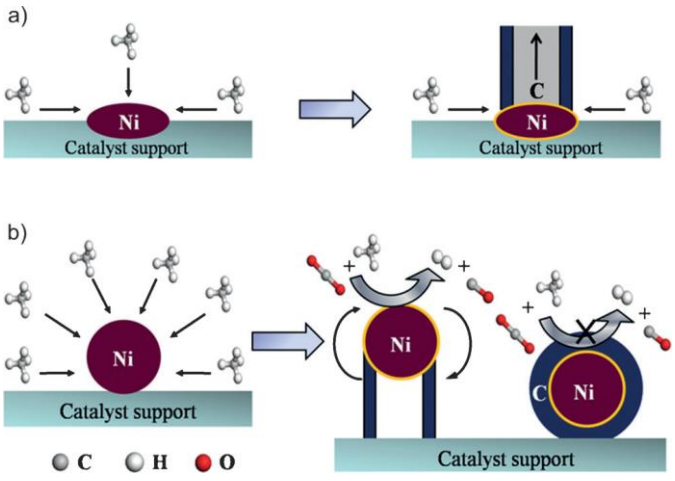

Figure I-11: Schematic representing the influence of Ni insertion in the catalyst on coke formation during DRM [82]

I.4.2.2. Alterations in Al_2O_3 nature

Trials were also made to increase the surface area of Al_2O_3 (Table in the Appendix) and further enhance the nickel dispersion and catalytic properties. Thus, the type of Al_2O_3 support was changed from being *commercial*, to *nanoflakes hollow hierarchical spheres* [83], *nanosheets/nanoplates* [84], *over coated oxide by ALD* [85], and *mesoporous* oxide [77]. The Ni deposited on *hollow hierarchical spheres* Al_2O_3 were in strong interaction with good dispersion, but the formation of coke during DRM was not eliminated [83]. A comparison was done between *nanosheets* and *nanoplates* alumina-based samples. The study showed that the *nanosheets* sample exhibited higher activity due to possessing a higher surface area (245 $m^2.g^{-1}$ compared to 48 $m^2.g^{-1}$ for the nanoplates) enhancing therefore Ni dispersion and metal-support interaction contributing to a better stability over 300 minutes time on stream [84]. Kim W. et al. [86] compared a unique *nanosheet* morphology to a random Al_2O_3 morphology prepared by *co-precipitation method*. The results demonstrated that the Al_2O_3 *nanosheet* catalyst exhibited better coke tolerance in DRM due to random-connected large intersheet pore channels that facilitate transport of reactant product molecules and heavy coke precursors. Whereas, the *precipitation* catalyst possesses randomly small distributed pores, trapping coke precursors to form coke particles that deactivate the catalyst (Figure I-12). Coating Ni/Al_2O_3 catalysts with *alumina ALD overcoats* have proved resistance to sintering and coking with higher stability compared to the uncoated material attributed to the formation of $NiAl_2O_4$ species that preserves the small nickel particle size [85]. However, most of the initial active sites were encapsulated by the *ALD alumina* resulting in lower initial activity in DRM. Recently, attention was directed towards synthesizing *mesoporous* Al_2O_3 supports that can boost activity and stability. Several methods were applied such as the nanocasting method (SBA-15 or Carbon as hard templates) or the modified sol-gel self-assembly

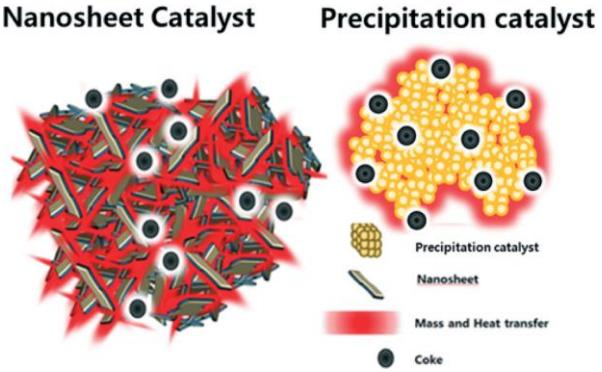

Figure I-12: Schematic illustrating the catalyst morphology effect on coke catalyst deactivation [86]

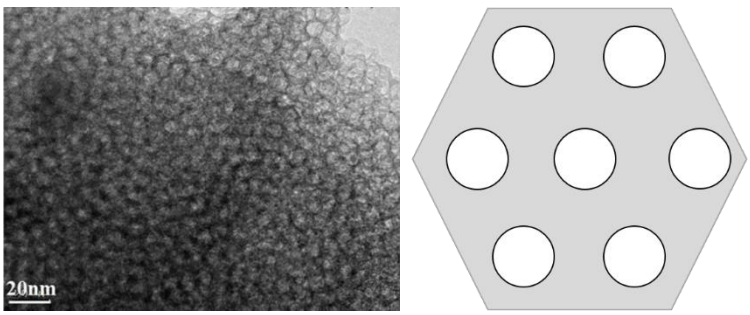

Figure I-13: Porous alumina structure [77]

process with the presence of a soft template (CTAB or P123) as structuring agent (Figure I-13) [87,88]. Compared with the first pathway requiring more than one impregnation and calcination steps, the evaporation-induced self-assembly (EISA) method was the most successful one with Al_2O_3 support carrying ordered hexagonal pores and high surface area (225 $m^2.g^{-1}$) available for Ni species during impregnation. This structure formed rigid, stable and high dispersion of Ni metals inside the mesoporous cage of alumina limiting the nickel sintering to reach a cluster size of 15 nm and resulting in highly active amorphous carbon.

I.4.2.3. Doped Ni-Al_2O_3 catalyst

Besides developing monometallic catalysts with different support modifications and Ni deposition methods, studies were done also on alloying nickel with a second metal to alter the catalyst surface properties (not presented in the Table Appendix). This second metal forms bimetallic materials where Ni is alloyed to a noble [37,89–103] or a transition metal [104–112] having distinctive bi-functional assets when in contact with Al_2O_3 support. However, the bimetallic systems are outside the scope of this thesis, where Ni is the focus since it has better performance than any other transition metal even when used alone and it is way cheaper than noble metals that is being avoided. Same reasoning goes for tri-metallic Ni-alumina catalysts [113–128] that make the system more complex, expensive and far from the purpose required. Adding dopants to reduce and remove carbon deposition on Ni-Al_2O_3 is an interesting approach. Thus, we focused on basified dopants and magnesium specifically since it is less expensive than other dopants seen in literature like Ce [82,129–136], La [137–143], and Mn [144,145].

Basic metal oxides have received a great attention in DRM because of their high Lewis basicity that enhances chemisorption of CO_2 (acidic gas) and improves coke resistance. Barium, calcium and magnesium were applied in dry reforming [146–150]. However, Ba has been barely used because Ni tends to sinter in presence of Barium forming big aggregates and barium carbonates. It may also lead to nickel re-oxidation during handling of catalyst and carbon deposition with large particle size of 20 nm [149]. Ni-doped calcium alumina catalyst revealed in a study an important role in inducing high basicity but did not eliminate the occurrence of carbon and the Ni nanoparticle size obtained was quite large (21 nm) resulting in catalyst deactivation [150]. Ni alloyed with Mg on commercial alumina sample provided the highest CH_4 and CO_2 conversions compared to Ba and Ca supported samples [151,152].

The author explained the difference in performances by a study done on Ni supported on MgO, CaO, and BaO [153]. CO temperature programed desorption results (TPD) showed in this study that Mg promoted sample produces less amount of CO_2 from CO compared to Ba and Ca samples. This means that the Mg-containing sample is more resistant to the disproportionation side reaction $2CO \rightarrow C + CO_2$ over Ni sites implying higher stability. In addition, MgO is the only face-centered cubic type promoter with lattice parameter (a= 4.21 Å, A-B= 2.11 Å) and bond distance close to NiO (a= 4.19 Å, A-B= 2.10 Å) [153,154]. Due to this similarity, a solid solution can be formed retarding reduction of NiO to Ni strengthening the interaction with the Al_2O_3 support and reducing Ni segregation. It is also important to deem in mind that NiO amount should not be too low compared to Mg since only a very small amount of Ni will segregate at the solid-gas interface during reduction curtailing the catalyst activity. Ni-Mg-Al_2O_3 used so far in DRM still faces certain deficiencies that are elaborated in Chapter III.

I.5. Thesis objectives and methodology

Based on this review on dry reforming of methane and on recent advances of Ni-alumina, obtaining highly active and stable catalyst has not been reached. Studies have demonstrated that different parameters during the material preparation can greatly influence its behavior during catalytic test. Needless to say, the one-pot method seems to be the best solution for Ni addition within Al_2O_3 support. The shape of alumina has to be constructed in a way that ensures occlusion and confinement of nickel particles within the support structure to avoid sintering as much as possible. MgO is the most suitable basic dopant to Ni-Al_2O_3 suppressing carbon formation. In this context, the objectives of this thesis is to take advantage of the different positive routes described above to go even further in the elaboration of highly active and stable catalyst for DRM. The proposed approaches are the following:

1. In ***chapter 3***: To combine Mg-dopant with Ni precursors by one-pot within the synthesis of mesoporous alumina catalyst. Altering the EISA method, Ni, Mg and Al precursors are all mixed together to synthesize highly uniform dispersed Ni and Mg among the mesoporous framework of alumina. This technique takes advantages of two features: first, Ni is trapped within the parallel ordered mesopores that cease particle sintering, and second, the presence of MgO suppresses carbon formation by enhancing the chemisorption and activation of CO_2. A target will be also to find the

optimum Mg loading that seems from bibliography (as will be introduced in the chapter) to play a determining role.

2. In ***chapter 4***: To adopt a novel technique derived from one-pot and different type of alumina support as a new way of occluding Ni inside the pores. Thus, we chose an Al-containing Metal-organic framework (MOF) as sacrificial precursor to prepare the catalysts. This route combines the advantages of high porosity, high surface area and intimate mixing between the nickel and support components to synthesize highly stable and active Ni/alumina catalysts for DRM.
3. In ***chapter 5***: To extrapolate the study of the catalytic performances of the most interesting synthesized mesoporous Ni-alumina based materials (tested in chapters 3 and 4 in DRM) to another reaction of potential interest as well, namely CO_2 methanation reaction.
4. In ***chapter 6***: To move to extended and more realistic reactant mixtures for methane reforming reaction after finishing from the conventional model mixtures. Treatment of biomass wastes do not only result in CH_4 and CO_2 formation but includes H_2 and CO. As a result, a product gasification mixture composition from a Lebanese industry containing CH_4, CO_2, H_2 and CO was treated under Ni-Mg-Al_2O_3 based catalysts in reforming reaction to investigate the efficiency of our catalysts under harsh conditions.

To achieve our purpose, many characterization techniques were applied and used in order to analyze the materials prepared. They will be presented first, in ***chapter 2*** where the equipment and experimental conditions for characterizations in addition to the set-up of both DRM and CO_2 methanation catalytic tests and considerations on thermodynamic equilibrium are elaborated. Then, above-mentioned chapters (3 to 6) will systematically recall some

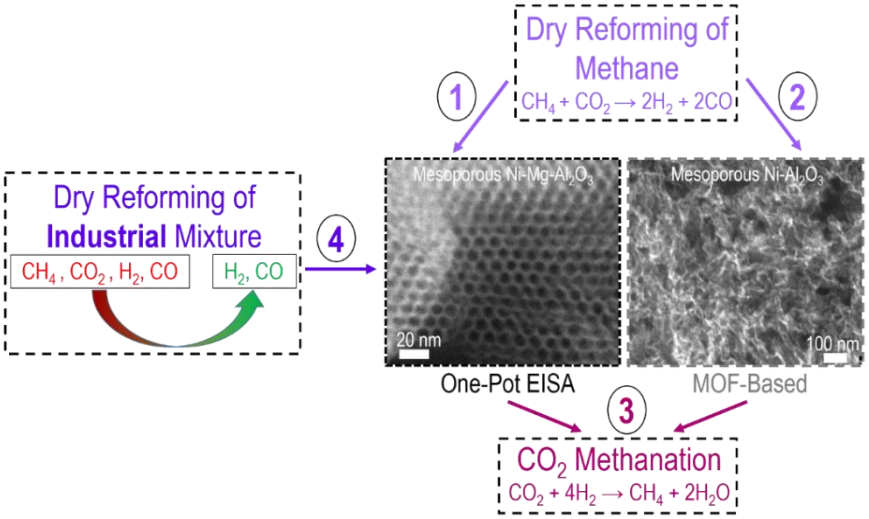

bibliographic elements specific to the treated topic, then introduce the conditions of preparation of the studied samples, analyze (if relevant) their physicochemical properties (both in calcined and reduced states) and finally discuss catalytic features.

II. Chapter 2: Technical Part

The methods adopted for synthesizing the materials employed in this thesis will be presented in the respective chapters where these materials will be studied. The aim of the present chapter is to give a rigorous explanation about the characterization techniques used to determine the physico-chemical properties of the samples prepared embracing the structure, the texture, the reducibility and the state of the active phase in the catalyst system. After explaining each technique used, the catalytic schemes of both dry reforming and CO_2 methanation will be elaborated in details along with the appropriate conditions used in each reaction. This last part will also include a discussion on thermodynamic equilibrium which has to be considered to estimate catalysts performances.

II.1. Characterization techniques

II.1.1. Physicochemical techniques

II.1.1.1. N_2-Sorption

Principle of the technique: This technique provides information about surface area, pore volume and pore diameter. It is based on a gas-solid adsorption phenomenon involving intermolecular forces (Van der Waals), analysed on a volumetric basis at constant temperature. The volume of adsorbed gas (nitrogen in our case) is measured as a function of partial pressure (P/P_0). The adsorption process is followed by a desorption that coexists to represent the opposite operation in which the amount of adsorbed species decreases. The recorded values at increasing and decreasing P/P_0 allow for the plotting of adsorption-desorption isotherms. If the adsorption and desorption curves do no coincide, a hysteresis loop appears. The shape of the isotherms informs on the types of pores present in the materials that can include macropores (pore width

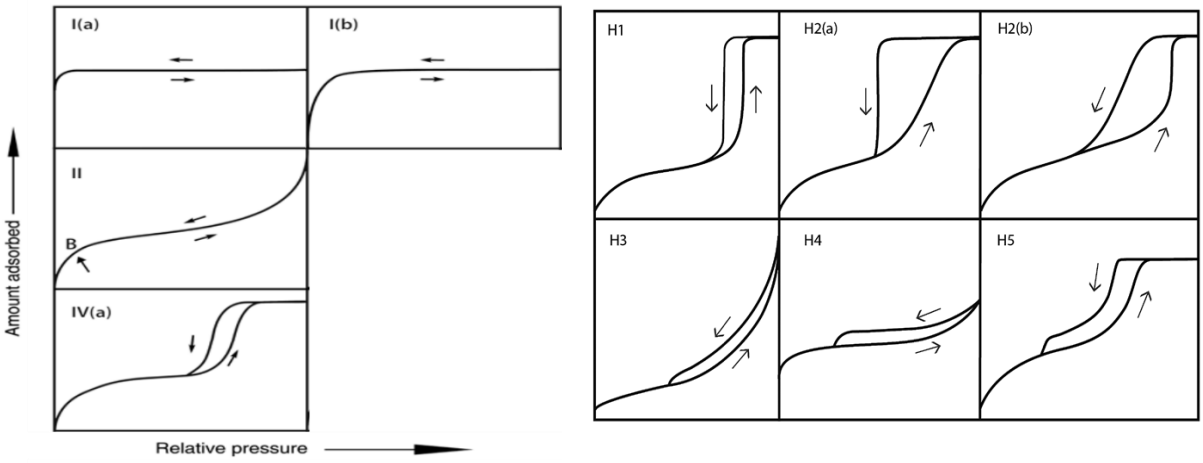

Figure II-1: Classification of physisorption isotherms (left graphs) and hysteresis loops (right graphs) [157]

> 50 nm), mesopores (2 < pore width < 50 nm) and micropores (pore width < 2nm) [155,156]. There exist 6 distinct types of isotherms identified by IUPAC (International Union of Pure and Applied Chemistry), among which three of them only will be of interest in our study (Figure II-1): type I is dedicated to microporous materials with **(a)** narrow micropores (< 1 nm in diameter) and **(b)** wide micropores (with diameter between 1 and 2.5 nm) giving capillary condensation at very low pressure, type II is typical of nonporous/macroporous adsorbents characterized by monolayer then multilayer adsorption on surfaces, and type IV is related to mesoporous samples with the presence of capillary condensation in the mesopores giving a hysteresis. For this latter type, many different kinds of hysteresis loops have been reported where the main ones are illustrated in Figure II-1. To elaborate, H1 loop is given by materials with a narrow range of uniform mesopores, H2 loop is found in more complex pore structure where network effect is crucial associated to pore blocking, and the unusual type H5 hysteresis could be found in plugged hexagonal template silica having open and partially blocked mesopores. H3 resembles a type II isotherm that belongs to plate-like particles such as clays or to macropore networks not fully filled with pore condensate. H4 loop possesses an adsorption branch that is a composite of types I and II and is found in zeolites and micro-mesoporous carbons.

Procedure: Nitrogen adsorption-desorption experiments were conducted on an ASAP 2020 Micromeritics apparatus that contains degas and analysis ports. 70-80 mg of the sample (support, materials calcined and reduced) to be analysed was enclosed in a glass tube and degassed under vacuum for 2 hours at 250 °C with a rate of 10 °C.min^{-1} in order to remove all impurities (H_2O, CO_2) from the surface of the sample prior to N_2-sorption analysis. After degassing, the sample was placed in a liquid nitrogen bath (-196 °C). The adsorption isotherms were obtained by introducing stepwise known volumes of N_2 into the cell (adsorption) then evacuating the cell progressively (desorption), and plotting the volumes as a function of the equilibrium pressure P/P_0 at each step in the range of 0 to 1.

Derived results: The values of surface area, pore volume and pore diameter were obtained directly from the machine software that did automatically the calculations:

a) Surface area (Brunauer-Emmet-Teller method): The conventional linear equation applied is the following:

$$\frac{\frac{P}{P_0}}{n\times(1-\frac{P}{P_0})} = \frac{1}{n_m\times C} + \frac{C-1}{n_m\times C}\times\frac{P}{P_0}$$

where,

- n is the volume of gas adsorbed at relative P/P_0 at standard temperature and pressure (0 °C, 760 mmHg) and is deduced from the isotherm curve (y-axis)
- P/P_0 is the total pressure over the vapor pressure of the adsorbate at experimental temperature conditions and is deduced from the isotherm curve (x-axis)
- n_m is the specific monolayer capacity, calculated as specified below
- C is the BET constant related to heat of adsorption and this parameter is exponentially related to the energy of monolayer adsorption.

A convenient way to derive n_m is to plot $P/P_0/(n \times (1-P/P_0))$ as a function of P/P_0 to form a linear relation expressed by BET plot. The y-intercept of this line corresponds to $1/n_mC$ and its slope is $C-1/n_mC$. This linearity of the BET plot is restricted to a range of $\frac{P}{P_0}$ of 0.05-0.3. The second part in the BET method is to calculate the BET surface area from the monolayer capacity based on the equation: $a_{S\,BET}=\frac{n_m*NA*\sigma_m}{m}$

where, σ_m is the molecular cross sectional area taken by the adsorbate molecule in the complete monolayer (σ_m (N_2): 0.162 nm^2), a_s (BET) is the BET specific of the adsorbent (catalyst) of mass m (g), NA is the Avogadro's number ($6.023*10^{23}$ $molecules.mol^{-1}$) and n_m is the volume adsorbed at monolayer coverage (ml) [155].

b) Pore volume: The total pore volume is determined from the amount of vapor adsorbed at a relative partial pressure close to unity (P/P_0 = 0.95-0.99) and taking into consideration that the pores are filled with the adsorbate in the bulk liquid state. The microporous volume is determined by t-plot method using: $t = t_m*(V_{exp}/V_m)$ where t is the thickness of adsorbed multilayer, t_m is the thickness of each layer (t_m=3.54 Å (N_2)). The low linear region intercept with the y-axis corresponds to microporous volume [156].

c) Pore size: The pore size distribution curves are applied on the desorption branches of the adsorption-desorption curves by applying the Kelvin equation: $r_k=\frac{-2\sigma v}{RT\ln(\frac{P}{P_0})}$ where, r_K is the Kelvin radius, σ is the surface tension of the liquid condensate, v is the molar volume of the liquid condensate. The pore radius (r_p) for the cylindrical pores is calculated by the sum of Kelvin radius (r_K) and the film thickness of adsorbed multilayer (t): $r_p = r_K + t$ [156].

II.1.1.2. X-ray diffraction (XRD)

Principle of the technique: This technique determines the crystalline structure and size of crystalline domains in the catalyst. An incident X-ray beam is directed towards the solid

material used in which the intensity of the diffracted X-ray is collected (Figure II-2). Diffraction occurs when the angle between the incident rays and a crystallographic plan is identical to the angle between this plan and the diffracted rays. The resulting constructive interference of the diffracted beam enhances the diffracted intensity following what is called the Bragg's law $2d\sin\theta=n\lambda$ [157] where, θ is half the diffraction angle, n is the order of diffraction (equal to 1), λ is the wavelength of the radiation, d is the distance between two planes of the same crystallographic family (Å) with indices hkl.

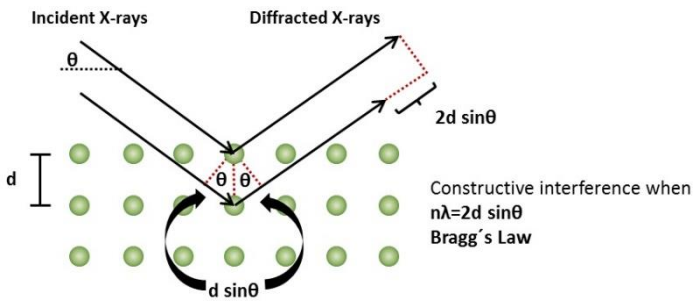

Figure II-2: Mode of X-ray diffraction

Procedure: The small angle XRD patterns were measured in the 2 Theta range between 0.5 and 5°on a Brüker D8 diffractometer (available at LRS, Paris) operating at 30 kV and 10 mA, using the CuKα wavelength (1.5418 Å) and a step size of 0.01° (1 s per step). These patterns were recorded for the calcined and reduced Ni-based materials. The wide angle XRD measurements were conducted on a PANalytical XPert^3 diffractometer in Lebanon (Cu Kα, λ=1.5405 nm) in a 2 Teta range between 5 and 90°. A voltage of 30 kV was used with a current of 10 mA and a step size of 0.02° at 2 seconds time per step.

Derived results: The nature of the nano-crystalline phases in the samples are determined by a direct comparison of the obtained diffraction patterns to standard powder XRD files found in the International Center for Diffraction Data (ICDD). The particle size of the crystal domains is calculated based on the full width at half maximum using Scherrer equation: $D= K.\lambda/\beta.\cos\theta$ where, D is the average nanocrystals size (A), K is the shape factor (0.9 for spherical particles), λ is the X-ray wavelength (1.5405 A), β is the full width at half maximum (FWHM) calculated from the Warren equation: $\beta=\sqrt{(\beta^2_{measured} - \beta^2_{reference})}$ with $\beta_{reference}=0.18°$, and θ is the peak position (radians).

II.1.1.3 X-ray fluorescence (XRF)

Principle of the technique: X-ray fluorescence (XRF) is a technique of non-destructive chemical analysis (Al and Ni in our case). This is made possible by the respond of atoms to the interacted X-radiation. When the sample is illuminated by an intense X-ray beam (incident beam), the sample is excited by the primary X-radiation and emits X-rays along a spectrum of wavelengths which characteristics depend on the type of atoms present in the material. To

elaborate, when the atoms in the sample absorb X-ray energy by ionization, electrons from the inner electron shells (K) are knocked and ejected. The resultant void is replaced by electrons from an outer higher energy orbital (L or M shell) releasing energy (fluorescence radiation) due to the decreased energy of the inner electron orbital compared with the outer one. This energy released generates emission X-rays in the form of Kα and Kβ radiation that is a characteristic of a particular material evaluated by a detector [158] (Figure II-3).

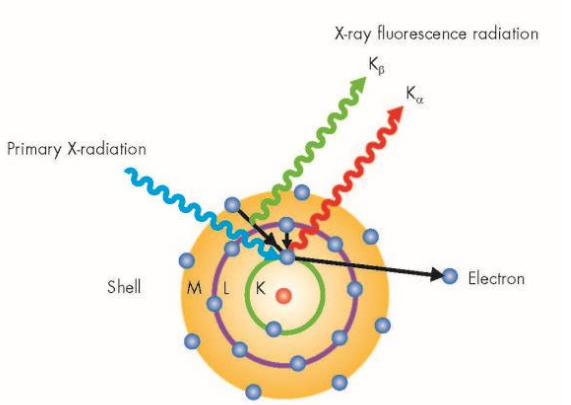

Figure II-3: Principle of X-ray fluorescence

Procedure: XRF was performed on an XEPOS spectrometer (Spectro Ametek). Quantitative data were obtained using the MicroPowder method combining the well-established fundamental parameters approach to XRF spectrometer calibration (calibration curve previously established from NiO and alumina mixtures with known chemical compositions) with automatic correction for matrix effects by using the Compton backscatter information from the sample to calculate the matrix interference.

Derived results: The content in elements obtained by the analyses were used to calculate the chemical compositions of the material studied (Al, Ni, Si).

II.1.2. Electron microscopies

II.1.2.1. Transmission electron microscopy (TEM)

Principle of the technique: Information about the support morphology and nickel nanoparticles dispersion will be trivially identified in this technique. The electron beam passes through the sample where the electrons are absorbed as a function of sample density, thickness, and chemical nature. The electrons interaction forms an image on Ni-Al_2O_3 material morphology with Ni particles appearing as black dots since it is thicker than Al_2O_3 support. This technique can be used also in diffraction mode opening the feature of determining reticular distances and crystalline zones that facilitates identifying the nature of the particle present in correlation with the **I**nternational **C**enter for **D**iffraction **D**ata (ICDD) sheets. The chemical composition can be also determined when enough energy is present in the electron beam ejecting a core-level electron energy from an atom that is further filled by a higher-level electron energy. The difference between these two energy levels emits an X-ray energy that is a

characteristic of an element. Combined scanning transmission electron microscopy-High angular annular dark field (STEM-HAADF) and energy dispersive X-ray (EDX) mapping visualize further the Ni distribution in ultra-thin sections of a selected sample. The response of the signals in HAADF mode depends on the contrast of atomic number of the elements present in the sample. It detects heavy elements (in our case Ni (Z=28) dispersed on supports (Al_2O_3 in this report, Z=19) and make it clearer to visualize occlusion of Ni inside the pores compared to normal TEM mode [159,160]. Using the EDX mapping complements HAADF experiment by chemically analyzing the elements present on the catalyst that also gives an indication about the homogenous distribution of each of them.

Procedure: A JEOL-JEM 2010 electron microscope operating at 200 keV (LaB_6 gun) was used for transmission electron microscopy (TEM) experiments. The observations were done on ultrathin sections of the samples prepared by mixing a few milligrams of the powder embedded in a resin, and heated at 60 °C for 48h to provoke polymerization. The polymerized blocks were cut by an ultra-microtome so we could obtain slices (50-70 nm in thickness) deposited on copper grids covered with a carbon membrane layer. Combined STEM-HAADF and EDX Mapping was performed on a JEOL-JEM 2100Plus microscope. The analysis was performed on areas of diameter between 100-250 nm.

Derived results: For the mesoporous materials, when the organized alumina grains are parallel to the electron beam, organized parallel channels are detected, whereas, the perpendicular orientation of the grain to the beam shows hexagonal pore apertures at high magnification. Average sizes of nickel particles (calcined, reduced and spent materials), when visible, were estimated using the ImageJ software and taking at least 500 particles into consideration. This technique also allows for visualization of carbon deposits if present.

II.1.2.2. Scanning electron microscopy (SEM)

Principle of the technique: SEM provides information on the external surface topology of the grains. A specimen is scanned with a focused beam of electron that interacts with the electrons of the material observed generating pictures to study the surface topography (secondary electrons imaging) but also to check existence of external nano-metal particles (backscattered electrons imaging).

Procedure: Scanning Electron Microscopy (SEM) images were taken on a Hitachi SU-70 SEM-FEG microscope (LaB6 Gun) with an electron acceleration tension of 7 kV. The samples were deposited on the analysis Al support and observed in mixed mode (70% of secondary electrons and 30% of retro-diffused signals).

Derived results: The grain morphology and external surface of the sample are visualized with depiction of external Ni particles if present and visualization of carbon species over spent catalysts.

II.1.3. Spectroscopies

II.1.3.1. X-ray photoelectron spectroscopy (XPS)

Principle of the technique: It allows for a clear understanding of the nature and chemical states of the elements present on a material surface. Photoelectrons are ejected from core energy levels of different atoms in the sample after X-ray bombardment. They are then collected and their kinetic energy (E_k) measured is transformed to binding energy (E_B) by a given incident energy of the X-ray beam ($h\nu$): $h\nu = E_k + E_B$ [161]. The XPS curve is plotted using the emitted photoelectron intensity as a function of the binding energy.

Procedure: An Omicron (ESCA+) X-ray photoelectron spectrometer with Al Kα ($h\nu$ =1486.6 eV) X-ray source having a 300 W electron beam power was used to visualize the XPS spectra. The sample was first evacuated under a vacuum of less than 10^{-10} mbar, then a monochromatic X-ray (Al Kα) irradiated the sample and excited the electrons.

Derived results: The surface composition of the material is determined by attributing the observed energy peaks to a specific element and quantifying their area using the Casa XPS software.

II.1.3.2. Raman spectroscopy

Principle of the technique: The sample is illuminated with a monochromatic laser beam that creates a scattered light upon interaction with the sample molecules. The strike monochromatic radiation scatters in all direction after the collision with the sample. Most of the scattered radiation acquire similar frequency to that of the incident one (Rayleigh scattering) A very small fraction of the scattered light has a distinct frequency than that of the incident light which allows the construction of the Raman spectrum. With higher incident frequency than that of the scattered one, Stokes lines are seen in the Raman spectrum whereas anti-stokes lines appear when the frequency of the scattered radiation is higher. Conventional Raman spectroscopy measures Stokes bands because they are more intense than anti-stokes bands at normal temperature. The latter are usually used to measure fluorescing samples that interfere with Stoke bands. The Raman spectrum appears in the form of intensity as a function of wavenumber shift that is a characteristic of a chemical component. The Raman spectrum

provides further information about the quantity of the component present inferred from the intensity of the spectrum, stress and strain states identified from the peak shift, the degree of crystallinity revealed by the width of the peak and crystal symmetry and orientation detected from the polarization state [162].

Procedure: Raman measurements were conducted on a Kaiser microscope optical system (RXN1) containing a charge-coupled detector. The laser beam (λ = 785 nm) was focused by adjusting the microscope to an objective of 50X long working distance (8 mm) lens. The spectra obtained were collected over a range of 150-3200 cm^{-1} with a 10 mW laser power, 10 seconds acquisition time and 30 accumulation per each spectrum.

Derived results: In our case, Raman was adopted to identify the presence of carbon and its properties on the spent catalysts after DRM reaction. Graphene and graphite in particular have stacks of sp^2 bonded planar graphene sheets that give a Raman spectrum with a main G band at around 1585 cm^{-1}. Carbon nanotubes are composed of rolled up graphene sheets in the form of hollow tubes that induce an additional D band that is located at 1350 cm^{-1}. The presence of this latter peak depicts a defect in the structure of carbon formed and lessen its degree of crystallinity. This assumption is more estimated by the calculation of the intensity ratio between these 2 bands. For instance the lower the I_D/I_G ratio, the higher is the degree of crystallinity of the carbon and the more difficult becomes its removal.

II.1.4. Thermal techniques

II.1.4.1. Temperature programmed reduction (TPR)

Principle of the technique: Temperature programmed reduction (TPR) is a technique used to characterize the reducibility and amount of reducible species in a sample. A flow of H_2 diluted in Ar passes through the sample that is progressively heated. The composition of the gas is continuously compared to a reference gas and any consumption of hydrogen by the studied material can be detected based on the variation of a thermal conductivity detector (TCD). Before reaching the detector, the gas flow is circulated into an ice bath in order to trap any water

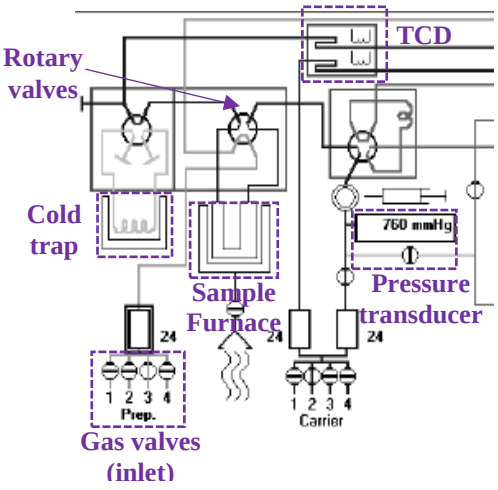

Figure II-4: TPR schematic

produced during the reduction reaction (in our case $NiO_{(s)} + H_{2(g)} \rightarrow Ni^0_{(s)} + H_2O_{(g)}$) and to guarantee the detection of the sole H_2 component (Figure II-4).

Procedure: Measurements were performed on an Autochem 2920 equipment (Micromeritics) (Figure II-4). The calcined samples (80 mg) were deposited on a quartz wool inside a U-shaped quartz reactor and the H_2 consumption profiles were registered during heating from 25 °C till 900 °C with a rate of 10 °C.min^{-1} and a 5 vol% H_2/Ar flow of 30 ml.min^{-1} at 1 atm.

Derived results: The amount of hydrogen consumed by each material was evaluated by integrating the area under the TCD curve over the reduction temperature range. Different reduction peak temperatures could give an idea about the interaction between the active phase (Ni) and the alumina support used with higher reduction temperature triggering stronger metal-support interaction.

II.1.4.2. Thermo-gravimetric analysis (TGA) coupled with differential thermal analysis (DTA)

Principle of the technique: Thermogravimetric analysis (TGA) coupled with differential thermal analysis (DTA), depicts weight changes (TGA) and exothermic or endothermic heat flow (DTA) as a function of both time and temperature during heating. The increase in temperature decomposes components that their corresponding weight loss/gain can be calculated and the components nature can be as well identified by mass spectrometry (MS).

Procedure: Experiments were performed on a TA SDT Q600 instrument working in horizontal mode. One of the two alumina crucibles was filled with about 10 mg of sample while the other (reference) crucible was kept empty. Both were located in the heating chamber and equipped with thermocouples to follow simultaneously weight and heat flow changes during heating, carried out in air flow (50 ml.min^{-1}) from room temperature to 900 °C with a ramping rate of 5 °C.min^{-1}. A capillary placed at the exit of the chamber and connected to a Fisons VG Thermolab Mass Spectrometer was also used to perform continuous mass spectrometry (MS) analysis of the exhaust gases.

Derived results: We used this technique for the detection in our samples of carbon and nitrate species able to be oxidatively decomposed upon heating in air accompanied by a weight loss. When present, the associated exothermic behavior was detected by the positive increase of the heat flow and MS was used to identify the nature of the evolved gaseous products.

II.1.4.3. Hydrogen chemisorption

Principle of the technique: H_2-chemisorption measurements allow for the estimation of the number of metal surface sites which is used in the calculation of turn over frequency (TOF) for any metal-containing catalyst for a specific reaction. This method is of peculiar interest when the optimization of a catalytic formulation is targeted as it estimates the available metal surface area of samples resulting from various preparation procedures and conditions (temperature, type of support), and thus provides an indirect information about the catalytic reactivity of the catalyst. Metal adsorption sites must be accessible in large amount to the probe molecule. Weakly adsorbed species "R" (reversible adsorption) are most often present on the surface of the support, whereas more strongly chemisorbed species "I" (irreversible adsorption) are usually bound to metals [163] (Figure II-5). To distinguish between reversible and irreversible adsorption, a second chemisorption isotherm is run after the sample is evacuated following the first chemisorption isotherm to remove the weakly adsorbed molecules. In this 2nd chemisorption isotherm measurement, the surface metal sites are already covered by a monolayer of chemisorbed species and thus the recorded H_2 uptake is only related to the reversibly adsorbed species. The isotherm due to irreversible adsorption of the probe (Figure II-6) is obtained by subtracting the uptake of the reversibly adsorbed species (2nd isotherm) from the total uptake (reversible + irreversible, 1st isotherm). The dissociative adsorption of H_2 occurs onto 2 surface metal sites ($H_2 + 2M_s \rightarrow 2H\text{-}M_s$, M_s is a surface metal atom (Ni)).

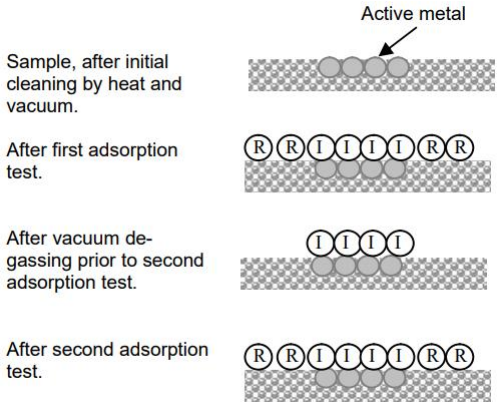

Figure II-5: Steps required to determine chemisorption isotherm

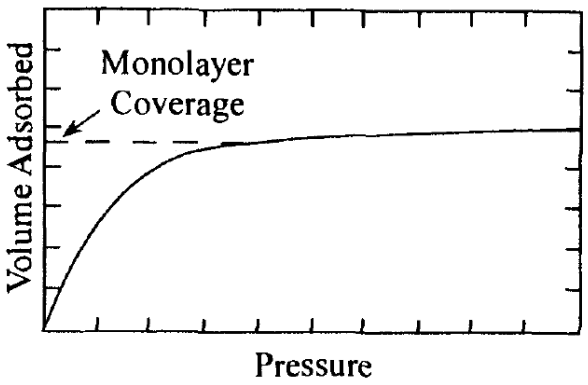

Figure II-6: Chemisorption isotherm

Procedure: H_2-chemisorption measurements were conducted on BELsorp-max (MicrotracBEL) apparatus. The samples (~ 200 mg) were firstly reduced under hydrogen for 2 hours at 650/800 °C with a heating rate of 10 °C.min^{-1} before evacuation at 620/770 °C for 1h. Then the H_2-chemisorption experiments were performed at 298 K in the 0-50 kPa domain with intermediate evacuation of the samples for 2 h at 298 K between the first and the second isotherm.

Derived results: The fraction of metal exposed (dispersion) was estimated from the H_2 chemisorption measurements using the following equation: Dispersion (%) = N_S/N_T, where, N_S represents the number of surface metal atoms obtained from the chemisorption data and N_T is the total number of metal atoms present in the sample. TOF can be then calculated by the following formula: $TOF=\frac{(CH_{4,in}-CH_{4,out})\times AB_{Ni}\times F}{D_{Ni}\times W\times X_{Ni}}$ ($CH_{4,in}$ and $CH_{4,out}$ are the inlet and outlet concentrations of CH_4 respectively, AB_{Ni} is the atomic weight of Ni, F is the total flow rate ($mol.s^{-1}$), W is the mass of the catalyst (g), XNi is the Ni content ($g_{Ni}.g_{cat}^{-1}$), D_{Ni} is the Ni dispersion).

II.2. Experimental catalytic tests set-ups

This part describes the equipment and conditions used to perform the methane reforming reaction (both dry reforming of methane alone, and reforming of waste pyrolysis mixture) and the CO_2 methanation reaction. Before doing that, thermodynamic equilibrium is calculated for each type of reaction and the employed procedure is explained. This is important to understand the choice of experimental conditions (temperature) and to properly evaluate latter catalysts performances.

II.2.1. Conditions for Dry Reforming of Methane

II.2.1.1. Thermodynamic equilibrium curves for standard DRM

Thermodynamic equilibrium was estimated based on the HSC (H, S and C stand for enthalpy, entropy and heat capacity respectively) 7.1 chemistry software using the Gibbs free energy principle. As a first step, CH_4 and CO_2 are inserted in the software as initial reactants with CH_4:CO_2 ratio of 1 and H_2O, H_2, and CO as expected components products. The temperature is varied between 100 and 1000 °C at a constant atmospheric pressure. Figure II-7

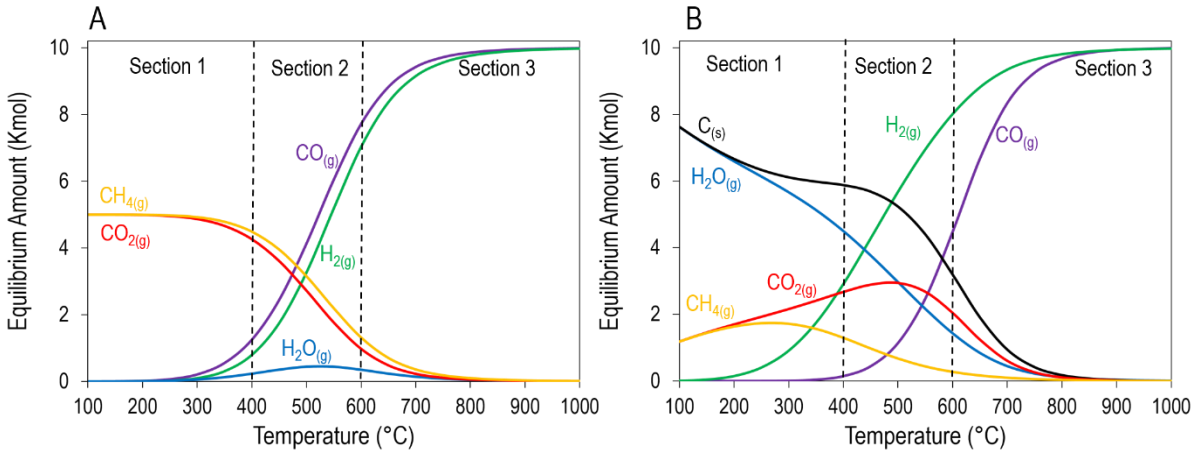

Figure II-7: Thermodynamic equilibrium curve for DRM (CH_4:CO_2 = 1:1) reactants and products at P= 1 atm (A) without and (B) with carbon as side product and Argon as diluent

A illustrates the results obtained under such parameter conditions showing the evolution of concentrations of all gaseous components as a function of temperature. In this figure, CH_4 and CO_2 concentrations remain constant and no products (H_2, CO) are formed at low temperatures (section 1). DRM starts to occur at temperatures above 400 °C with maximum CH_4 and CO_2 conversions attained at 800 °C (section 3), confirming indeed the endothermic behavior of this reaction. The expected H_2:CO ratio at high reaction temperature is 1. The only possible side reaction in this case is the RWGS dominating in section 2 producing H_2O and lowering the H_2:CO ratio (<1). In the experiments 650 °C was used instead of 800 C because it favors lower energy consumption and still limits carbon formation favoring the main DRM reaction.

In the second step, carbon is allowed to take place in DRM and therefore was added as an additional product component to H_2, CO and H_2O. Figure II-7 B illustrates the thermodynamics calculations results in presence of carbon. It clearly shows that carbon influences the DRM reaction by retarding its occurrence. For instance, at low to moderate reaction temperatures (sections 1, 2) side reactions prevail like CO dehydrogenation and CO disproportionation producing C(s) and H_2O, thus hampering the main reaction. DRM prevails at temperatures above 600 °C (section 3) shifting the maximum CO_2 and CH_4 conversions to 900 °C.

Thermodynamics equilibrium curves for reforming of waste pyrolysis product mixture are presented and discussed in details in chapter VI.

II.2.1.2. Equipment for reforming reactions

Dry reforming experiments were performed in Lebanon at the University of Balamand using a **M**icro**a**ctivity-**R**eference catalytic reactor **MAR** (PID Eng. and Tech., Spain) unit,

Figure II-8: MAR equipment and Micro-GC

(Figure II-8). This unit encompasses a hot box, a reaction system and valves control elements. A Gilson high performance liquid chromatography (HPLC) pump is present on the top of the unit to generate water if needed (not used in our case). A computer equipped with remote control system can be seen next to the MAR including communications through Ethernet capable of following continuously all variable parameters including pressure, temperature, hot box temperature, and gas flow rates. This MAR is connected online to an Inficon3000 gas chromatograph Micro-GC unit to analyze the reactor outlet (reactant and product gases). This Micro-GC is composed of thermal conductivity detectors (TCD) and two columns for gas composition detection: molecular sieve column (column A) adsorbs CH_4 (retention time (RT): 2.2 min), CO (RT: 3.2 min) and H_2 (RT:0.8 min) gases and plot U column (column B) adsorbs CO_2 (RT: 0.65 min) gas. CH_4 is detected as well on Plot U column but the Mol Sieve column has been used for CH_4.

The PID (Process Integral Development) diagram (Figure II-9) provides a detailed description of the interior operation, divided into 3 main parts. The first one includes the gas delivery system including in our case CH_4, CO_2, H_2 and Ar gases connected each to a mass flow controller to obtain the required flow rate before being mixed together in a gas mixer. The 2nd part of the scheme involves the hot box inside which the main reactor is settled. Thus, the mixed gas reactants are entered into the hot box that is equipped with an electric forced convention heater to control the temperature (between 160 and 180 °C) to restrict any possible condensation. The preheated streams then merge into a 6-port valve controlled to direct the flow path either towards the reactor or rerouting it towards the system bypassing the reactor. Reaching the fixed bed tubular reactor (Hastelloy X), the gas flow inside is up-down where the reactants are fed from the upper part and the products are collected from the lower part of the reactor. The reactor is equipped with a thermocouple in contact with a catalyst bed placed inside a porous plate deposited between 2 layers of quartz wool, it has a length of 305 mm, an external diameter of 14.5 mm, an internal diameter of 9 mm, a maximum recommended temperature of 1200 °C and a maximum pressure of 100 bar. The product gases at the reactor outlet pass through the hot box to the 6-port valve reaching the liquid-gas separator (Peltier) to condense the liquid at low temperature. The remained gases are again directed to the hot box under controlled pressure (micrometric regulating valve) before being analyzed online by micro gas chromatography.

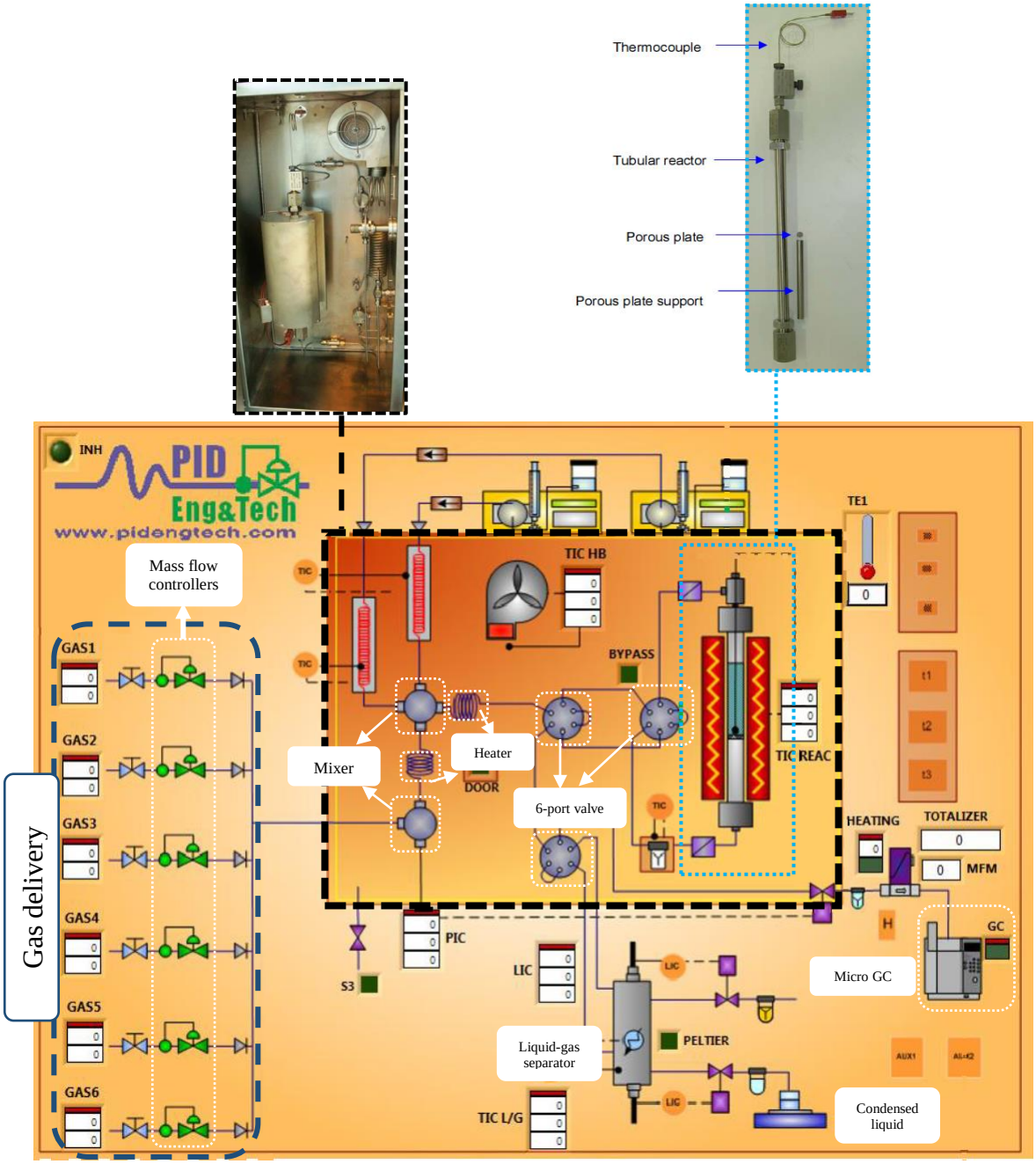

Figure II-9: General scheme of dry reforming system

II.2.1.3. Explanation of procedure adopted

Any calcined sample is first introduced inside the Hastelloy-X reactor and a leak test is performed prior to the reaction. It is done by using argon as an inert gas with a flow rate of 50 $ml.min^{-1}$ that contributes to a continuous increase of pressure until reaching a set value of 5 bar (otherwise a leak is present in the line connections). After attaining 5 bar, the gas inlet (Ar) is closed, and the maintaining of the pressure for a sufficient period of time (5 minutes) is

controlled to ensure the absence of leak after positioning the tubular reactor. Then, the catalyst is reduced *in-situ* at 650/800 °C for 2 h (after heating at a rate of 10 °C.min^{-1}) in a 30 ml.min^{-1} flow of 5 vol% H_2/Ar (Figure II-10) to convert all NiO species into active metallic Ni^0 needed for the reaction to occur ($NiO_{(s)} + H_{2(g)} \rightarrow Ni^0 + H_2O_{(g)}$). Then, the flow is switched to the reactant mixtures, chosen as CH_4/CO_2=1/1 or $CH_4/CO_2/H_2/CO$= 0.75/1/1.57/0.85 in this work, with a gas hourly space velocity (GHSV) of 180 or 72 L.g^{-1}.h^{-1} (for 20 or 50 mg of catalyst, respectively). The activity is then measured while increasing the temperature from 250 °C till 800 °C at a rate of 5 °C.min^{-1}. Also, stability measurements were done at 650°C for 13/40/100 h time on stream (Figure II-10). The reactants (CH_4, CO_2) and the products (H_2, CO) are quantified by Micro GC analysis. The results obtained as concentrations are converted to CH_4 and CO_2 conversions and H_2/CO ratio using the following equations:

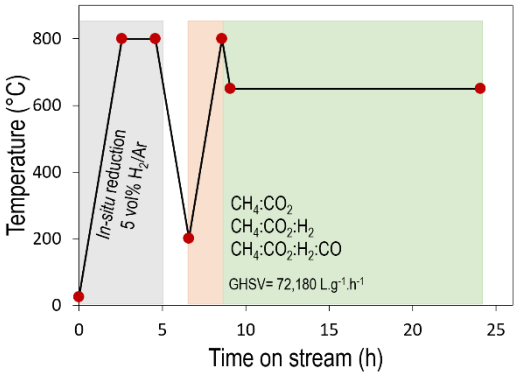

Figure II-10: Temperature profile during *in-situ* reduction (grey area), activity (orange area), and stability (green area) tests in DRM

$$CH_4 \text{ conversion } \% = \frac{(CH_4(in) - CH_4(out))}{CH_4(in)} \times 100$$

$$CO_2 \text{ conversion } \% = \frac{(CO_2(in) - CO_2(out)}{CO_2(in)} \times 100$$

$$H_2/CO = \frac{H_2 \text{ generation rate}}{CO \text{ generation rate}}$$

II.2.2. CO_2 methanation reaction

II.2.2.1. Thermodynamic equilibrium curves for CO_2 methanation

Similar to DRM, HSC chemistry software is used to see the behavior of CO_2 reactant under equilibrium conditions. H_2 and CO_2 are inserted in the software as initial reactants with H_2:CO_2 ratio of 4:1, and H_2O and CH_4 as expected components products. The temperature is varied between 250 and 600 °C and the pressure was increased from 1 to 100 bars. Figure II-11 illustrates the results obtained by showing the variation of CO_2 conversion as a function of pressure and temperature. As seen, the conversion of CO_2 increases with increasing pressure

and decreasing temperature. Consequently, elevated conversions can only be achieved at low temperatures or high pressures. However, a very high operating pressure does not lead to a significant increase of the methane yield [164]. Performing the reaction at high temperature, above 400 °C, results in the formation of CO as a by-product because the reverse water gas shift reaction becomes more favorable and CH_4 formation is banned. This phenomenon prevails at temperatures above 550 °C. Thermodynamically, there is no carbon accumulation under mild operation conditions (100-400 °C) [165,166].

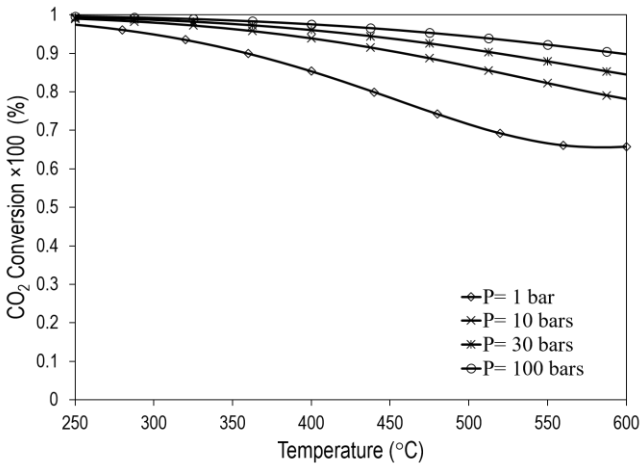

Figure II-11: Thermodynamic CO_2 conversion as a function of temperature and pressure obtained from HSC chemistry software.

II.2.2.2. Equipment for catalytic methanation

CO_2 methanation experiments were performed in Portugal at Instituto Superior Tecnico (University of Lisbon) using a quartz reactor placed inside a **TermoLab** electric vertical oven

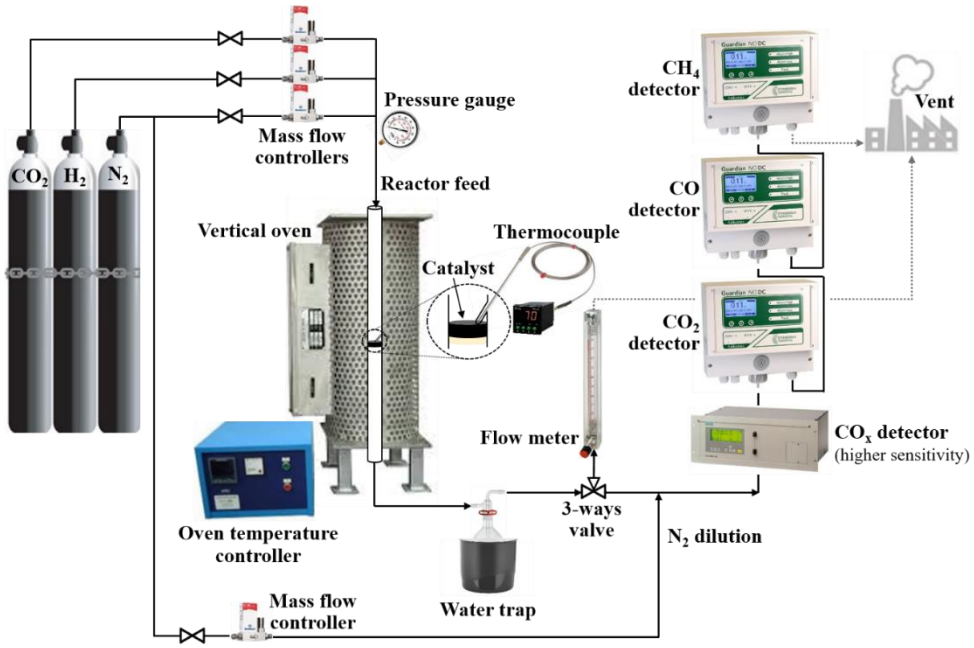

Figure II-12: General scheme of the CO_2 methanation system

unit (Figure II-12). Inside the reactor lies the catalytic bed on a porous plate that is in contact with a thermocouple to control the temperature. Similar to the DRM reaction, the reactants flow

from the upper part of the reactor and the products are collected from the bottom of the reactor. The products obtained go to a water trap placed next to the quartz reactor to condensate the H_2O produced ($CO_{2(g)} + 4H_{2(g)} \rightarrow CH_{4(g)} + 2H_2O_{(g)}$) and the remaining gas passes through a 3-ways valve either to an in-line flow meter to measure the outlet flow or to several gas detectors to analyze the product gas (dry base results). To this end, four gas IR detectors are available: the Ultramat 23 Siemens one is used to detect low amount of CO_x gases (<1 vol% CO_2, CO) and three Guardian NG Edinburg sensors are available for higher ranges of CO_2, CH_4, and CO (<10 vol%). CO usually has a low selectivity, thus the low concentrations detector is needed. Concerning the CO_2 component, its concentration will be always higher than 5 vol% and therefore the reading is sufficient from the Guardian sensor only. The reactant gases (H_2 and CO_2) are regulated with mass flow controllers (Brooks) with 99.99% purity before reaching the reactor inlet. N_2 gas (purity: 99.99%) is used as a diluent at the exit of the reactor to dilute the product gases before reaching the detectors in order to reach a concentration and a flow (500 $ml.min^{-1}$) suitable for the apparatus sensitivity.

II.2.2.3. Explanation of procedure adopted

200 mg of catalyst is used for the CO_2 methanation reaction. As for DRM, the catalyst is first pre-treated in-situ at 650/800 °C for 1 h with a heating rate of 5 °C.min^{-1} and an 80 vol% H_2/N_2 flow of 250 $ml.min^{-1}$ at atmospheric pressure to reduce nickel oxide species to metallic Ni^0 which is also the active phase for methanation (Figure II-13). After reduction, the reactor is cooled down to 250 °C and the feed gas is switched to CO_2 methanation reactants containing H_2, CO_2 and N_2 with a molar ratio of 36:9:10 respectively. The activity is then followed while increasing the temperature gradually from 250 °C till 450 °C (50 °C step size) with a heating rate of 5 °C.min^{-1} and a total flow of H_2 and CO_2 equal to 288 $ml.min^{-1}$. At each temperature, CO_2 conversion and CH_4 selectivity are measured for 3 successive times after stabilization. The stability test was conducted at 300 °C

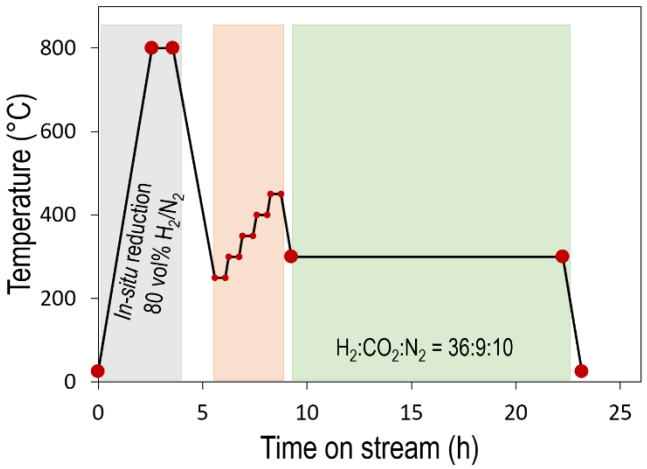

Figure II-13: Temperature profile during *in-situ* reduction (grey area), activity (orange area), and stability (green area) tests in CO_2 methanation

for 10/20 h time on stream (Figure II-13). The conversion of CO_2 as well as selectivity to CH_4 and CO are calculated relying on the inlet and outlet molar flow rates following the formulas:

$$CO_2 \text{ conversion } (\%) = \frac{F_{CO2,inlet} - F_{CO2,outlet}}{F_{CO2,inlet}} \times 100$$

$$CH_4 \text{ selectivity} = \frac{F_{CH4,outlet}}{F_{CO2,inlet} - F_{CO2,outlet}} \times 100$$

$$CO \text{ selectivity} = \frac{F_{CO,outlet}}{F_{CO2,inlet} - F_{CO2,outlet}} \times 100$$

III. Chapter 3: Effect of magnesium loading over ordered mesoporous Ni_5-Mg_y-Al_2O_3 DRM catalysts

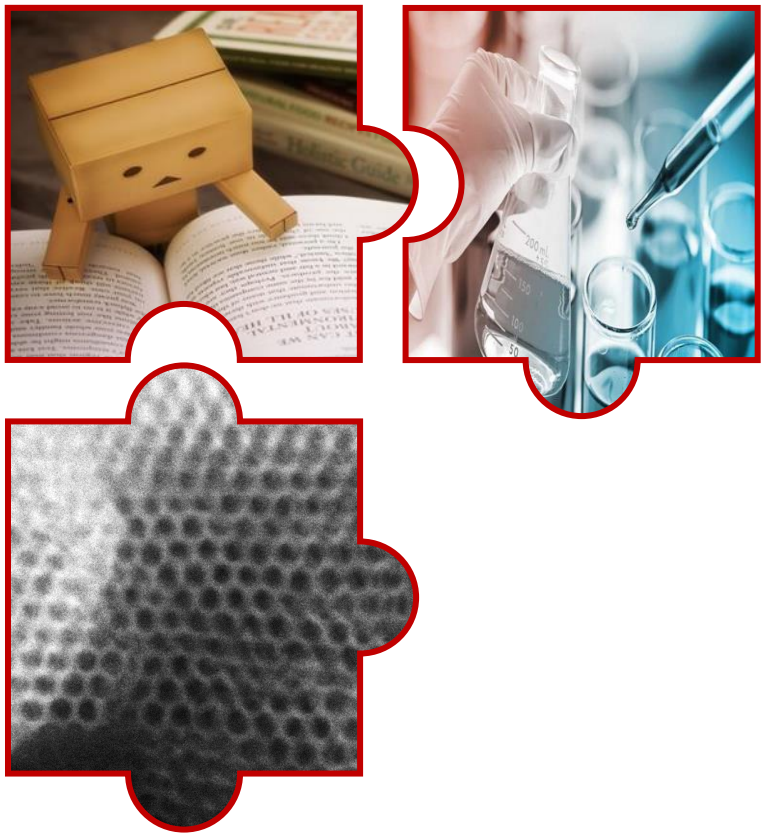

This chapter is an elaboration of one of the thesis aim that is to improve the stability of ordered Ni-alumina mesoporous catalyst for dry reforming of methane by addition of an appropriate amount of Mg to increase the basicity. Mg can act as a promoter by increasing the number of basic sites in the catalyst that strengthen chemisorption of CO_2 and boost catalytic performances. The state of the art specific to mesoporous Ni-Mg-Al_2O_3 materials used for reforming reactions will be recalled and compared with the present work. Our methodology was to fix the nickel content and vary the MgO one in order to understand the origin of the existence of an optimum magnesium content, so it has been varied from 0 to 26 wt%. The method of preparation will be explained in details, followed by the physicochemical characterizations of the obtained materials. The resulting catalytic performances will be presented and explained in accordance with the physico-chemical properties.

III.1. Literature review

Several preparation methods have been used in the literature for the preparation of alumina-based catalysts containing both nickel and magnesium and were applied in DRM reaction with a CH_4:CO_2 ratio of 1: sol-gel [148], two-step hydrothermal [167], impregnation [168–170] and co-precipitation [171–173]. Table III-1 summarizes some of these studies by specifying the method of preparation, the Ni and Mg amounts along with their order of addition. Some of the textural and structural properties are also summarized among with the catalytic conditions and performances of each catalyst. In brief:

- The impregnation, a method used to deposit Ni and Mg on an already existing alumina support, resulted in large Ni particle sizes up to 24 nm with a huge decrease in catalytic activity (~50%). Arbag H. [170] reported in his study the influence of Ni and Mg impregnation sequence on alumina. He concluded that the simultaneous impregnation of Ni and Mg on an Al_2O_3 support (Mg-Ni@MA) led to the best catalytic stability due to the strong metal-support interaction triggered

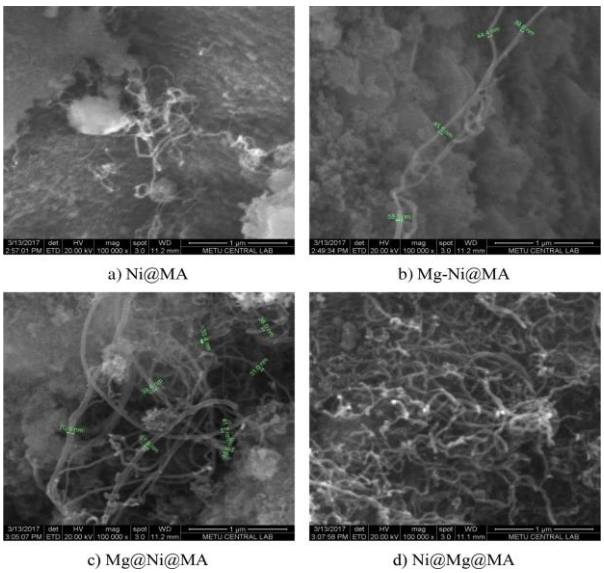

Figure III-1: SEM images of spent Ni/Mg/Al_2O_3 catalysts [170]

Table III-1: Bibliographic listing of Ni-MgO-Al_2O_3 catalysts synthesized by different techniques and their performances in DRM

Sample	Method of Preparation	Ni(wt%)	Order of Ni/Mg addition	MgO(wt%)	Al_2O_3 (wt%)	Particle Size (nm)	BET SA ($m^2.g^{-1}$)	PD (nm)	PV ($cm^3.g^{-1}$)	T(°C), P(atm)	Cw(mg), GHSV,CH_4:CO_2:N_2	TOS (hr)	Conversions (%)		$C_{(s)}$ (%)
													XCH_4	XCO_2	
Ni-MgO-Al_2O_3[148]	Sol-gel	15	Together with Al precursor	-	85	15.1	140	2.5	n.m.	800, 1	100,36,1:1:1	40	56-44	61-50	n.m.
				5	80	13.7	133	3.6					76-71	84-79	n.m.
				24	61	6.6	115	4.3					82-79	88-86	n.m.
				37	48	8	147	6.1					90-87	93-91	n.m.
				52	***33***	***8.5***/15.5^s	***177***	***6.2***					***84-84***	***89-89***	***20***
				65	20	8.8	193	4.9					83-82	88-88	n.m.
				80	5	6	99	11.3					88-85	92-90	n.m.
Ni/MgO-Al_2O_3[167]	Two-step hydrothermal	10	Mg and Al precursors added to $Ni(OH)_2$ nanoparticles	45	45	11.6/15^s	162	3.4	0.45	650,1	100,60,49:49:2	10	35	40	57
				70	30	10.6/14^s	149	3.3	0.34				40	50	54
				75	***15***	***6.8***/7.2^s	***135***	***3.8***	***0.28***				***52***	***63***	***37***
				79	12	8.8/13^s	117	5.6	0.35				45	55	60
				82	8	8.9/13^s	50	6.4	0.36				30	45	51
				90	0	11.1/13^s	39	6.6	0.21				8	20	32
Ni/Mg/Al_2O_3 [168]	Impregnation	7	After Al Commercial Al_2O_3	2	40	24	105	n.m.	n.m.	800,1	n.m.,36, 1:1:1	25	99-85	99-85	n.m.
				4	40	17	99						97-55	97-45	
				5	40	14	94						95-50	95-50	
Ni/MgO-Al_2O_3 [170]	Co-impregnation	5	Same time	***3***	***92***	***11.8***	***56***	***30***	***0.49***	***750, 1***	***100, 36, 1:1:1***	***4***	***42-40***	***60-59***	***5***
Ni-Mg-Al[172]	Co-precipitation	11 mol%	A solution of Ni, Mg, Al with solution of NaOH added in 50 ml H_2O	0 mol%	89	7.8^r/10^s	150^r	4.1^r	0.45^r	750,1	50,28,1:1	60	70-40	72-45	35
				5 mol%	84	6.7^r/7.8^s	124^r	4.7^r	0.35^r				82	84	17
				10 mol%	***79***	***6.2^r***/7.6^s	***143^r***	***5.5^r***	***0.42^r***				***87***	***91***	***10***
				20 mol%	69	6.4^r/7.5^s	131^r	5.9^r	0.37^r				80	82	12
				30 mol%	59	6.5^r/7.8^s	125^r	5.6^r	0.33^r				73	82	15
Ni-Mg-Al[173]	Co-precipitation	10	A solution of Ni, Mg, Al added to Na_2CO_3	Mg/Al:0.25	-	16.8^r/19^s	145	8	0.45	800,1	50,60,1:1	4	78-80 (78.5)	82-84	13.4
				Mg/Al:0.43		15.3^r/18^s	179	6.9	0.43				85-86 (85)	86-87	5
				Mg/Al:0.67		***11.6^r***/15^s	***223***	***4.6***	***0.42***				***84-85 (84.7)***	***86-86***	-
				Mg/Al:1		11.9^r/13^s	218	4.2	0.46				83-84 (83.6)	85-86	-
				Mg/Al:4		9.4^r/11^s	190	3.9	0.36				82-83 (82.7)	85-85	-
Ni/MgO-Al_2O_3[174]	Impregnation	5	Ni impregnated on one-pot Mg Al	1	99	n.m.	208	6.6	0.31	700,1	100,15,1:1	100			
				2	98		184	7.8	0.37						
				3	97		188	4.9	0.27						
				5	***95***		***163***	***7.8***	***0.28***				***77-73***	***77-73***	***8***
				8	92		159	5.6	0.27						
				10	90		163	7.8	0.33						

SA : surface area, PD : pore diameter, PV : pore volume, C_w : catalyst weight, GHSV : gas hourly space velocity in $L.g^{-1}.h^{-1}$, TOS : time in stream, XCH_4/XCO_2 : conversions of CH_4 and CO_2 respectively, ^{r,s}: reduced and spent materials

by the formation of a NiO-MgO solid solution. However, it still resulted in the formation of carbon filaments even if in less amount compared to the other impregnation sequences. The authors suggest that the formation of carbon is due to the occurrence of a partial phase transformation of alumina from γ-Al_2O_3 to α-Al_2O_3 and $MgAl_2O_4$ spinel phase during calcination and reduction which alters the porous structure of the catalyst leading to a decrease in the surface area (56 $m^2.g^{-1}$) and altering the Ni-support interaction.

- The co-precipitation method led to catalysts with acceptable surface areas and Ni particle sizes ranging between 6.5 and 17 nm. Again, the method did not prevent the formation of whiskers carbon, oxidation of metallic Ni and sintering thus affecting the stability in long term tests [171–173].
- The 2-step hydrothermal technique giving non-porous materials was the least efficient (lower catalytic activity) with sintering and large amounts of carbon deposition were observed on all the catalysts after only 10 h reaction independently from the Mg amount added [167].
- The sol-gel pathway came up with porous materials having non ordered mesoporosity. The catalysts were somehow stable through time with little deactivation, but, even the best catalyst with 52 wt% MgO encountered carbon nanotubes formation with sintered Ni crystallites from 8 to 15 nm.
- Leilei Xu et al. compared the deposition of Ni by incipient wetness impregnation on mesoporous and non-porous Mg-Al_2O_3 support. As mentioned earlier, using Al_2O_3 support with ordered mesoporosity serves as a good way to confine nickel inside the pores resisting sintering and subsequent coke deposition. Thus, non-porous Ni/Mg-Al_2O_3 was less stable with 28.3% carbon formation compared to 8 wt% for the mesoporous Ni/Mg-Al_2O_3 sample [174].

Studies have been tackled also on hydrotalcite catalysts since they are cheap with basic properties that showed good activity in DRM. However, these catalysts suffer from fast sintering and coke formation due to their poor texture disturbing Ni dispersion [175–177]. For example, in a recent study done by Bruna Rego de Vasconcelos et al., a hydrotalcite catalyst needed 70 wt% of Mg to enhance its stability. However, even with this high amount of Mg, core-shell carbon and carbon nanotubes were inevitably present [178].

Based on the above-mentioned literature, a lack is still present in synthesizing a stable porous Ni-Al_2O_3 catalyst taking advantage of the Mg basic properties in casting carbon. In

addition, all the aforementioned ways of doping Ni with Mg suffer from certain deficiencies like the need of a long preparation time (i.e. several impregnations/calcinations) [108,167,168,171,173], tough conditions as high temperature [148,167], hard operation steps [167,171,173], and expensive substrates.

More interestingly, it can be noted from the data in Table III-1 that, regardless of the preparation protocol used, there is always an intermediate optimum amount of magnesium that leads the highest activity and stability of CH_4 and CO_2 conversions. To illustrate this, Figure III-2 reports the conversion of CH_4 as a function of Mg amount (expressed as Mg/Al molar ratio) for the representative work taken from the table. The scale applied for these studies is not always the same because of the distinct preparation methods used, shifting the trends in Mg contents. Nevertheless, all examples in Figure III-2 show an optimum in Mg content giving the best conversion level. An explanation of such specific behavior has to our knowledge not been detailed yet and will be targeted in this chapter. Thus, the current work aims in producing a

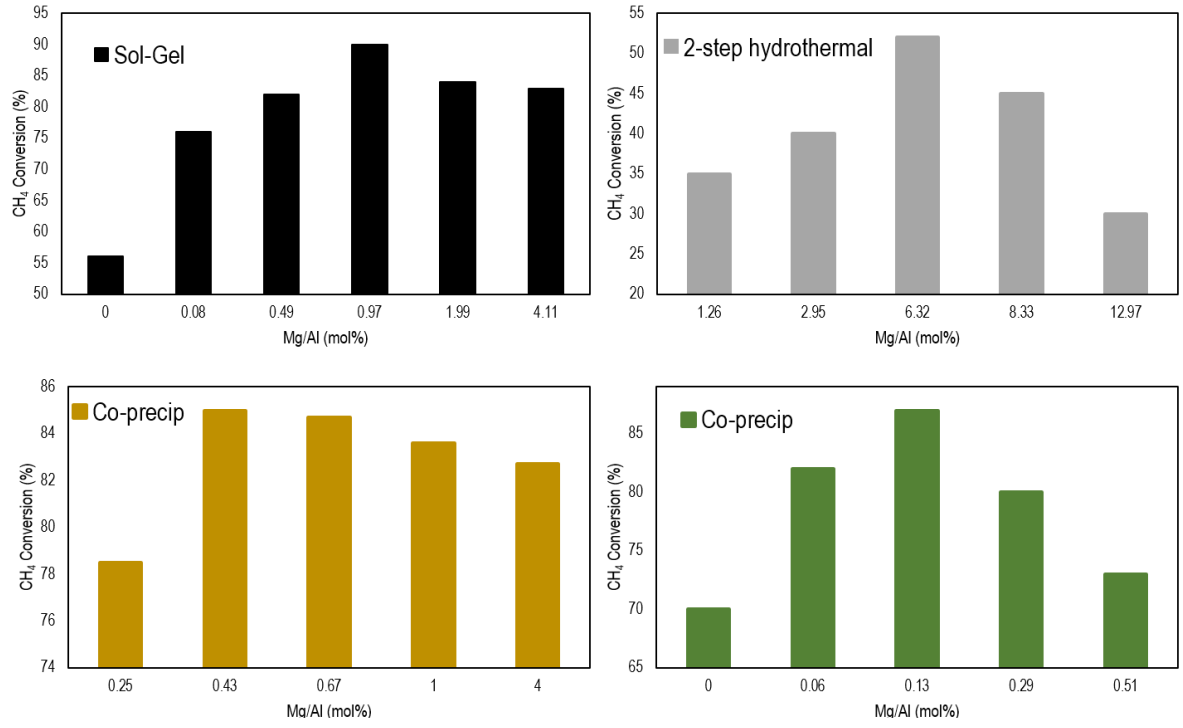

Figure III-2: Variation of CH_4 conversion as a function of Mg content in different methods of Ni-Mg-Al_2O_3 preparation present in literature: Sol-gel [148], 2-step hydrothermal [167], co-precipitation [172], and co-precipitation [173]

defined catalyst porosity, using fewer preparation steps than the previous mentioned ones. Moreover, an inspection on Mg content influence regarding the physicochemical properties and the catalytic performance of Ni-Mg-Al_2O_3 material that resembles a parabola (volcano-shape curve) is constructively demonstrated.

III.2. Synthesis of mesoporous one-pot Ni_5-Mg_y-Al_2O_3 materials

III.2.1. Synthesis principle

Nickel-based mesoporous alumina promoted by MgO was prepared using an alteration of the evaporation induced self-assembly (EISA) method. Figure III-3 represents the principle of EISA route. P123, used as surfactant, is mixed with absolute ethanol and metal precursors to form a micelle solution. P123 surfactant stabilizes Al and other metal species (Mg, Ni) through complexation bonds and inhibits agglomeration of alumina nanoparticles. Aluminum isopropoxide was used as Al metal precursor because it is assigned as a base and extra oxygen donor with no acid generated when reacting slowly with ethanol. It is also crucial for achieving homogeneous composition in the entire framework. Ethanol is a polar solvent which presence improves the proton transfer in the system donating oxygen and promoting the inorganic-inorganic interaction necessary for the polymerization of mesostructured oxide materials. HNO_3 acid is added to the mixture to influence the polymerization of the inorganic metal precursor of the hydrolysis and condensation rates. This acid has a larger aqueous ionic radius compared to other acids leading to weak complexation ability protecting the balance between organic/inorganic interfaces [179–181]. During the evaporation of ethanol, the composite mesostructure with ordered arrays of surfactant micelles embedded within the alumina matrices are formed. Then, the unidimensional materials are obtained after thermal decomposition of the template micelles.

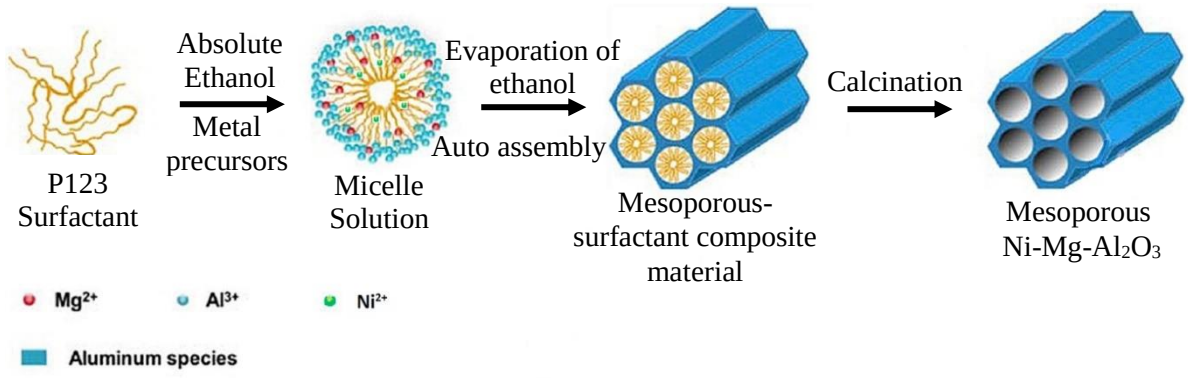

Figure III-3: A representative schematic of the mechanism involved in the synthesis of mesoporous Ni-Mg-Al_2O_3 catalyst

The one-pot EISA is an alteration of the EISA that embraces a direct addition of a second metal within the synthesis of mesoporous alumina. This method of preparation was tried by our group in a previous PhD thesis, where Ni was added simultaneously to Al precursor. The

obtained material confined Ni inside the alumina walls leading to excellent dispersion and good catalytic performance in bi-reforming of methane [65] compared to impregnated alumina samples that face calamitous sintering and coke deposition. In our case, this preparation is extended and several Mg weight percent were added during the synthesis to produce in one shot ordered mesoporous Ni-Mg-Al_2O_3 catalysts where the effect of Mg amount is investigated in details.

III.2.2. Synthesis procedure

A series of alumina based samples with 5 wt% nickel and different magnesium loading was prepared. The method used is the well-known one-pot evaporation induced self-assembly (EISA) method [180,181] applied for synthesis of mesoporous Ni-Al_2O_3 materials. In our case, we modified this method to include magnesium within the synthesis. The procedure of the catalysts preparation steps is described in Figure III-4. First, 7 g of P123 Pluronic triblock copolymer ($EO_{20}PO_{70}EO_{20}$, M_n=5800, Sigma-Aldrich, 435465) was dissolved in 140 ml of absolute ethanol (CH_3CH_2OH, M_n=46.07, Sigma-Aldrich, 64175) at ambient temperature (25 °C) under intense stirring. During the stirring process (Figure III-4 A), 11.63 ml of 65 wt% nitric acid (HNO_3, M_n=63.01, Johnson Matthey S.A) was added simultaneously with **A mmol** of aluminum isopropoxide (**$Al[OCH(CH_3)_2]_3$**, M_n=204.24, Sigma-Aldrich, 220418), **B mmol** of nickel nitrate hexahydrate (**$Ni(NO_3)_2.6H_2O$**, Mn=290.79, Sigma-Aldrich, 72253), and **C mmol** of magnesium nitrate hexahydrate (**$Mg(NO_3)_2{\cdot}6H_2O$**, M_n=256.41, Sigma-Aldrich, 203696) to the solution, where A, B and C vary depending on the desired molar composition of

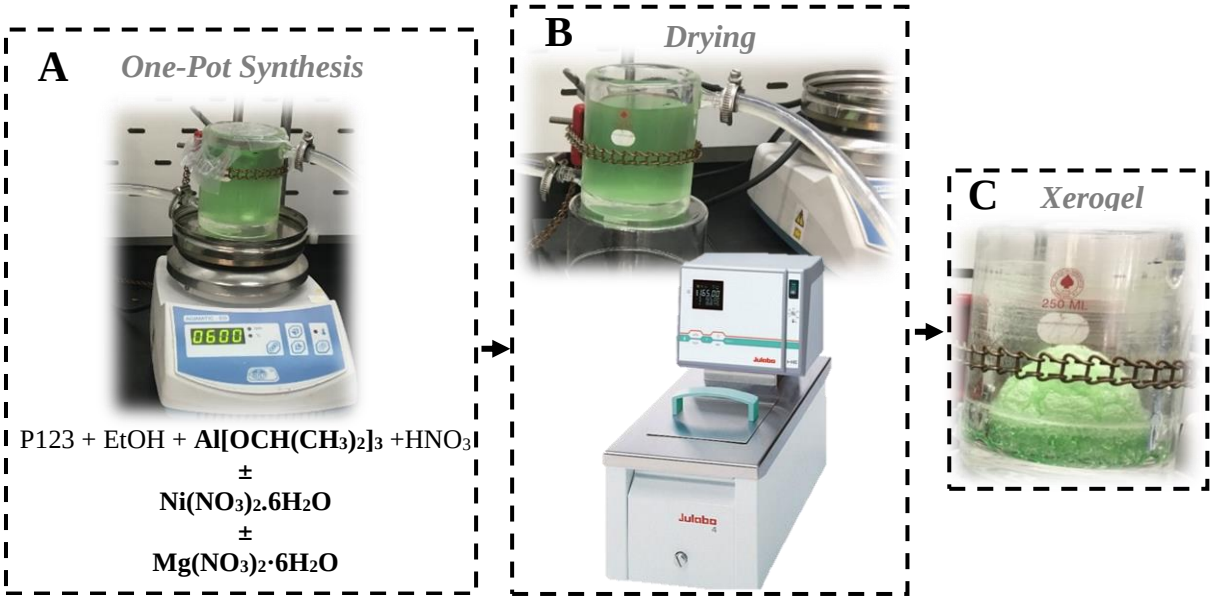

Figure III-4: Chronological steps summary of preparing mesoporous one-pot Ni_x-Mg_y-Al_2O_3 following EISA route

the solid but keeping the total (**A**+ **B**+ **C**) value constant at 10 mmol (details in Table III-2). All mentioned chemicals were employed in the catalysts preparations as received and without additional purifications. The obtained mixture was then covered with a polyethylene film (PE) and stirring was kept overnight to reach a complete dissolution of the chemicals added. Then, the solution was dried at 60 °C for 48 h to slowly evaporate ethanol and HNO_3 with the aid of a Julabo that circulates water to regulate and control the temperature (Figure III-4 B). The resulting Xerogel (Figure III-4 C) was calcined in a muffle furnace under air at 600 °C for 5 h with a heating rate of 0.5 °C.min^{-1} (thin bed conditions). The samples obtained were denoted as Ni_x-Mg_y-Al_2O_3 where x and y correspond to the molar percentage of Ni and Mg, respectively calculated as follows: $x= n_{Ni} / (n_{Ni} + n_{Al} + n_{Mg}) *100$ and $y= n_{Mg} / (n_{Ni} + n_{Al} + n_{Mg}) *100$; n represents the number of atoms of each element.

Note that the "y" numbers of Mg 0, 5, 10, 15, 30 and 50 are mole contents. They correspond to Mg weight percentage detailed in Table III-2 and that are 0, 2.5, 5, 7, 15, and 26 wt%, respectively.

Table III-2: Summary of the synthesis conditions of the Ni_5-Mg_y-Al_2O_3 mesoporous materials prepared by one-pot EISA route

Sample code	Metal contents (wt%) Ni	Mg	$Ni_xMg_yAl_z$ atomic formula*	Weight of chemical added (g) P123	$Al[OCH(CH_3)_2]_3$	$Ni(NO_3)_2.6H_2O$	$Mg(NO_3)_2 \cdot 6H_2O$
Al_2O_3	-	-	$Ni_0Mg_0Al_{100}$	7	14.3	0	0
Ni_5-Al_2O_3	5	0	$Ni_5Mg_0Al_{95}$		13.6	1.02	0
Ni_5-Mg_5-Al_2O_3		2.5	$Ni_5Mg_5Al_{90}$		12.9	1.02	0.9
Ni_5-Mg_{10}-Al_2O_3		5	$Ni_5Mg_{10}Al_{85}$		12.2	1.02	1.8
Ni_5-Mg_{15}-Al_2O_3		7	$Ni_5Mg_{15}Al_{80}$		11.5	1.02	2.7
Ni_5-Mg_{30}-Al_2O_3		15	$Ni_5Mg_{30}Al_{65}$		9.3	1.02	5.4
Ni_5-Mg_{50}-Al_2O_3		26	$Ni_5Mg_{50}Al_{45}$		6.5	1.02	9
Mg_{50}-Al_2O_3	0	26	$Mg_{50}Al_{50}$		7.1	0	9

* Atomic formula does not take into account oxygen

III.3. Textural and structural properties of the calcined Ni_5-Mg_y-Al_2O_3 materials

III.3.1. Porosity by N_2-sorption technique

The nitrogen physisorption isotherms of the calcined Ni_5-Mg_y-Al_2O_3 samples as well as their corresponding pore size distributions are displayed in Figure III-5. All the materials exhibit a type IV isotherm with H1 hysteresis loop attributable to mesoporous solids [155]. All samples with a magnesium weight percent between 0 and 7 wt% (Figure III-5 A) exhibit capillary steps of very steep hysteresis loop, which suggests the presence of uniform mesopores carrying cylindrical shaped patterns [155] [180,182]. Further increase in magnesium weight (Ni_5-Mg_{30}-Al_2O_3 and Ni_5-Mg_{50}-Al_2O_3 samples) leads to a decrease in the steepness of capillary condensation step and alteration in the hysteresis loop (Figure III-5 B) indicative of some loss of mesopores ordering. Simultaneously, a shift of the condensation step to a higher relative pressure is seen, revealing the formation of larger mesopores [180]. This is indeed confirmed by the BJH curves derived from the desorption part of the N_2-sorption presented as insets in Figure III-5. For instance, Ni_5-Mg_{30}-Al_2O_3 and Ni_5-Mg_{50}-Al_2O_3 exhibit broader pore size distribution leading to larger mean pore diameter compared to the other samples with narrow pore size distribution and eventually a smaller pore diameter.

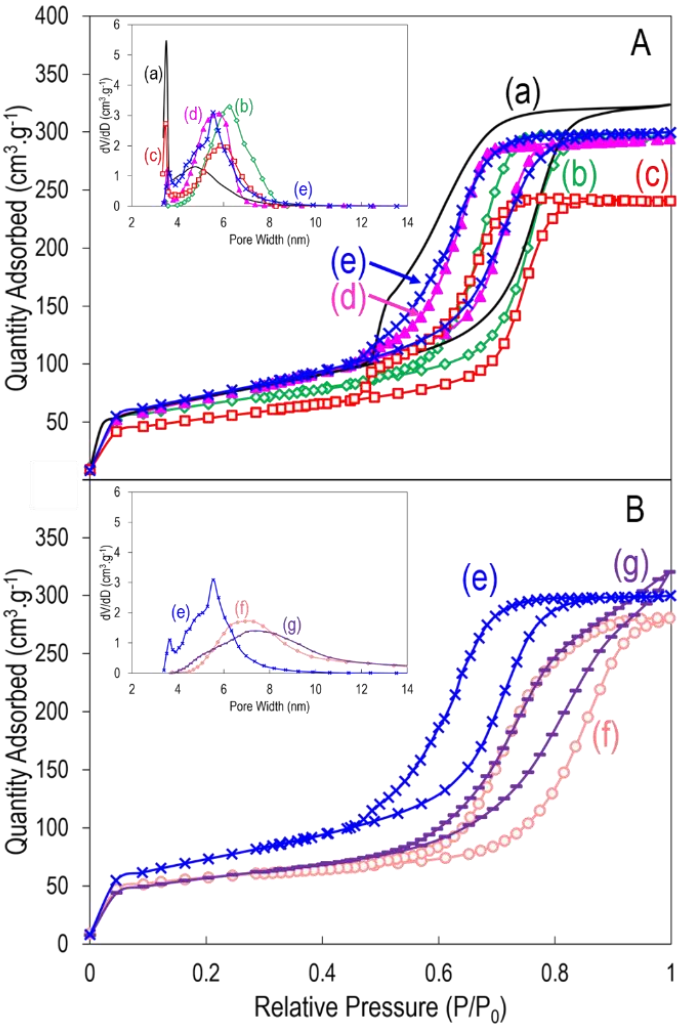

Figure III-5: Nitrogen adsorption/desorption isotherms and pore size distribution profiles (insets) of Ni_5-Mg_x-Al_2O_3 catalysts calcined at 600 °C: (a) Al_2O_3, (b) Ni_5-Al_2O_3, (c) Ni_5-Mg_5-Al_2O_3, (d) Ni_5-Mg_{10}-Al_2O_3, (e) Ni_5-Mg_{15}-Al_2O_3, (f) Ni_5-Mg_{30}-Al_2O_3, (g) Ni_5-Mg_{50}-Al_2O_3

Table III-3 reports the values of surface areas (SA) and pore volumes (PV) of all the prepared materials. For the sake of easy comparison, the Table reports the data obtained for calcined samples (this section) but it also includes those measured in a next section for reduced (section III.5) materials. An increase in Mg content up to 7 wt% did not have a significant effect or change on the BET surface area and pore volume of the solids in comparison with pure alumina. They all demonstrate high SA between 230 and 262 $m^2.g^{-1}$ with comparable PV (0.47-0.52 $cm^3.g^{-1}$). Whereas, Ni_5-Mg_{30}-Al_2O_3 and Ni_5-Mg_{50}-Al_2O_3 have lower surface area of about 25% less than Al_2O_3 support confirming the presence of irregular mesopores with probably blocking parts (plugs).

It can be also noted on Figure III-5 that the physisorption curve of pure Al_2O_3 shows a second small desorption step at lower partial pressures (P/P_0=0.5) unlike the nickel-magnesium based catalysts. This could be attributed to the presence of plugs in the mesopores creating inkbottle sections within the channels which is absent in Ni and Mg enriched samples having only one desorption step at P/P_0=0.8 corresponding to open pores [183,184]. Similar behavior has been seen in literature, where scientists proposed that the addition of nickel nitrate could ameliorate the ordered mesoporosity of the alumina support [180] and contribute to larger mesopores by acting as sustained-released agents to maintain an acidic equilibrium environment. According to these authors, the nickel nitrate precursor contains crystallographic water that hydrolyzes and produces in-situ H^+ by being transformed into free water in nitrate. The hydrolysis process of the nitrates can be also affected by the trace water in ethanol and the relative humidity in the air above the solution.

Table III-3: Porous characteristics of calcined and reduced Ni_5-Mg_y-Al_2O_3 materials

Sample	Ni content[a] (wt%)	S.A. [b] ($m^2.g^{-1}$)	V_{tot} [b] ($cm^3.g^{-1}$)	Mean [b] (nm)
Al_2O_3	-	258 *(127)*	0.52 *(0.28)*	4.8 *(5.3)*
Ni_5-Al_2O_3	5.0	229 *(246)*	0.49 *(0.54)*	6.2 *(6.6)*
Ni_5-Mg_5-Al_2O_3	5.0	235 *(207)*	0.40 *(0.62)*	5.8 *(8.5)*
Ni_5-Mg_{10}-Al_2O_3	4.52	258 *(207)*	0.47 *(0.40)*	5.8 *(5.1)*
Ni_5-Mg_{15}-Al_2O_3	4.91	262 *(229)*	0.49 *(0.38)*	5.5 *(5.7)*
Ni_5-Mg_{30}-Al_2O_3	4.93	196 *(144)*	0.48 *(0.36)*	6.9 *(7.6)*
Ni_5-Mg_{50}-Al_2O_3	4.96	200 *(172)*	0.52 *(0.42)*	7.4 *(8.0)*

a: Ni amount determined by XRF, b: total surface area (S.A.), total pore volume (V_{tot}) and mean pore diameter (mean) calculated from the N_2 sorption isotherms for calcined (normal font) or reduced (in brackets) materials properties

III.3.2. Structural properties and crystallite type/size by small and wide angle XRD

The influence of the metal loading was also investigated using small angle XRD as seen in Figure III-6 A. Small angle X-Ray Diffraction has been widely applied on ordered mesoporous materials such as SBA-15 [185], MCM-41 [186] and Al_2O_3 [180] to prove the presence of two-dimensional structure. Pure Al_2O_3 exhibits a strong diffraction peak around 0.7-0.9° and a weak diffraction peak around 1.5-1.7° characteristic of [100] and [110] plane

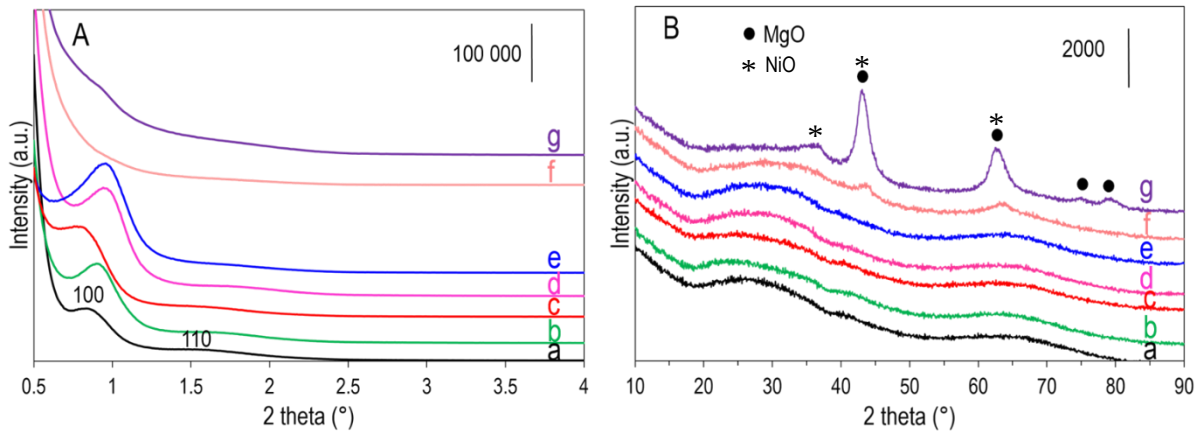

Figure III-6: (A) low and (B) wide angles XRD patterns of Ni_5-Mg_x-Al_y catalysts calcined at 600 °C: (a) Al_2O_3, (b) Ni_5-Al_2O_3, (c) Ni_5-Mg_5-Al_2O_3, (d) Ni_5-Mg_{10}-Al_2O_3 , (e) Ni_5-Mg_{15}-Al_2O_3, (f) Ni_5-Mg_{30}-Al_2O_3, (g) Ni_5-Mg_{50}-Al_2O_3

reflections, respectively. This behavior is an evidence of the presence of hexagonally ordered mesopores with *p6mm* symmetry [180,181]. These reflection peaks are also detectable in Ni_5-Mg_y-Al_2O_3 samples having an Mg wt% range from 0 to 7 wt% and are more intense in the case of Ni_5-Mg_{10}-Al_2O_3, and Ni_5-Mg_{15}-Al_2O_3 which means that the hexagonal arrangement is highly uniform in the latter samples [187]. Magnesium (dissolution of magnesium nitrate into Mg^{2+}) triggers certain interaction between non-ionic surfactant P123 and metal ions (Ni^{2+}), leading to a better ordered structure than Ni effect [188–190]. An appropriate amount Mg^{2+} ions play a key role in accelerating the coalescence of surfactant to form micelles preserving the Al-OH concentration species needed to form 2D-hexagonal structure. Contrarily, this better uniformity is lost in Ni_5-Mg_{30}-Al_2O_3 and Ni_5-Mg_{50}-Al_2O_3 catalysts that show no visible peaks in the small angle XRD patterns suggesting the absence of ordered porosity. This could be due to Mg^{2+} incorporation into mesoporous alumina framework and production of Mg-O bonds with longer lengths than those of Al-O bonds. Thus, the mesostructure faces an expansion since the ionic radius of Mg^{2+} is larger than that of Al^{3+}, hindering the merge of the micelle composite. This is the reason why it was not possible to calculate the pore thickness for these samples, contrarily to the previous more ordered samples for which the thickness is usually close to 5 nm for Ni-

based samples and slightly higher (7.3 nm) for Al_2O_3 (Table III-4) shifting the peaks to lower angles as seen in Figure III-6 A.

Note that Ni_5-Mg_5-Al_2O_3 sample is always out of the trend followed by the other Mg-based materials. This could be due to the fact that this sample was firstly prepared and the preparation procedure was not fully optimized by that time, and it will be excluded from the rest of the comparison.

Table III-4: Interplanar spacing and unit cell parameter of calcined and reduced Ni_5-Mg_y-Al_2O_3 samples

Samples	Calcined			Reduced		
	d_{100}^*(nm)	a_0^*(nm)	t^*(nm)	d_{100}^*(nm)	a_0^*(nm)	t^*(nm)
Al_2O_3	10.5	12.1	7.3	10.3	11.9	6.6
Ni_5-Al_2O_3	9.8	11.3	5.1	9.7	11.2	4.7
Ni_5-Mg_5-Al_2O_3	10.9	12.5	6.7	n.d.	n.d.	n.d.
Ni_5-Mg_{10}-Al_2O_3	9.4	10.8	5.0	8.4	9.7	4.6
Ni_5-Mg_{15}-Al_2O_3	9.5	10.7	5.2	8.7	10.1	4.4
Ni_5-Mg_{30}-Al_2O_3	-	-	-	-	-	-
Ni_5-Mg_{50}-Al_2O_3	-	-	-	-	-	-

d_{100}^*: host Al_2O_3 periodicity (interplane distance) derived from low-angle XRD
a_0^*: lattice parameter, $a_0 = 2d_{100}/\sqrt{3}$
t^*: pore wall thickness, $t = a_0 - D_{BjH}$
n.d. not determined

The wide angle XRD curves with different magnesium content are presented in Figure III-6 B. Mesoporous alumina support (curve a) has no visible diffraction peak indicating an amorphous Al_2O_3 walls oxide. Ni_5-Mg_y-Al_2O_3 samples having Mg content of 7 wt% or less, exhibit no apparent NiO, MgO, and even Al_2O_3 diffraction peaks as well. This observance means that NiO, MgO, and Al_2O_3 crystallites are either lower than the detection limit in XRD (smaller than 3 nm) or that the nickel and Al_2O_3 present are not crystalline (amorphous phase). The absence of crystallite domains suggests homogeneous elements distribution and high metal dispersion. Compared to other nickel-magnesium mesoporous alumina prepared using different methods [108,148,167,168,171,173] (Table III-1), the nickel particle size is here much smaller which assures that the one-pot method plays a crucial role in ensuring high nickel dispersion.
Adding higher amount of Mg (15-26 wt%) contributes to the appearance of MgO (JPCDS: 01-079-9866) diffraction peaks. The size of the crystal domains is around <3 and 5 nm for Ni_5-Mg_{30}-Al_2O_3 and Ni_5-Mg_{50}-Al_2O_3, respectively (Table III-5) at $2\theta = 63°$. This reveals a disturbance in the Mg dispersion in the samples with high Mg loadings. NiO species with mean sizes high enough to become detectable might be also present as deduced from the peaks at 2θ equal to 37, 43 and 63° but they however superpose those of MgO having similar positions, making their identification questionable.

Table III-5: Ni average particle size for calcined, reduced and spent materials

Sample	Particle size (nm)[a]		
	Calc. ΦNiO	Red. ΦNi^0	Spent ΦNi^0
Al_2O_3	n.d. *(n.d.)*	-	-
Ni_5-Al_2O_3	n.d. *(n.d.)*	4 *(4.6)*	n.p.
Ni_5-Mg_5-Al_2O_3	n.d. *(n.d.)*	4.3 *(n.p.)*	n.p.
Ni_5-Mg_{10}-Al_2O_3	n.d. *(n.d.)*	5.6 *(5.3)*	n.p.
Ni_5-Mg_{15}-Al_2O_3	n.d. *(n.d.)*	4.4 *(4.5)*	4.2 *(5)*
Ni_5-Mg_{30}-Al_2O_3	<3* *(n.p.)*	4.7 *(7.4)*	n.p.
Ni_5-Mg_{50}-Al_2O_3	5.0* *(n.p.)*	7.7 *(8.8)*	9.7

a: mean size values estimated from XRD (normal font) by applying the Scherrer equation considering the Ni^0 reflection at $2\theta = 51.9°$, and from the histograms obtained from representative TEM images (in brackets), n.d.: not detectable, * MgO crystalline domains, n.p. not performed

III.3.3. Visualization of porosities by TEM

High resolution transmission electron microscopy (HRTEM) and high angular annular dark field (HAADF) observations were performed on selected samples using ultra-thin microtomic sections for higher quality and better identification of porosity. Figure III-7 shows typical micrographs obtained for the calcined mesoporous Ni_5-Al_2O_3 sample. Sticking to the HRTEM mode when the alumina grains are parallel to the electronic beam, arranged and parallel channels are intelligible and clear (Figure III-7 A). Moreover, Figure III-7 A' is the result of a perpendicular orientation of the grain to the beam and depicts very regular hexagonal pore apertures at high magnification (2D p6mm hexagonally structured mesoporous channels) confirming N_2-sorption results. Both orientations show absence of Ni particles to the naked eye, in line with the absence in section III.3.2 of any XRD detection of NiO crystals for this sample. In order to have more precise and clearer observations, STEM-HAADF images (Figure III-7 B-B') were performed on the same sample since it plays more on the atomic contrast and could help differentiate between Ni and Al species. However, again, the pictures did not contribute to detection of any Ni-based particles distinct from the alumina. These results, in coherence with XRD ones, insist on the excellent dispersion of Ni with a size of nano-clusters undetectable or inserted inside the wall of the mesoporous alumina framework.

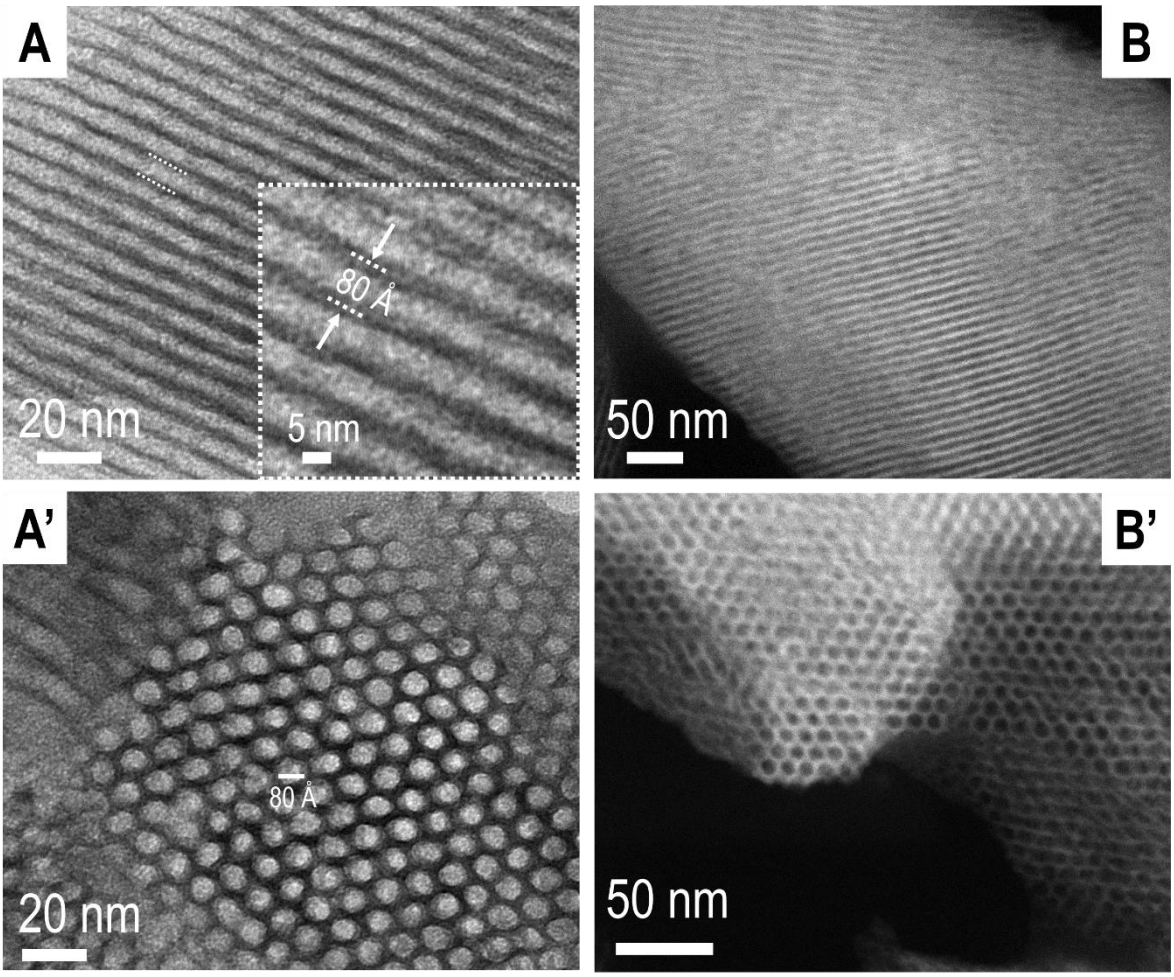

Figure III-7: Representative HRTEM (A-A') and STEM-HAADF (B-B') micrographs of calcined mesoporous Ni_5-Al_2O_3 showing the intimate mixing between Ni and its alumina support after synthesis; (B-B') are pictures for preliminary experiments done on MPQ-Paris Diderot microscopy (JEOL ARM 200F, coll. J. Nelayah)

In agreement with textural properties discussed above (section III.3.1), the successive increase of MgO content till 7 wt% does not alter the well-organized parallel channels and the honeycomb orientation of the alumina pores (Figure III-8 A-A'). Again, no Ni-based particles are detected by HRTEM and Ni remains homogenously spread on the alumina support. On the contrary, further magnesium increment (Figure III-8 B-B') confirms the deterioration of the structured channels and pores (suspected in N_2-sorption), and formation of ill-defined pore morphology. Few nickel oxide particles start to appear at this stage, indicating a less homogeneous distribution of Ni, and Ni-based (NiO) particles become clearly distinct when 26 weight percent of magnesium is present in the sample. In addition, Figure III-8 B' depicts a darker zone over alumina support that could be due to magnesium segregation justifying the MgO peaks observed in XRD experiments that are superposing those of NiO peaks. This hypothesis cannot be confirmed without making mapping and HAADF on the same area of the

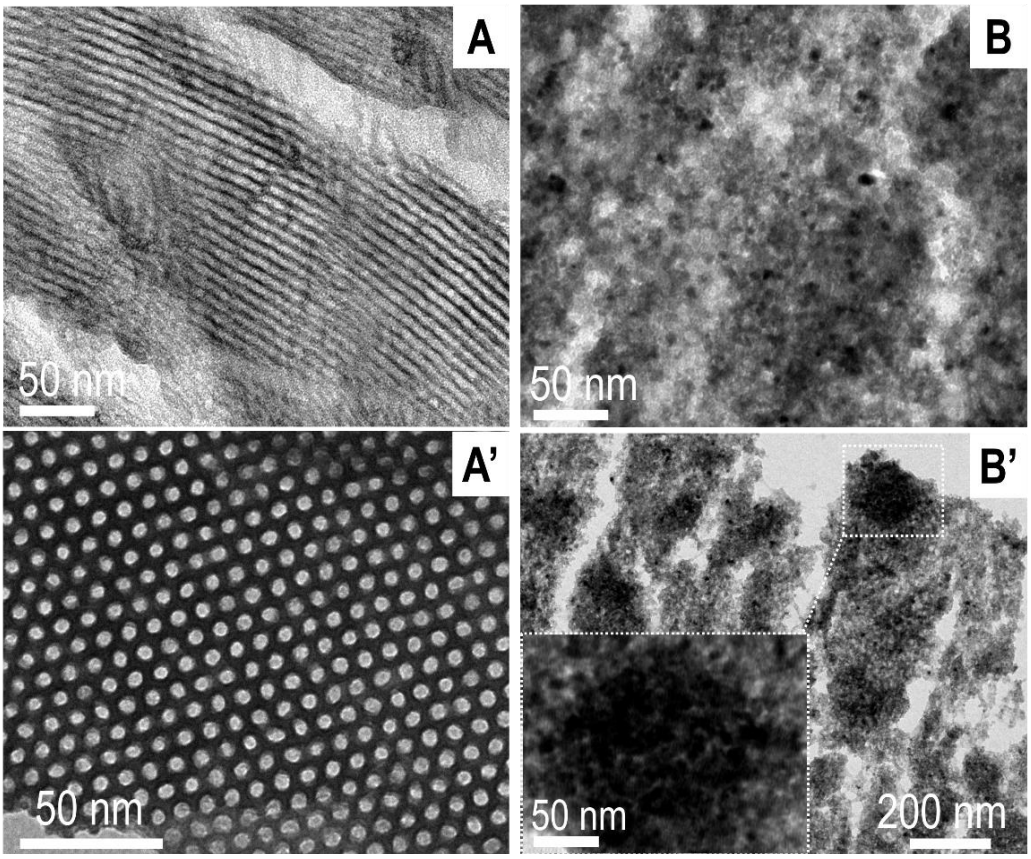

Figure III-8: Representative STEM micrographs of calcined mesoporous (A-A') Ni_5-Mg_{15}-Al_2O_3 and (B-B') Ni_5-Mg_{50}-Al_2O_3 catalysts

calcined sample. This experiment was not done on the calcined material, but was performed on the reduced one confirming in the upcoming paragraphs the assumption made.

III.3.4. Additional collaborative experiments to characterize samples basicity

Infra-red measurements were done to verify how the addition of Mg affects the basicity of the sample. These experiments were performed in collaboration with Politechnico University in Torino that is also a part of the ERANETMED European project SOL-CARE. The five evaluated samples are: Al_2O_3 (black curve), Ni_5-Mg_5-Al_2O_3 (pink curve), Ni_5-Mg_{15}-Al_2O_3 (red curve), Ni_5-Mg_{30}-Al_2O_3 (green curve) and Ni_5-Mg_{50}-Al_2O_3 (blue curve). The CO_2 adsorption was done at room temperature on calcined samples outgassed directly at 500 °C followed by desorption at room temperature. Figure III-9 presents Infra-red spectra for all the tested materials. The bands centered around 1560 and 1415 cm^{-1} are attributed to unidentate carbonates, and those around 1650 and 1375 cm^{-1} are assigned to bidentate carbonates. As the Mg amount increases from 0 to 7 wt%, the intensities for all bands progressively increase indicating a small enhancement of CO_2 affinity with the surface. This process is strongly accentuated when going from 7 to 15 wt% Mg (Ni_5-Mg_{30}-Al_2O_3), especially for bands of

unidentate carbonate species (1560 and 1415 cm^{-1}). This shows a sudden increase in basicity that is in line with the formation of stronger basic O^{2-} sites generated by some MgO segregation. When the segregation becomes more important (Ni_5-Mg_{50}-Al_2O_3), the Mg dispersion is extremely diminished (prevalence of bulk MgO) providing less accessible basic sites and therefore the intensities of unidentate carbonate are decreased due to strong decrease in the amount of adsorbed CO_2. More studies obtained by Infra-red spectroscopy have been analyzed confirming the results observed (TEM, XRD, EDS mapping) on these materials but are not detailed in the thesis.

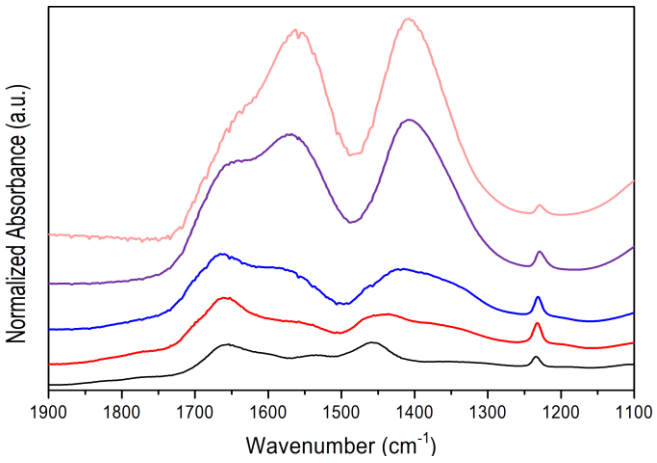

Figure III-9: CO_2 adsorption by Infra-red measurements on mesoporous: Al_2O_3 (black curve), Ni_5-Mg_5-Al_2O_3 (pink curve), Ni_5-Mg_{15}-Al_2O_3 (red curve), Ni_5-Mg_{30}-Al_2O_3 (green curve) and Ni_5-Mg_{50}-Al_2O_3 (blue curve)

III.4. Reducibility of mesoporous Ni_5-Mg_y-Al_2O_3 catalysts

Figure III-10 displays the TPR (temperature-programmed reduction) profiles of calcined Ni_5-Mg_y-Al_2O_3 materials with different Mg contents. Beginning with the Al_2O_3 support, no reduction peak is observed confirming that the support does not play a role in H_2-consumption. Ni_5-Mg_y-Al_2O_3 materials with Mg content up to 7 wt% show a single hydrogen reduction peak at a temperature range between 640 and 710 °C. For all these samples, the H_2-uptake calculated from the area under the curve (Figure III-10) is close to the theoretical value (860 µmol.g^{-1}) confirming the sole Ni reduction and the expected 5 wt% Ni content (Table III-6). The absence of a reduction peak in the range of 300-400 °C reveals that there is no free NiO species [88,169,191] and that

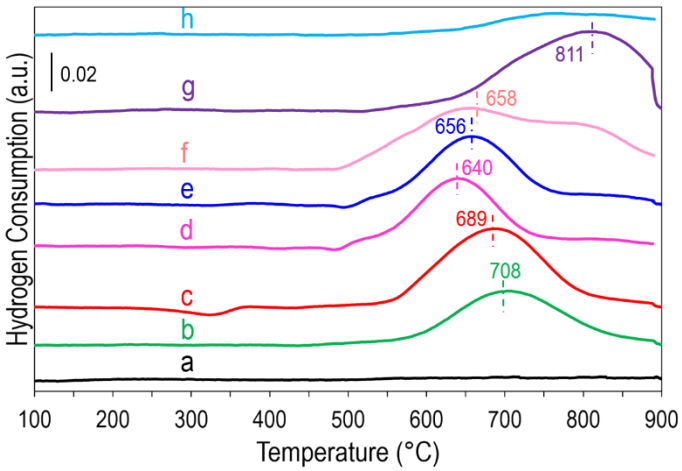

Figure III-10: H_2-TPR profiles of mesoporous Ni_5-Mg_x-Al_2O_3 catalysts calcined at 600 °C: (a) Al_2O_3, (b) Ni_5-Al_2O_3, (c) Ni_5-Mg_5-Al_2O_3, (d) Ni_5-Mg_{10}-Al_2O_3, (e) Ni_5-Mg_{15}-Al_2O_3, (f) Ni_5-Mg_{30}-Al_2O_3, (g) Ni_5-Mg_{50}-Al_2O_3, (h) Mg_{50}-Al_2O_3

Ni is strongly interacting with the alumina support at high temperatures, revealing high dispersion of Ni particles. This behavior is similar to surface spinel mixed-phases nickel aluminate species [180]. In our case, it could be explained by the fact that in one-pot synthesis nickel atoms replace tetrahedral coordinated alumina atoms forming solid solutions in the form of Ni-O-Al structures. This species could be a stoichiometric $NiAl_2O_4$ phase or a surface Ni in alumina-mixed layers as demonstrated by XPS measurement [88] (Figure III-11). For instance, for both Ni_5-Al_2O_3 and Ni_5-Mg_{15}-Al_2O_3 samples, the position of the $Ni2p_{3/2}$ peak centered at 856 eV and accompanied with a shake-up satellite peak around 862 eV excludes the presence of pure NiO which binding energy is expected at 853 eV.

Table III-6: H_2-uptake of calcined Ni_5-Mg_y-Al_2O_3

Sample	H_2 consumption ($\mu mol.g^{-1}$)	(T-E)/T (%)
Al_2O_3	-	-
Ni_5-Al_2O_3	815	5
Ni_5-Mg_5-Al_2O_3	921	7
Ni_5-Mg_{10}-Al_2O_3	863	0.34
Ni_5-Mg_{15}-Al_2O_3	905	5
Ni_5-Mg_{30}-Al_2O_3	1125	30
Ni_5-Mg_{50}-Al_2O_3	1175	35

T: Theoretical value of expected H_2-consumption, E: Experimental value of H_2-consumed

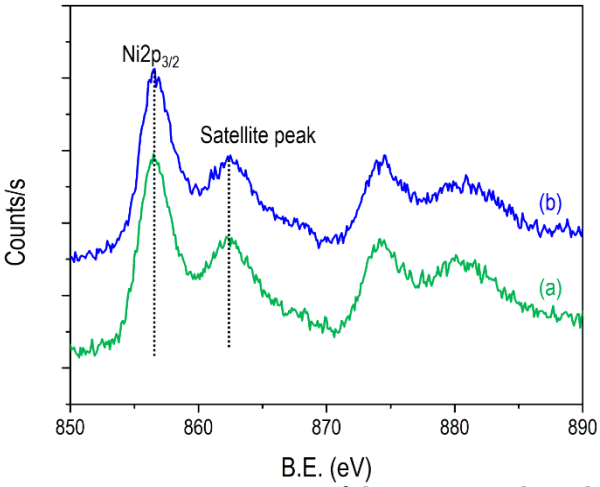

Figure III-11: XPS spectra of the Ni2p in calcined (a) Ni_5-Al_2O_3 and (b) Ni_5-Mg_{15}-Al_2O_3 materials

Another important feature can be also observed in Figure III-10. The reduction peak is shifted to a slightly lower temperature from Ni_5-Al_2O_3 to Ni_5-Mg_{15}-Al_2O_3 when increasing Mg amount to 7 wt%. This behavior could be attributed to a competitive formation of $NiAl_2O_4$ or $MgAl_2O_4$ clusters. Increasing the Mg content gradually would inhibit the formation of $NiAl_2O_4$ spinel and boost the appearance of $MgAl_2O_4$ species, which facilitates the reduction of nickel oxide particles, lowers the interaction towards alumina, and shifts the reduction peak to a lower temperature [169,174,192].

Increasing further the amount of Mg (Ni_5-Mg_{30}-Al_2O_3) induces a small deviation of the reduction peak towards a higher temperature with an additional peak shoulder noticeable at around 800 °C. This phenomenon is more pronounced in the case of Ni_5-Mg_{50}-Al_2O_3 with 26 wt% Mg where the reduction temperature for the whole single peak position is shifted to about

810 °C. The big amount of Mg compared to Ni can increase the bond strength for Ni-O in the close vicinity of Mg^{2+} cations, forming NiO-MgO solid solution, thus hindering and retarding the reduction of the NiO species [171,193]. Ni_5-Mg_{30}-Al_2O_3 and Ni_5-Mg_{50}-Al_2O_3 also exhibit around 30% higher H_2-consumption than the theoretical value. As the Ni content is confirmed by fluorescence (Table III-3), and Al_2O_3 support does not consume hydrogen (curve a in Figure III-10), TPR was performed on Mg_{50}-Al_2O_3 free of nickel. Curve h of the TPR profile in Figure III-10 shows a small reduction peak at a very high temperature corresponding to 277 µmol.g^{-1} of H_2 consumed. Thus, the additional H_2 amount induced in Ni_5-Mg_{30}-Al_2O_3 and Ni_5-Mg_{50}-Al_2O_3 materials is possibly indicative of some Mg derived species.

III.5. Textural and structure properties of reduced Ni_5-Mg_y-Al_2O_3 materials

Similar to the calcined samples, the reduced (650 °C/2h) Ni_5-Mg_y-Al_2O_3 materials were characterized by N_2-sorption, XRD, and TEM to follow their structural and textural behavior in presence of metallic Ni^0, the active phase in DRM.

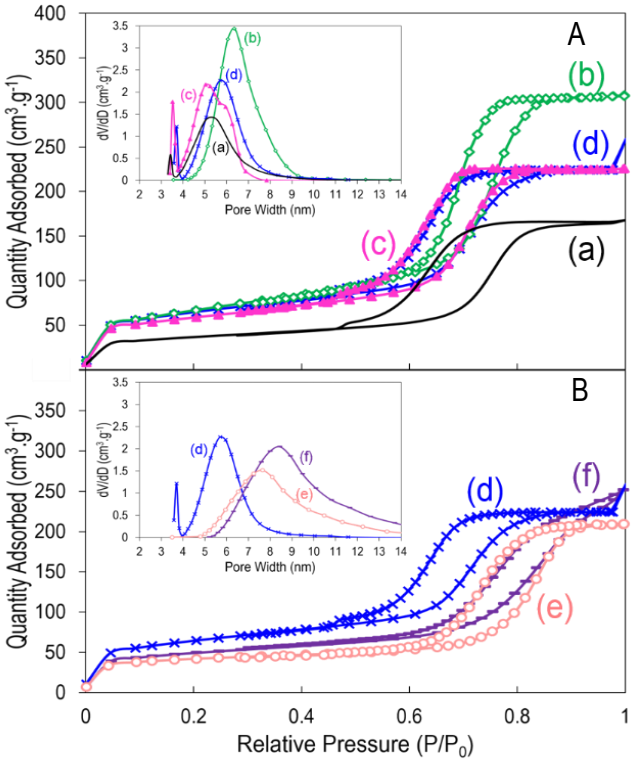

Figure III-12: Nitrogen adsorption/desorption isotherms and pore size distribution profiles (insets) of Ni_5-Mg_x-Al_2O_3 catalysts reduced at 650 °C for 2 hours: (a) Al_2O_3, (b) Ni_5-Al_2O_3, (c) Ni_5-Mg_{10}-Al_2O_3, (d) Ni_5-Mg_{15}-Al_2O_3, (e) Ni_5-Mg_{30}-Al_2O_3, (f) Ni_5-Mg_{50}-Al_2O_3

III.5.1. Porosity by N_2-sorption technique

The N_2-sorption isotherms (Figure III-12) of the Ni_5-Mg_y-Al_2O_3 samples examined after reduction display similar isotherm shapes and pore size distribution profiles as their calcined counterparts. They conserve a type IV isotherm with H1 hysteresis loop, preserving their porous characteristics after reduction. Their pore size distribution remains narrow for the catalysts containing 7 wt% Mg and wide for Ni_5-Mg_{30}-Al_2O_3 and Ni_5-Mg_{50}-Al_2O_3. Nevertheless, the surface area and pore volume were somehow smaller for all the treated catalysts regardless the amount of Mg present (Table III-3). The loss in S_{BET} values is equal to 50 % for Al_2O_3, 26 % for Ni_5-Mg_{30}-Al_2O_3, and 7-15 % for all the

others. This observed decline in the textural properties could arise from a shrinkage of the material skeleton (Al_2O_3 framework) due to the high reduction temperature (650 °C).

III.5.2. Porosity properties and Ni particle size by small and wide angle XRD

Paying attention to the small angle XRD curves (Figure III-13 A), the two diffraction peaks, at circa 0.90° and 1.5°, ascribed to the [100] and [110] plane reflections respectively, are still visible after reduction for all mesoporous Ni_5-Mg_y-Al_2O_3 with Mg content below 15 wt%. Such observation indicates again that the one-pot ordered mesoporous Ni_5-Mg_x-Al_2O_3 catalysts with limited Mg content have a good thermal stability, and the high reduction temperature did not strongly affect their 2D hexagonal alumina structure that conserves its *p6mm* symmetry. However, the peak intensities are slightly lower and shifted to higher angles identifying pore

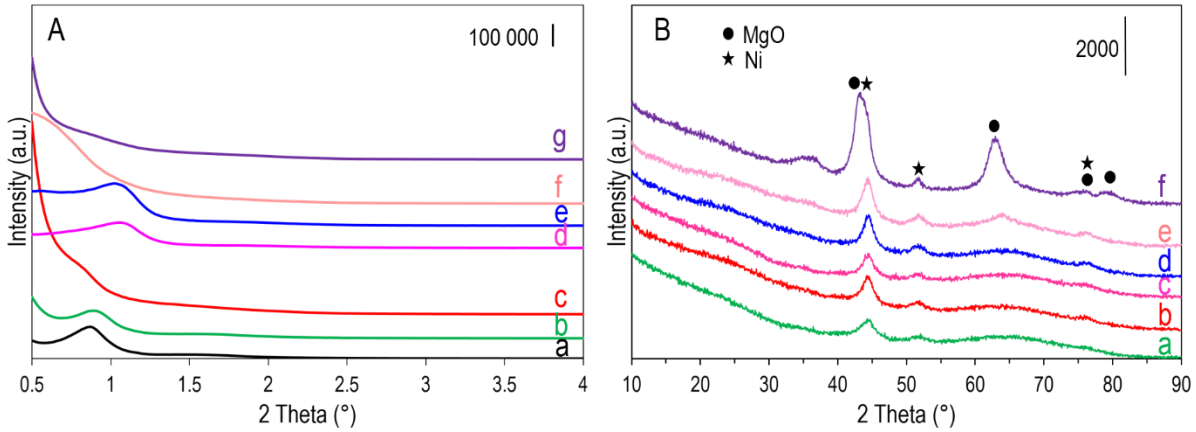

Figure III-13: (A) small angle and (B) wide angle XRD patterns of in-situ H_2-reduced Ni_5-Mg_x-Al_2O_3 catalysts: (a) Al_2O_3, (b) Ni_5-Al_2O_3, (c) Ni_5-Mg_5-Al_2O_3, (d) Ni_5-Mg_{10}-Al_2O_3, (e) Ni_5-Mg_{15}-Al_2O_3, (f) Ni_5-Mg_{30}-Al_2O_3, (g) Ni_5-Mg_{50}-Al_2O_3

shrinkage as shown in physisorption. Indeed, the lattice parameter (Table III-4) decreases slightly from 12.1 (Al_2O_3), 11.3 (Ni_5-Al_2O_3), 10.8 (Ni_5-Mg_{10}-Al_2O_3) and 10.7 (Ni_5-Mg_{15}-Al_2O_3) nm at calcined states to 11.9, 11.2, 9.7 and 10.1 nm for reduced samples, respectively.

Concerning the influence of reduction on the dispersion and location of Ni species, the wide angle XRD (Figure III-13 B) for all Ni_5-Mg_y-Al_2O_3 reduced catalysts exhibit different curves shape compared to the calcined ones. Ni^0 species appear in all samples with a broad peak (indexed as a star on the graph) and face centered cubic (FCC) unit cell (Ref. code:03-065-0380) at 2θ equal 44°, 52° and 76° highlighting on a phase transition from clusters in spinel structures (Ni-O-Al) invisible by XRD to metallic Ni^0. This phase transition could have also contributed to the loss in textural properties (surface area, pore volume), but at a limited extent in view of the limited Ni content. In the Ni_5-Mg_{50}-Al_2O_3 catalyst MgO peaks, still appear

simultaneously with Ni^0 species stressing on the presence of NiO-MgO solid solution as demonstrated before in TPR experiments. Subsequently, all catalysts except the one containing 26 wt% Mg, exhibit small Ni^0 nanoparticles size in the range of 4-5 nm (Table III-5), much below than those classically reported in literature for Ni-Mg-alumina catalysts (Table III-1). When very high amount of Mg is added (26 wt%), the nickel particles are larger (mean size 7.7 nm).

III.5.3. SEM and TEM for reduced Ni_5-Mg_y-Al_2O_3 catalysts

Representative SEM images (not performed for calcined materials) are done on three chosen in-situ reduced samples. Mesoporous Ni_5-Al_2O_3 (Figure III-14 A) and Ni_5-Mg_{15}-Al_2O_3

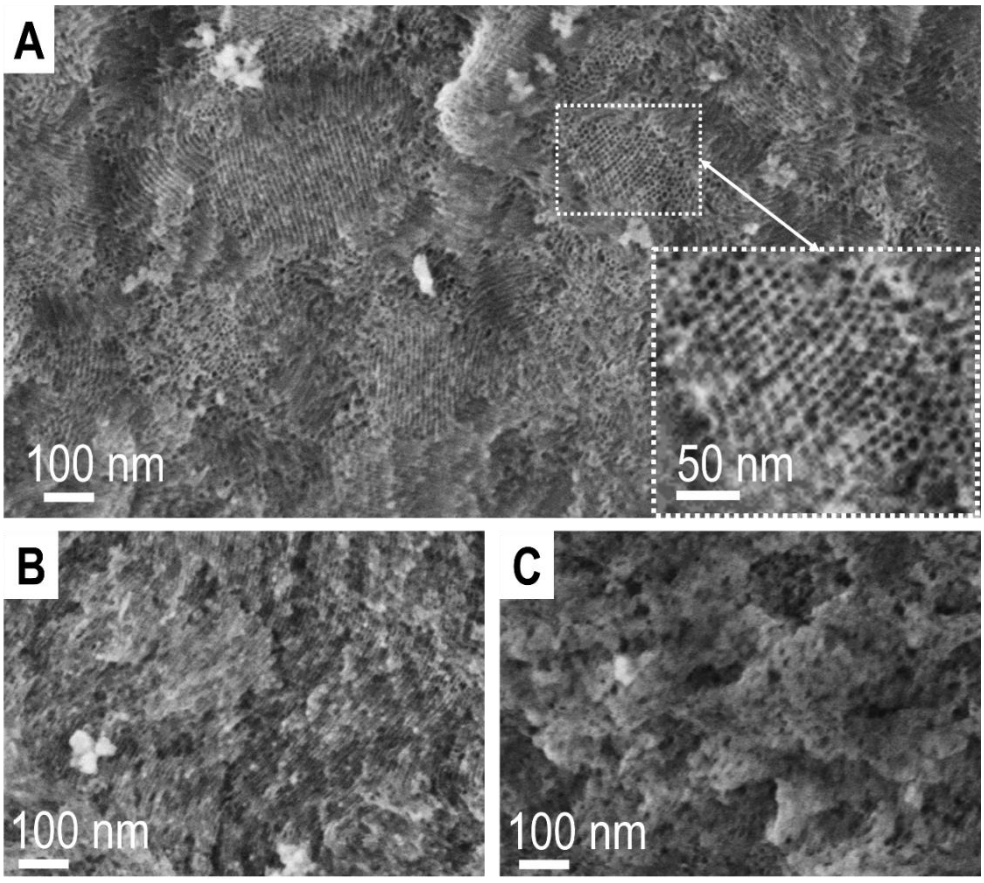

Figure III-14: SEM micrographs of in-situ reduced (650 °C/2h, H_2/Ar) (A) Ni_5-Al_2O_3, (B) Ni_5-Mg_{15}-Al_2O_3, (C) Ni_5-$Mg_{50}Al_2O_3$

(Figure III-14 B) catalysts reveal that the grains appear in a bulk mass having a smooth homogenous external topography without any cracks or defects. Moreover, the periodic porous organization is intelligible displaying ordered hexagonal arrangement of pores along the [001] direction with honeycomb mesoporous structure (inset in Figure III-14 A) and linear porous channel along the [110] direction. On the other hand, and in agreement with the textural

properties obtained in N_2-sorption Ni_5-Mg_{50}-Al_2O_3 (Figure III-14 C) presents amorphous porosity with random distribution and disappearance of parallel channels. Besides, there is no evidence of external Ni or Mg nano-particles in all the three samples, with no bright color on the alumina surface that could diffuse due to their high electronic density elements. Thus, the metals are embedded inside the alumina framework after reduction as will be demonstrated in TEM results.

Consistently, the high dispersion in the reduced materials seen by XRD in Ni_5-Al_2O_3 and Ni_5-Mg_{15}-Al_2O_3 is confirmed by STEM-HAADF observations (Figure III-15, Figure III-16 A-A''). It was focused on this technique for further implication on Ni and Mg position and distribution over Al_2O_3 support. All of the Ni^0 nanoparticles population appear either as very small dark spots (TEM) or as white dots (HAADF) on the grey alumina matrix and are located inside the regular hexagonal arrangement of the porous structure or embedded and anchored inside the alumina framework wall. These pictures also reveal an average particle size of 4.6 and 4.5 nm for mesoporous Ni_5-Al_2O_3 and Ni_5-Mg_{15}-Al_2O_3 respectively in line with results obtained in wide angle XRD measurements (Table III-5). Thus, the one-pot EISA method

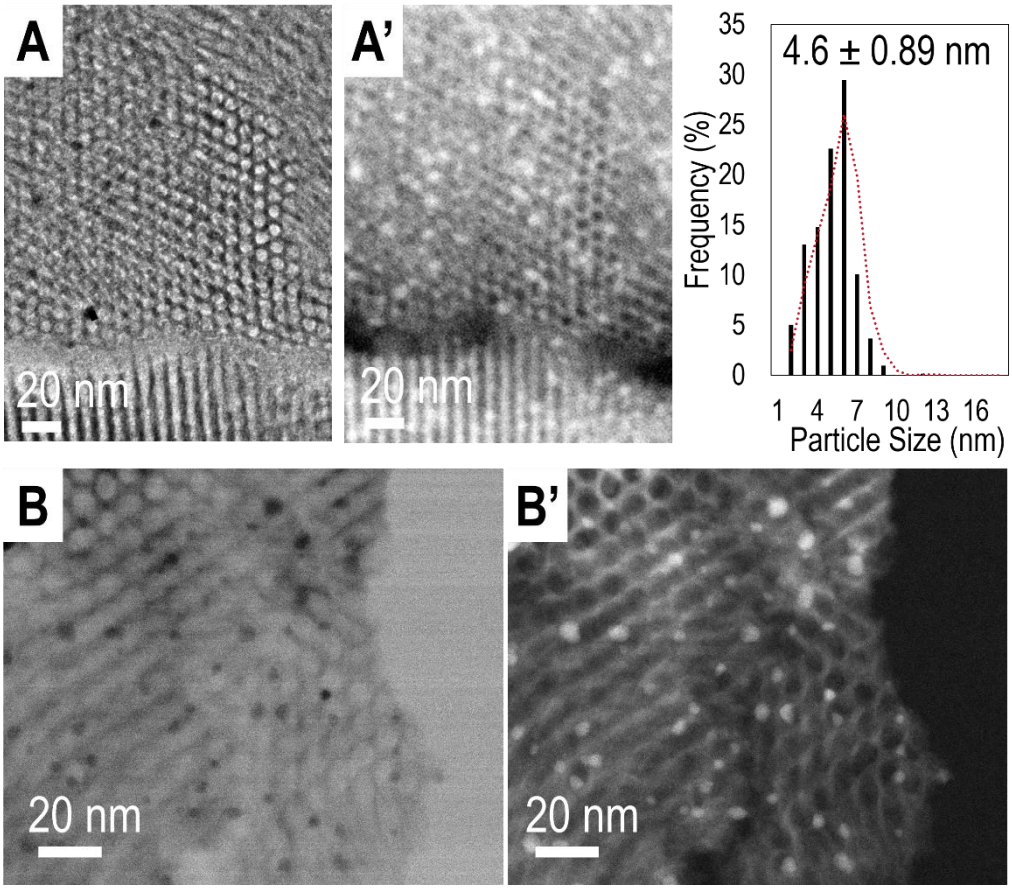

Figure III-15: Representative (A-A'), (B-B') STEM-HAADF micrographs of reduced mesoporous Ni_5-Al_2O_3 showing presence of Ni nano-species after reduction

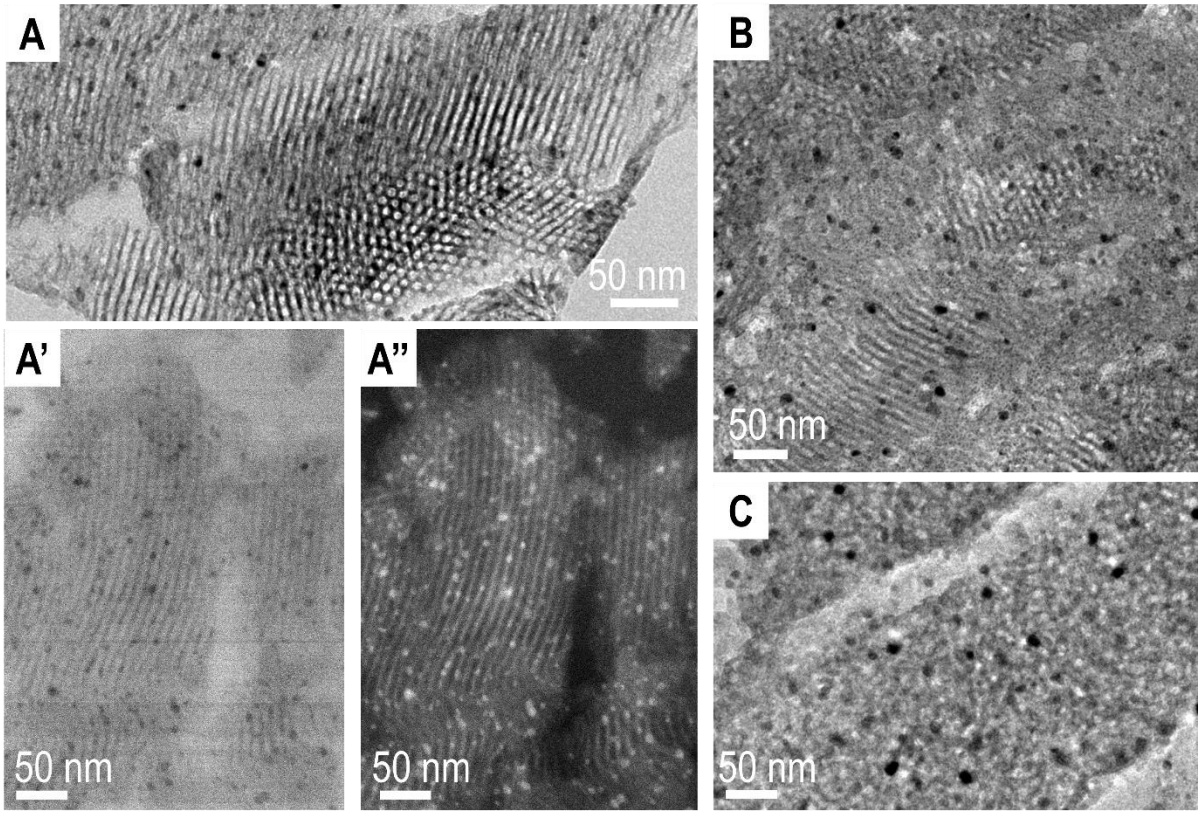

Figure III-16: Representative standard HRTEM micrographs of reduced (650 °C/2h) mesoporous (A) Ni_5-Mg_{15}-Al_2O_3, (B) Ni_5-Mg_{30}-Al_2O_3 and (C) Ni_5-Mg_{50}-Al_2O_3 and STEM-HAADF (A'-A'') of Ni_5-Mg_{15}-Al_2O_3 showing presence of Ni nano-species after reduction

proved to be very efficient in withstanding harsh thermal conditions (calcination, reduction) with 5 wt% Ni and up to 7 wt% Mg content. This route starts to lose its ordered mesoporosity impact when higher amount of MgO is added. For example, Figure III-16 B shows HRTEM image of Ni_5-Mg_{30}-Al_2O_3 with part of the sample featuring parallel channels and another part with complete random porosity. The influence of MgO on the pore size and morphology is confirmed by Ni_5-Mg_{50}-Al_2O_3 (Figure III-16 C) catalyst that still shows its total disordered porosity as its calcined form. In the high Mg% samples, the nickel particles formed are no longer present inside the mesostructured skeleton and are randomly scattered with larger Ni^0 particle sizes of 8.8 nm for Ni_5-Mg_{50}-Al_2O_3 sample (Table III-5).

Confirmation about metallic Ni^0 occlusion and dispersion within the alumina matrix after reduction is provided by locally pointed EDS mapping analyses (Figure III-17) performed over selected alumina grains. This method locates Ni or MgO existence that is not clearly visible by TEM what drove us to go further in our study and understand the good/bad dispersion of nickel/magnesium. The EDS mapping supports the earlier XRD and TEM findings and assert on the homogeneous and excellent dispersion of nickel particles on mesoporous alumina parent

for Ni_5-Al_2O_3 and its preservation in Ni_5-Mg_{15}-Al_2O_3 (Figure III-17 A, B). Additional feature was noticeable in this type of experiment is the presence of Mg element all over the alumina matrix that accentuates on the fact that magnesium particles are as dispersed as nickel and superposed. Figure III-17 C, demonstrates, as mentioned before, that when Mg content is increased up to 26 wt% it triggers a detrimental disturbance in Ni repartition. This disturbance is also seen for Mg element where Al_2O_3 support shows some areas more enriched in magnesium than other places with a driven segregation as indicated by the white arrows on EDS maps.

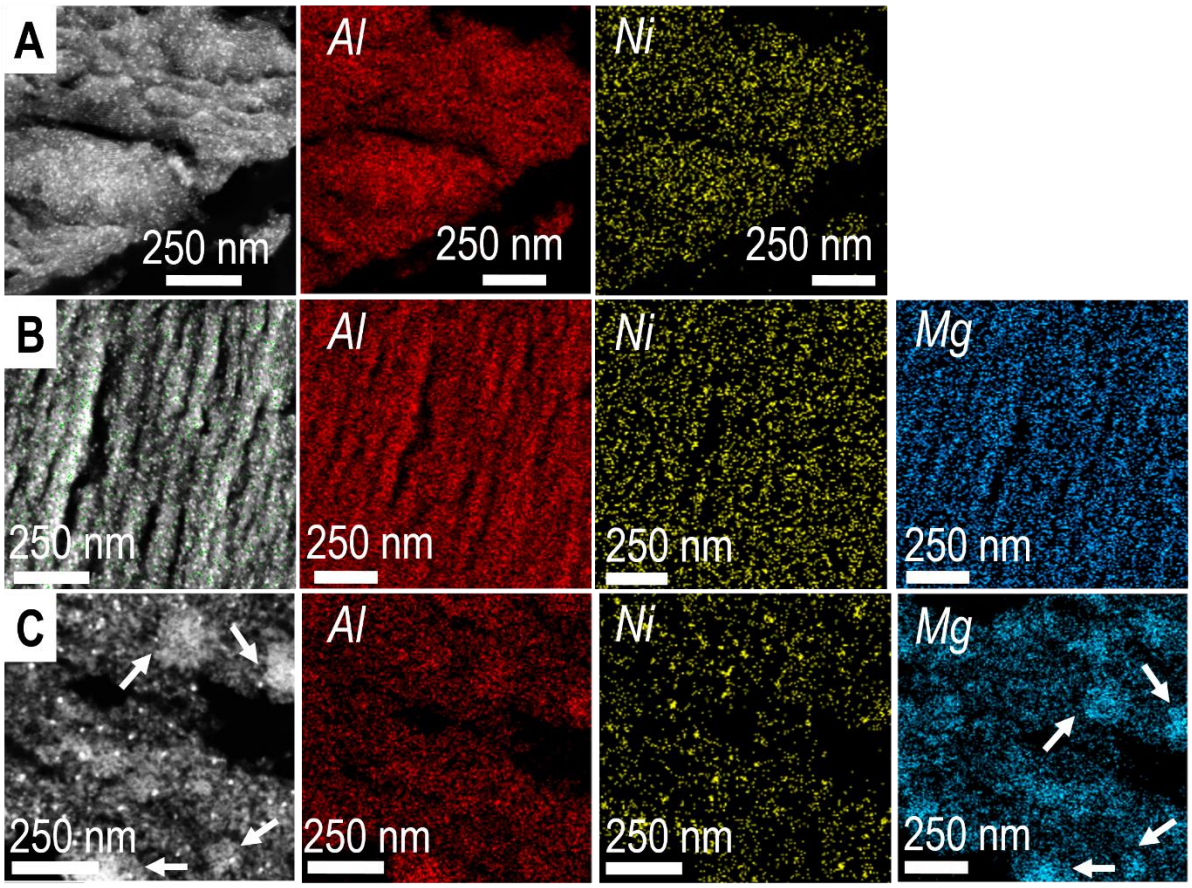

Figure III-17: HAADF with EDS mapping images of (A) Ni_5-Al_2O_3, (B) Ni_5-Mg_{15}-Al_2O_3, and (C) Ni_5-Mg_{50}-Al_2O_3. Atoms of Al (red), Ni (yellow), and Mg (blue) were identified within EDS maps

III.5.4. Ni dispersion derived from H_2-TPD and H_2-chemisorption

The H_2-TPD experiments performed over reduced catalysts provide further information about the metal dispersion determined from the amount of desorbed hydrogen. The related profiles displayed in Figure III-18 show two distinct desorption domains independent from the

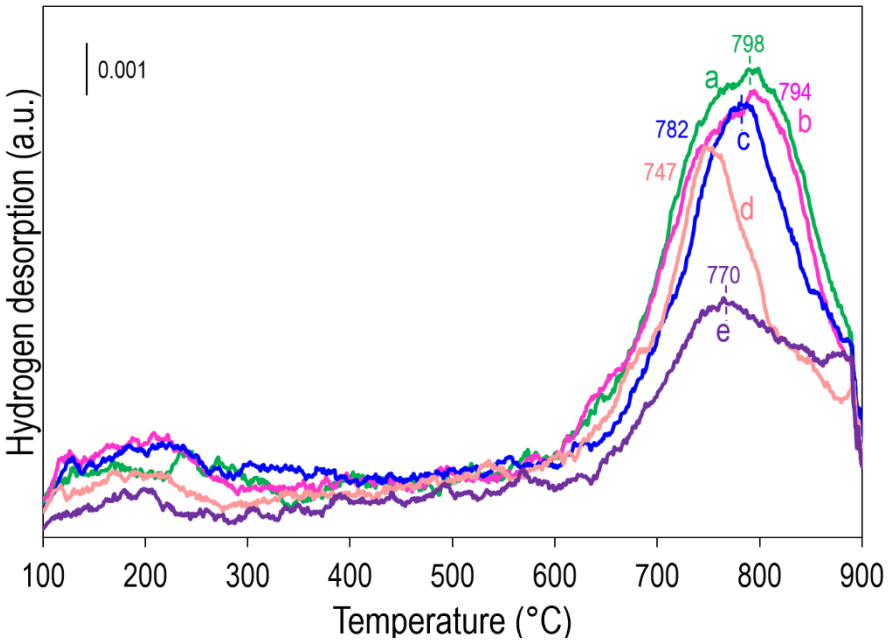

Figure III-18: H_2-TPD profiles of alumina based-materials: (a) Ni_5-Al_2O_3, (b) Ni_5-Mg_{10}-Al_2O_3, (c) Ni_5-Mg_{15}-Al_2O_3, (d) Ni_5-Mg_{30}-Al_2O_3, and (e) Ni_5-Mg_{50}-Al_2O_3

amount of MgO present. Hydrogen atoms desorbed at temperatures below 450 °C, represent exposed surfaces of low dispersed Ni^0 nanoparticles. The domain with the higher desorption temperature above 600 °C is due to surfaces of Ni^0 particles immersed in the alumina layer. The relative surface area of the high temperature desorption peak is much larger than that at low temperature for all Ni_5-Mg_y-Al_2O_3 catalysts asserting on the strong metal support interaction seen in TPR and the occlusion of Ni species within the alumina matrix as assumed in TEM of calcined samples. However, the integrated areas of Ni_5-Mg_{30}-Al_2O_3, and Ni_5-Mg_{50}-Al_2O_3 are somehow smaller than the others because MgO species could cover some surface Ni particles [194]. A good dispersion is achieved following the one-pot strategy and it is conserved with magnesium-based samples up to 7 wt% (Ni_5-Al_2O_3: 18%, Ni_5-Mg_{10}-Al_2O_3: 17%, Ni_5-Mg_{15}-Al_2O_3: 16.5%, Ni_5-Mg_{30}-Al_2O_3: 11.8% and Ni_5-Mg_{50}-Al_2O_3: 10%). The results obtained are somehow close to dispersion obtained from H_2-chemisorption method except for Mg-free mesoporous Ni_5-Al_2O_3 sample (Ni_5-Al_2O_3: 9.8%, Ni_5-Mg_{10}-Al_2O_3: 16.7%, Ni_5-Mg_{15}-Al_2O_3: 15.3%, Ni_5-Mg_{30}-Al_2O_3: 8.9% and Ni_5-Mg_{50}-Al_2O_3: 12.8%).

III.7. Dry reforming of methane reaction

The above characterization properties of the calcined and reduced samples, clearly indicate that there exists an optimal magnesium content in our series of samples with regard to their structural and porous properties. Indeed, the incorporation of Mg up to a certain extent (7

wt%) preserves the mesoporous alumina framework and leads to samples with high repartition of both Ni and Mg species. In contrary, a higher amount of magnesium leads to non-homogeneous and less ordered samples having lower surface area and pore volume, and in which the oxide Al_2O_3 and MgO phases are segregated. This seen trend resembles the "volcano-shape" curve seen at the beginning of this chapter for catalytic performances taken from bibliography and that will be also seen below for our series of catalyst tested in DRM.

III.7.1. Activity in DRM of Ni_5-Al_2O_3 and Ni_5-Mg_{15}-Al_2O_3 at a GHSV of 36 $L.g^{-1}.h^{-1}$

Catalytic tests in DRM were first carried out on two of the prepared catalysts, Ni_5-Al_2O_3 and Ni_5-Mg_{15}-Al_2O_3, using 100 mg of sample each time, giving a GHSV of 36 $L.g^{-1}.h^{-1}$ as often applied in the literature (see Table III-1). The CH_4:CO_2 ratio of used reactants was 1 and the conversions were measured for 50 hours time on stream (Figure III-19). In such conditions, both catalysts exhibited somehow similar performances with high CH_4 and CO_2 conversions close to thermodynamic equilibrium curve (estimated from the HSC software, as explained in chapter II), much better than literature catalysts presented in Table III-1 prepared by other techniques. For example, if we take the Ni-Mg-Al_2O_3 sample synthesized by the 2-step hydrothermal method [167], having the closest experimental test conditions as ours, we see that the conversions obtained are almost half of those of the current results with very high percentage of coke produced (37%). This reveals a very high activity for both of our catalysts, in line with the excellent Ni dispersions deduced above from physicochemical characterizations on both samples.

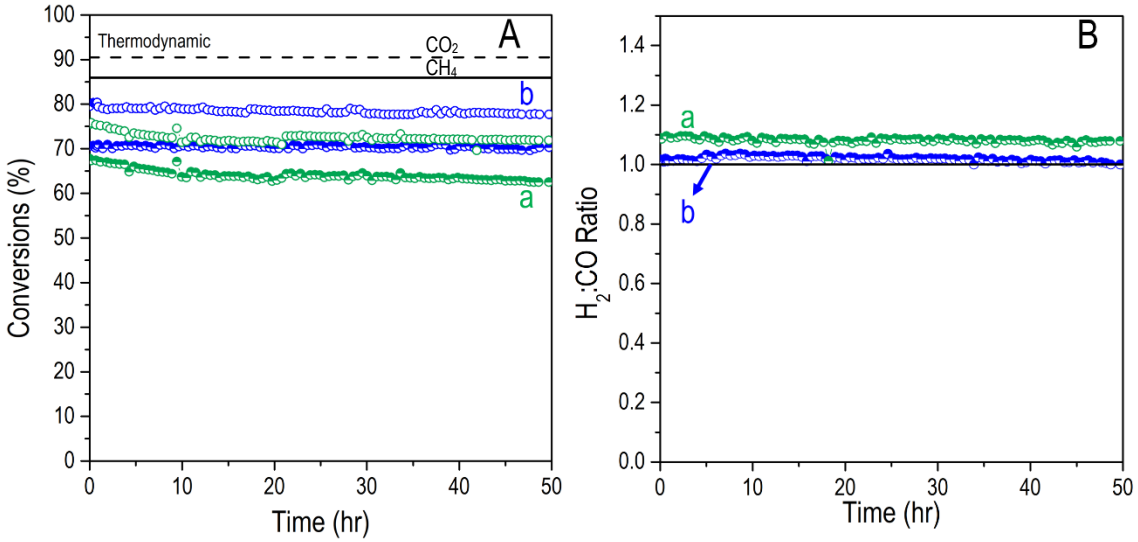

Figure III-19: Variation of (A) CH_4 (filled circle) and CO_2 conversion (empty circle), and (B) H_2:CO ratio as a function of time on stream during DRM (T= 650 °C, P=1 atm, CH_4:CO_2=1:1, GHSV= 36 $L.g^{-1}.h^{-1}$) over (a) Ni_5-Al_2O_3 and (b) Ni_5-Mg_{15}-Al_2O_3

Looking in more details, Ni_5-Mg_{15}-Al_2O_3 leads to slightly higher conversions (by 4 wt% in CO_2 conversion) as well as a slightly higher stability than Ni_5-Al_2O_3 that faces around 5% loss of its activity after 50 hours, attributable to higher coke deposition since the H_2:CO value is higher than 1 (Figure III-19 B). This agrees well with the proposal discussed in chapter I that adding a moderate amount of Mg boosts the creation of basic sites that favor CO_2 chemisorption on the catalyst, and hence its reaction with formed carbon species, thus reducing carbon deposition. Nevertheless, the promoting effect of Mg is not clearly intelligible, and cannot be analyzed with great accuracy, because of the operating conditions (limited GHSV) that lead to conversions close to equilibrium.

III.7.3. Performances of the Ni_5-Mg_y-Al_2O_3 catalysts at a GHSV of 180 $L.g^{-1}.h^{-1}$

III.7.3.1. Light off curves

Higher GHSV (180 $L.g^{-1}.h^{-1}$) was applied to lower the conversions and allow for a correct comparison of performances between the prepared Ni_5-Mg_y-Al_2O_3 catalysts. Figure III-20 shows results of light off curves (conversions followed while increasing the temperature) for four chosen catalysts (Ni_5-Al_2O_3, Ni_5-Mg_{15}-Al_2O_3, Ni_5-Mg_{30}-Al_2O_3, and Ni_5-Mg_{50}-Al_2O_3). Both CH_4, and CO_2 conversions in graphs A and B increase with temperature no matter what is the amount of MgO indicative of an endothermic DRM as demonstrated in the thermodynamics graphs in chapter II. Conversions on mesoporous Ni_5-Mg_{15}-Al_2O_3 are always the highest compared to the other three samples, and by more than 20% for instance at the temperature of 750 °C. Increasing further the amount of Mg (Ni_5-Mg_{30}-Al_2O_3) is no longer beneficial and leads to a catalyst with similar activity to that of the Mg-free Al_2O_3 based sample.

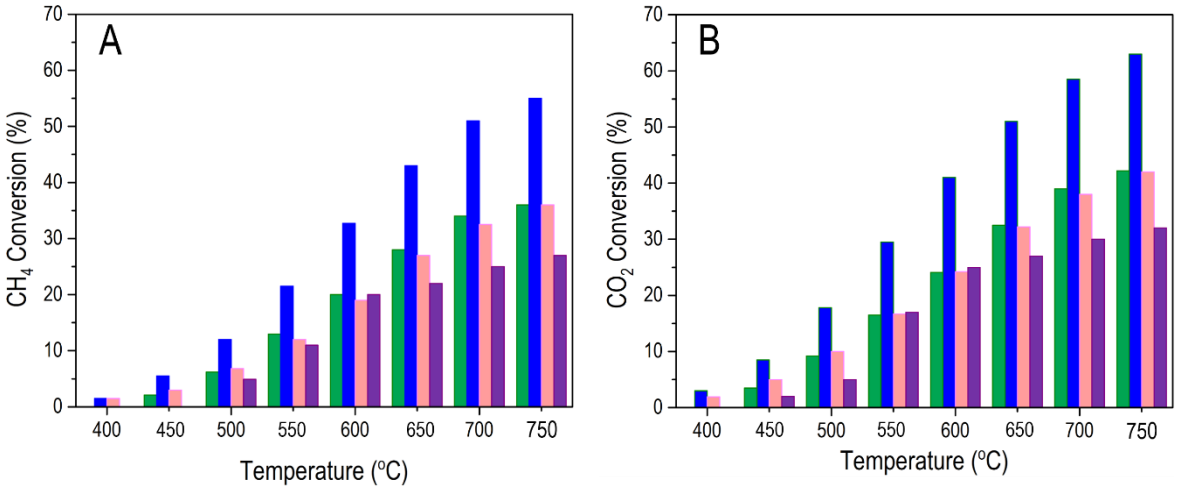

Figure III-20: Variation of (A) CH_4 and (B) CO_2 conversion levels as a function of temperature (400-800 °C) during DRM (P=1 atm, CH_4:CO_2=1:1, GHSV=180 $L.g^{-1}.h^{-1}$) over (green) Ni_5-Al_2O_3, (blue) Ni_5-Mg_{15}-Al_2O_3, (pink) Ni_5-Mg_{30}-Al_2O_3, (purple) Ni_5-Mg_{50}-Al_2O_3

Moreover, Ni_5-Mg_{50}-Al_2O_3 with the highest Mg content shows a continuous decline in conversion.

The H_2:CO product ratios obtained over the 4 catalysts as a function of temperature is presented in Figure III-21. As the temperature increases, the H_2:CO ratio in mesoporous Ni_5-Mg_y-Al_2O_3 increases to reach values close to 1 at 650 and 750 °C as expected thermodynamically. However with 26 wt% of Mg (Ni_5-Mg_{50}-Al_2O_3) the H_2:CO ratio is lower than 1 highlighting on the probable appearance of reverse water gas shift reaction.

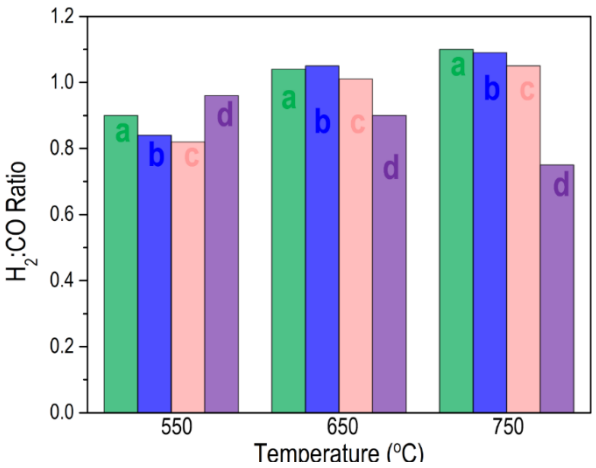

Figure III-21: Variation of H_2:CO ratio as a function of temperature during DRM (P=1 atm, CH_4:CO_2=1:1, GHSV=180 $L.g^{-1}.h^{-1}$) over (a) Ni_5-Al_2O_3, (b) Ni_5-Mg_{15}-Al_2O_3, (c) Ni_5-Mg_{30}-Al_2O_3, (d) Ni_5-Mg_{50}-Al_2O_3

III.7.3.2. Stability of Ni_5-Mg_y-Al_2O_3 catalysts

Stability tests of the aforementioned samples were done at 650 °C and the catalytic results are shown in Figure III-22 as a function of time on stream. Ni_5-Mg_{15}-Al_2O_3 (curve b) was the most stable catalyst through time with 0% loss in activity compared to 2% loss for both Ni_5-Al_2O_3 (curve a) and Ni_5-Mg_{30}-Al_2O_3 (curve c), and 6% loss for Ni_5-Mg_{50}-Al_2O_3 (curve d) after 12 hours test. The H_2:CO ratio was also very close to 1 for the 7 wt% Mg alumina based catalyst

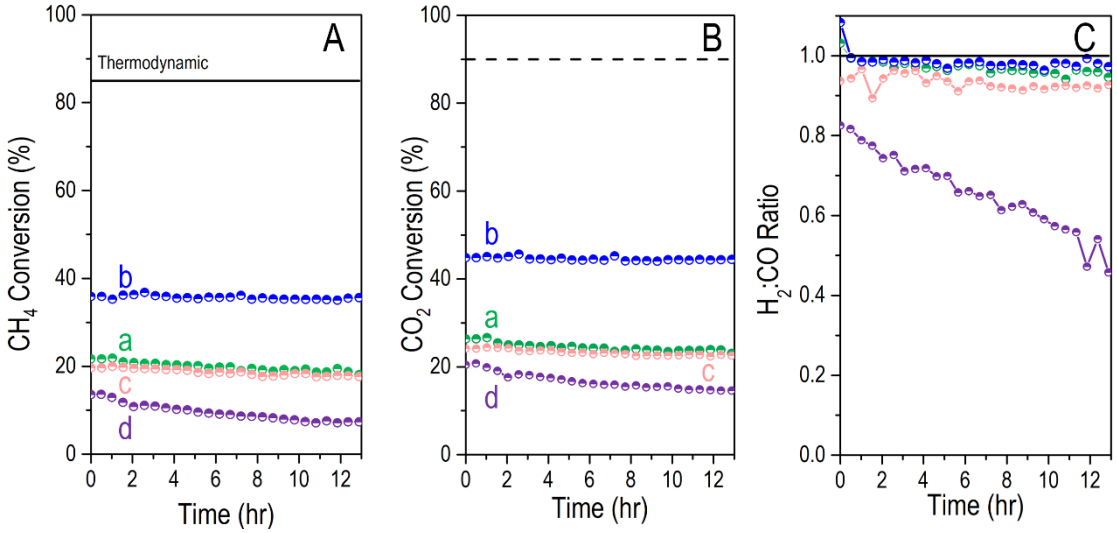

Figure III-22: Variation of (A) CH_4 conversion, (B) CO_2 conversion, and (C) H_2:CO ratio as a function of time on stream during DRM (T= 650 °C, P=1 atm, CH_4:CO_2=1:1, GHSV=180 $L.g^{-1}.h^{-1}$) over (a) Ni_5-Al_2O_3, (b) Ni_5-Mg_{15}-Al_2O_3, (c) Ni_5-Mg_{30}-Al_2O_3, (d) Ni_5-Mg_{50}-Al_2O_3. Thermodynamic values of CH_4 and H_2:CO (straight black line) and CO_2 (dashed black line) are calculated using the HSC 7.1 software

in contrast to the sample carrying the highest amount of Mg (26 wt%) that exhibits a much lower value of 0.82 and decreases through time indicating a strong influence of RWGS reaction over this sample. This difference in catalytic behavior can be explained by the influence of Mg loading on the structural and textural properties of the samples. Indeed, the moderate amount of Mg (7 wt%) contributed to well-ordered alumina walls support with equal repartition of Mg and Ni species and small Ni nanoparticles. In addition, the Mg present helps in enhancing CO_2 chemisorption and activation that cast any source of carbon formed during CH_4 activation. However, increasing a lot the amount of Mg, as in the case of Ni_5-Mg_{50}-Al_2O_3, degrades the uniform porosity (as seen in the previous sections), weakens Ni dispersion, and strengthens MgO segregation. The extensive amount of Mg triggers tremendous CO_2 sites that help in directing the reverse water gas shift reaction retarding and hindering the activity of the main reaction [195].

The XRD for the spent samples (Table III-5) agree well with the catalytic test results. Ni_5-$Mg_{15}Al_2O_3$ has a 4.2 nm Ni^0 particle size that is quite similar to its reduced value and therefore no sintering has occurred under the harsh reaction conditions imposed. On the other hand, the nanoparticle size of Ni_5-Mg_{50}-Al_2O_3 increased from 8.8 nm in its reduced form to 9.7 nm after reaction implying some sort of sintering and growth of metallic Ni^0 that could also boost deactivation.

III.7.4. Turn over frequency and activation energy of Ni_5-Mg_y-Al_2O_3 catalysts

Turn over frequency (TOF) are used to make a direct comparison between the samples since they consist of normalized values taking into account the dispersion and number of metallic active sites. The TOF of each sample was calculated by taking an average value of the conversion at 650 °C after 2 hours reaction and presented in Table III-7. The TOF value increased from 5.77 s^{-1} in Ni_5-Al_2O_3 to 6.64 s^{-1} in Ni_5-Mg_{15}-Al_2O_3 that is the maximum value achieved, then decreased to reach 3.03 s^{-1} in Ni_5-Mg_{50}-Al_2O_3.

Table III-7: Apparent activation energies (Ea) for the prepared Ni_5-Mg_y-Al_2O_3 catalysts

Sample	TOF (s^{-1})	$EaCH_4$ ($kJ.mol^{-1}$)	$EaCO_2$ ($kJ.mol^{-1}$)	Reference
Ni_5-Al_2O_3	5.77	35.92	26.32	This work
Ni_5-Mg_{15}-Al_2O_3	6.64	28.14	22.30	This work
Ni_5-Mg_{30}-Al_2O_3	6.23	34.30	26.22	This work
Ni_5-Mg_{50}-Al_2O_3	3.03	36.59	28	This work
Ni_7-Ce_y-Al_2O_3	-	41.40	-	[134]
Ni_7-Ce_y-Al_2O_3	-	38.93	-	[82]
Ni_{13}-La_y-Al_2O_3	3.45-5.77	44.38	-	[196]
Ni-Pt-Al_2O_3	-	104.67	-	[195]
Ni_5-CaO_{21}-Al_2O_3	-	108.85	98.74	[197]
Ni-Al_2O_3	0.6	70.60	69.00	[198]
Ni-γAl_2O_3	-	51.9	56.1	[199]
Ni-K/CeO_2-Al_2O_3	-	46.1	46.2	[200]

To further understand the promotion effect of MgO for DRM, the activation energy (E_a) of all the catalysts was obtained based on Arrhenius formula over a temperature range of 550-700 °C with much higher space velocity of 666 $L.g^{-1}.h^{-1}$ guarantying both low conversion levels (<15%) and absence of transport effect necessary for obtaining kinetics information. The relationship between natural logarithm of CH_4 consumption rate and reciprocal of temperature is depicted in Figure III-23 and the values of Ea are presented in Table III-7. The intrinsic experimental data of each catalyst are taken after 60 minutes time on stream to ensure stable performance.

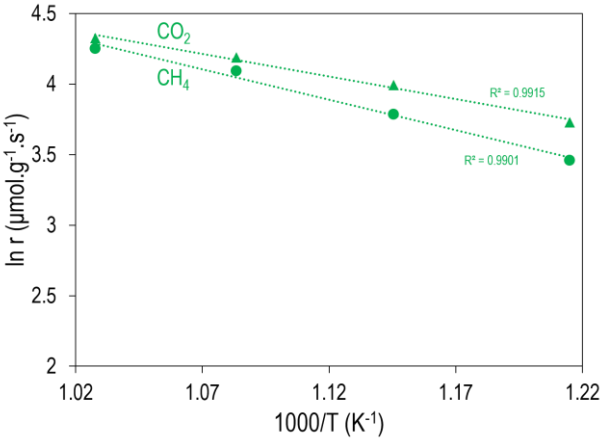

Figure III-23: Example of Arrhenius plot in DRM of Ni_5-Al_2O_3 catalyst

As estimated from literature, the methane apparent activation energies in DRM for all Ni based catalysts is in the range of 20-360 $kJ.mol^{-1}$. This wide range of values is dependent on the type of support, the nature of promoters, and the catalytic tests conditions applied. It can be mentioned that our results of Ea are in the same order of magnitude compared to literature [196,197]. As shown in Table III-7, regardless of the amount of Mg added, the Ea of CH_4 consumption for all catalysts studied is higher than that of CO_2. This means that the Ea of CH_4 is more sensitive to temperature change than CO_2 [195,199–202], consequently higher CO_2

conversions compared to CH_4 are obtained. In addition, Ni_5-Mg_{15}-Al_2O_3 has the lowest activation energy for CH_4 and CO_2 consumption (28.14 and 22.30 kJ.mol^{-1}, respectively) and the trend is in good agreement with what was obtained in the activity of those catalysts. Thus, the addition of a proper amount of magnesium promoter can remarkably reduce the energy consumption of the system by lowering adsorbed CH_4 and CO_2 species E_a in DRM. However, with a very high amount of Mg (15-26 wt%), the activation barrier becomes higher and the Ea value increases. Not to mention, that the values of Ea obtained in this study are lower than several Ni-Al_2O_3 based catalysts studied in literature (Table III-7) independent of the amount of promoter present.

III.7.5. Power law rate expression for Ni_5-Al_2O_3 catalyst

The influence of the partial pressures of CH_4 and CO_2 on the DRM rate was studied over mesoporous Ni_5-Al_2O_3 catalyst. A constant CH_4 partial pressure of 0.05 atm was used as the CO_2 partial pressure was varied between 0.01 and 0.05 atm and vice versa. The CH_4 consumption rates in the kinetics measurements ($-r_{CH4}=\frac{X_{CH4}\times F_{CH4}}{W_{cat}}$; XCH_4 is CH_4 conversion, FCH_4 is the initial flow rate of CH_4 (mmol.s^{-1}) and W_{cat} is the catalyst weight (g)) are calculated from the slopes of the conversions versus residence time plots. The emperical power low $-r_{CH4}=K\times P^{a}_{(CH4)}\times P^{b}_{(CO2)}$ was used to estimate the reaction orders (a, b) and the apparent rate constant (K) by applying the non-linear regression analysis in POLYMATH 6.1 software choosing Levenberg-Marquardt algorithm. The obtained rates in Table III-8 and their corresponding partial pressure values obtained at 650 °C were utilized in order to calculate and provide the values of the reactants orders presented. Results of the regression analysis give the following values: a= 0.75, b= 0.99 and K= 13.48 (mmol.g^{-1}.s^{-1}.atm$^{-(a+b)}$) with a variance (σ^2) of 6.242E^{-06}. Both CH_4 and CO_2 orders were close to 1, similar to a study done by Wang S. et al. who demonstrated that when the partial pressure of CO_2 is below 8.4 kPa, the reaction order of CO_2 is almost 1 [203]. On the other hand, the power constant for CO_2 is higher than the order of CH_4 suggesting that the reaction is more sensitive to CO_2 partial pressure than CH_4 partial pressure. This dependence of Ni-Al_2O_3 on CO_2 partial pressure might be probably due to the utilization of oxygen coming from CO_2 to clean deposited carbon in agreement with the deactivation seen in stability results. As for the Ni_5-Mg_{15}-Al_2O_3, the amount of basic sites present could enhance the chemisorption of CO_2 that provides the oxygen needed in removing carbon, hence limiting CO_2 dependency [204]. However, this is just a hypothesis that needs to be justified by similar kinetics experiments on the Mg-based material. The kinetics of DRM as

the simple power-law model is a simple model that provides rough estimation of the parameters, but is insufficient under a large extent of partial pressure data. Description of the mechanistic steps is needed by using Langmuir-Hinshelwood model to describe DRM kinetics. This process was also tackled in the core of the thesis but is not presented because it has not finished yet.

Table III-8: Initial rates of DRM at 650 °C over mesoporous Ni_5-Al_2O_3 catalyst

Partial pressures (atm)		CH_4/CO_2	Reaction rate (mmol.g^{-1}.s^{-1})
CH_4	CO_2		
0.01	0.05	0.2	0.0188
0.02	0.05	0.4	0.0363
0.03	0.05	0.6	0.0548
0.04	0.05	0.8	0.0645
0.05	0.05	1	0.0701
0.05	0.04	1.2	0.0576
0.05	0.03	1.6	0.0441
0.05	0.02	2.4	0.0284
0.05	0.01	4.8	0.0159

III.8. Conclusion

Ni_5-Mg_y-Al_2O_3 ordered mesoporous catalysts containing a wide range of Mg wt% (0-26 wt%) were synthesized using the evaporation induced self-assembly procedure associated to a "one-pot" methodology. Based on extensive physicochemical properties seen through the chapter, the inclusion of a maximum of 7 wt% Mg loading preserves high and homogenous Ni dispersion with simultaneous excellent Mg repartition. Mesoporous Ni_5-Mg_{15}-Al_2O_3 acquired also organized porosity that is even better than Al_2O_3 and Ni_5-Al_2O_3. For instance, Mg^{2+} ions facilitate the rate of hydrolysis of P123 and aluminum precursor especially that some AlO_x sites in the mesoporous alumina are preferable doping sites for Mg atoms. These good structural and textural characteristics, in addition to the enhanced basicity seen by infra-red (creation of basic sites) that accelerates CO_2 chemisorption, contributed to superior catalytic performances (lowest activation energy) with the best activity and stability among the rest of the samples.

On the contrary, if we continue to increase the amount of Mg (15-26 wt%), Ni species lose their excellent repartition over the alumina support and MgO is segregated. The organized

mesoporosity also disappears forming Mg-O bonds with longer length than those of Al-O bonds expanding the Al_2O_3 structure. As a result, the catalytic performance faces a calamitous decrease (increase in activation energy) especially that the excessive number of basic sites can lead to CO_2 coverage of active Ni sites. Hence, this chapter has justified the reason behind observing a "volcano-shape" curve in most of the Ni-Mg-Al_2O_3 studies.

IV. Chapter IV: Porous nickel-alumina derived from metal-organic framework (MIL-53): a new approach to achieve active and stable catalysts in methane dry reforming

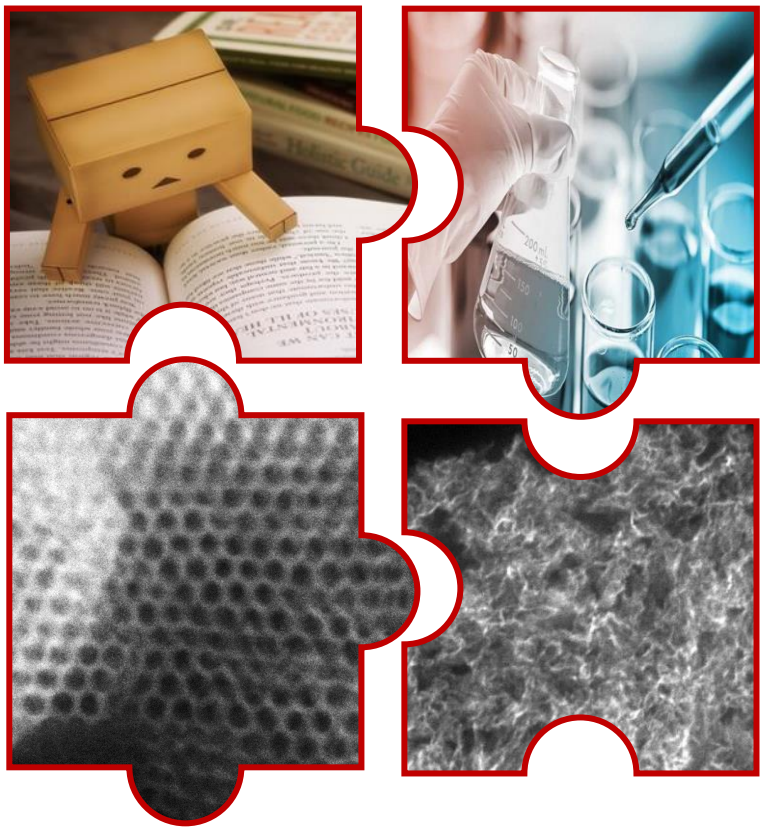

This chapter tackles a second strategy of synthesizing a material that combines the features of high porosity, high surface area and intimate mixing between Ni metal and Al_2O_3 support with high activity and stability in DRM. A short literature review about MOF materials will be elaborated specifying the selected type in this thesis. The preparation steps will be then described in details along with the proper textural and structural properties of the novel obtained Ni-Al_2O_3 materials that were then treated in DRM reaction to compare their performance to those of a commercial-based catalyst.

IV.1. Literature review

MOFs (**M**etal **O**rganic **F**ramework) are highly porous hybrid materials made by a regular assembly of metal clusters connected to one another's by multifunctional organic linkers. For example, MOF structures can be synthesized using common organic ligands like 1,4-benezenedicarboxylic acid, its functionalized forms and 1,3,5-benzenedicarboxylic acid in conjunction with metal nodes of Zn^{2+}, Cu^{2+}, Cr^{3+}, Al^{3+}, Fe^{3+} and Zr^{4+} [205]. MOF abbreviation is usually used as a general name of a class of compounds, however there are many MOFs named according to the place of their discoveries such as UiO (**U**niversitetet **i** **O**slo), MIL (**M**aterials of **I**nstitut **L**avoisier), and HKUST (**H**ong **K**ong **U**niversity of **S**cience and **T**echnology). Other MOFs have zeolites topology with metal ions surrounded by tetrahedra made of nitrogen atoms and connected through imidazole rings that are designated as ZIF (**Z**eolite **I**midazole **F**ramework). MOFs, in general, are characterized by extremely high specific surfaces and pore volumes that make them of great interest as host materials as was

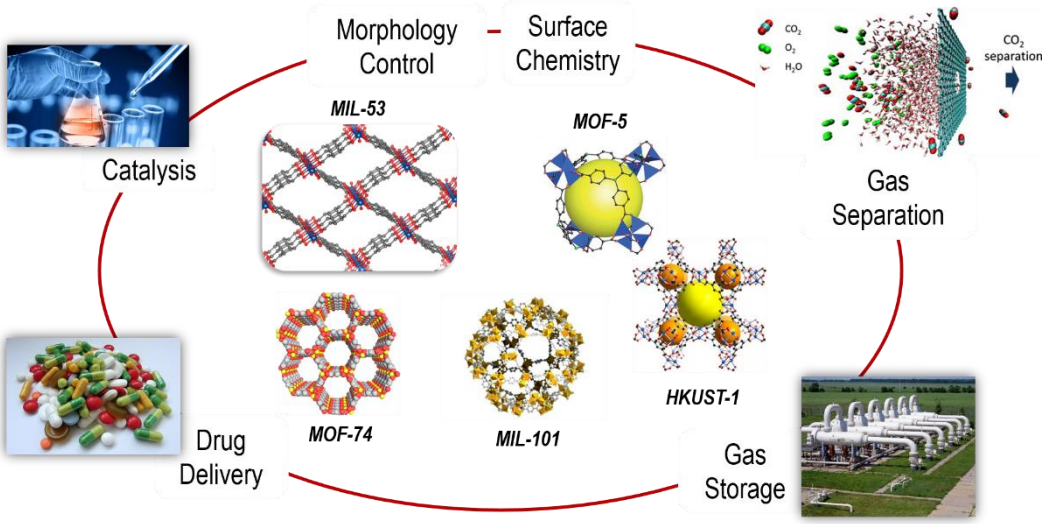

Figure IV-1: Types of several MOFs and their applications

already demonstrated in many applications such as gas storage, molecular separation, sensing, drug delivery or magnetism (Figure IV-1) [206]. In the field of catalysis, the high accessibility of their metal nodes and their reactivity have started to be exploited as well, even if stability issues in the conditions of catalysis still often remain to be solved.

Besides, the scope of MOF application was recently broadened to another level. Indeed, these hybrid materials are used as sacrificial templates to synthesize either carbonaceous or purely inorganic materials with unique textural properties depending on the thermal treatment used for their transformation [207–210]. Starting with the carbon-based supports, there is quite abundant literature about it. The first 8 lines in Table IV-1 summarize the reported Ni/C-based catalysts doped with nickel derived from MOF and details the treatment conditions applied as well as surface areas obtained and types of applications. In all cases, to obtain a carbon support from the MOF, the sample was thermally treated in an inert gas (N_2, Ar). The Ni particle size ranged from 5 nm when coupled with Pt to 50 nm when present alone. The surface area could be as small as 7 $m^2.g^{-1}$ and as large as 750 $m^2.g^{-1}$.

As our main interest in the present work concerned metal oxides (more specifically alumina) derived from MOFs, Table IV-1 also embraces the different existing bibliographic examples on such systems. To obtain metal oxide, the MOF structure has then to be thermally treated under air or pure O_2. As seen in the table, in the case of alumina, no active metal phase was added and the prepared materials, with surface areas varying from 50 to 270 $m^2.g^{-1}$, were not tested in any application. For these samples, Table IV-2 details the differences between the type of the parents MOF used, the ligand nature, the Al source and the thermal treatment applied. Despite the fact that these alumina were already reported, they were not chosen in our study because they have expensive ligand or Al source in addition to the high temperature and long time required for the preparation of the MOF that is later calcined to obtain the Al_2O_3 oxide.

In this thesis, the selected MOF is instead an aluminum-based MIL-53(Al) composed of aluminum hydroxyl chains connected by terephthalate organic linkers and running along one-dimensional channels. The benefit of this MIL-53(Al) is that it is synthesized using a microwave within 30 minutes reaction only, the linker and Al source are cheaper than the ones mentioned in Table IV-2. Moreover, MIL-53(Al) is made from the assembly of relatively inexpensive components, namely hydroxyl-aluminum species and terephthalate linkers, which can be extracted from natural or recycled feedstock [211,212] making this MOF-derived strategy economically and ecologically viable.

Table IV-1: Summary about Ni/C and oxides-MOF-derived materials and their applications

Sample	Derived MOF	Treatment	Particle size (nm)	Surface area ($m^2.g^{-1}$)	Application
Ni@C-N[213]	MOF	Ar	17.4	100-200	Alkanes oxidation
Ni/C[214]	MOF	N_2	19-40	7, 51, 389	4-nitrophenol reduction
Ni/C[215]	NiOF	N_2	11	130	Super capacitors
Ni-Zn/C[216]	ZIF-8	N_2	n.m.	750	CO_2 capture and separation
Ni/C[217]	MOF	Ar	18-50	18-165	H_2 evolution reaction
CuNi/C[218]	MOF	N_2	15	91	Furfural Conversion to cyclopentanone
Ni/C[219]	MOF	N_2	n.m.	460-600	Super capacitors
Pt-Ni/PC[220]	MOF-5	Ar	5	234	Fuel cells
Mn_3O_4[221]	Mn-MOF	Air	-	108-160	No Application
Co_3O_4[210]	ZIF-67	Air	8-28	22-120	Gas sensing
ZnO/Co_3O_4[222]	ZIF-8@ZIF67	Air	n.m.	2-25	CO_2 photo reduction
Cr_2O_3/Al_2O_3[207]	MIL-101	O_2	30	102	Isobutane dehydrogenation
ZrO_2[209]	UiO-66	Air	3.1	174	No Application
Cu/ZnO[223]	HKUST-1	Air	24	5.5	Hydrogenolysis of glycerol
Au/TiO_2[224]	MIL-125	O_2	n.m.	20	CO_2 reduction
Al_2O_3[225]	MOF A520	Air	-	205	No Application
Al_2O_3[226]	MIL-110	Air	-	138	No Application
Al_2O_3[226]	MIL-100	Air	-	123	No Application
Al_2O_3[227]	MIL-96	Air	-	56	No Application
Al_2O_3[228]	MIL-53	O_2	-	88	No Application
Al_2O_3[228]	DUT-5	O_2	-	270	No Application

Table IV-2: Differences in the synthesis of Al-based MOF_s

Al-based MOFs	Ligand Type	Al source	Method of preparation
MOF A520	Fumaric acid	$Al_2(SO_4)_3.18H_2O$	Glass container/60 °C, 4h
MIL-110	Trimethyl-1,3,5-benzenetricarboxylate	$Al(NO_3)_3.9H_2O$	Autoclave/210°C,72h
MIL-100	Trimethyl-1,3,5-benzenetricarboxylate	$Al(NO_3)_3.9H_2O$	Autoclave/210°C,3.5h
MIL-96	Trimethyl-1,3,5-benzenetricarboxylate	$Al(NO_3)_3.9H_2O$	Autoclave/210°C,24h
DUT-5	*Biphenyl-4,4′-dicarboxylic acid*	$Al(NO_3)_3.9H_2O$	Autoclave/180°C,24h
MIL-53	Benzene-1,4-dicarboxylic acid	$Al(NO_3)_3.9H_2O$	Autoclave/220°C,72h

This MIL-53(Al) will be impregnated for the first time with nickel precursor and used as a source of porous Ni-Al_2O_3 catalyst that will be applied in dry reforming of methane reaction. The MIL-53(Al) host gathers the attributes required to obtain a porous nickel-alumina solid solution after its calcination: on one hand, it possesses a high porosity and metal-cluster accessibility expected to favor the homogeneous dispersion of nickel species within the oxide structure; on the other hand, it contains organics whose decomposition enables the formation of porosity in the obtained alumina [228]. An additional benefit is the occurrence in this structure of aluminum bridging hydroxyl groups lying along the inorganic chains that can interact with the nickel precursors and hence act as anchorage sites.

IV.2. Synthesis of mesoporous Ni-Al_2O_3 derived from MOF (MIL-53(Al))

The parent Al-containing MIL-53(Al) material was synthesized according to a known microwave-based procedure reported to provide nanocrystallites of homogeneous distribution in shape and size [229]. Figure IV-2 describes in details the step of MIL-53 preparation. It consists in mixing 1.21 g of **$AlCl_3.6H_2O$** (M_n=241.43, Sigma-Aldrich, 237078) and 0.42 g of **benzene-1,4-di-carboxylic acid** (M_n=166.13, Sigma-Aldrich, 185361) with 3 ml **water** and 5 ml of **dimethylformamide** (DMF) (M_n=73.09, Sigma-Aldrich, PHR1553) (Figure IV-2 A), then transferring the mixture into a 50 ml reactor and heating it in a microwave oven for 30 minutes at 125 °C at a heating ramp of 2 °C.min^{-1} and with a power of 200 W (Figure IV-2 B). The stability of these parameters are followed through synthesis on the screen of the microwave displaying a graph for example of power and temperature as a function of time (inset Figure IV-2 B). The solid obtained was recovered by centrifugation and washed six times in 10 ml of

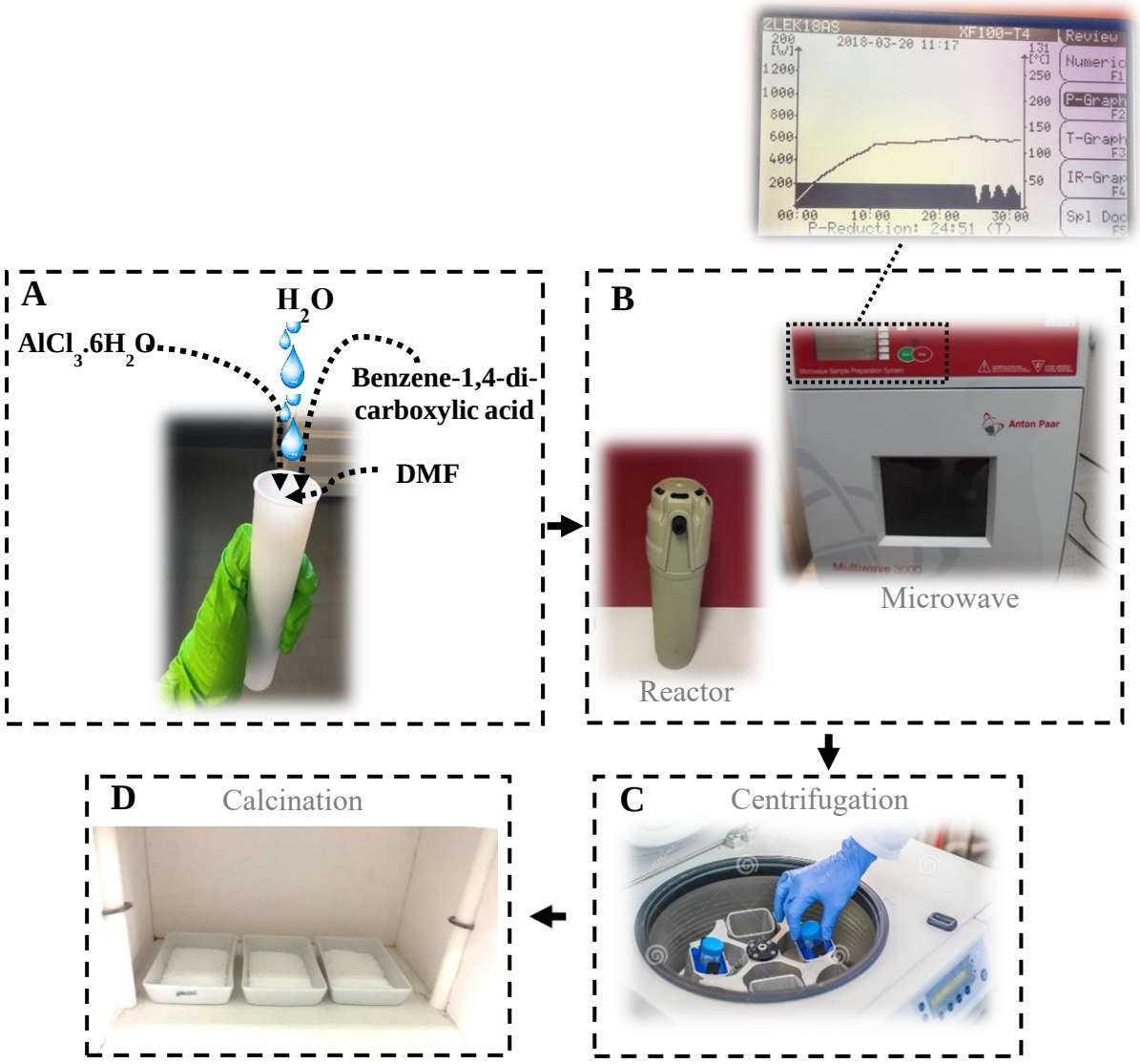

Figure IV-2: Chronological steps summary of preparing mesoporous Ni-Al_2O_3 with 5wt% nickel following the new metal organic framework route

DMF then in 10 ml of deionized water to ensure full removal of unwanted residues (Figure IV-2 C). After the last centrifugation, the white powder was dried for 24 h at 70 °C and heated in air (Figure IV-2 D) at 220 °C for 72 h to remove the structuring agent and obtain activated **MIL-53** sample.

Nickel introduction was carried out by incipient wetness impregnation performed on the **MIL-53** sample freshly dehydrated at 80 °C in an oven overnight. The procedure consisted in adding dropwise a $Ni(NO_3)_2.6H_2O$ aqueous solution with a volume equal to the pore volume of the MOF support (as estimated from N_2-sorption analysis) and a Ni concentration established as to correspond to a Ni/Al atomic ratio in the sample of 0.07 (i.e. final Ni content in the dry catalyst of 5 wt%). The solid obtained after drying at room temperature for 24 h is hereafter denoted **Ni/MIL-53** (Figure IV-3). Part of it was kept as such to perform hydration-dehydration

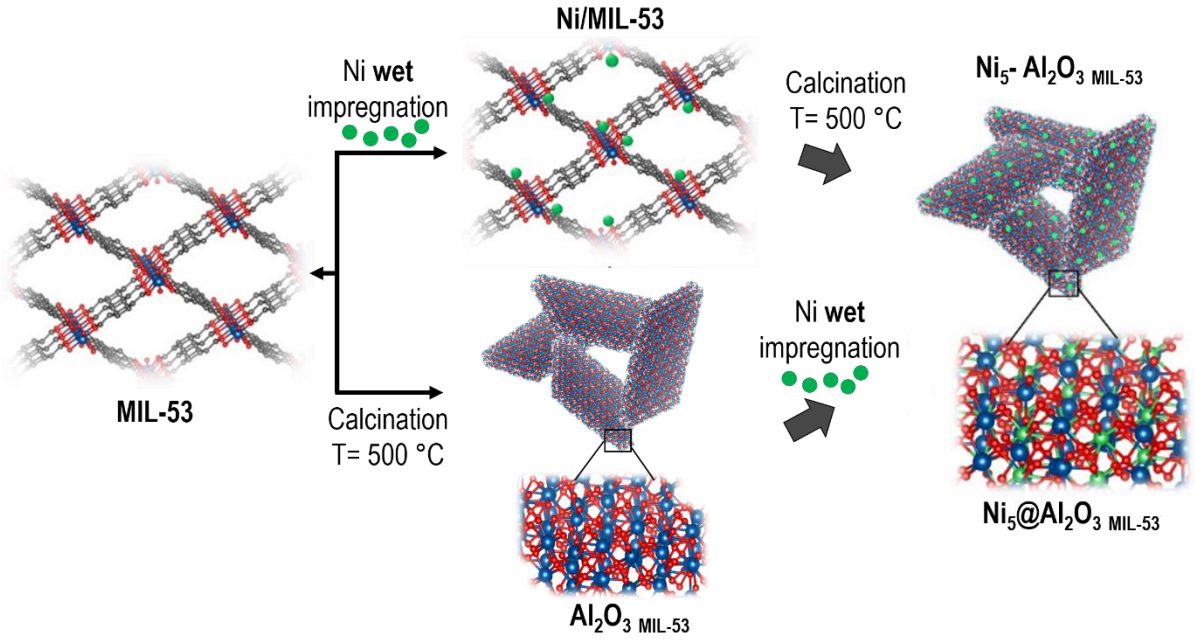

Figure IV-3: Schematic representing two types of Ni-Al_2O_3 catalyst derived from MIL-53 framework based on the order of Ni impregnation with respect to calcination

tests and the other part was submitted to calcination in air for 5 h at 500 °C (thin bed conditions, heating rate 0.5 °C.min^{-1}) to give **Ni_5-Al_2O_3 MIL-53**.

For comparison purposes, a reference sample was also prepared to check the influence of calcination order. To elaborate, **MIL-53** material was first placed in a ceramic plate and heated in static air at 500 °C (heating rate 0.5 ° C.min^{-1}) for 5 h to remove the organic linkers and lead to an alumina material (**Al_2O_3 MIL-53**). Then, the alumina support obtained was impregnated by 5 wt% Ni using same conditions as above (pre-calcined MIL-53) followed by a second calcination in air at 500 °C (Figure IV-3). To distinguish between these two nickel-based alumina catalysts, the latter sample was denoted as **Ni_5@Al_2O_3 MIL-53**. These two alumina-based materials derived from MOF were compared to a disctinct commercial alumina support. It is a conventional γ-alumina support obtained by calcination at 500 °C in air of a commerical bohemite (Sasol Plural, alumina hydrate AlOOH). The obtained alumina was impregnated with 5wt% Ni following the same incipient wetness impregnation strategy mentioned previously and labeled as **Ni_5@Al_2O_3 COM**. The materials involved in this chapter are summarized in Table IV-3.

Table IV-3: Summary of the mesoporous Ni-Al_2O_3 catalysts prepared by the MIL-53 route

Sample	Support	Mode of Ni insertion	Ni content (wt%)
MIL-53	Synthesized	-	-
Ni_5-Al_2O_3 $_{MIL-53}$		I.W.I Prior MIL calc.	5
Ni_5@Al_2O_3 $_{MIL-53}$		I.W.I After MIL calc.	
Ni_5@Al_2O_3 $_{COM}$	Commercial	I.W.I	

IV.3. Physicochemical Characteristics of the parent MIL-53, activated MIL-53 and impregnated Ni_5-Al_2O_3 $_{MIL-53}$ materials

IV.3.1. Structure of the as-synthesized and activated MIL-53 materials

After synthesis in microwave conditions, the parent MIL-53 sample was first characterized by X-ray diffraction (Figure IV-4 a). The pattern is similar to that reported in the literature for a MIL-53 material synthesized with the same microwave procedure (MW) [229]. This validates the formation of the targeted MIL-53 framework, even if small differences can be observed between this XRD pattern and the ones reported after synthesis under conventional heating [229]. This can be due to the dynamic properties of the MIL-53 structure which pore size is strongly sensitive to guest adsorption (so-called "breathing behavior") [230]. Hence,

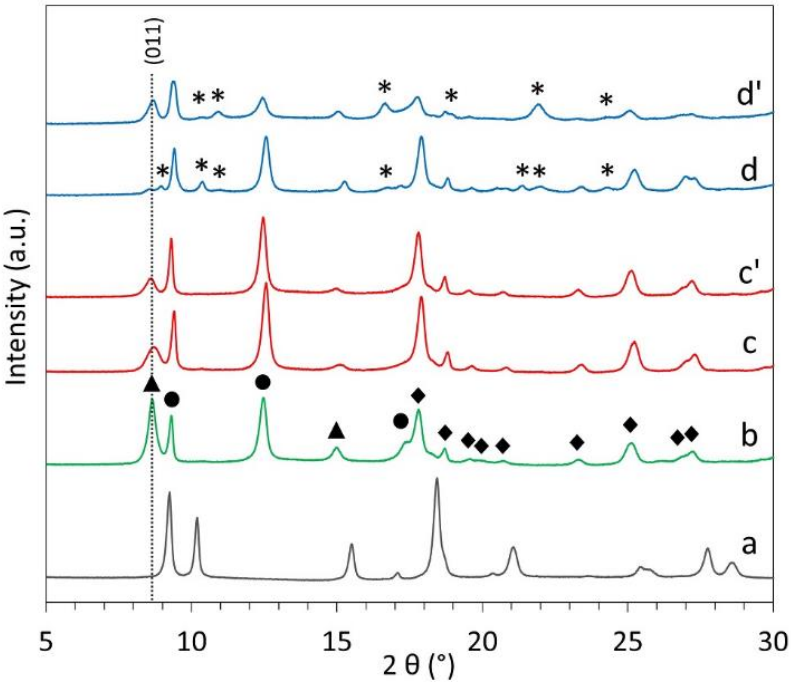

Figure IV-4: X-ray diffraction patterns of: (a) as synthesized MIL-53(Al), (b) activated MIL-53, (c) rehydrated MIL-53 dried in room atmosphere or (c') at 200 °C, (d) impregnated Ni/MIL-53 dried in room atmosphere or (d') at 200 °C. Triangles and spheres indicate the peak positions corresponding to the open and closed forms of the MIL-53 structure, respectively (as reported in [230]). Diamonds show unattributed reflections that may correspond to an intermediate state. Stars indicate peaks appearing after nickel impregnation. The dot vertical line shows the position of the 011 reflection characteristic of the MIL-53 large-pore phase.

different synthesis methods could lead to variations in the amounts of molecules (solvent and unreacted linkers) trapped within the pores due to different crystal formation rates.

After activation at 220 °C in air (to remove all adsorbates from the pores), the diffractogram changes to a completely different one (sample MIL-53, Figure IV-4 b), in accordance with the dynamic nature of the MIL-53 structure mentioned above. One can note however that the new XRD pattern is not composed only of peaks belonging to the large pore form of MIL-53 (indicated by black triangles, typical of empty pores), but it also contains peaks related to the narrow pore form (indicated by black spheres) as well as reflections characteristic of an intermediate state between the open and closed forms (indicated by black diamonds). This multiphasic structural state is related to the thermal history of the sample as already described by others for MIL-53 [231] and can be taken as representative of the "activated form".

IV.3.2. Structural properties of impregnated Ni/MIL-53

As shown in Figure IV-4 d, all the peaks corresponding to this activated form are still present after Ni impregnation (Ni/MIL-53), even if slightly shifted and with distinct relative intensities for some of them. More importantly, new tiny peaks appear at unusual positions and they are visible both after drying in room atmosphere and at 200 °C (identified by stars, Figure IV-4 d and d', respectively). Such new reflections were to our knowledge never reported for MIL-53, strongly suggesting that nickel cations are inserted within the pores where they provoke structural deformation by interacting with the framework as in the case of adsorbed organic guest molecules [232].

In order to confirm the origin of these new reflections, a series of experiments was done with the aim to demonstrate that they appear only in the presence of Ni and do not simply come from different hydration states generating cell volumes and symmetry changes in response to the above-mentioned "breathing behavior". We prepared to this end a nickel free hydrated MIL-53 sample to be compared to freshly impregnated Ni/MIL-53. This was done by immersing the freshly activated MIL-53 powder into a volume of pure water equivalent to the one used for Ni impregnation. XRD patterns were then taken, after submitting both rehydrated MIL-53 and impregnated Ni/MIL-53 to the same successive drying treatments consisting first in natural drying in room atmosphere (Figure IV-4 c and d) then in drying at 200 °C for 24h (Figure IV-4 c' and d'). Whatever the treatment, the additional tiny peaks (indicated by black stars) were present for Ni/MIL-53 (Figure IV-4 d and d') but not for MIL-53 (Figure IV-4 c and 2c').

Together with the limited intensity of these peaks that fits well the limited Ni content in the samples, this systematic difference is in line with a local framework distortion due to interaction with nickel cations occluded within the pores. Such distortion also agrees with the small shift to higher angle of the (011) reflection (at $2\theta = 8.7°$) of the large-pore phase pattern, which is particularly disturbed after nickel impregnation (Figure IV-4 d).

IV.3.3. Effect of the addition of Ni on porous characteristics

The presence of nickel within the pores is further supported by the strong decrease of the saturation volume of N_2 adsorbed at low relative pressure ($P/P_0 = 0.2$) in Ni/MIL-53 (Figure IV-5 c) compared to both activated MIL (Figure IV-5 a) and rehydrated MIL (Figure IV-5 b), which corroborates a pore hindrance linked to the presence of Ni^{2+}. Accordingly, the microporous volume drops from 0.40 $cm^3.g^{-1}$ (activated MIL-53) to 0.09 $cm^3.g^{-1}$ upon nickel impregnation (Ni/MIL-53) and the BET specific surface simultaneously diminishes from 1130 $m^2.g^{-1}$ (MIL-53) to 300 $m^2.g^{-1}$ (Ni/MIL-53). By comparison, the pore volume is much less affected (0.32 $cm^3.g^{-1}$) upon simple MIL rehydration without nickel. In such case, a small decrease is also noted, probably due to some (but limited) loss of structural integrity after water adsorption. This could also explain the XRD peak broadening seen for both rehydrated (MIL-53) and impregnated (Ni/MIL-53) series of samples ((011) reflection at $2\theta = 8.7°$ mainly, Figure IV-4). Noteworthy, the N_2 adsorption-desorption isotherms of all materials (MIL-53, rehydrated MIL-53 and Ni/MIL-53, Figure IV-5 a-c) also display a marked step at relative

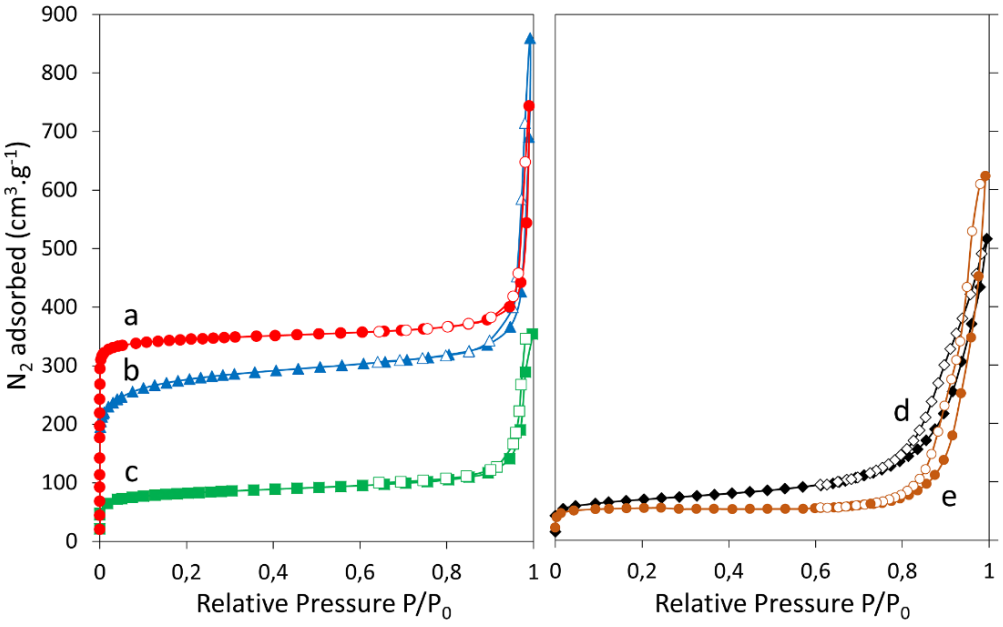

Figure IV-5: N_2 physisorption isotherms after degassing at 120 °C of: (a) freshly activated MIL-53, (b) rehydrated MIL-53, (c) Ni/MIL-53, (d) Ni_5-$Al_2O_{3\ MIL-53}$ and (e) Ni_5^0-$Al_2O_{3\ MIL-53}$. Filled and empty symbols correspond to adsorption and desorption isotherms, respectively.

pressures above $P/P_0 = 0.9$ characteristic of a substantial intercrystalline meso-macro porosity occurring between aggregated nanocrystals.

IV.3.4. Organic linkers removal followed by thermogravimetric analysis

Another evidence of the intimate mixing between the nickel precursor species and the porous network in Ni/MIL-53 is given by thermogravimetric analyses as discussed in this paragraph. This technique was applied to study the decomposition in air of the carbonaceous (terephthalate) linkers constitutive of the parent MIL-53, the aim being to form the oxide alumina matrix.

Figure IV-6 A shows the TGA profiles obtained on freshly activated MIL-53, rehydrated MIL-53 and impregnated Ni/MIL-53 (curves a to c, respectively). A weight loss of about 15 % between 200 °C and 420 °C is distinctly seen for impregnated Ni/MIL-53 (Figure IV-6 A c) but not for the Ni-free materials. As confirmed by the simultaneous MS detection of NO (mass 30) in the exhaust gas (Figure IV-6 B, bottom, blue curve), this weight loss

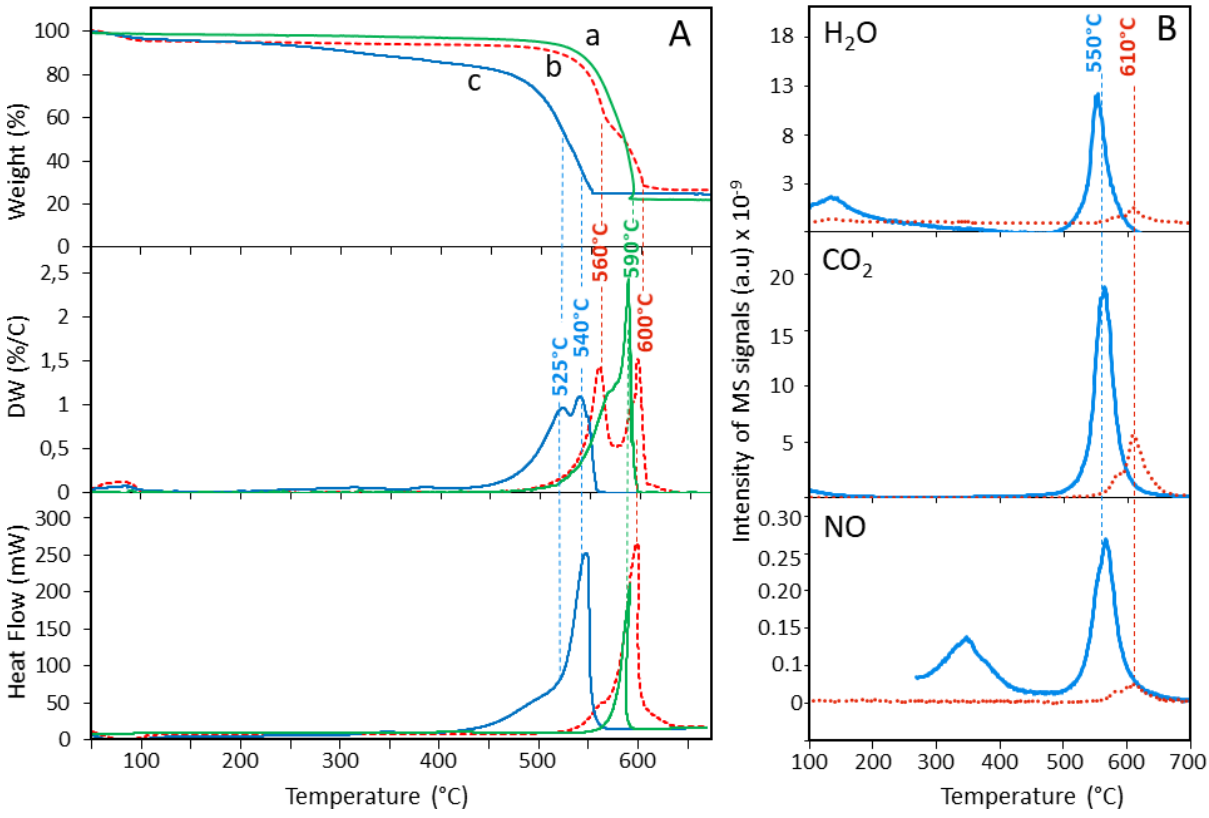

Figure IV-6: (A) TGA (top curves), DTG (middle curves) and DTA (bottom curves) profiles for samples: (a) freshly activated MIL-53, (b) rehydrated MIL-53 and (c) impregnated Ni/MIL-53. (B) Mass spectrometry profiles corresponding to the detection of H_2O (mass 18), NO (mass 30) and CO_2 (mass 44) for hydrated MIL-53 (red dotted lines) and impregnated Ni/MIL-53 (blue lines). The temperatures of peak maxima in B are slightly higher than in A due to the delay for the exhaust gases to reach the MS analysis chamber.

corresponds to the thermal decomposition of nitrates introduced together with nickel during the impregnation step.

From the curves in Figure IV-6, it can be also seen that the oxidizing nitrogen oxide species (such as NO) formed within the pores of Ni/MIL-53 during the heating induce a lowering by more than 60 °C of the temperature at which the linkers degradation occurs (important weight loss between 400-550 °C, Figure IV-6 c, top) compared to both freshly activated and rehydrated MIL-53 (process shifted to 500-650 °C for both of them, Figure IV-6 a and b). The DTG profiles (Figure IV-6 B, middle curves) reveal that the degradation takes place in two steps, as previously reported for the amino-teraphthalate MIL-125(Ti) [233]. The second step is accompanied by an evolution of CO_2 for both MIL-53 and Ni/MIL-53 and also of NO for Ni/MIL-53 (see respective curves in Figure IV-6 B), and the process is strongly exothermic as seen from the DTA profiles (Figure IV-6 A, bottom curves). Hence, all data indicate that the linkers degradation is displaced towards a significantly lower temperature after nickel impregnation, giving the following scenario during heating of Ni/MIL-53: (1) the temperature increase up to 150 °C leads to the dehydration of the hexahydrate nickel nitrate used as nickel precursor according to the equation $Ni(NO_3)_2.6H_2O \rightarrow Ni(NO_3)_2 + 6H_2O$, the theoretical mass loss of 59% for this event being close to the 50% measured by TG; (2) this is followed between 200 and 400 °C by nitrates decomposition into NO_x (NO, NO_2, etc.) [234] with simultaneous formation of a NiO-based phase (for the sake of neutrality preservation); (3) then, strongly adsorbed NO_x oxidizers remaining within the pores in close proximity (or in contact) with the organic linkers promote their decomposition, decreasing the temperature at which it occurs [235].

In view of these TG profiles, we decided to set the calcination temperature of Ni/MIL-53 during sample preparation (to form Ni_5-$Al_2O_{3\ MIL-53}$) at 500 °C, a temperature high enough to degrade the linkers but guaranteeing as well the development of the porosity and the large surface area of the pure mineral final phase. Indeed, it was recently reported that a temperature close to the onset of the parent MOF calcination temperature is optimal for the preparation of inorganic structures with preserved morphology and dimensions [210], which is important for preserving an intercrystalline porosity and large surface area in the obtained catalyst.

IV.4. Physicochemical properties of the calcined Ni_5-Al_2O_3 $_{MIL-53}$, $Ni_5@Al_2O_3$ $_{MIL-53}$, and $Ni_5@Al_2O_3$ $_{COM}$

IV.4.1. Morphologies, porous characteristics and Ni location in calcined Ni_5-Al_2O_3 $_{MIL-53}$

Figure IV-7 and Figure IV-8 show typical SEM and TEM micrographs of the parent (MIL-53) and impregnated then calcined (Ni_5-Al_2O_3 $_{MIL-53}$) materials. In both scanning (Figure

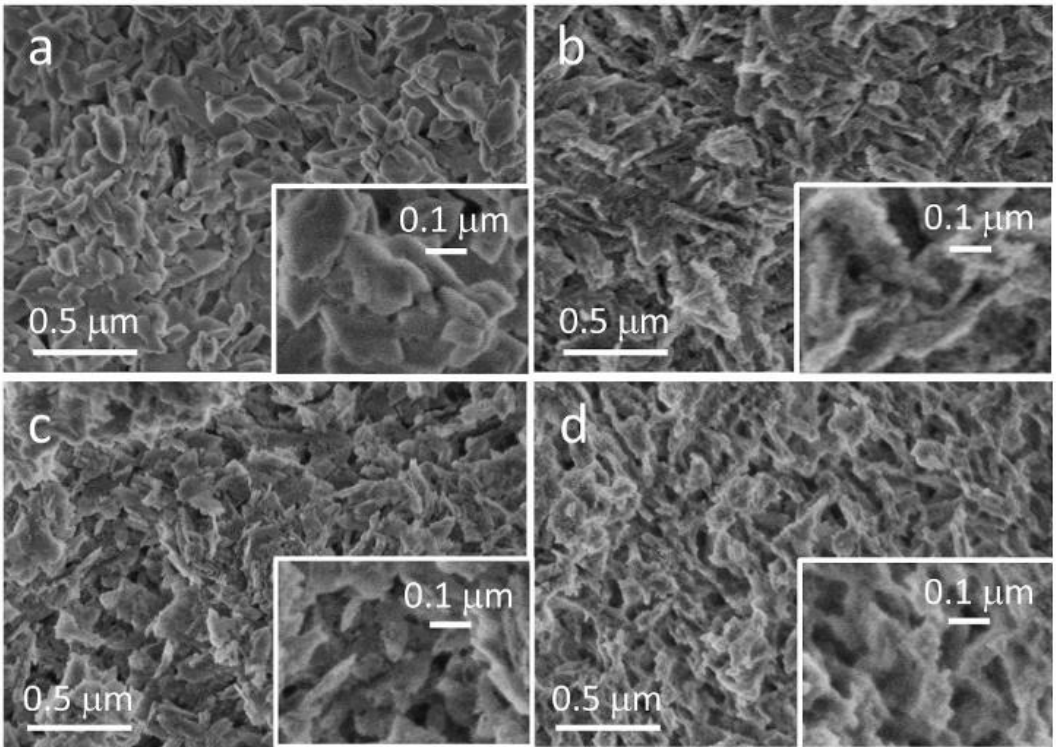

Figure IV-7: Representative SEM images of (a) MIL-53, (b) Ni_5-Al_2O_3 $_{MIL-53}$, (c) Al_2O_3 $_{MIL-53}$ and (d) $Ni_5@Al_2O_3$ $_{MIL-53}$

IV-7 a) and transmission (Figure IV-8 a) modes, MIL-53 appears as slightly elongated aggregated nanocristallites with uniform sizes of approximately 20 nm in length. Such morphology is coherent with the high intercrystalline volume identified above from N_2 physisorption. After calcination at 500 °C (sample Ni_5-Al_2O_3 $_{MIL-53}$, Figure IV-7 b and Figure IV-8 b), the size and shape of the nanograins are globally preserved although they tend to become thinner, forming fused ill-defined and more defective alumina flakes that are actually composed of several randomly interwoven nanosheets (inset in Figure IV-8 b). This is in line with the N_2 isotherm of this sample that displays features typical of layered mesoporous materials, namely (i) a progressive increase of the adsorbed N_2 volume, observed here at P/P_0 higher than 0.75 and (ii) a slit-type hysteresis spread over P/P_0 values, ranging here from 0.75 to 1 (Figure IV-5 d) and revealing a relatively polydisperse size distribution of large mesopores. The BET specific surface of 239 $m^2.g^{-1}$ is still high, even if much smaller than in the parent

MIL-53 material (Table IV-4) due to the organic linkers removal, and the microporous volume is close to that in Ni/MIL-53 (Figure IV-5 d and c, respectively).

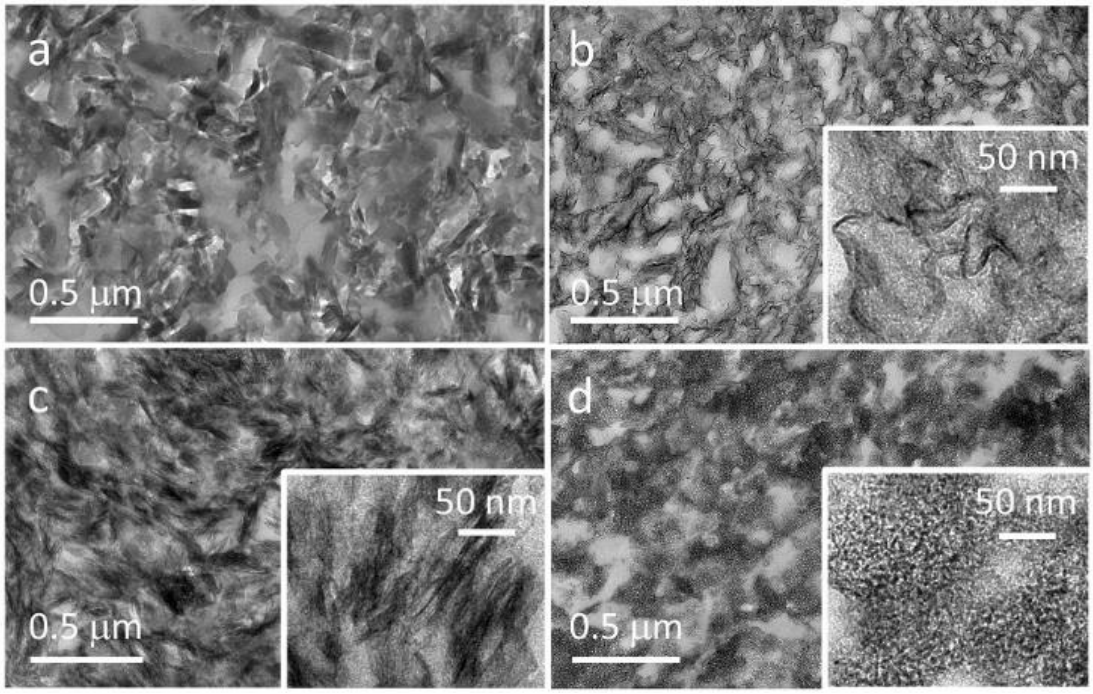

Figure IV-8: Representative HR-TEM images of (a) MIL-53, (b) Ni_5-$Al_2O_{3\ MIL-53}$, (c) $Al_2O_{3\ MIL-53}$ and (d) $Ni_5@Al_2O_{3\ MIL-53}$

Table IV-4: Textural characteristics, reduction temperature and nickel content

Sample names	Textural properties of calcined samples[a]			Reduction temperature (°C)	Ni content[b] (wt%)	Ni^0 nanoparticle size after reduction (nm)[c]		Ni^0 nanoparticle dispersion after reduction (%)[d]
	S.A. ($m^2.g^{-1}$)	V_{tot} ($cm^3.g^{-1}$)	Φ mean (nm)			reduced	spent	
MIL-53	1130	0.80	n.d					
Ni_5-$Al_2O_{3\ MIL-53}$	239	0.82	10	830	5.1 *(5.2)*			
Ni_5^0-$Al_2O_{3\ MIL-53}$	200	1.02	16			6.8 (*5.3*)	7.5	19 *(18.3)*
$Al_2O_{3\ MIL-53}$	318	1.19	6.2					
$Ni_5@Al_2O_{3\ MIL-53}$	244	0.94	5.1	700/820	4.7 *(4.6)*			
$Ni_5^0@Al_2O_{3\ MIL-53}$	130	0.55	5.6			10.2 (*8.0*)	11.0	12 *(11.8)*
$Al_2O_{3\ COM}$	185	0.51	9.2					
$Ni_5@Al_2O_{3\ COM}$	168	0.47	9.9	630/800	5 *(5)*			
$Ni_5^0@Al_2O_{3\ COM}$	125	0.43	10.3			22 (*18*)	29	5.6 *(9.6)*

a: total surface area (S.A.), total pore volume (V_{tot}) and mean pore diameter (mean) calculated from the N_2 sorption isotherms.

b: Ni content from TPR taking into account that the theoretical amount is 860 µmol.g^{-1}, In brackets: values determined by XRF.

c: mean size values calculated from the histograms of TEM, In brackets: values estimated from XRD by applying the Scherrer equation of the Ni^0 reflection at 2θ =51.9°. The particle sizes could not be identified by XRD after test because of the lack of sufficient sample amount.

d: nanoparticle dispersion calculated from the formula $D = 6\times10^9\times (V_{Ni}/A_{Ni})\times(1/d)$ where d is the particle size (estimated from XRD), V is the volume of Ni atom in the bulk metal and A is the area of the Ni surface atom [236,237]. In brackets: nanoparticle dispersion calculated from H_2-chemisorption

According to XRD (Figure IV-9 a), these nanosheets structurally correspond to a cubic spinel $NiAl_2O_4$ phase with (400) and (440) planes giving main peaks at 2θ = 45.0° and 65.6° [238–240]. They do not contain any peak attributable to crystalline NiO, confirming the intimate mixing between Ni and the oxide support. This also demonstrated by the temperature program reduction profile of Ni_5-Al_2O_3 $_{MIL-53}$ that displays only one peak centered at a high temperature of about 830°C (Table IV-4 and Figure IV-10 a) typical of the formation of the spinel $NiAl_2O_4$ phase [241,242].

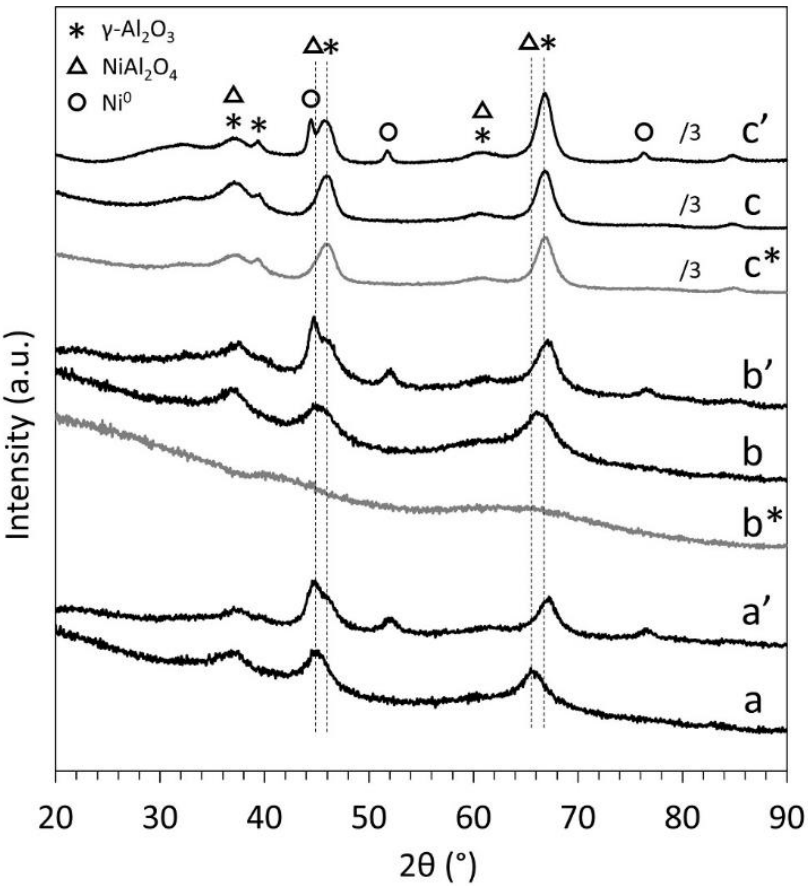

Figure IV-9: Diffractograms of the Ni containing samples: (a) Ni_5-Al_2O_3 $_{MIL-53}$, (a') Ni_5^0-Al_2O_3 $_{MIL-53}$, (b) $Ni_5@Al_2O_3$ $_{MIL-53}$, (b') $Ni_5^0@Al_2O_3$ $_{MIL-53}$, (c) $Ni_5@Al_2O_3$ $_{COM}$, (c') $Ni_5^0@Al_2O_3$ $_{COM}$. The diffractograms of the preformed alumina supports (light grey lines) are shown for comparison: (b*) Al_2O_3 $_{MIL-53}$ and (c*) Al_2O_3 $_{COM}$. Intensities are divided by 3 in patterns c*, c and c'.

The high and homogeneous Ni dispersion throughout the sample is also visible from STEM-HAADF and EDX elemental mappings that show the superimposed Ni and Al distributions on a representative Ni_5-Al_2O_3 $_{MIL-53}$ grain (Figure IV-11). Analysis of the selected area electron diffraction (SAED) patterns was also done on the calcined sample showing reticular distances (Figure IV-12) in the diffraction ring at d1 =1.8 Å and d2= 1.3 Å close to reticular distances d=2 Å and

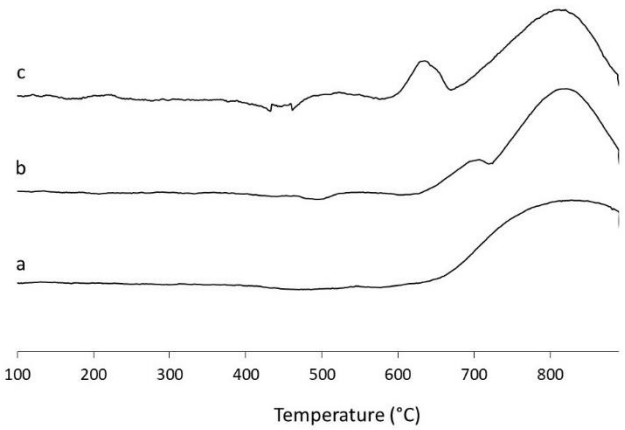

Figure IV-10: Temperature program Reduction analyses of the samples (a) Ni_5-Al_2O_3 $_{MIL-53}$, (b) $Ni_5@Al_2O_3$ $_{MIL-53}$, and (c) $Ni_5@Al_2O_3$ $_{COM}$.

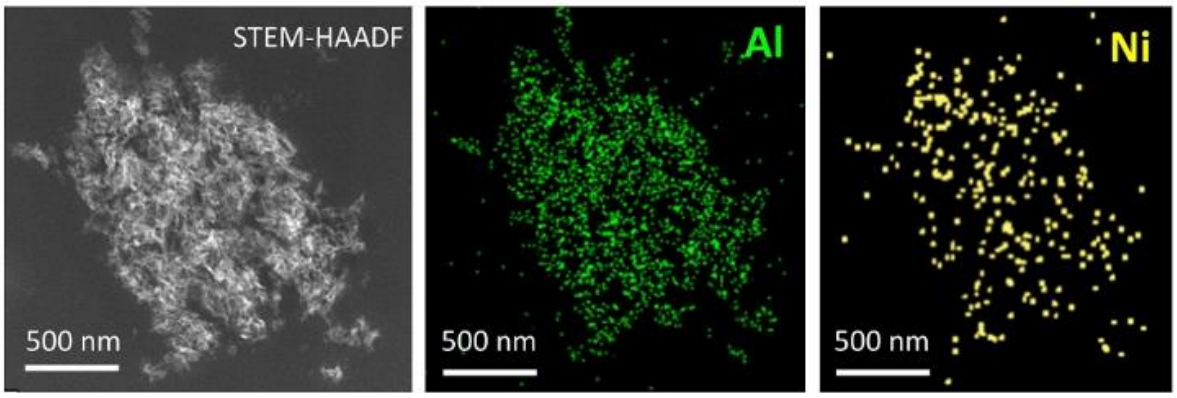

Figure IV-11: STEM-HAADF image of Ni_5-$Al_2O_{3\ MIL-53}$ (left) and EDX elemental mappings of the same area for Al (in green) and Ni (in yellow).

1.4 Å that can be estimated above from XRD for $NiAl_2O_4$ and also not far from those typical of γ-Al_2O_3 (d= 1.4 Å and 1.98 Å attributed to (440) and (400) planes, respectively). On the contrary, the lattice spacing expected around 2.4 Å and 2.1 Å for (111) and (200) crystal planes of NiO [243] are not distinguished confirming the absence of such phase as discussed above.

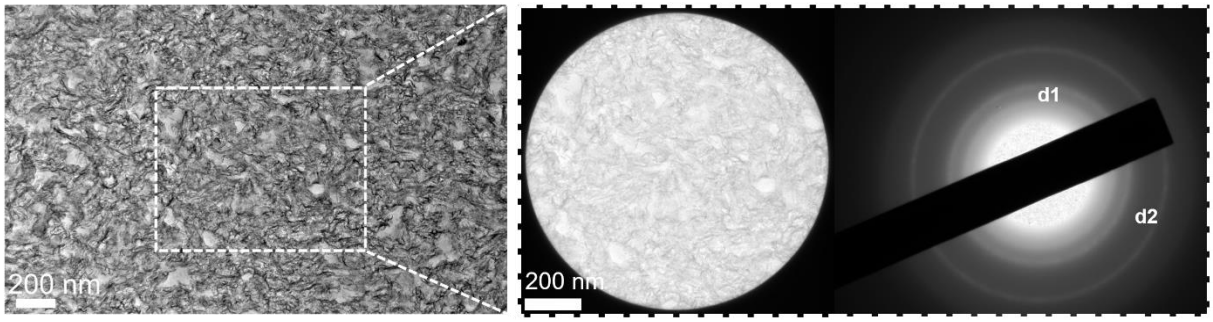

Figure IV-12: Representative TEM micrographs with its corresponding local SAED image over selected grain zones of calcined Ni_5-$Al_2O_{3\ MIL-53}$

IV.4.2. Comparative properties of calcined $Ni_5@Al_2O_{3\ MIL-53}$ prepared by impregnation of $Al_2O_{3\ MIL-53}$

In order to evaluate the impact on the material properties of the adopted preparation procedure (i.e. impregnating first the activated MIL-53 with nickel then calcining it), a different order was applied by first calcining the activated MIL-53 (to obtain $Al_2O_{3\ MIL-53}$) then impregnating and calcining it at 500°C (to remove adsorbed nitrates and water molecules). This second sequence order, in which the impregnation is done on a preformed alumina support (here $Al_2O_{3\ MIL-53}$), resembles a conventional preparation route.

From XRD, the structure of $Al_2O_{3\ MIL-53}$ is typical of an amorphous alumina (Figure IV-9 b*). It changes after Ni impregnation and calcination (sample $Ni_5@Al_2O_{3\ MIL-53}$, Figure IV-9 b) to a crystalline phase very similar to that in Ni_5-$Al_2O_{3\ MIL-53}$ except for two reflections

(2θ at 45.8° and 66.5°) that appear broadened and subtly shifted towards positions typical of γ-Al_2O_3 (2θ = 46.2° and 67.0°). This suggests a coexistence of both phases, as also supported by the TPR profile that contains two peaks, (i) a main one at high temperature (with maximum at T = 820 °C, Figure IV-10 b) indicative of some inclusion of nickel within the oxide matrix as in Ni_5-$Al_2O_{3\ MIL-53}$, and (ii) a smaller one centered at about 700 °C characteristic of nickel interacting less strongly with the alumina support (most probably nickel oxo-clusters on the external surface of the alumina grains).

In term of morphology, the preformed alumina support appears as nanograins composed of both packed and interwoven nanosheets (sample $Al_2O_{3\ MIL-53}$, Figure IV-7 c, Figure IV-8 c) and this amorphous two-dimensional aspect is lost after nickel impregnation and calcination, turning to aggregates of tiny nanocrystals with ill-defined shapes (sample $Ni_5@Al_2O_{3\ MIL-53}$, Figure IV-7 d, Figure IV-8 d). This final morphology significantly differs from the lamellar shape seen above for Ni_5-$Al_2O_{3\ MIL-53}$. Moreover, the grains appear assembled, forming a polycrystalline structure with polymodal porosity, in line with the three well defined steps observed in the N_2 adsorption isotherm of this sample (Figure IV-13 a), typical of the coexistence of micro, meso and macropores.

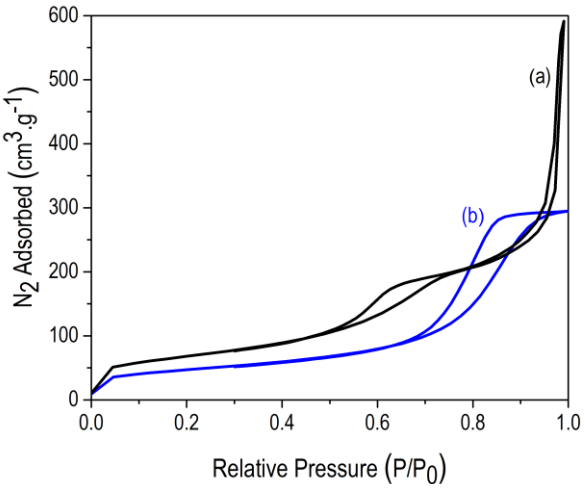

Figure IV-13: N_2 physisorption isotherms of the samples: (a) $Ni_5@Al_2O_{3\ MIL-53}$ and (b) $Ni_5@Al_2O_{3\ COM}$

Therefore, the order of the "calcination / Ni^{2+} impregnation" sequence, which affected the temperature of degradation of the MIL organic linkers (TG/SM data, Figure IV-6), also impacts the structure, texture and reducibility of the final material. To sum up, impregnation of the nickel cations within the activated MIL-53 to position them along the aluminum chains of the framework before the calcination step (Ni_5-$Al_2O_{3\ MIL-53}$) allows for a somewhat better dispersion (Table IV-4) and stabilization of nickel through their insertion into interwoven 2-dimensional alumina nanosheets. Notably, another advantage of this sequence order is to

require only one calcination step during material preparation instead of two for conventionally impregnated $Ni_5@Al_2O_{3\ MIL\text{-}53}$.

IV.4.3. Physicochemical properties of conventional $Al_2O_{3\ COM}$ and $Ni_5@Al_2O_{3\ COM}$

For the sake of comparison, a last material ($Ni_5@Al_2O_{3\ COM}$) was prepared by conventional nickel impregnation of a commercial γ-alumina ($Al_2O_{3\ COM}$) and tested as traditional reference catalyst. Both $Ni_5@Al_2O_{3\ COM}$ and its support $Al_2O_{3\ COM}$ show four main diffraction peaks, which are typical of crystalline γ-Al_2O_3 (Figure IV-9 c* and c, respectively). No evidence of spinel phase can be observed on the diffractogram of $Ni_5@Al_2O_{3\ COM}$, although diffraction peaks corresponding to a small fraction of this phase might be masked by those of the γ-Al_2O_3 phase. The TPR trace of this material displays two peaks, as for $Ni_5@Al_2O_{3\ MIL\text{-}53}$, but centered at lower temperatures than previously (630 °C and 800 °C, Figure IV-10 c), indicating a weaker Ni-support interaction than in both MOF-based samples, especially Ni_5-$Al_2O_{3MIL\text{-}53}$. Similarly to $Ni_5@Al_2O_{3\ MIL\text{-}53}$, a fraction of the nickel in $Ni_5@Al_2O_{3\ COM}$ is probably existing in the material as amorphous NiO, as revealed by the TPR signal observed at relatively low temperature (T < 700°C).

The significantly higher dispersion and stabilization of Ni in Ni_5-$Al_2O_{3\ MIL\text{-}53}$ sample can be explained as follows: the impregnation of nickel nitrate on the parent MIL-53 with especially high surface area enables the initial occlusion of the nickel precursors along the organic linkers and $[Al(OH)O]_n$ clusters decorating the pores, leading after the MOF calcination step (organic removal) to the formation of an Al_2O_3-$NiAl_2O_4$ phase in which nickel and aluminum cations are intimately mixed in a homogenous oxide phase. In contrast, impregnation of a preformed alumina (obtained by calcination of either MIL-53 or boehmite) then impregnation and calcination leads to a mixture of alumina, $NiAl_2O_3$ and NiO with an overall weaker interaction between nickel and the alumina matrix. Interestingly, the presence of nickel at the very first step of the preparation seems to direct the formation of the crystalline spinel $NiAl_2O_4$ phase during calcination (giving Ni_5-$Al_2O_{3\ MIL\text{-}53}$), while no spinel phase is formed when starting from pure MIL-53 (giving amorphous $Al_2O_{3\ MIL\text{-}53}$).

IV.5. Physicochemical properties of reduced Ni_5-Al_2O_3 $_{MIL-53}$, Ni_5@Al_2O_3 $_{MIL-53}$, and Ni_5@Al_2O_3 $_{COM}$

Previous to catalytic tests, all the prepared nickel-alumina materials were treated under a flowing H_2 atmosphere to obtain reduced Ni^0, the active phase for DRM. The H_2 consumption during TPR was used to estimate the amount of reducible Ni^{2+} in all nickel containing samples, considering the consumption of one H_2 molecule per Ni^{2+} cation. For all samples, the Ni content is in accordance with that measured by X-fluorescence and close to the expected 5 wt% Ni, even if slightly lower, by less than 10%, for sample Ni_5^0@Al_2O_3 $_{MIL-53}$ (Table IV-4).

The XRD patterns of the samples reduced at 800 °C are shown in Figure IV-9 and compared to those before reduction. The reduction of Ni_5-Al_2O_3 $_{MIL-53}$ to Ni_5^0-Al_2O_3 $_{MIL-53}$ leads to the formation of new diffraction peaks assignable to the (111), (200) and (220) planes of crystalline Ni^0 (at 2θ = 44.5°, 51.9° and 76°, respectively, Figure IV-9 a'). Bands attributable to an alumina-based phase are still present but they are slightly shifted (compared to those before reduction) towards positions characteristic of pure γ-Al_2O_3 which attests of Ni extraction from the oxide matrix towards the pore surface.

The reduction of the sample was followed by H_2 in-situ XRD techniques (done at University of Lille in collaboration with "unité de catalyse et chimie du solide" (UCCS)) in the temperature range of 25-850 °C (Figure IV-14). In good agreement with XRD and TPR measurements, the reduction does not start before 700 °C and it is at this temperature also that we start to see disappearance of $NiAl_2O_4$ spinel and presence of metallic Ni^0 species and γ-Al_2O_3 phase.

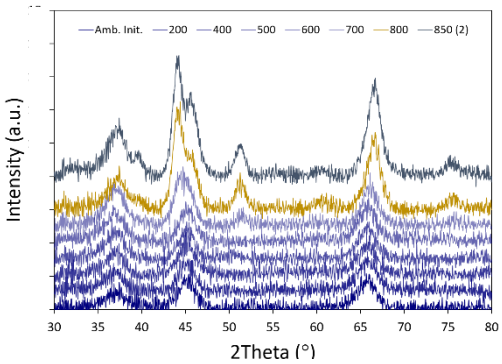

Figure IV-14: In-situ XRD patterns of Ni_5-Al_2O_3 $_{MIL-53}$ during reduction by hydrogen (5% H_2 in Ar) up to 850 °C

Application of the Scherrer equation (Figure IV-9) to the Ni^0 reflection at 2θ = 51.9° leads to a mean Ni^0 nanoparticle size of 5.3 nm, slightly smaller than the value estimated by HR-TEM after measuring the sizes of at least 500 nanoparticles (Table IV-4). Considering the TEM image of Ni_5^0-Al_2O_3 $_{MIL-53}$ shown in Figure IV-15 a and the non-symmetrical shape of the histogram of particles sizes for this sample (Figure IV-16), it can be assumed that this average size discrepancy comes from contrast issues making uneasy the detection of the smallest

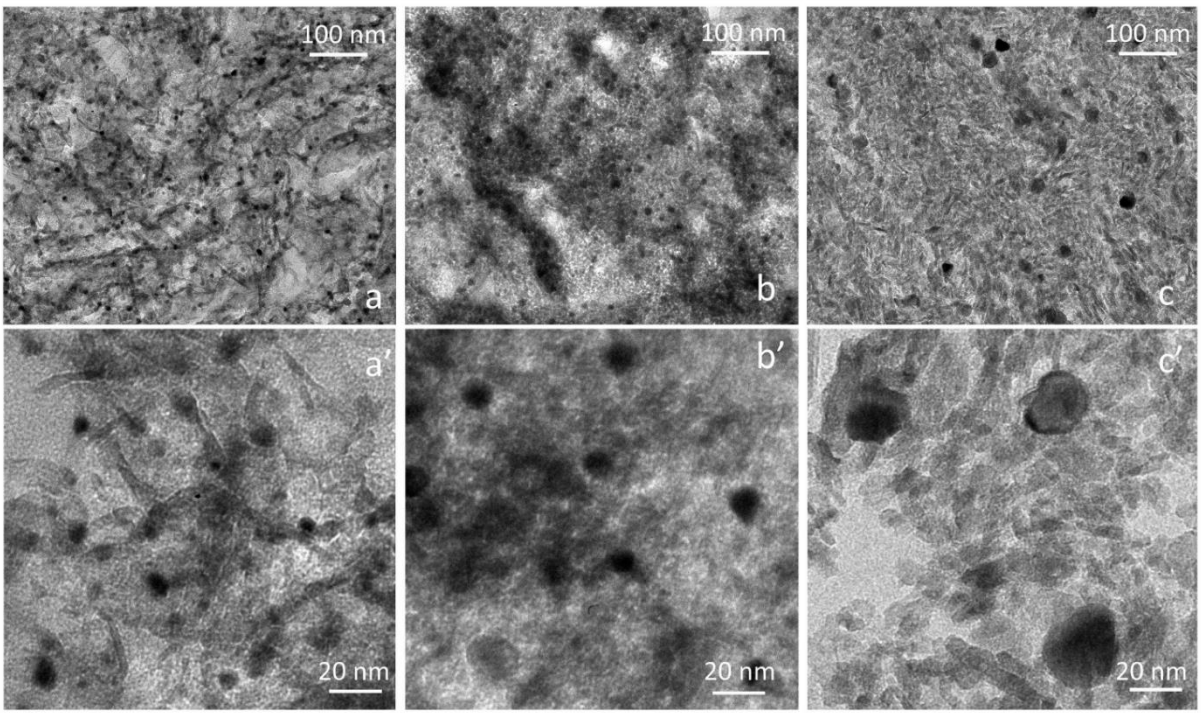

Figure IV-15: HR-TEM images of the reduced samples: (a and a') Ni_5^0-$Al_2O_{3\ MIL\text{-}53}$, (b and b') $Ni_5^0@Al_2O_{3\ MIL\text{-}53}$, (c and c') $Ni_5^0@Al_2O_{3\ COM}$.

nanoparticles (from 2 to 4 nm) on the alumina grains, in spite of the good resolution of HR-TEM images. In this sample, all detected nickel nanoparticles are homogeneously distributed all over the support which still appears as interwoven alumina sheets (as in Ni_5^0-$Al_2O_{3\ MIL\text{-}53}$ before reduction).

The preservation of the morphology after reduction is also attested by textural features, the N_2 physisorption isotherm of Ni_5^0-$Al_2O_{3\ MIL\text{-}53}$ still showing a slit-like hysteresis typical of a layered material composed of poorly organized interlayered pores (Figure IV-5 e). The amount of N_2 adsorbed at $P/P_0 > 0.8$ is however higher than that before reduction (Table IV-4), indicating the formation of

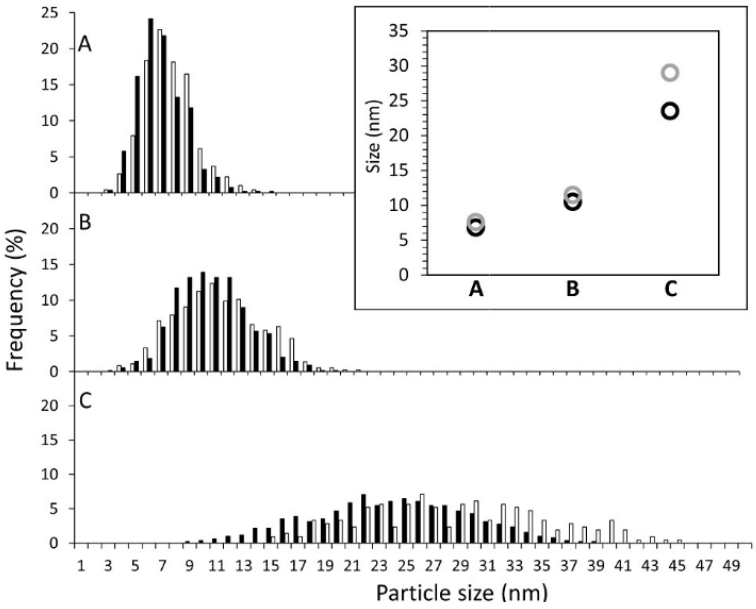

Figure IV-16: Histograms established from at least 500 Ni^0 nanoparticles in typical HR-TEM images of (A) Ni_5^0-$Al_2O_{3MIL\text{-}53}$, (B) $Ni_5^0@Al_2O_{3\ MIL\text{-}53}$ and (C) $Ni_5^0@Al_2O_{3\ COM}$ before and after 13h of catalytic test (black and white bares, respectively). Related mean sizes are shown in (D) for the catalysts before (black circles) and after (grey circles) test

additional large mesopores within the material. This increase of the total pore volume and mean pore size upon reduction is likely due to the exfoliation of the packed nanosheets through (i) the transformation of the $NiAl_2O_4$ spinel phase into γ-Al_2O_3 and (ii) the formation of the Ni^0 nanoparticles that may tend to further space apart the nanosheets one from another.

The reduction of nickel impregnated on the two preformed alumina supports (Al_2O_3 $_{MIL-53}$ and Al_2O_3 $_{COM}$) led similarly to the appearance of homogeneously dispersed Ni^0 nanoparticles (Figure IV-15 b and c, respectively), but the particles and their size distributions were systematically larger than on Ni_5^0-Al_2O_3 $_{MIL-53}$ (Table IV-4), especially in the case of Ni_5^0@Al_2O_3 $_{COM}$ (size = 22 nm) (Figure IV-16). Hence, the homogeneous $NiAl_2O_4$-based spinel nanophase formation seen during the first steps of preparation of Ni_5^0-Al_2O_3 $_{MIL-53}$ and issued from initial nickel insertion within the pores of the MOF with high surface area before linker decomposition seems to play an important role towards metal stabilization with a positive effect that remains after partial extraction from the alumina matrix upon reduction.

IV.6. Catalytic activity and stability in dry reforming of methane

VI.6.1. Catalytic activity of Ni_5^0-Al_2O_3 $_{MIL-53}$ and Ni_5^0@Al_2O_3 $_{COM}$

Figure IV-17 A, B illustrates the activity test for both Ni_5^0-Al_2O_3 $_{MIL-53}$ and Ni_5^0@Al_2O_3 $_{COM}$ catalysts in addition to the expected thermodynamic values at different temperatures (light off measurements). A slightly higher CO_2 than CH_4 conversion is also depicted over the entire temperature range accounting for the RWGS reactions that consumes CO_2 and increases its

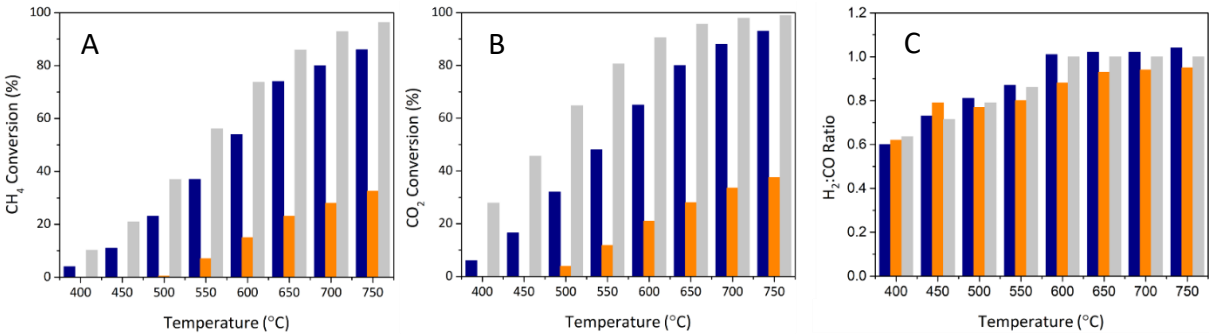

Figure IV-17: (A) CH_4, (B) CO_2 conversions, and (C) H_2:CO product ratio during DRM upon continuous increase of temperature from 400 °C till 750 °C over in-situ reduced (800 °C/2h): (blue) Ni_5^0-Al_2O_3 $_{MIL-53}$, and (orange) Ni_5^0@Al_2O_3 $_{COM}$. Grey columns are the calculated values at the thermodynamic equilibrium for the CO_2, CH_4 conversions and H_2:CO ratio

conversion level. This trend is seen over both catalysts. However, the conversions of Ni_5^0@Al_2O_3 $_{COM}$ catalyst starts at higher temperature (450 °C) compared to those of Ni_5^0-Al_2O_3 $_{MIL-53}$ (390 °C) with 25% less conversion values. This difference in conversions and the superior

performance of the MOF-based sample over the commercial one is due to the large particle size (22 nm) and the lower dispersion acquired by the latter (5.6 %) decreasing the available Ni^0 active sites for CH_4 and CO_2 reactants. As for the H_2:CO molar ratio presented in Figure IV-17 C as a function of temperature, they appear to be always less than the thermodynamic values for $Ni_5^0@Al_2O_{3\ COM}$ suggesting the occurrence of RWGS, whereas for Ni_5^0-$Al_2O_{3\ MIL\text{-}53}$ it is always close to 1 showing a selective DRM operation, with limitation to a great extent of side products ($C_{(s)}$ and H_2O).

V.6.2. Catalytic stability of Ni_5^0-$Al_2O_{3\ MIL\text{-}53}$, $Ni_5^0@Al_2O_{3\ MIL\text{-}53}$ and $Ni_5^0@Al_2O_{3\ COM}$

Finally, the stability test experiments of Ni_5^0-$Al_2O_{3\ MIL\text{-}53}$ were tested at 650 °C in the reaction of dry reforming of methane and compared to those of $Ni_5^0@Al_2O_{3\ MIL\text{-}53}$ and $Ni_5^0@Al_2O_{3\ COM}$ (Figure IV-18 and Table IV-5). Temperature of 650°C was selected as seen in chapter III in order to be able to compare the performances of the three different catalysts at conversion of reactants below 100%. Stability over a longer reaction time (100h) was also investigated for Ni_5^0-$Al_2O_{3\ MIL\text{-}53}$. Figure IV-18 A and B show that the CO_2 and CH_4 conversions on both MOF-derived catalysts (a and b) are high, close to thermodynamic

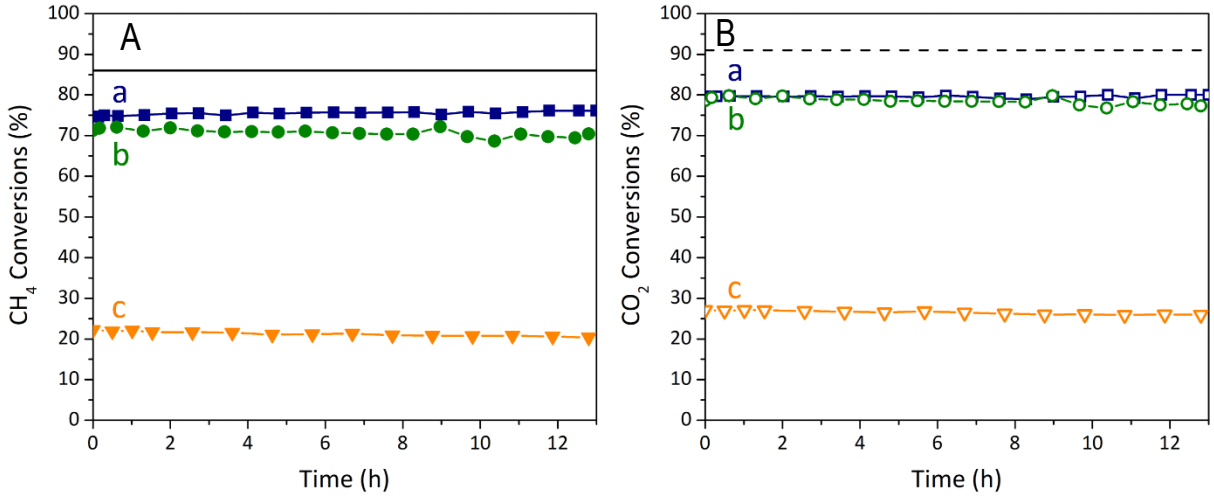

Figure IV-18: Comparison of the catalytic performances in DRM of (a) Ni_5^0-$Al_2O_{3\ MIL\text{-}53}$, (b) $Ni_5^0@Al_2O_{3\ MIL\text{-}53}$ and (c) $Ni_5^0@Al_2O_{3\ COM}$ as a function of (A) CH_4 and (B) CO_2 conversions measured during 13h of reaction. Black continued and dashed lines are the calculated values at the thermodynamic equilibrium for the CH_4 and CO_2 conversions, respectively

equilibrium, and much higher (2 to 3 times) than those on $Ni_5^0@Al_2O_{3\ COM}$. The selectivity to DRM on Ni_5^0-$Al_2O_{3\ MIL\text{-}53}$ is also remarkable, as attested by two features that indicate limited occurrence of side reactions: (i) the close CH_4 and CO_2 conversions that differ by only 7% and

(ii) the H_2:CO ratio very close to 1 (Figure IV-19). A rather good selectivity to DRM is also observed on $Ni_5^0@Al_2O_{3\ MIL\text{-}53}$ but with a H_2:CO ratio higher than 1 that suggests the occurrence of some CH_4 decomposition ($CH_4(g) \rightarrow C(s) + 2H_2(g)$). Noteworthy Ni_5^0-$Al_2O_{3\ MIL\text{-}53}$ is not only the most active catalyst but it is also very stable as its performance after the prolonged 100 h on stream remains nearly equal to that measured at the early stage of the reaction (Figure IV-20).

Table IV-5: Catalytic test results for all the prepared catalysts

Catalyst	Conversion (%)						Molar composition of main products (H_2/CO)			Coke content (%)	
	t=0.5h		t=13h		t=100h		t=0.5h	t=13h	t=100h	t=13h	t=100h
	X_{CH4}	X_{CO2}	X_{CH4}	X_{CO2}	X_{CH4}	X_{CO2}					
Ni_5-$Al_2O_{3MIL\text{-}53}$	75	79	76	79	74	80	1.02	1.01	1.03	0	0
$Ni_5@Al_2O_{3MIL\text{-}53}$	71	79	70	77	n.p.	n.p.	1.12	1.09	n.p.	5	n.p.
$Ni_5@Al_2O_{3COM}$	22	27	20	26	n.p.	n.p.	0.93	0.89	n.p.	7	n.p.

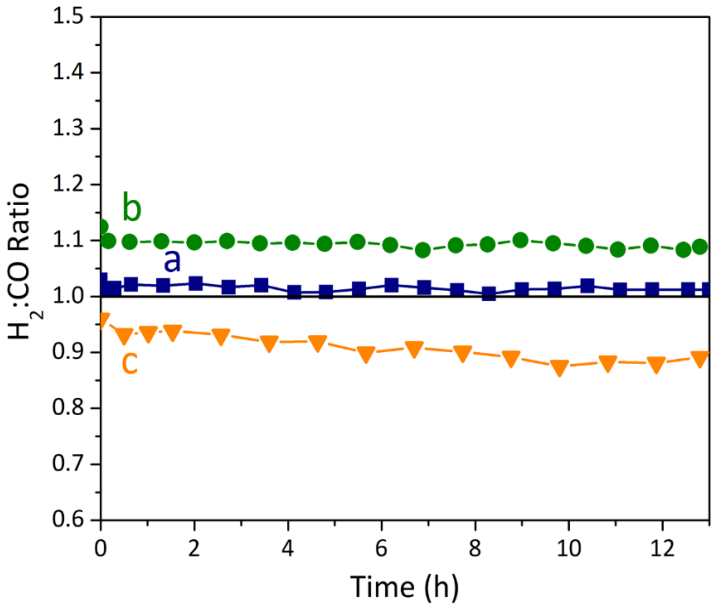

Figure IV-19: H_2:CO ratios in DRM (a) Ni_5^0-$Al_2O_{3\ MIL\text{-}53}$, (b) $Ni_5^0@Al_2O_{3\ MIL\text{-}53}$ and (c) $Ni_5^0@Al_2O_{3\ COM}$

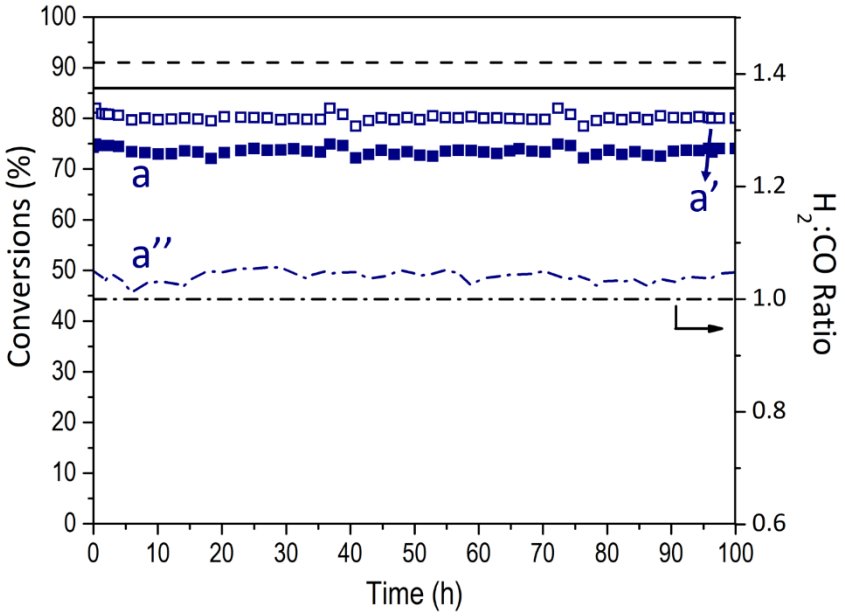

Figure IV-20: Catalytic performances in DRM of Ni_5^0-Al_2O_3 MIL-53, as a function of (a) CH_4 and (a') CO_2 conversions measured during 100h of reaction. Black continued and dashed lines are the calculated values at the thermodynamic equilibrium for the CH_4 and CO_2 conversions, respectively

VI.6.3. Characterization of spent catalysts after DRM

VI.6.3.1. Carbon formation

The formation of carbon deposits on the surface of the spent Ni_5^0@Al_2O_3 MIL-53 material is indeed confirmed by the 5 % weight loss detected at T = 600°C when submitted to the D and G bands visible by Raman spectroscopy (Figure IV-21) as well as by TGA analysis (Figure IV-22) [27] and by the observation of carbon nanotubes on the catalyst surface by scanning electron microscopy (Figure IV-23 b and b').

Regarding the Raman signals, the two main bands (D and G) are typical of the doubly degenerated phonon mode of C atoms in the sp2 carbon networks with high degree of symmetry and of order (graphitic carbon, G-band, 1600 cm^{-1}) and of a disordered structural mode of carbon species (D-band, 1300 cm^{-1}). The

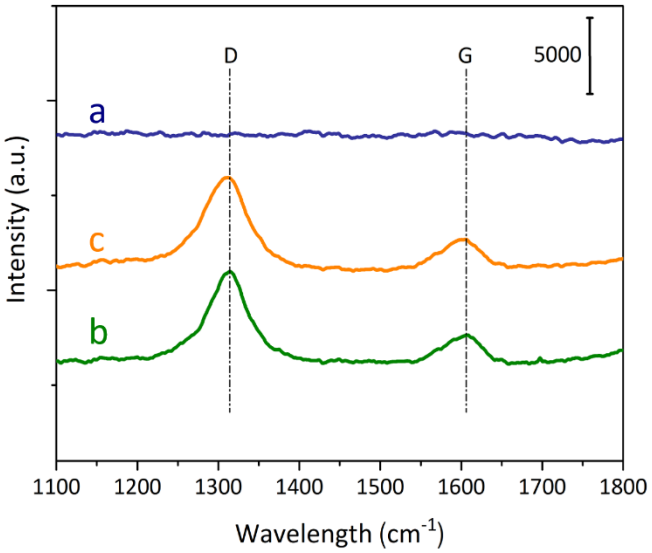

Figure IV-21: Raman spectroscopy profiles of the spent catalysts: a) Ni_5^0-Al_2O_3 MIL-53, (b-) Ni_5^0@Al_2O_3 MIL-53, and (c) Ni_5^0@Al_2O_3 COM

intensity ratio between these two bands can be used as an indicator of the crystalline degree and of the presence of defects in the carbon species; the smaller the ratio (<1) the higher the structural order. Here, both $Ni_5^0@Al_2O_{3\ MIL\text{-}53}$ and $Ni_5^0@Al_2O_{3\ COM}$ have a ratio significantly higher than 1 (4.6 and 4.2 respectively) which indicates the disordered character of the carbon deposits, in line with the occurrence of carbon nanotubes observed on these samples by electron microscopy.

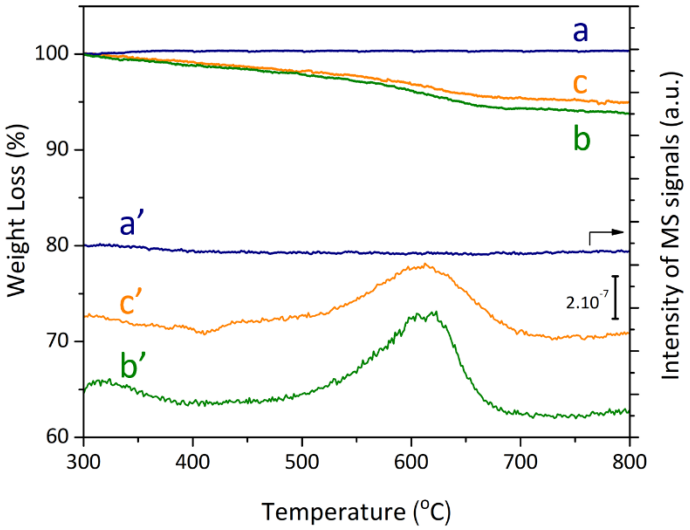

Figure IV-22: TGA profiles (at the top) associated to MS signals corresponding to CO_2 (at the bottom) of the spent (a-a') Ni_5^0-$Al_2O_{3\ MIL\text{-}53}$, (b-b') $Ni_5^0@Al_2O_{3\ MIL\text{-}53}$, and (c-c') $Ni_5^0@Al_2O_{3\ COM}$

Such deposits are similarly clearly identified on the spent $Ni_5^0@Al_2O_{3\ COM}$ catalysts, with a TGA weight loss (7 %) even higher (Figure IV-22) in spite of the low activity of this

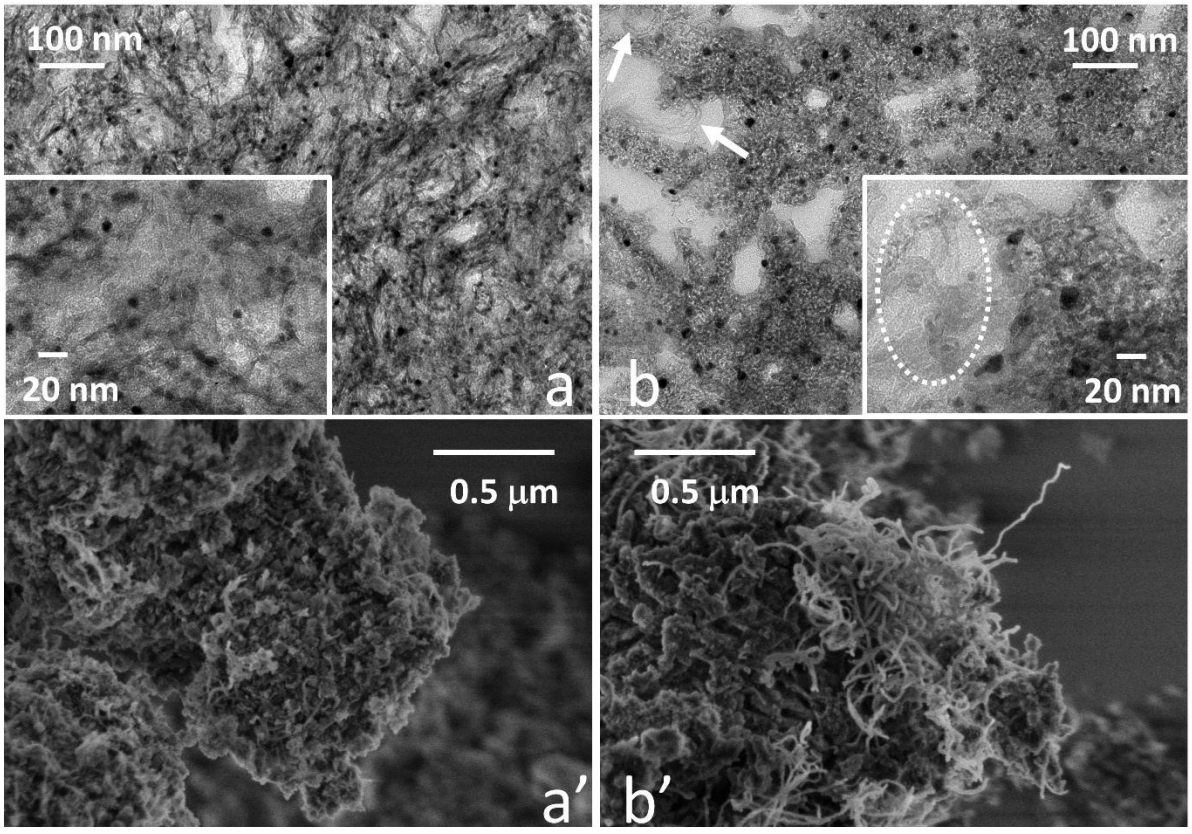

Figure IV-23: TEM (a,b) and SEM (a',b') images of spent (a,a') Ni_5-$Al_2O_{3\ MIL\text{-}53}$ and (b,b') $Ni_5@Al_2O_{3\ MIL\text{-}53}$. The dashed oval and white arrows in (b) highlight the presence of carbon nanotubes

catalyst (low conversion level) and with D and G bands still clearly displayed on the Raman spectrograph (Figure IV-21 c). In contrast, such deposits are not detected on the most active Ni_5^0-$Al_2O_{3\ MIL\text{-}53}$ material, even after the 100 h test, neither by TGA, nor by Raman spectroscopy or electron microscopy (Figure IV-23 a and a').

VI.6.3.2. Side reactions

The occurrence of side reactions on the reference $Ni_5^0@Al_2O_{3\ COM}$ material is confirmed by the products H_2:CO, which is initially below 1 and decreases with time (Figure IV-19 c), indicating some H_2 consumption through reverse water-gas shift (RWGS) reaction ($CO_2 + H_2 \leftrightarrow CO + H_2O$) and/or direct reduction of CO_2 ($CO_2 + 2H_2 \leftrightarrow C + 2H_2O$) that consumes a part of the produced H_2 although this reaction is not possible being rather encountered in the 100-400 °C temperature range.

VI.6.3.3. Ni dispersion

These results demonstrate the superior performances of the catalysts prepared from MIL-53, especially of Ni_5^0-$Al_2O_{3\ MIL\text{-}53}$ over $Ni_5^0@Al_2O_{3\ COM}$. The superiority of Ni_5^0-$Al_2O_{3\ MIL\text{-}53}$ in term of conversion is in line with the better Ni^0 dispersion in this sample (Figure IV-23 a and Table IV-4). It moreover reveals, together with the remarkable selectivity of Ni_5^0-$Al_2O_{3\ MIL\text{-}53}$ to DRM all along the run (higher than on $Ni_5^0@Al_2O_{3\ MIL\text{-}53}$ also prepared from MIL-53), a preservation of the active sites and hence a persistent strong nickel-support interaction even in the harsh conditions of reaction. This is seen by the high and comparable nickel dispersion both after reduction (Figure IV-15 a, a' and Figure IV-16 a) and after reaction (Figure IV-16 a and Figure IV-23 a). In contrast, a significant sintering takes place in $Ni_5^0@Al_2O_{3\ COM}$ which the mean nickel particle size increases by about 30% after test (Table IV-5 and Figure IV-23 c,d). The formation in Ni_5^0-$Al_2O_{3\ MIL\text{-}53}$ of the stable spinel nickel aluminate phase, favored by the initial proximity between the nickel cations and the aluminum carboxylate clusters within the pore of MIL-53 during the calcination step, is believed to be at the origin of the stability of the dispersed Ni^0 nanoparticles. It could result from the presence of a remaining nickel aluminate spinel nanophase at the interface between the support and the metal nanoparticles after reduction that might insure a strong anchorage of the nanoparticles onto the resulting alumina support. One can also speculate that the layered texture of the material, which is remarkably well preserved during the 100h of reaction (Figure IV-23 a), contributes to the stability of the active phase as well by isolating and enhancing the occlusion of the nanoparticles, each of them being caught between two alumina sheets. This nanoparticle

confinement effect may also explain the absence of carbon production on this sample. This explanation is in line with previous data showing that the occlusion of nickel nanoparticles within the mesopores of alumina supports prevent the catalysis of carbon nanotube formation, which occurs only from the nickel nanoparticles located on the external surface of the support [244].

IV.7. Comparison of Ni_5^0-$Al_2O_{3\ MIL-53}$ with other materials in literature

It is worth adding that although the nickel nanoparticles reported here are not the smallest reported in the literature so far (the application of atomic layer deposition recently afforded nanoparticle size below 3 nm [245]), this study demonstrates the potential of MOFs as sacrificial hosts for preparing highly dispersed nickel nanoparticles whose size is below than those prepared by employing other type of oxides as stable nickel cation hosts, such as alkaline earth metal substituted $MZr_{1-x}Ni_xO_3$-δ perovskites [246] or the lanthanum zirconate pyrochlore La_2Zr_2-xNi_xO_7-δ [247]. Noteworthy, the use of MOF results in materials with a relatively high surface area (S. A.= 240 $m^2.g^{-1}$) compared to that obtained with other types of purely inorganic sacrificial nickel host cited above (S.A. < 20 $m^2.g^{-1}$), which can be seen as an additional benefit of this strategy in view of catalysis applications.

To end, and as a comparison Ni_5-$Al_2O_{3\ MIL-53}$ showed superior performance than an organized mesoporous based alumina catalyst. Organized mesoporous Al_2O_3 was prepared following the EISA route and impregnated with 5wt% Ni (Ni_5-$Al_2O_{3\ Meso}$). The latter exhibited lower surface area than that of the MOF-based catalyst by 25% accompanied with a lower reduction temperature emphasizing on the less Ni-support interaction. This leads to larger particle size with retarded activity and appearance of carbon at the end of the reaction (Table IV-6).

Table IV-6: Comparison between Ni_5-$Al_2O_{3\ MIL-53}$ and Ni_5-$Al_2O_{3\ Meso}$

Catalyst	Maximum reduction temperature (°C)	Surface Area ($m^2.g^{-1}$)	Particle size (nm)		Activity at 650 °C		C(s)
			reduced	spent	t=0.5h	t=13h	
Ni_5-$Al_2O_{3MIL-53}$	830	239	6.8	7	75-79	76-79	No
Ni_5-$Al_2O_{3\ Meso}$	708	182	8.5	10	41-46	41-47	Yes

IV.8. Conclusion

In this work we highlighted on the benefit of using aluminum carboxylate MIL-53 as a sacrificial nickel precursor host to prepare a dry methane reforming catalyst composed of nickel nanoparticles dispersed within a porous γ-Al_2O_3 lamellar phase. The higher surface area of this metal-organic framework compared to preformed porous alumina supports allows for a more efficient dispersion of the nickel precursors and, in turn, for a superior dispersion and uniformity of the nickel nanoparticles obtained after the MOF calcination and subsequent reduction steps. Consequently, the performances in terms of activity, selectivity and stability of this new catalyst for dry reforming of methane within the reaction conditions applied in this study are higher than those of comparative nickel@alumina catalysts prepared by conventional nickel impregnation of preformed alumina supports. The results displayed in this report demonstrate that MOF can be considered as a promising hybrid alternative to the sacrificial inorganic and non-porous hosts (perovskite, hydrotalcites) used so far to stabilize nickel species towards the synthesis of catalysts based on nickel metal nanoparticles.

V. Chapter V: Mesoporous nickel-alumina catalysts for CO_2 methanation

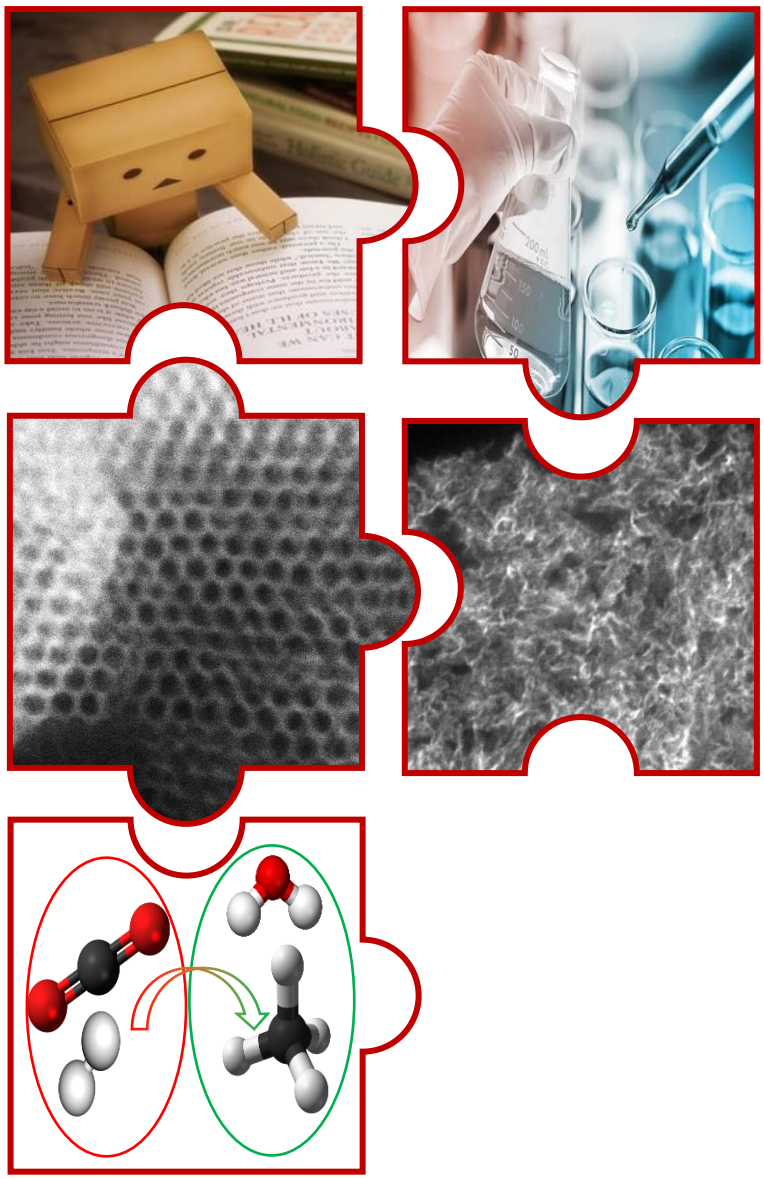

The objective of chapter V is to check if the good materials seen in the previous chapters are efficient in another reaction of strong interest in the energy domain, CO_2 methanation. The principle of this application is to produce methane by converting CO_2 (greenhouse valorization) together with H_2 (generated by electrolysis from renewable energy surplus (wind/sun)). A brief summary about CO_2 methanation process and the Ni-Al_2O_3 based catalysts state-of-art are first reported. Then the preparation method and the composition of the Ni-Al_2O_3 materials used are described including different Ni loading and other classical Ni-based support (for comparison), before presenting their physicochemical properties and catalytic performances in this specific reaction. Note that this work was done in collaboration with the Portuguese team (University of Lisbon) in the core of the ERANETMED project providing me with the opportunity to do a 1 month internship in their laboratory and using the available facilities (i.e. CO_2 methanation equipment).

V.1. Literature Review

V.1.1. General definition

CO_2 methanation is the hydrogenation of CO_2 to methane, also known as Sabatier reaction. This process is receiving great attention because it is based on the production of CH_4 (chemical and energy production) from CO_2 (valorization of greenhouse gas) and H_2 that can be generated by electrolysis of water using excess of renewable electric energy (from solar and wind) produced in low consumption periods [28,248–250]. This wind to natural gas (CH_4) concept frequently called power-to-gas (P2G) relies on the existing gas grid infrastructures for storing and converting the generated fuel to electricity as seen in Figure V-1[28]. CO_2 methanation projects are dominant in Germany due to the transformation of its energy system to a 100% renewable one, triggered by the huge demand to chemically store the electric energy and the need to compensate the intermittency of wind and solar energy provision. The produced methane can be applied in the chemical industry, lowering

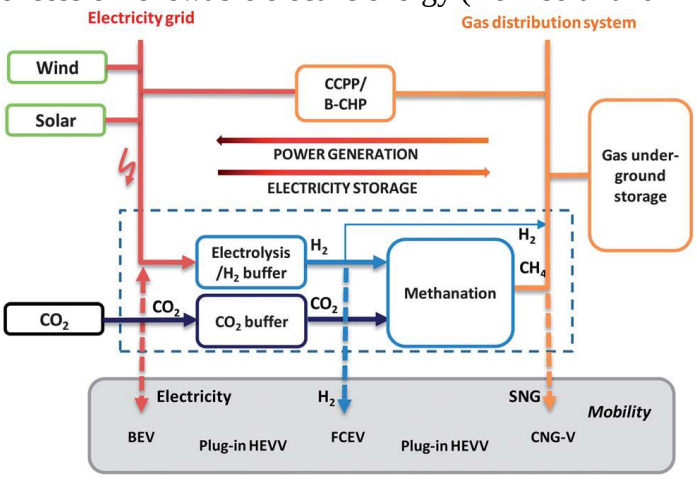

Figure V-1: Schematic describing wind to natural gas concept for bidirectional coupling of the electricity and gas grids [28]

the carbon footprint and the energy requirements. Complementary, this CH_4 can be also reused in DRM reaction. Moreover, an additional advantage in terms of energy saving is, as illustrated in Figure V-2, is that the energy produced during methanation (exothermic reaction) can be used to provide heat to perform DRM (endothermic reaction) (Modification of Eva-Adam process) [28,250,251].

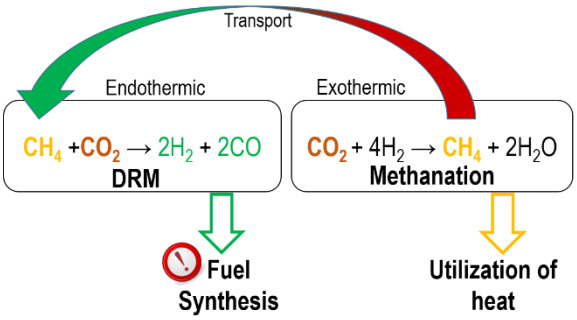

Figure V-2: Chemical energy storage using heat from renewables and DRM and methanation as energy carriers [251]

As already presented in chapter II, thermodynamic analysis demonstrates that, with a stoichiometric feed gas H_2/CO_2 of 4 and a temperature range of 200-350 °C, the main products will be only CH_4 and H_2O. As a result, the assumed methanation reaction is the following: $CO_2 + 4H_2 \leftrightarrow CH_4 + 2H_2O$. Since this reaction is an eight-electron process to fully reduce carbon dioxide to methane with significant kinetic limitations, a catalyst is mandatory to achieve acceptable rates and selectivity. Despite the difference in operating temperatures between DRM and CO_2 methanation, the catalysts used for both reactions have many similarities and the good catalysts found for DRM could be also suitable for methanation.

V.1.2. Catalysts applied in literature

In the state of the art regarding CO_2 methanation catalysts, many studies are based on nickel due to its high activity, selectivity and comparatively low price [248,252–254]. However, the operating temperatures should be high enough to avoid the potential formation of highly toxic nickel carbonyls from carbon monoxide, which defines the possible temperatures range between 200 and 550 °C [164]. Table V-1 illustrates some of the newest research studies that applied Ni-Al_2O_3 based catalysts in CO_2 methanation, summarizing the preparation method, nickel amount, some of the physicochemical properties of the reported materials and their performances towards CO_2 methanation. This table shows that, as observed in dry reforming of methane, Ni nanoparticles were also deposited on Al_2O_3 support using different insertion methods. However, a direct comparison between the reported catalysts is difficult due to the differences in the operating conditions used. Needless to say, Ni/Al_2O_3 materials prepared by standard impregnation methods [253,254] lead to relatively large particle sizes (10-30 nm), weakening the interaction with the support and favoring agglomeration processes during the course of the reaction. Ni/Al_2O_3 materials prepared by deposition-precipitation resulted in

smaller particle sizes (e.g. 3.2 nm) [255] but, the Ni interaction with Al_2O_3 was poor, leading to low activity (CO_2 conversion of 22%). The occurrence of deactivation during the test was attributed to the oxidation of the most active Ni sites in the presence of O_2 impurities. Moreover, as observed for DRM in chapter III, some reported studies on methanation also revealed that the addition of a basic additives such as Mn, CaO, Mg, Sr, Ba, or La ameliorate performances [256–258] due to an enhancement of the chemical adsorption of CO_2 that decreases in turn its activation energy [257].

Table V-1: Bibliography of some of the current Ni-Al_2O_3 based catalysts applied in CO_2 methanation

Catalyst	Preparation method	Ni amount (wt%)	S.A. ($m^2.g^{-1}$)	Particle size (nm)	GHSV ($L.g^{-1}.h^{-1}$)/ T(°C)	XCO_2 (%)	SCH_4 (%)	TOF (CO_2, s^{-1})
Ni/Al_2O_3[255]	DP[a]	10	200	3.7	26700*/300	22	85	8.10^{-2}
Ni/Al_2O_3[259]	*In-situ* growth	20	143	5	2.4 / 265	90	99	$2.4.10^{-3}$
Ni/Al_2O_3[253]	I.W.I[b]	15	260	n.m.	2400* / 260	17	15	$6.57.10^{-3}$
Ni/Al_2O_3[254]	W.I.	125	n.m.	10-30	52300* / 500	71	86	n.m.
Ni-Al_2O_3[260]	EISA	15	206	4	91[c]/ 400	82	97	n.m.
Ni/Al_2O_3[261]	Microwave	20	163	10	4.2 / 325	85	90	n.m.
Ni-Ru-Mn-Al_2O_3[262]	I.W.I	60	47	n.m.	0.5 / 400	100	72	n.m.
Ni-CaO/Al_2O_3[256]	I.W.I	15	7	n.m.	n.m. / 450	66	92	n.m.
Ni-Ru-CaO -Al_2O_3[194]	EISA	10	308	5	30 / 380	84	100	$2.15.10^{-3}$
Ni-CaO/Al_2O_3[257]	I.W.I	20	144	11.2	16000*/500	70	42	n.m.
Ni-Mg/Al_2O_3[257]	I.W.I	20	170	10.8	16000*/500	67	35	n.m.
Ni-Sr/Al_2O_3[257]	I.W.I	20	157	9.3	16000*/500	72	50	n.m.
Ni-Ba/Al_2O_3[257]	I.W.I	20	161	11.1	16000*/500	67	55	n.m.
Ni-La/Al_2O_3[258]	I.W.I	13.6	100	10	55000*/377	n.m.	78	n.m.

a: deposition-precipitation, b: incipient wetness impregnation, c: H_2:CO_2 = 5:1
*: unit in h^{-1}, n.m.: not mentioned, S.A.: surface area, XCO_2: CO_2 conversion, SCH_4: CH_4 selectivity

Some reports on preparation methods, similar to ours, involving *in-situ* growth (one-pot Ni addition), microwave or EISA techniques can also be found in literature for methanation, but not numerous. They resulted in better catalytic performance with improved CO_2 conversion and CH_4 selectivity, but still suffered from deactivation due to sintering (from 5 to 8.5 nm) [259], oxidation [260], or little carbon formation [261].

The use of MOF-based catalysts is also not null in CO_2 methanation as it was in DRM, but it is very new and introduced, to our knowledge, to few research studies involving expensive noble metals [263–265], cobalt [266], and nickel [267,268] nanoparticles with different size. However, even for Ni-MOF, the catalysts were very distinct from ours since they were mostly

used in non-calcined form. In the example given by Zhen et al. [267] MOF-5 was used to disperse 5 to 12.5 wt% Ni. The best catalyst, with 10 wt% Ni, gave 75% CH_4 yield at 320 °C (GHSV=125 $ml.min^{-1}.g^{-1}$, P= 1atm) and had a metal Ni average size of 9 nm. The same authors showed that, under similar catalytic test conditions, the activity of 20 wt% Ni deposited on MIL-101 [268] was better than other nickel-supported materials (γ-Al_2O_3, SiO_2, TiO_2). Even though these MOFs displayed good catalytic performances in CO_2 methanation, they are unstable at high temperature and thermally decompose.

For this reason, MOFs can be used instead as a sacrificial template resulting in carbonaceous or purely inorganic materials depending on the thermal treatment adopted. This route has not been applied so far, to our knowledge, for Ni-based MOF and the catalyst prepared following this method in CO_2 methanation is a Co metal [266]. In this study the MOF used is ZIF-67 pyrolyzed under N_2 atmosphere, and later reduced with H_2 to obtain Co-based porous carbon (PC) with Co nanoparticles between 7-20 nm in size. This catalyst had a high surface area of 346 $m^2.g^{-1}$ with a CH_4 yield of 52 % at 270 °C (GHSV=1200 $ml.min^{-1}.g^{-1}$, P= 30 atm) and no sintering of Co nanoparticles which make them enticing compared to Co supported on commercial activated carbon catalyst.

From this aspect, and attracted by the high surface area and metal dispersion that our mesoporous Ni-Mg-Al_2O_3 synthesized by one-pot method (chapter III) and Ni-Al_2O_3 derived from MIL-53(Al) (chapter IV) have, and their encouraging results in DRM, we thought that these new materials can also bring new outcomes to the field of CO_2 methanation.

V.2. Synthesis of mesoporous one-pot Ni_x-Mg_y-Al_2O_3 and Ni_x-Al_2O_3 derived from MIL-53(Al) materials

The preparation methods followed for the two sets of materials studied in this chapter are similar to the elaborated explanation in section III.2 for mesoporous Ni_x-Mg_y-Al_2O_3 and section IV.2 for mesoporous Ni_x-Al_2O_3 derived from MIL-53(Al). The only difference that might reside between the samples from this chapter and the previous ones is the amount of Ni added. Table V-2 and Table V-3 summarize all the mesoporous magnesium-based alumina and MOF derived samples, respectively. Some of the obtained Ni-Al_2O_3 samples (MOF-based materials specifically) were also compared to other more classical materials used in the Portuguese partner team as listed at the bottom of Table V-3. They all contain 15 wt% Ni

deposited by incipient wetness impregnation on Cs-USY zeolite (Si/Al_{global} of 38) [269,270], mesoporous commercial SBA-15 [271], and one-pot EISA alumina supports.

Table V-2: Summary of the prepared one-pot mesoporous Ni_x-Mg_y-Al_2O_3 samples

Sample code	$Ni_xMg_yAl_z$ atomic formula	Metal contents (wt%) Ni	Mg	Weight of chemical added (g) P123	$Al[OCH(CH_3)_2]_3$	$Ni(NO_3)_2.6H_2O$	$Mg(NO_3)_2 \cdot 6H_2O$
Al_2O_3	$Ni_0Mg_0Al_{100}$	-	-	7	14.3	0	0
Ni_5-Al_2O_3	$Ni_5Mg_0Al_{95}$	5	0		13.6	1.02	0
Ni_5-Mg_{15}-Al_2O_3	$Ni_5Mg_{15}Al_{80}$		7		11.5	1.02	2.7
Ni_5-Mg_{50}-Al_2O_3	$Ni_5Mg_{50}Al_{45}$		26		6.5	1.02	9
Ni_{10}-Mg_{15}-Al_2O_3	$Ni_{10}Mg_{15}Al_{75}$	10	7		10.7	2.03	2.7
Ni_{15}-Mg_{15}-Al_2O_3	$Ni_{15}Mg_{15}Al_{70}$	15			10.0	3.05	2.7
Ni_{20}-Mg_{15}-Al_2O_3	$Ni_{20}Mg_{15}Al_{65}$	20			9.3	4.07	2.7

Table V-3: Summary of mesoporous Ni_x-Al_2O_3 materials derived from MIL-53 framework

Sample	Support	Mode of Ni insertion	Ni contents (wt%)
MIL-53	Synthesized	-	-
Ni_5-Al_2O_3 MIL-53		I.W.I Prior MIL calc.	5
$Ni_{15}Al_2O_3$ MIL-53			15
Ni_{20}-Al_2O_3 MIL-53			20
$Ni_{15}@Al_2O_3$ MIL-53		I.W.I After MIL calc.	15
Ni_{15}@USY	Commercial	I.W.I	15
Ni_{15}@SBA-15			
Ni_{15}-Al_2O_3 One-Pot	Synthesized	One-pot	

The following results are divided into two parts. The first part tackles the magnesium-based mesoporous alumina materials and the effect of nickel and magnesium amount on CO_2 methanation. The second part includes the MOF based alumina samples with different nickel contents that are in turn compared to other Ni-based samples and evaluated also in CO_2 methanation reaction.

V.3. Physicochemical properties followed by CO_2 methanation over mesoporous Ni_x-Mg_y-Al_2O_3 materials

V.3.1. Variation of Mg content and its influence on CO_2 methanation

V.3.1.1. Physicochemical properties

In this part, three samples were chosen for comparison: Ni_5-Al_2O_3, Ni_5-Mg_{15}-Al_2O_3 and Ni_5-Mg_{50}-Al_2O_3. To avoid repetition, their physicochemical properties results are not presented here since they are detailed in Chapter III, and Table V-4 summarizes certain values. Note that the values in brackets and italic font for the surface area and pore volume as well as the italic font for the nickel nanoparticles size correspond to the reduced form of the materials.

Table V-4: Physicochemical properties of calcined and reduced (*in italic*) Ni_x-Mg_y-Al_2O_3 materials

Catalyst code	h index [a]	V_{tot} [b] (cm^3/g)	S.A. [b] (m^2/g)	ΦNi^0 [c] (nm)	Dispersion[d] (%)
Ni_5-Al_2O_3	0.55	0.49 *(0.32)*	234 *(173)*	*4.6*	*21*
Ni_5-Mg_{15}-Al_2O_3	0.45	0.56 *(n.d.)*	240 *(n.d.)*	*4.5*	*21*
Ni_5-Mg_{50}-Al_2O_3	0.38	0.54 *(n.d.)*	205 *(n.d.)*	*8.8*	*11*
Ni_{10}-Mg_{15}-Al_2O_3	0.41	0.57 *(0.52)*	247 *(219)*	*5.85*	*17*
Ni_{15}-Mg_{15}-Al_2O_3	0.46	0.54 *(0.45)*	203 *(160)*	*6.37*	*15*
Ni_{20}-Mg_{15}-Al_2O_3	0.45	0.47 *(0.48)*	197 *(198)*	*9*	*11*

[a] determined from TGA-DSC experiments; [b] total surface area (S.A.) and total pore volume (V_{tot}) calculated from the N_2 sorption isotherms, in brackets: reduced materials; [c] value estimated from the histograms obtained from representative TEM images of each reduced sample; [d] nanoparticle dispersion calculated from TEM of reduced samples

V.3.1.2. Surface adsorption properties

The interaction with water was evaluated since H_2O is a reaction product that could have an eventual relevant inhibitory role in the methanation reaction [166,269,272–278]. In addition, and in the specific case of zeolites (crystalline alumina-silicate materials) water could be chemically adsorbed on CO_2 activation sites, playing another inhibitory role in the reaction [269,279,280]. The strength of the water interaction with the catalysts was estimated by determining the h index by TGA-DSC experiments that were done in Portugal. Briefly, an h index value close to 1 indicates that the samples are not strongly interacting with water (most of the water molecules will be easily desorb below 150 ºC) while indexes close to 0 indicate stronger interaction between water and the catalysts (only a small fraction of water molecules desorb below 150 ºC). As seen in Table V-4, increasing the Mg loading strengthens the interaction between water and the samples with h index decreasing from 0.55 in Ni_5-Al_2O_3 to

0.38 in Ni_5-Mg_{50}-Al_2O_3. This decrease can lead to a higher water concentration over the catalysts during the reaction and higher inhibitory effect.

The interaction of the samples with CO_2 was also characterized by collecting CO_2 isotherms (experiments performed in Portugal by degassing the calcined samples then adsorbing CO_2 at 0 °C). This technique, was adopted in the present study for comparing the affinity of the samples towards CO_2. Results, illustrated in Figure V-3, present the same CO_2 uptake for all the three materials at high pressures but, in terms of affinity (low relative pressure points), Ni_5-Mg_{50}-Al_2O_3 presents significantly enhanced CO_2 uptakes. This agrees with the higher content of CO_2 adsorbed on this sample compared to those containing 0 and 7 wt% Mg as seen by Infra-red data in chapter III (Figure III-9).

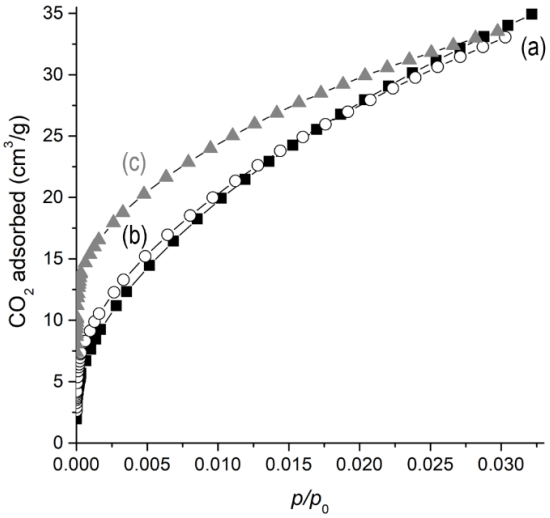

Figure V-3: CO_2 isotherms obtained for (a) Ni_5-Al_2O_3, (b) Ni_5-Mg_{15}-Al_2O_3 and (c) Ni_5-Mg_{50}-Al_2O_3 samples

V.3.1.3. CO_2 methanation on Ni_5-Mg_y-Al_2O_3 mesoporous materials

Catalytic test results of these materials are depicted in Figure V-4. CO_2 conversions increase with temperatures, and do not follow the trend of the theoretical CO_2 conversion curve that starts at very high value (97 %) and decrease with temperatures. This difference is due to the presence of a barrier in the kinetics that limits CO_2 activation. As for the variation in Mg content, mesoporous Ni_5-Mg_{15}-Al_2O_3 catalyst has higher CO_2 conversions than Ni_5-Al_2O_3 over all temperatures range. This behavior resembles what was seen for DRM reaction and solidifies the efficiency of Mg in enhancing performances of the catalyst by increasing the surface basicity that

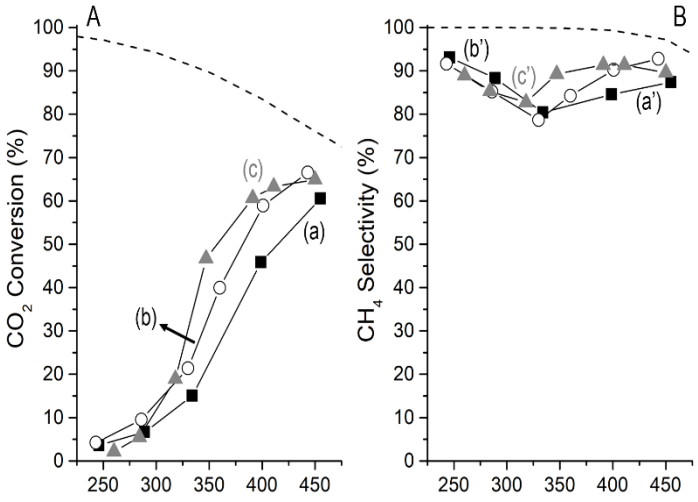

Figure V-4: (A) CO_2 conversion and (B) CH_4 selectivity of (a-a') Ni_5-Al_2O_3, (b-b') Ni_5-Mg_{15}-Al_2O_3, and (c-c') Ni_5-Mg_{50}-Al_2O_3

intensifies CO_2 chemisorption and, subsequently, activates CO_2 during the course of the reaction [182,281–287]. A suggested mechanism can explain the difference: on Ni_5-Al_2O_3 catalyst, CO_2 methanation is expected to be indicated by dissociation of CO_2 into carbon species (CO_{ads}) and an oxygen species (O_{ads}) over the catalyst surface. CO_{ads} then reacts with H atoms to generate CH_4 through several reaction mechanism steps on Ni active sites, responsible for dissociating H_2 into H atoms. When Mg is added to the sample, the formation of CO_{ads} is increased suppressing its desorption process into CO leading to higher CH_4 selectivity. Reaching 26 wt% of Mg (Ni_5-Mg_{50}-Al_2O_3), CO_2 conversion is not improved and its behavior looks similar to the 7 wt% Mg sample. This unimproved activity could be related to the lower Ni dispersion (11%), higher interaction with water (h index: 0.38) and damage in the structured mesoporosity. In addition, excessive Mg basic promoter would firmly adsorb CO_2 as seen in CO_2 adsorption curves, making its desorption step more difficult covering Ni neighbor active sites and hindering H_2 activation. The results agree well with the performance of the materials in DRM reaction. For further investigation on the effect of Ni content in the mesoporous alumina samples in the next paragraphs, Ni_5-Mg_{15}-Al_2O_3 was selected as having the best compromise between Mg promoter content (7 wt%), metallic dispersion (21 %), catalyst reducibility and CO_2 affinity.

V.3.2. Influence of Ni content in Ni_x-Mg_{15}-Al_2O_3 catalysts with constant Mg loading

V.3.2.1. Ni_x-Mg_{15}-Al_2O_3 structural, textural, and surface properties

The Ni amount was varied from 5 to 20 wt% keeping a constant Mg content of 7 wt%. Till a Ni content up to 10 wt%, no diffraction peaks are observed in the XRD patterns (Figure V-5) similarly to the behavior seen in Chapter III, stressing on the high dispersion achieved in this type of sample when adding a low to moderate nickel amount. Reaching 15 wt% Ni (Ni_{15}-Mg_{15}-Al_2O_3), new diffraction peaks appear at different diffraction angles (2θ = 37°, 43°, and 63.5°) and become more intense in the case of Ni_{20}-Mg_{15}-Al_2O_3

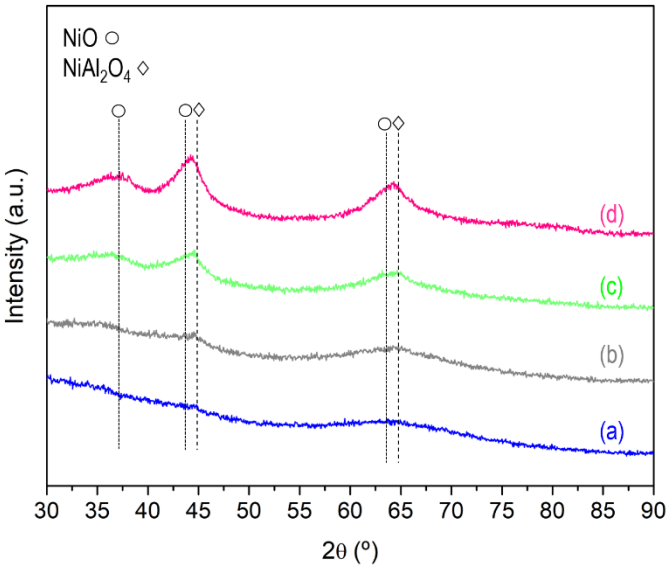

Figure V-5: XRD patterns of calcined (a) Ni_5-Mg_{15}-Al_2O_3, (b) Ni_{10}-Mg_{15}-Al_2O_3, (c) Ni_{15}-Mg_{15}-Al_2O_3, and (d) Ni_{20}-Mg_{15}-Al_2O_3 samples

(curve d). The peaks are broad and no fully symmetrical revealing a possible simultaneous presence of two species ($NiAl_2O_4$ and NiO), and disturbing repartition of Ni particles in response to the increase of Ni loading.

The water strength affinity (Table V-4) was not affected by the change of Ni content with comparable h values of 0.41-0.46. Thus, the inhibitory effect of water in the reaction is not expected to vary from one sample to another.

Regarding the textural properties, these materials also present the characteristics of mesoporous materials with type IV isotherm and H1 hysteresis loop (Figure V-6 A) accompanied with narrow pore size distribution and average pore diameter of 6-9 nm. As the Ni loading increases from 5 to 20 wt%, a gradual decrease in both pore volumes and surface areas occurs (Table V-4), due to more nickel species filling the pores of alumina support and limiting N_2 accessibility.

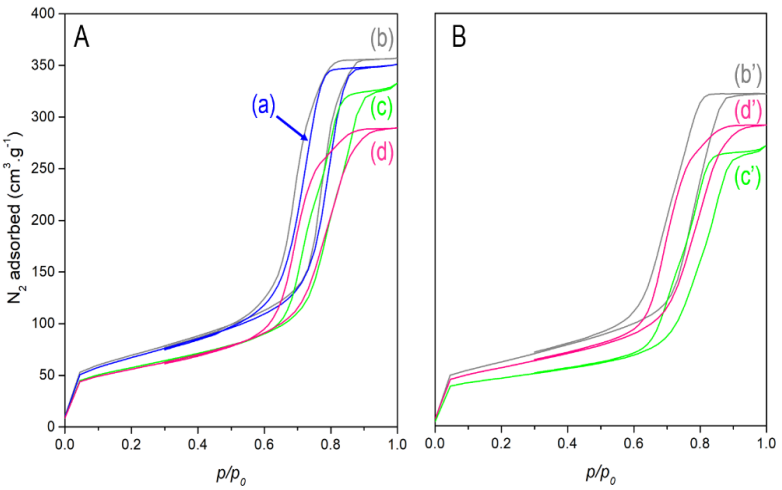

Figure V-6:N_2-sorption curves of (A) calcined and (B) reduced (a-a') Ni_5-Mg_{15}-Al_2O_3, (b-b') Ni_{10}-Mg_{15}-Al_2O_3, (c-c') Ni_{15}-Mg_{15}-Al_2O_3, and (d-d') Ni_{20}-Mg_{15}-Al_2O_3 samples

V.3.2.2. Surface properties and reducibility of Ni_x-Mg_{15}-Al_2O_3 samples

CO_2 affinity (Figure V-7 A) profiles vary as follows: Ni_5-Mg_{15}-Al_2O_3 >> Ni_{15}-Mg_{15}-Al_2O_3 > Ni_{10}-Mg_{15}-Al_2O_3 > Ni_{20}-Mg_{15}-Al_2O_3. This means that when Ni is present in lower quantity compared to Mg, the interaction with CO_2 increases. In contrast, similar or higher Ni loading than Mg in the alumina samples limits the accessibility of CO_2 to the adsorption sites.

The reducibility of these samples (Figure V-7 B) behaves similarly to the samples in Chapter III with a unique reduction peak between 600 and 800 ºC, asserting on the strong metal support interaction even with high Ni loadings. Reduction peaks of both Ni_{15}-Mg_{15}-Al_2O_3 and Ni_{20}-Mg_{15}-Al_2O_3 samples are shifted to a slightly higher temperature than Ni_5-Mg_{15}-Al_2O_3, in agreement with XRD measurements, showing presence of Ni as $NiAl_2O_4$ [287–289], retarding their reduction. The H_2-uptake was in agreement with the Ni percentage present in each sample

with around 800 µmol.g^{-1} H_2 consumed for Ni_5-Mg_{15}-Al_2O_3, 1600 µmol.g^{-1} for Ni_{10}-Mg_{15}-Al_2O_3, 2400 µmol.g^{-1} for Ni_{15}-Mg_{15}-Al_2O_3, and 3300 µmol.g^{-1} consumed for Ni_{20}-Mg_{15}-Al_2O_3.

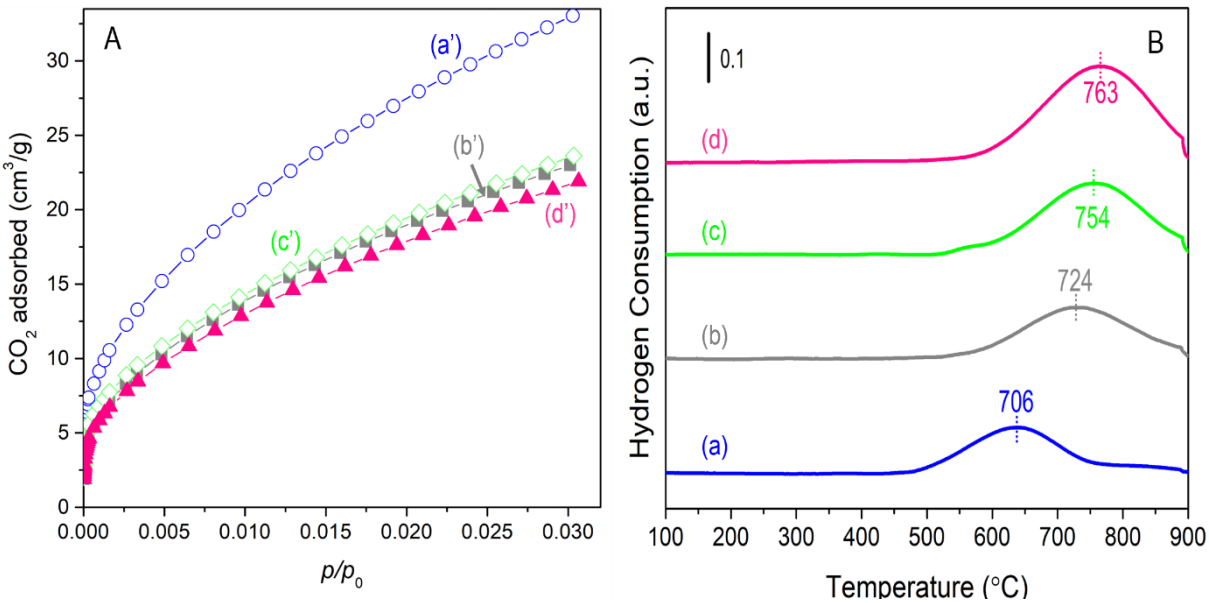

Figure V-7: (A) CO_2 isotherms and (B) H_2-TPR profiles of calcined (a-a') Ni_5-Mg_{15}-Al_2O_3, (b-b') Ni_{10}-Mg_{15}-Al_2O_3, (c-c') Ni_{15}-Mg_{15}-Al_2O_3, and (d-d') Ni_{20}-Mg_{15}-Al_2O_3 samples

Reduced Ni_x-Mg_{15}-Al_2O_3 samples exhibit an increment of metallic nickel particle size from 4.5 to 9 nm in the Ni content range of 5-20 wt% as demonstrated by TEM (Table V-4).

V.3.2.3. CO_2 methanation on mesoporous Ni_x-Mg_{15}-Al_2O_3 catalysts

All the reduced samples were tested in CO_2 methanation (Figure V-8). When going from the Ni_5-Mg_{15}-Al_2O_3 to Ni_{10}-Mg_{15}-Al_2O_3 then Ni_{15}-Mg_{15}-Al_2O_3 catalysts the activity (CO_2 conversion) progressively increases in line with the increment in Ni content, each metal site being active for the dissociation of H_2 into H atoms [290–294]. This increase is however not totally proportional to Ni content due to slight changes in the metal dispersion (Table V-4). When moving from Ni_{15}-Mg_{15}-Al_2O_3 to Ni_{20}-Mg_{15}-Al_2O_3, the CO_2 conversion is no longer

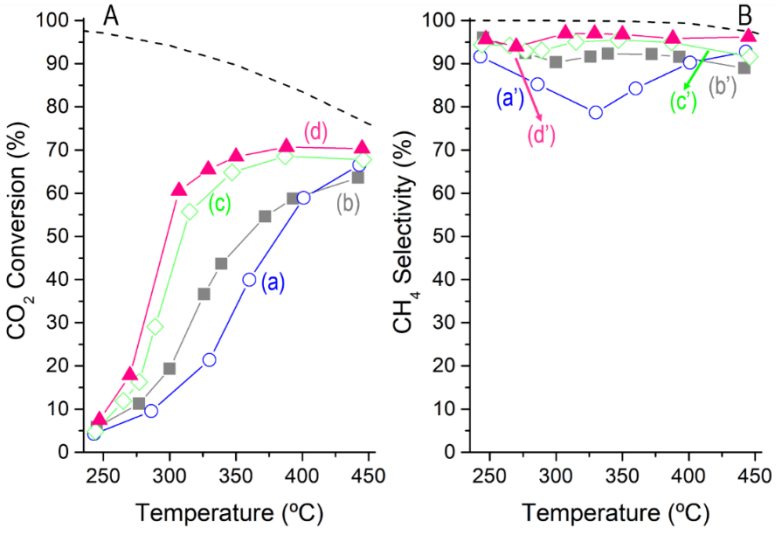

Figure V-8: (A) CO_2 conversion and (B) CH_4 selectivity of (a-a') Ni_5-Mg_{15}-Al_2O_3, (b-b') Ni_{10}-Mg_{15}-Al_2O_3, (c-c') Ni_{15}-Mg_{15}-Al_2O_3, and (d-d') Ni_{20}-Mg_{15}-Al_2O_3 samples

improved because of the significantly lower Ni dispersion. In the frame of this work, we were not able to perform H_2-TPD and TOF calculations on the series of samples with varying Ni content that would be necessary to reach a better quantification of activities as was done in chapter III for DRM.

Stability tests carried out on both Ni_5-Mg_{15}-Al_2O_3 and Ni_{15}-Mg_{15}-Al_2O_3 at 315 ºC for 10 hours (Figure V-9) demonstrate high stability of the samples through time with no evidence of any deactivation. This performance suggests the absence of sintering of nickel nanoparticles. Note also that the selectivity to methane is close to 100% on Ni_{15}-Mg_{15}-Al_2O_3 while it is 10 % less on Ni_5-Mg_{15}-Al_2O_3 on which some side product (notably CO) is formed due less sites for H_2 dissociation.

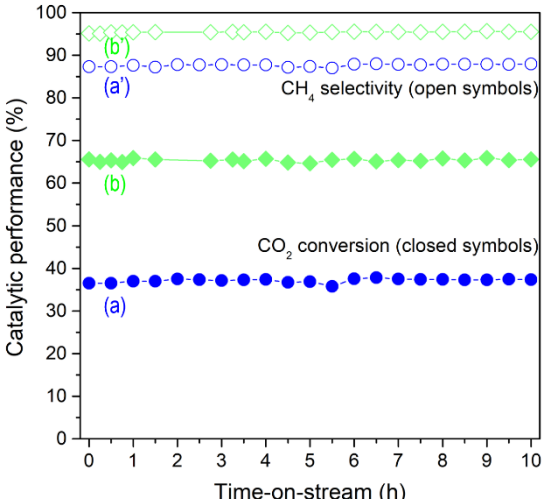

Figure V-9: Stability test in terms of (a-b) CO_2 conversion and (a'-b') CH_4 selectivity of (a-a') Ni_5-Mg_{15}-Al_2O_3 and (b-b') Ni_{15}-Mg_{15}-Al_2O_3

To conclude this part, the results of the most promising sample (Ni_{15}-Mg_{15}-Al_2O_3) were compared to other Ni-based prepared by conventional or by one-pot method in literature (Table V-5). All the presented studies used much more favorable contact times (almost six times higher than the one used in this work) and milder conditions than ours. Therefore, a direct comparison is complicated, but, with the harsh conditions used, in our case, the results obtained for mesoporous Ni_{15}-Mg_{15}-Al_2O_3 are comparable and even better (first 2 rows) than those shown in the table, indicating promising future for these materials in the CO_2 methanation reaction.

Table V-5: Comparison of the performances revealed by the most promising Ni-Mg-Al_2O_3 material from the present work with other traditional (first two rows) and one-pot Al_2O_3 samples reported in the literature

Catalyst	**Catalytic tests conditions**			**Best catalytic performances achieved**			**Ref.**
	P (bar)	*H_2:CO_2*	*GHSV ($ml.min^{-1}.g^{-1}$)*	*T (ºC)*	*CO_2 conversion (%)*	*CH_4 selectivity (%)*	
15Ni-20Ca/Al_2O_3	1	4:1	-	450	66	92	[256]
10Ni-8Mg/Al_2O_3	1	4:1	16000 h^{-1}	500	67	35	[257]
10Ni-8Ca-Al_2O_3	1	4:1	250	350	76	98	[284]
10Ni-3Pr-Al_2O_3	1	4:1	250	350	74	98	[295]
10Ni-1Ru-2Ca-Al_2O_3	1	4:1	500	380	84	>99	[194]
Ni_{15}-Mg_{15}-Al_2O_3	1	4:1	1440	350	65	95	This work

V.4. Physicochemical properties followed by CO_2 methanation over mesoporous Ni_x-Al_2O_3 materials derived from MIL-53 framework

V.4.1. Textural and structural properties of calcined samples

Figure V-10 A (curves a-b) shows the XRD patterns of Ni_5-Al_2O_3 $_{MIL-53}$ (same sample as in chapter IV) and Ni-enriched (15 wt% Ni) Ni_{15}-Al_2O_3 $_{MIL-53}$ calcined materials derived from MIL-53. Both samples exhibit the same three main peaks seen at 2θ = 37°, 45.0° and 65.6° in chapter IV that structurally correspond to a cubic spinel $NiAl_2O_4$ phase with (220), (400) and (440) planes (JCPDS: 001-1299) [28,48,49] with higher intensity in Ni_{15}-Al_2O_3 $_{MIL-53}$ sample. The absence of NiO crystalline peaks confirms the assumption of an intimate mixing between Ni and the oxide support even with higher nickel loading (15 wt%). For instance, NiO species reacts with alumina during the high temperature calcination to form a new stable crystal phase

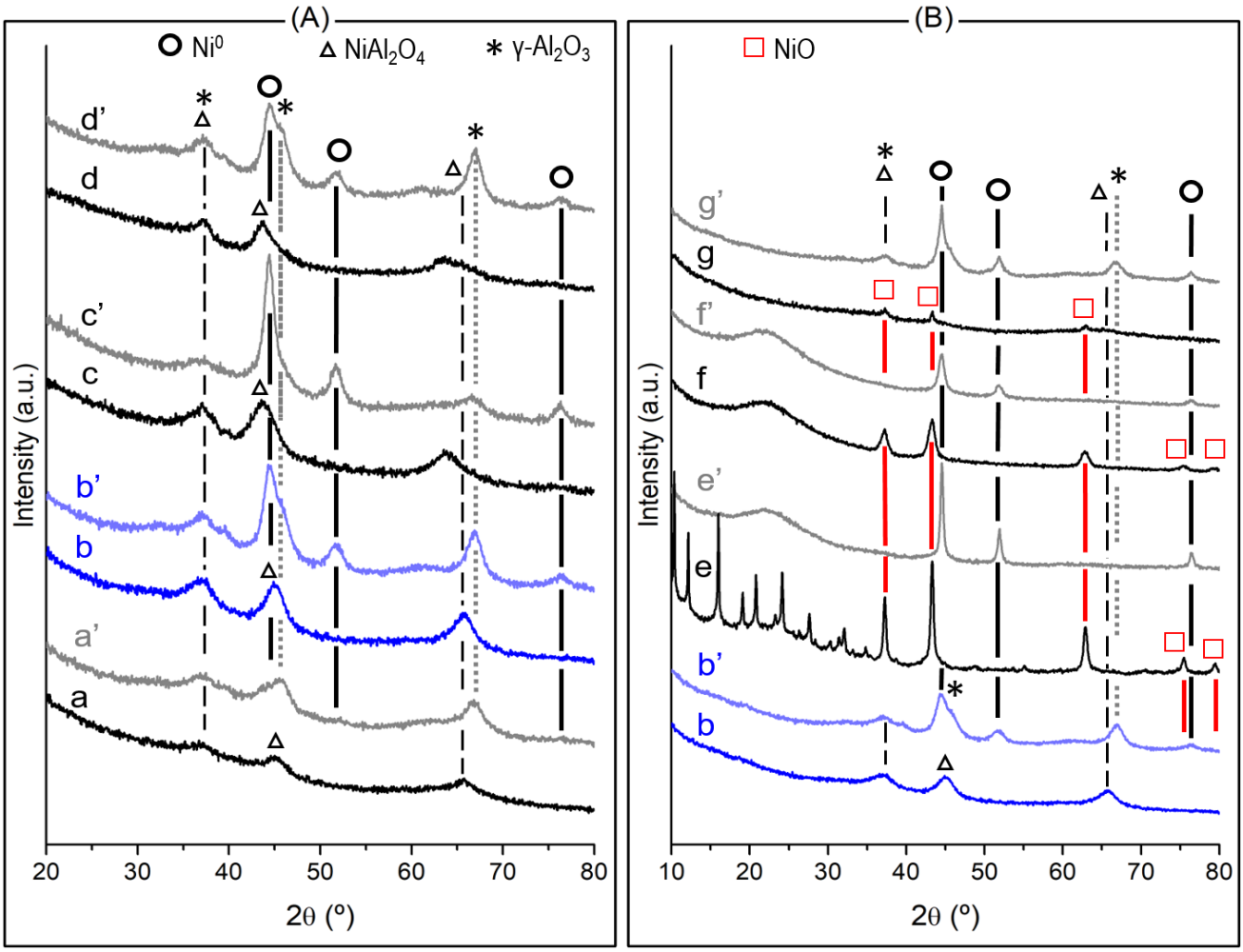

Figure V-10: XRD patterns of calcined (a-g) and reduced (a'-g') samples respectively: a-a') Ni_5-Al_2O_3 $_{MIL-53}$, b-b') Ni_{15}-Al_2O_3 $_{MIL-53}$, c-c') Ni_{20}-Al_2O_3 $_{MIL-53}$, d-d') Ni_{15}@Al_2O_3 $_{MIL-53}$, e-e') Ni_{15}@USY, f-f') Ni_{15}@SBA-15, and g-g') Ni_{15}-Al_2O_3

that belongs to a cubic system with Fd-3 m space group. The spinel structure consists of an ensemble of tetrahedral coordination occupied with bivalent Ni^{2+} and octahedral coordination filled with trivalent Al^{3+} cations. This scattering can be altered when Ni^{2+} partially adopts the octahedral site while the tetrahedral site hosts Al^{3+} together with Ni^{2+} ions resulting in a family of compounds of inverse spinel structure known as $Ni_{1-x}[Ni_xAl_{2-x}]O_4$ where $0<x<1$. This structure flexibility could enhance the interaction between Ni and the support, restrict the aggregation of metallic Ni sites, and increase their dispersion [169,173,296].

The diffraction peak ($2\theta = 65.6°$) of Ni_{20}-$Al_2O_{3\ MIL\text{-}53}$ containing 20 wt% Ni is shifted slightly to the left, which could reveal the presence of a small fraction of NiO species in addition to $NiAl_2O_4$. Same observation was detected for $Ni_{15}@Al_2O_{3\ MIL\text{-}53}$ where nickel is impregnated after MIL-53 calcination suggesting a lower degree of interaction with the support and confirming that the order of nickel impregnation with respect to calcination has an influence towards nickel dispersion [297,298].

Ni_{15}-$Al_2O_{3\ MIL\text{-}53}$ was compared to other materials prepared with different support type having a fixed 15 wt% Ni percentage (Figure V-10 B). Ni_{15}@USY (e), Ni_{15}@SBA-15 (f), and Ni_{15}-Al_2O_3 (g) show diffraction peaks at $2\theta = 37.2°$, 43.1° and 62.8° attributed to NiO species that correspond respectively to the planes (111), (200) and (220) with face centered cubic cell (JCPDS: 01-071-4750) suggesting lower interaction with the support and larger particle size. Table V-6 indicates NiO average particle size of 17.2 nm, 8.6 nm, and 8 nm for Ni_{15}@USY, Ni_{15}@SBA-15, and Ni_{15}-Al_2O_3 respectively.

Table V-6: Ni-nanoparticle sizes of the calcined and reduced materials, and metallic Ni dispersion on reduced samples

Catalyst code	**ΦNiO[a] (nm)**	**ΦNi⁰ [b] (nm)**	**Ni⁰ dispersion [c] (%)**
Ni_5-$Al_2O_{3MIL\text{-}53}$	-	- *(7.0)*	14
Ni_{15}-$Al_2O_{3MIL\text{-}53}$	-	5.6 *(8.6)*	12
Ni_{20}-$Al_2O_{3\ MIL\text{-}53}$	-	7.1 *(9.4)*	11
$Ni_{15}@Al_2O_{3MIL\text{-}53}$	-	6.2 *(9.2)*	11
Ni_{15}@USY	17.2	18.9 *(25)*	4
Ni_{15}@SBA-15	8	9.7 *(17.1)*	6
Ni_{15}-$Al_2O_{3\ one\text{-}pot}$	8.6	8.8 *(9.0)*	11

a: value of NiO particle size estimated from XRD diffractograms of calcined materials; b: value of metallic Ni^0 nanoparticle estimated from XRD of reduced materials, in brackets: nanoparticle size from the histograms obtained from representative TEM images of each samples; c: nanoparticle dispersion calculated from TEM

Increasing the Ni amount from 5 to 20 wt% does not alter the shape of the isotherm in all Ni-Al_2O_3 materials derived from MIL-53 and all of them resembles the shape already seen and discussed in chapter III. Ni_5-$Al_2O_{3\ MIL-53}$, Ni_{15}-$Al_2O_{3\ MIL-53}$, and Ni_{20}-$Al_2O_{3\ MIL-53}$ have close values of surface area (230-250 $m^2.g^{-1}$, Table V-7) and pore volume (0.97-1.09 $cm^3.g^{-1}$) indicating that this method is adequate for a wide range of nickel loadings (5-20 wt%). Regarding $Ni_{15}@Al_2O_{3\ MIL-53}$ sample that is calcined then impregnated, its surface area (156 $m^2.g^{-1}$) and pore volume (0.42 $cm^3.g^{-1}$) are lower by 30 and 50% respectively than the samples that are firstly impregnated by Ni on MIL-53(Al) framework and later calcined.

The textural properties obtained by physisorption are well confirmed by HRTEM images. For instance, both Ni_5-$Al_2O_{3\ MIL-53}$, and Ni_{15}-$Al_2O_{3\ MIL-53}$ present a fused ill-defined and defective alumina flakes composed of several randomly interwoven nanosheets with approximately 20 nm in length (Figure V-11 A, A' and B, B'). Ni_{15}-$Al_2O_{3\ MIL-53}$ (Figure V-11 B, B') has no detection of nickel particles confirming the results of XRD that reveal the presence of $NiAl_2O_4$ instead of NiO. This accentuates on the efficiency of MIL-53(Al) derived method to highly and homogeneously distribute Ni throughout the samples even if higher Ni amount is used.

Table V-7: Main textural properties of the calcined and reduced samples prepared in the present work

Catalyst code	**h index** [a]	**V_{micro}** [b] **($cm^3.g^{-1}$)**	**V_{meso}** [b] **($cm^3.g^{-1}$)**	**S.A.** [b] **($m^2.g^{-1}$)**
MIL-53	-	0.4	0.4	1130
$Al_2O_{3\ MIL-53}$	-	-	1.19	318
Ni_5-$Al_2O_{3\ MIL-53}$	0.64	-	0.97 *(0.85)*	230 *(225)*
Ni_{15}-$Al_2O_{3\ MIL-53}$	0.60	-	1.09 *(1.02)*	251 *(150)*
Ni_{20}-$Al_2O_{3\ MIL-53}$	0.58	-	1.05 *(0.71)*	245 *(175)*
$Ni_{15}@Al_2O_{3MIL-53}$	0.54	-	0.42 *(0.29)*	156 *(81)*
USY	-	0.208	0.271	298
Ni_{15}@USY	0.87	0.16 *(0.01)*	0.20 *(0.25)*	259* *(261)**
SBA-15	-	-	1.02	701
Ni_{15}@SBA-15	0.98	0.11 *(0.07)*	0.66 *(0.62)*	487 *(422)*
$Al_2O_{3\ One-Pot}$	-	-	0.52	258
Ni_{15}-$Al_2O_{3\ One-Pot}$	0.38	-	0.13 *(0.11)*	60 *(44)*

[a] determined from TGA-DSC experiments; [b] total surface area (S.A.), microporous (V_{micro}) and mesoporous (V_{meso}) pore volume calculated from the N_2 sorption isotherms, in brackets: reduced materials *S_{ext} determined using t-plot method for the zeolite sample after calcination and reduction

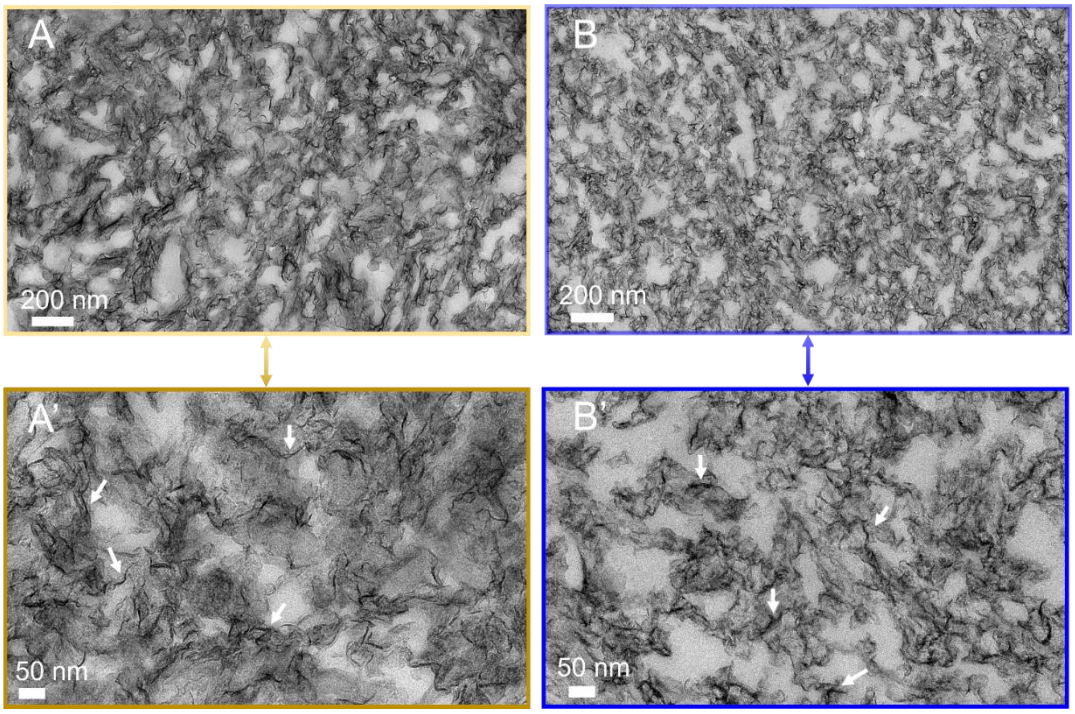

Figure V-11: HR-TEM Micrographs of fresh Ni-Al_2O_3 $_{MIL-53}$ catalysts: (A-A') Ni_5-Al_2O_3 $_{MIL-53}$, (B-B') Ni_{15}-Al_2O_3 $_{MIL-53}$.

The h indexes determined for the different Ni_x-Al_2O_3 $_{MIL-53}$ samples are somehow quite similar (~0.6 in all cases, Table V-7) neglecting any impact of this parameter on the catalytic performances.

V.4.2. Reducibility of Ni_x-Al_2O_3 $_{MIL-53}$ materials

The reducibility of all calcined Ni_x-Al_2O_3 $_{MIL-53}$ materials (Figure V-12 A) with different Ni wt% (5-20 wt%) present similar reduction profiles with one reduction curve occurring at temperatures above 500 °C. The absence of a second reduction peak at lower temperature indicates that the Ni species present in these sample are all strongly interacting with the support [271], as in spinel mixed phases with no weakly bounded Ni species [287–289]. These results agree well with what has been seen in XRD and TEM. Thus, the impregnation of nickel nitrate on the parent MIL-53 allows the formation of an Al_2O_3-$NiAl_2O_4$ phase in which nickel and aluminium cations are intimately mixed in a homogenous oxide phase over a wide range of Ni loading (5-20 wt%). Note that a small displacement in the maximum reduction temperature towards lower temperatures was observed for Ni_{20}-Al_2O_3 $_{MIL-53}$ (Figure V-12 A, c) insisting on the formation of small fraction of easier reducible Ni species that is in good agreement with XRD results showing a shift of the peak from 2θ of 65° to 63°.

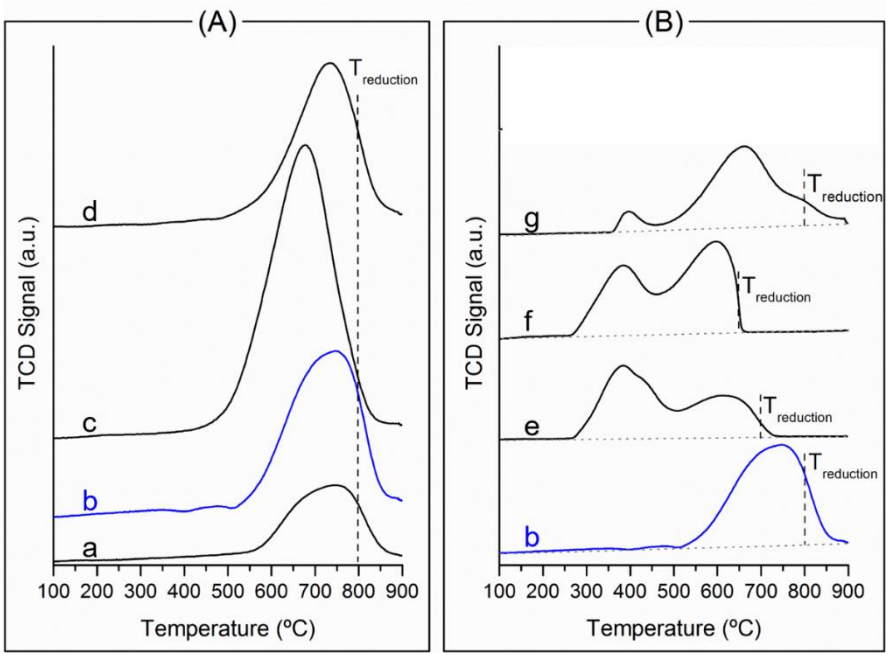

Figure V-12: H_2-TPR profiles for calcined (A) MOF-derived samples: (a) Ni_5-$Al_2O_{3\ MIL-53}$, b) Ni_{15}-$Al_2O_{3\ MIL-53}$, c) Ni_{20}-$Al_2O_{3\ MIL-53}$, and d) Ni_{15}@$Al_2O_{3\ MIL-53}$ and (B) other Ni-based materials: (e) Ni_{15}@USY, f) Ni_{15}@SBA-15, and g) Ni_{15}-Al_2O_3

Compared to other non-MOF samples, microporous (Ni_{15}@USY) or mesoporous (Ni@SBA-15, Ni_{15}-$Al_2O_{3\text{One-pot}}$) in texture, non-Al_2O_3 based materials Ni_{15}@USY and Ni_{15}@SBA-15 acquire the highest h index of 0.87 and 0.98, respectively due to the presence of silica that makes them more hydrophobic compared to alumina-based sample that is known to be hydrated when in contact with H_2O.

On the other hand, the non-MOF based materials present two reductions peaks at low (T< 500 °C) and high (T> 500 °C) temperatures, asserting the existence of different types of nickel species with distinctive metal-support interactions. Ni_{15}@USY (Figure V-12 B e) contains Ni species that are present mainly as NiO and whose reduction processes occur at ~320 ºC (NiO in the zeolite external surface) and 400 ºC (NiO in the zeolite supercages) as demonstrated elsewhere [269,287,299–301]. A smaller additional reduction peak occurred at a temperature above 600 ºC attributed to the reduction of NiO species present in the mesoporous cavities of this specific commercial zeolite [287,293,300,301]. Ni_{15}@SBA-15 (Figure V-12 B f) presents also two reduction peaks, one at ~400 ºC and the second one is at ~600 ºC, attributed to NiO species weakly (external surface) and strongly (mesoporous channels) interacting with the silica support, respectively [185,293,302]. Ni_{15}-$Al_2O_{3\ \text{One-pot}}$ (Figure V-12 B g) presents a main reduction peak at ~700 ºC, as in the case of the MOF-derived material, due to reduction of Ni strongly interacting with Al_2O_3 [303,304]. However, this sample presents also a less

relevant reduction process at ~400 ºC corresponding to the reduction of NiO species weakly interacting with Al_2O_3 matrix. These results are compatible with XRD measurements that showed clear peaks of NiO species.

V.4.3. Textural and structural properties of reduced materials

XRD patterns of the Ni_x-Al_2O_3 $_{MIL-53}$ samples reduced at 800 °C are shown in Figure V-10 (A) along with those before reduction. The reduction of all MIL-53 based materials contributed to the formation of new diffraction peaks attributed to (111), (200) and (220) planes of crystalline Ni^0 at 2θ of 44.5°, 51.9° and 76°, respectively (JCPDS: 03-065-0380). In addition, bands corresponding to gamma-alumina appear clearly in the reduced materials asserting on the Ni extraction from $NiAl_2O_4$ oxide phase to metallic Ni^0 on the pore surface. Scherrer equation was applied at 2θ of 51.9° for all the samples and it leads to a mean Ni particle size of <5 nm, 5.6 nm, 7.1 nm and 6.2 nm for Ni_5-Al_2O_3 $_{MIL-53}$, Ni_{15}-Al_2O_3 $_{MIL-53}$, Ni_{20}-Al_2O_3 $_{MIL-53}$ and Ni_{15}@Al_2O_3 $_{MIL-53}$ respectively (Table V-6). These particle sizes are systematically smaller than the ones between 9 and 20 nm reported in literature on other MOF materials [266,267].Thus, these data highlight again that this new strategy of occluding nickel inside the pores of alumina following MIL-53 route is very efficient and capable of producing small nickel particles even for high nickel loading.

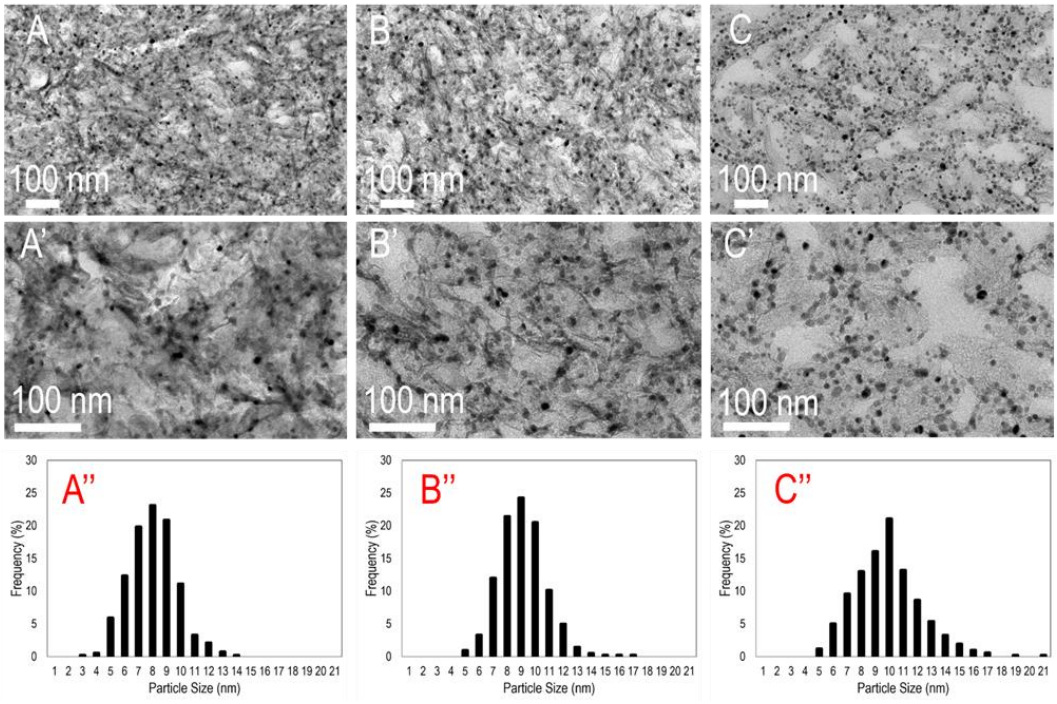

Figure V-13: HR-TEM Micrographs and Ni^0 particle size distribution of reduced catalysts: (A-A'') Ni_5-Al_2O_3 $_{MIL-53}$, (B-B'') Ni_{15}-Al_2O_3 $_{MIL-53}$, and (C-C'') Ni_{20}-Al_2O_3 $_{MIL-53}$

Particle sizes obtained from TEM (Table V-6) confirm further the trend seen in XRD even if the mean values are slightly higher in TEM (due probably to the difficulty to detect very small particles). Detected nickel particles (Figure V-13), independent from Ni loading, are homogeneously distributed all over the support, which still appears as interwoven alumina sheets. This morphology was also preserved in the physisorption shape of the reduced Ni_x-Al_2O_3 $_{MIL-53}$ samples showing a slit-like hysteresis typical of a layered material with unorganized interlayered pores. The surface area decreased due to shrinkage of material after harsh reduction temperature at 800 °C or to growth of Ni particles due to phase transformation of $NiAl_2O_4$ into gamma-alumina and metallic Ni^0 nanoparticles spacing apart the nanosheets one from another (Table V-6).

Compared with the non-MIL-53(Al) based materials, their particle size was larger with eventually lower dispersion (Table V-6). Ni_{15}@SBA-15 (9.7 nm (XRD)/ 17 nm (TEM)) and Ni_{15}@USY (19 nm (XRD)/ 25 nm (TEM)) had the lowest dispersion compared to other alumina-based samples. They demonstrated the weakest metal-support interactions with negative impact on the particle size, easily inducing sintering. These results confirm what was mentioned in literature about the importance of Al_2O_3 support in enhancing the metal-support interaction, increasing dispersion and enhancing stability compared to ZrO_2, TiO_2 and SiO_2 [59].

V.4.4. Catalytic performances of Ni-based catalysts

Ni_x-Al_2O_3 $_{MIL-53}$ catalysts derived from MIL-53 framework showed that increasing Ni content enhances the catalytic performances in terms of both CO_2 conversion and CH_4 selectivity as function of temperature (Figure V-14). The conversion of CO_2 increased when passing from 5 to 20 wt% Ni. This enhancement in methanation performances, could be attributed to the increase in the number of Ni^0 active sites available for H_2 dissociation [275,294,301,305–307].

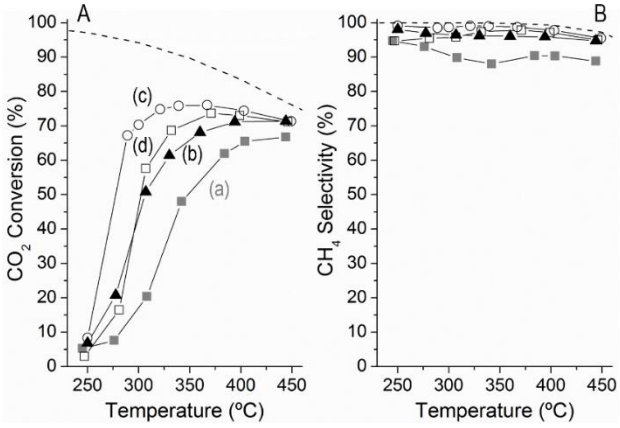

Figure V-14: (A) CO_2 conversion and (B) CH_4 selectivity of a) Ni_5-Al_2O_3 $_{MIL-53}$, b) Ni_{15}-Al_2O_3 $_{MIL-53}$, c-) Ni_{20}-Al_2O_3 $_{MIL-53}$, and d) Ni_{15}@Al_2O_3 $_{MIL-53}$

Ni_{15}-Al_2O_3 $_{MIL-53}$ with 15 wt% Ni was tested over a long period of 20 h at 350 °C (Figure V-15). It showed excellent stability proving resistibility towards any deactivation. The conversion of CO_2 was high about 72% with an outstanding selectivity of 98% that is constant during the time. These results affirm that Ni-Al_2O_3 catalysts derived from MOF framework are new and interesting materials for this environmental catalytic application, proving their efficiency in terms of both activity and stability. This excellent performance is further affirmed by TEM of the spent Ni_{15}-Al_2O_3 $_{MIL-53}$ catalyst after reaction (Figure V-16). The catalyst textural properties were preserved with high nickel dispersion and an average Ni particle size of 7.3 nm (confirmed by XRD) casting any chance of sintering. TGA experiment was also applied on the spent materials showing no weight loss at a temperature range of 200 and 900 °C confirming as well the absence of carbon.

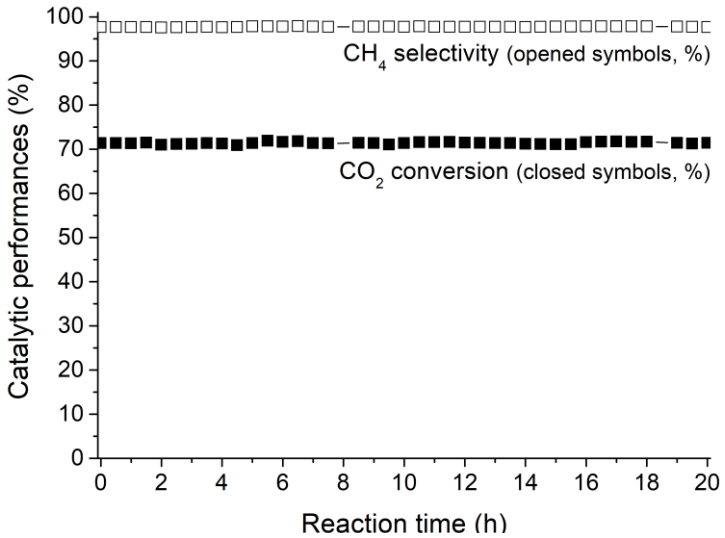

Figure V-15: Stability test of Ni_{15}-Al_2O_3 $_{MIL-53}$ over 20 h time on stream

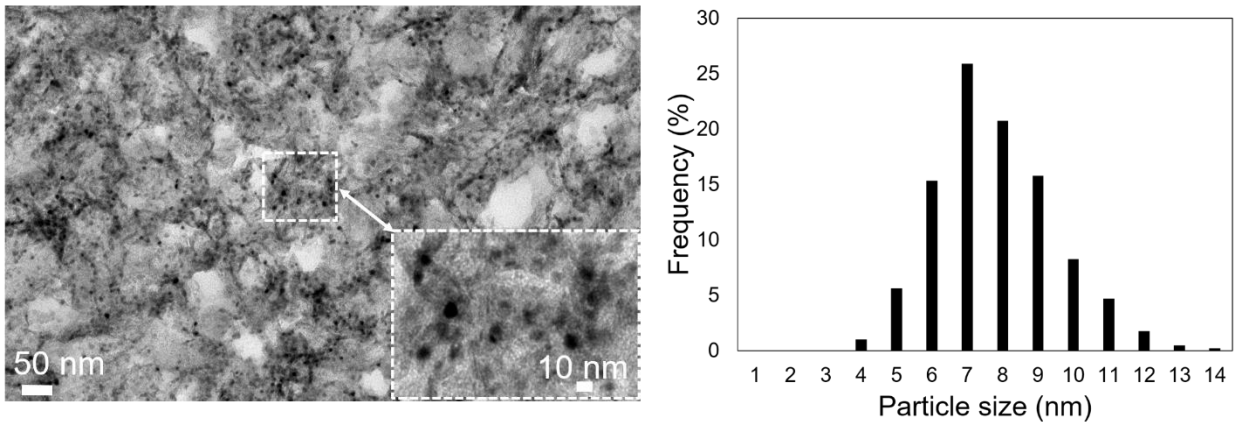

Figure V-16: TEM micrograph of spent Ni_{15}-Al_2O_3 $_{MIL-53}$ after CO_2 methanation reaction. Conditions: T=350 °C, GHSV=1440 $ml.g^{-1}.min^{-1}$, H_2:CO_2= 4:1

Again, Ni_{15}-Al_2O_3 $_{MIL-53}$ was compared to other non-MIL-53 materials (Figure V-17), this time with the catalytic performance. It is clear that Ni_{15}-Al_2O_3 $_{MIL-53}$ acquires the highest activity among all the presented samples over all temperature range. This behavior is expected since Ni_{15}-Al_2O_3 $_{MIL-53}$ possesses the strongest interaction between Ni active phase and Al_2O_3 support, the highest dispersion, and the smallest particle size (7 nm) avoiding possibilities of Ni sintering that decreases in turn the number of active metal sites. Note that Ni_{15}@USY should have the lowest activity since it has the worst parameters in terms of Ni particle size and Ni-support interaction. The reason behind such unexpected trend, could be due to some better CO_2 adsorption on this sample especially that zeolite can play a role in the catalytic test enhancing the interaction between its compensating cations and carbon dioxide. Similar phenomenon has been seen in one of the literature [269] showing that sintering in zeolites does not change catalytic performance.

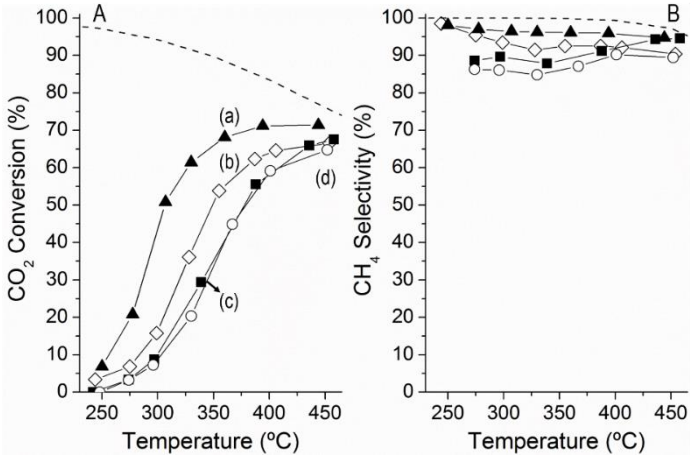

Figure V-17: (A) CO_2 conversion and (B) CH_4 selectivity of (a) Ni_{15}-Al_2O_3 $_{MIL-53}$, (b) Ni_{15}@USY, c) Ni_{15}@SBA-15, d) Ni_{15}-Al_2O_3

Ni_{20}-Al_2O_3 $_{MIL-53}$ was compared at the end to the catalytic performance test of a commercial Ni@γ-Al_2O_3 (25 wt% Ni). Figure V-18 A shows that Ni_{20}-Al_2O_3 $_{MIL-53}$ presents better activity than the commercial catalyst tested under the same conditions. This is due to the higher metallic surface area available in the MOF sample for the reaction and to the higher metal-support interactions, enhancing dispersion and boosting catalytic performance. Both samples were however stable over time (Figure V-18 B), with a CO_2 conversion of 75% and a CH_4 selectivity of 99% for Ni_{20}-Al_2O_3 $_{MIL-53}$ compared to 60% CO_2 conversion and 95% CH_4 selectivity for Ni@γ-Al_2O_3.

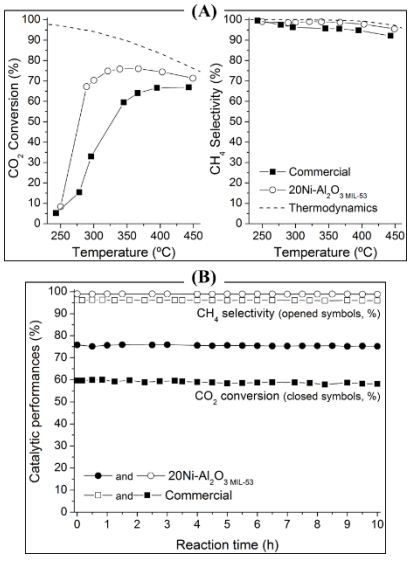

Figure V-18: (A) CO_2 conversion and CH_4 selectivity and (B) stability at 350 °C of Ni_{20}-Al_2O_3 $_{MIL-53}$ and Ni@γ-Al_2O_3

Finally, Ni_{20}-Al_2O_3 $_{MIL-53}$ was compared to other MOFs (as support or template) based materials applied in CO_2 methanation reaction (Table

V-8). Needless to say, the contact times used in the present work are less favorable than the ones reported in other studies. However, results indicate that using an Al-based MOF as precursor results in better outcomes in terms of both CO_2 conversion and CH_4 selectivity. Consequently, the presented work constitutes a great advance in the use of active, selective and stable Ni-MOF-derived materials for CO_2 methanation, especially when taking into account that few studies have been reported till the moment in this area.

Table V-8: Comparison of the performances revealed by the best MOF-derived material from the present work with similar reported catalysts in the literature.

Catalyst	MOF	Metal amount (wt%)	Catalytic tests conditions			Best catalytic performances achieved			
			P (bar)	*H_2:CO_2*	*GHSV ($ml.min^{-1}.g^{-1}$)*	*T (°C)*	*CO_2 conversion (%)*	*CH_4 selectivity (%)*	*TOF (s^{-1})*
1%Ru-ZrO_2[263]	UiO-66	1	30	4:1	317	350	96	99	n.a.
32.5%Co-PC[a][266]	ZIF-67	32.5	30	4:1	1200	270	53	99	n.a.
10%Ni/MOF-5[b][267]	MOF-5	10	1	4:1	125	320	75	>99	n.a.
Pd@UiO-66[b][264]	UiO-66	6	40	4:1	250	340	56	97	n.a.
Pt/UiO-66[b][265]	UiO-66	3		5.2:1	110	350	49	36	n.a.
20%Ni/MIL-101[b][268]	MIL-101	20	1	4:1	125	320	>99	>99	$1.41 \cdot 10^{-3}$
20%Ni-Al_2O_3*	MIL-53	20	1	4:1	1440	300	70	>99	$2.67 \cdot 10^{-1}$

[a] PC: Porous carbon; [b]MOF-5, UiO-66, MIL-101 structures not collapsed during the preparation nor the pre-activation, * This work

V.5. Conclusion

In summary, mesoporous Ni_5-Mg_y-Al_2O_3 and Ni_5-Al_2O_3 derived from MIL-53 framework, good in DRM (chapters III-IV), also exhibit good performances in CO_2 methanation reaction. As for DRM, in the Ni_5-Mg_y-Al_2O_3 series of catalysts, an optimum amount of 7 wt% Mg favors both CO_2 conversions and CH_4 selectivity avoiding MgO segregation and keeping sufficient basic sites to activate CO_2 species and enhance the reaction mechanism. This chapter also shows that Ni loading can be increased up to 15 wt% conserving to a certain extent very good dispersions in both the proposed one-pot EISA and MOF routes. This leads to enhanced conversion of carbon dioxide and high selectivity to methane provided by the high metallic surface area available for the dissociation of hydrogen. The obtained Ni_{15}-$Al_2O_{3\ MIL\text{-}53}$ catalyst has superior performances than USY zeolite, SBA-15 material and Ni-Al_2O_3 commercial or synthesized by a different method. Ni-Al_2O_3 derived from MIL-53 framework led to superior results compared to the few existing MOF-based materials already used in CO_2 methanation. Needless to say, the promising activity, selectivity and stability of the synthesized materials turn them into potential catalysts for a large-scale application of power-to-gas as in DRM.

VI. Chapter VI: Promotion of mesoporous nickel-alumina based catalysts by magnesium addition for reforming of waste gasification products

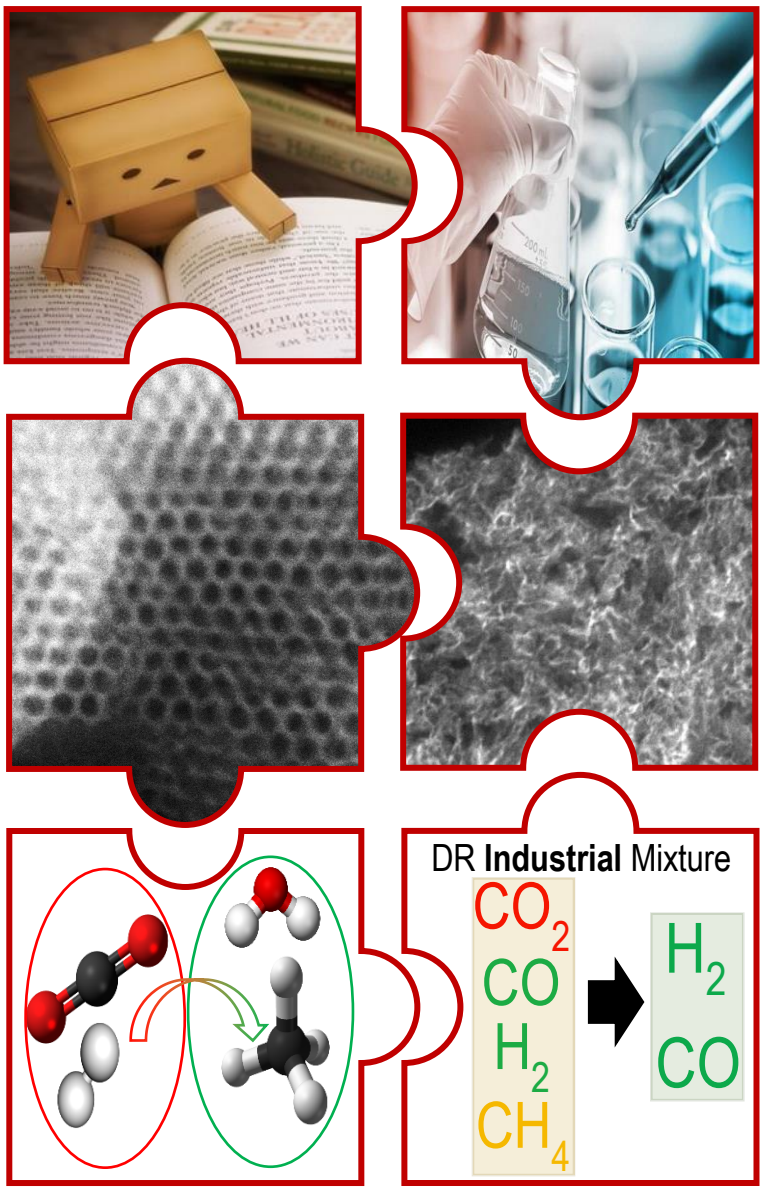

This chapter ends the thesis report by tackling dry reforming over a more complex mixture containing not only CH_4 and CO_2 in the feed, but also H_2 and CO. The addition of the product within the feed mixture makes the reaction more challenging, but more realistic. The non-conventional model mixture was taken from a pyrolysis product unit after treatment of biomass wastes in a Lebanese industry partner of the SOL-CARE project. A thermodynamic study was done on the obtained mixture in dry reforming to check the expected behavior. Then, the reaction was applied on mesoporous Ni_5-Mg_y-Al_2O_3 materials to investigate the efficiency of these catalysts, with good performance in standard DRM, under harsh conditions.

VI.1. Literature Review

As mentioned earlier in Chapter I of this report, biomass is one of the alternative sources of energy that can be used to limit the dependency on fossil fuels and their impact on the global environment. The process of conversion of biomass to energy encompasses a wide range of different renewable sources. The organic biomass wastes are derived from garbage, animal manure and biodegradable materials. This technology consists a thermochemical route to convert biomass. This method divided into 2 options which choice depends on the desired form of energy and on the type and quantity of biomass feedstock available [308–310]:

1. Combustion: It is the direct burning of biomass into air where the chemical energy stored inside it will be converted to heat, mechanical power and electricity that can be used for example in furnaces, boilers (heating water, cooking), and steam turbines. This method is wasteful of resources (low conversion efficiency, less than 25% chemical energy of the solids converted to thermal and electrical energy).

2. Pyrolysis and gasification: It is the partial oxidation of biomass in absence of O_2 or presence of air at around 500-800 °C [311]. Gaseous products mostly contain a mixture of CH_4, CO_2, H_2, and CO gases, some light hydrocarbons (chars), tars, ash and minor contaminants (NH_3, H_2S, SO_2) [312]. The produced gas can be burnt directly or used as a fuel for gas turbines and engines if it has low calorific value. Otherwise the gaseous mixture (CH_4, CO_2, H_2, CO) can be transformed under suitable reactions to syngas (H_2 and CO) and used as feedstock in the production of liquid fuels (Fischer-Tropsch synthesis) and methanol, each of which may be served as fuels for transportation.

It is recommended, for time saving and environmental considerations, to carry out gasification/pyrolysis in a unique one-stage reactor [313–316]. Nevertheless, no satisfactory production of clean syngas (H_2, CO) was obtained and formation of tar can block the reactor in

such conditions. A two-stage reactor [317–319] was developed where the waste is first pyrolyzed to produce a range of pyrolysis gases that pass directly to a second-stage catalytic reactor where catalytic reforming takes place to generate higher yield of hydrogen or syngas. Even if very attractive, such type of combined reactor will not be considered in this work because efforts are still needed to improve each individual step, and the focus will remain targeted towards the reforming stage to find a good catalyst that can handle the complex product mixture of the pyrolysis reaction.

As seen in chapter I, a great effort has been made in literature on developing reforming catalysts conducted using model compounds (CH_4, and CO_2 only), whereas those involving real raw material are still limited. Few studies worked on reforming of gasification/pyrolysis products using different type of catalysts. The final reforming product also had distinct syngas ratio (probably due to the type of waste used). For example, Juniza MD Saad et al. [320] performed catalytic dry reforming on evolved gas from pyrolysis of plastics. The composition of the pyrolysis product gas was not specified. Ni-Co-Al catalyst used increased syngas yields with an H_2:CO=0.5. However, carbon formation occurred during reaction deactivating the catalyst. Katsuya Kawamoto et al. [321] performed reforming after gasification on a wood feedstock sample. The complex mixture used was composed of 9% CH_4, 32% CO_2, 23% H_2 and 32% CO. In this study, mesoporous Ni/SBA-15 was applied playing on the mode of Ni insertion on the SBA-15 support which was either by impregnation or direct synthesis. Maximum concentrations were achieved when 20 wt% of NiO were added over SBA-15 with an H_2:CO ratio of 2.2. Yeshui Zhang [322] investigated four different Al_2O_3-based catalysts (Co/Al_2O_3, Cu/Al_2O_3, Fe/Al_2O_3 and Ni/Al_2O_3) prepared by incipient wetness impregnation and their effect in dry reforming of waste tires pyrolysis product. The composition of the reforming feed was not detailed. The highest gas yield and hydrogen production was achieved in Ni/Al_2O_3 with an H_2:CO ratio of 3.6 and the least amount of carbon nanotubes deposition.

Few other researchers relied on modeling and theoretical paths to evaluate the influence of H_2 or CO addition to CH_4 and CO_2 in the feed mixture [323,324]. Liu L. 328 et al. suggests that the addition of H_2 (CH_4:CO_2:H_2: 1:2:1) or CO (CH_4:CO_2:CO: 1:2:1) to the initial feed blocks the conversions of CH_4 and CO_2 directing different reactions. H. Hublot stated that CO_2 addition promotes DR reaction while CO had no kinetic effect 327. These studies did not rely on any experiment, and therefore no catalyst was synthesized and tested.

In our case, the realistic mixture to be applied in reforming was taken from a pilot plant pyrolysis product. The model gas composition provided from a Lebanese industry (INDEVCO) containing CH_4:CO_2:H_2:CO = 0.75:1:1.57:0.85 will be tested theoretically (HSC software) and experimentally (DRM on Ni_5-Mg_y-Al_2O_3 catalysts seen in chapter III). Before applying such mixture directly in reforming, the standard feed ratio was changed progressively from a standard reforming with a CH_4:CO_2=1 to CH_4:CO_2=0.75, till the addition of H_2 (CH_4:CO_2:H_2=0.75:1:1.57) and CO (CH_4:CO_2:CO=0.75:1:0.85) in the initial feed mixture. The results are then compared to the overall composition with the inclusion of CH_4, CO_2, H_2 and CO initially as reactants. Altering the initial feed composition to meet or be closer to realistic conditions make the reaction itself more complicated and more prone to side reactions (production of water and carbon deposition) which diminish the conversions compared to classical DRM.

VI.2. Thermodynamic analysis

Before doing the catalytic tests, we performed thermodynamic simulations to check the changes in the feed mixture going from the case of CH_4:CO_2 of 0.75:1 to CH_4:CO_2:H_2:CO = 0.75:1:1.57:0.85. Moreover, the regions of side reactions are specified in order to select the conditions where these reactions are limited. Table VI-1 summarizes the cases of inlet feed composition used and the obtained H_2:CO ratios by the software considering or not the presence of carbon $C_{(s)}$.

Table VI-1: The molar composition applied to the inlet feed mixture of DRM reaction and the thermodynamic values of H_2:CO ratio obtained in each case

Cases	Inlet feed Composition				H_2:CO HSC values					
					Sec.1		Sec.2		Sec.3	
	CH_4	CO_2	H_2	CO	No C	With C	No C	With C	No C	With C
Case 1	●	●			0.18-0.77	13000-10	0.77-0.9	10-0.96	0.9-0.8	0.96-0.8
Case 2	●	●	●		4700-5.9	55000-23	5.9-1.9	23-2	1.9-1.7	2-1.7
Case 3	●	●		●	0-0.2	6800-7.6	0.2-0.6	7.6-0.7	0.6-0.5	0.7-0.6
Case 4	●	●	●	●	1065-2	27000-17	2-1.2	17-1.5	1.2-1.15	1.5-1.15

VI.2.1. Thermodynamic analysis in absence of $C_{(s)}$

Figure VI-1 A simulates case 1 with CH_4:CO_2 ratio of 0.75:1. No reforming reaction takes place below 400 °C in region 1 (absence of products (H_2, CO) formation) stimulating the high temperature needed for the DR reaction to occur no matter what the feed composition is. Formation of the syngas is further promoted at higher temperatures. However, in this case

(excess of CO_2 with respect to CH_4), H_2O is formed even at high reaction temperature (650 - 1000 °C) with more CO product compared to H_2. This means that more CO_2 present in the feed mixture boosts the occurrence of the RWGS ($CO_2+H_2 \rightarrow CO+H_2O$) reaction consuming CO_2 and H_2 to produce CO and H_2O that leads to H_2:CO ratio always less than 1 (Table VI-1, case 1).

In case 2, H_2 is added to the initial feed mixture (Figure VI-1 B, CH_4:CO_2:H_2 = 0.75:1:1.57). As a result, CO_2 methanation ($CO_2+4H_2 \rightarrow CH_4+2H_2O$) side reaction is promoted at low temperatures (section 1) prevailing the production of H_2O and CH_4. As the temperature increases, a small increase in CO_2 production is noticed in section 2 stressing on the occurrence of WGS reaction making CO reacts with H_2O to form CO_2 and H_2. Section 3 is the region where the reforming reaction dominates with an H_2:CO ratio of 1.9 at 600 °C and 1.7 at 1000 °C.

When CO is added to the feed mixture (case 3, CH_4:CO_2:CO = 0.75:1:0.85), no reaction occurs at temperature below 400 °C as CO_2, CH_4, and CO equilibrium amount remains constant (Figure VI-1 C). Dry reforming starts to occur at temperature higher than 400 °C reaching an H_2:CO ratio of 0.6 at 600 °C and 0.5 at 1000 °C. The amount of H_2O reached at 1000 °C is slightly lower than that in case 1. This might be due to the excess of CO that can play a role in triggering WGS consuming H_2O and CO to form H_2 and CO_2.

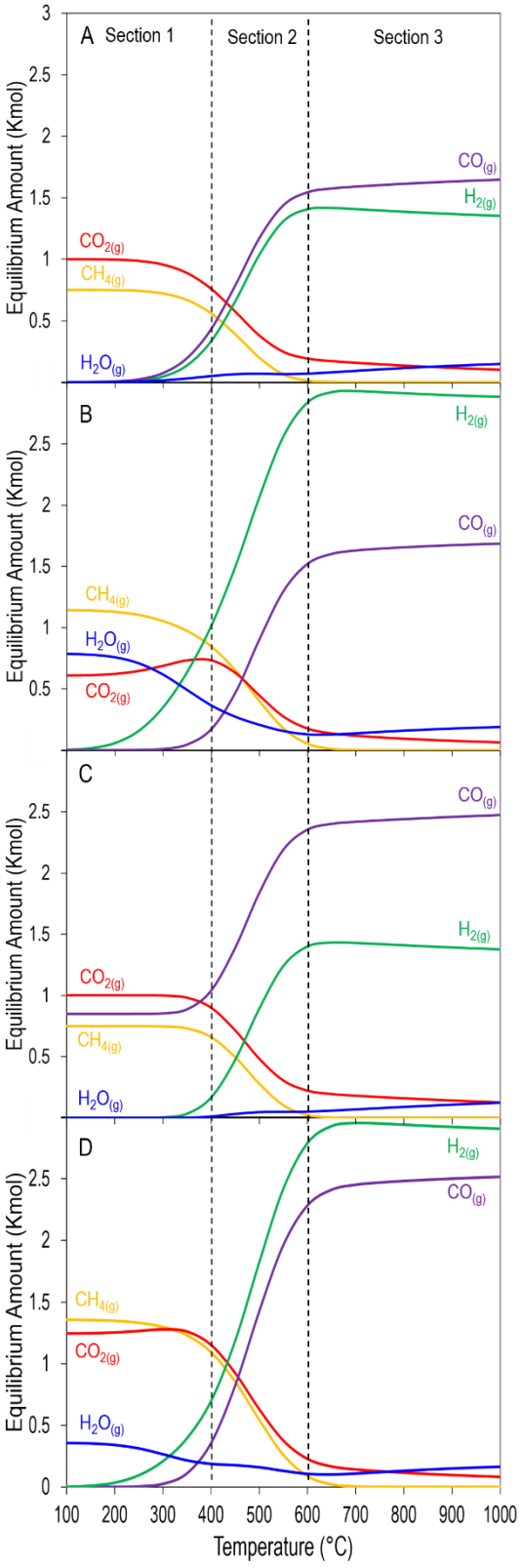

Figure VI-1: Thermodynamic equilibrium curves for DR reactants and products at P= 1 atm excluding carbon from the calculations

Case 4 involves the final pyrolysis product mixture (CH_4:CO_2:H_2:CO = 0.75:1:1.57:0.85), and is presented in Figure VI-1 D. At temperatures lower than 400 °C (section 1), the reactant mixture is more influenced by the presence of H_2 than CO inducing CO_2 methanation reaction. DR starts to occur in section 2 and prevails in section 3 with an inevitable presence of H_2O. In this case, the H_2:CO ratio is 1.2 at 600 °C and 1.15 at 1000 °C.

VI.2.2. Thermodynamic analysis in presence of $C_{(s)}$

Considering carbon as reactant and/or product in the thermodynamic calculations affect the shape of the curves especially in the low temperature region (Figure VI-2). For instance, in the case of CH_4:CO_2 = 0.75:1 (Figure VI-2 A), CO hydrogenation and CO disproportionation are dominant in section 1 and 2. In section 3, the profile becomes similar to the free-carbon case since the aforementioned reactions cannot occur at elevated temperatures.

When H_2 is added in addition to CH_4, and CO_2 (Figure VI-2 B), CO_2 hydrogenation is more common to occur in section 1 increasing the amount of carbon and H_2O, and CO disproportionation along with WGS reaction in section 2.

The presence of CO with CH_4 and CO_2 triggers CO disproportionation and hydrogenation reactions in section 1 and again WGS reaction in section 2 (Figure VI-2 C).

Figure VI-2 D, contains all the feed mixture combining the side reactions seen in the cases of B and C. The inhibition effect of carbon on the main reaction is noticed from the H_2:CO ratio achieved in Table VI-1 for all reactant conditions that are very high. Section 3, the favorable temperature range for reforming reaction, shows similar trend in the 4 cases as the carbon-free

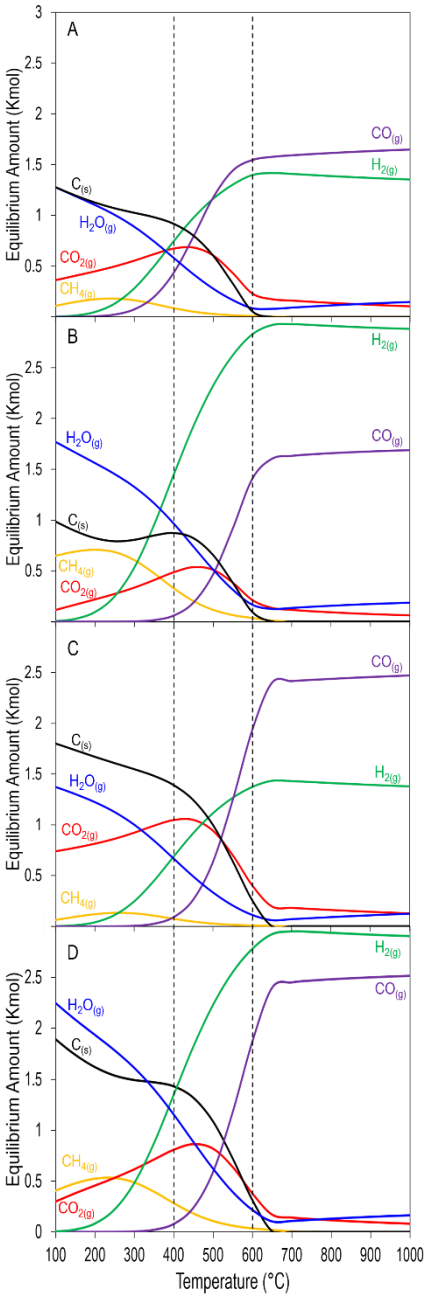

Figure VI-2: Thermodynamic equilibrium curves for DR reactants and products at P= 1 atm including carbon as side product

thermodynamic curves. This is explained by the fact that carbon forming reactions do not occur at elevated temperature above 600 °C which avoid the occurrence of side reactions seen in section 1 and 2. The only possible side reaction producing carbon at such elevated temperature is the CH_4 decomposition. However, it is seen from all the profiles that this reaction does not have an important influence under the reactant conditions applied, since $C_{(s)}$ formation is very little with H_2:CO values (Table VI-1) slightly higher than those of the free-carbon case.

The change in the reactant feed affects the selectivity with different values seen in each case for H_2:CO ratio. The presence of the complex mixture does not cast water production with a possibility of carbon formation making such realistic conditions more challenging than standard ones. The next paragraphs focus on the evaluation of the performances of mesoporous Ni_5-Mg_y-Al_2O_3 catalysts under similar reaction conditions.

VI.3. Catalytic performance of Ni_5-Mg_y-Al_2O_3 mesoporous catalysts

To measure the catalytic test in each reactant mixture case, the total gas hourly space velocity (GHSV) was set at 180 $L.g^{-1}.h^{-1}$. The reactant feed ratio was changed four times to check the influence of each stoichiometric mixture on the catalytic activity. Mesoporous Ni_5-Al_2O_3, Ni_5-Mg_{15}-Al_2O_3, and Ni_5-Mg_{30}-Al_2O_3 catalysts are tested in all feed mixture compositions. The aim is to estimate if these materials could withstand the harsh realistic conditions applied.

VI.3.1. Effect of methane to carbon dioxide ratio

In the case of a feed mixture of CH_4:CO_2 = 0.75:1 (Figure VI-3) CH_4 and CO_2 conversions as well as H_2:CO ratio increase with increasing temperature resembling more the

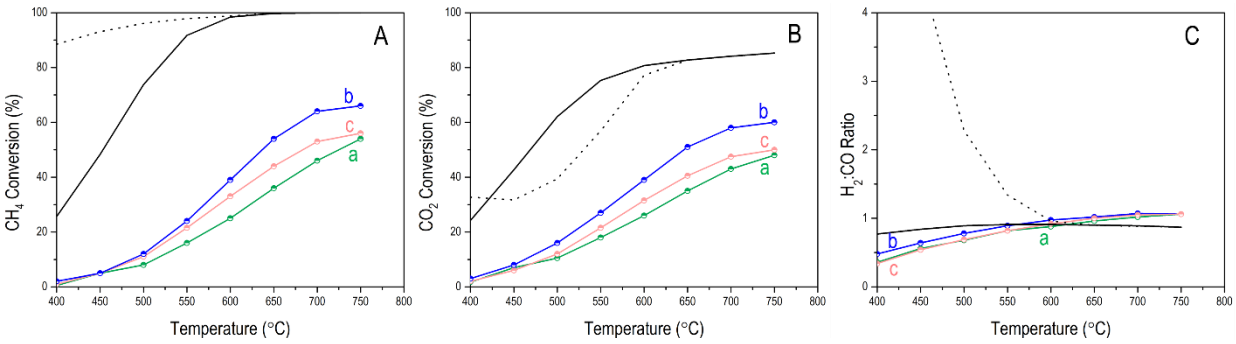

Figure VI-3: (A) CH_4 and (B) CO_2 conversions with (C) H_2:CO ratio as a function of temperature of: (a) Ni_5-Al_2O_3, (b) Ni_5-Mg_{15}-Al_2O_3, and (c) Ni_5-Mg_{30}-Al_2O_3; black line and black dashed line correspond to thermodynamic values without and with $C_{(s)}$; Initial feed mixture: CH_4:CO_2=0.75:1

thermodynamic curve in absence of $C_{(s)}$. This means that the dry reforming operation is done in a free-carbon formation or that the amount of carbon formed is very little. Moreover, the conversions for all catalysts (highest activity for Ni_5-Mg_{15}-Al_2O_3) were enhanced compared to standard dry reforming results (CH_4:CO_2 = 1:1) due to the presence of more CO_2 amount that shifts the reaction towards production of H_2 and CO. The excess of CO_2 also contributed to lower CO_2 conversions than CH_4 because some unreacted CO_2 will be left at the end of reaction. However, this difference between both conversions was not big since CO_2 plays the role of oxidant and could react with C deposits to form CO, but can also be further consumed by favoring the occurrence of RWGS producing more H_2O than the standard case (CH_4:CO_2 = 1:1) [325–327].

VI.3.2. Effect of H_2 addition to CH_4 and CO_2 feed stream

In process of adapting the mixture to the industrial case, hydrogen was added to the feed mixture with a stoichiometric ratio of CH_4:CO_2:H_2=0.75:1:1.57. Figure VI-4 shows the light off curves of the three tested catalysts. Both CH_4 and CO_2 conversions increase with

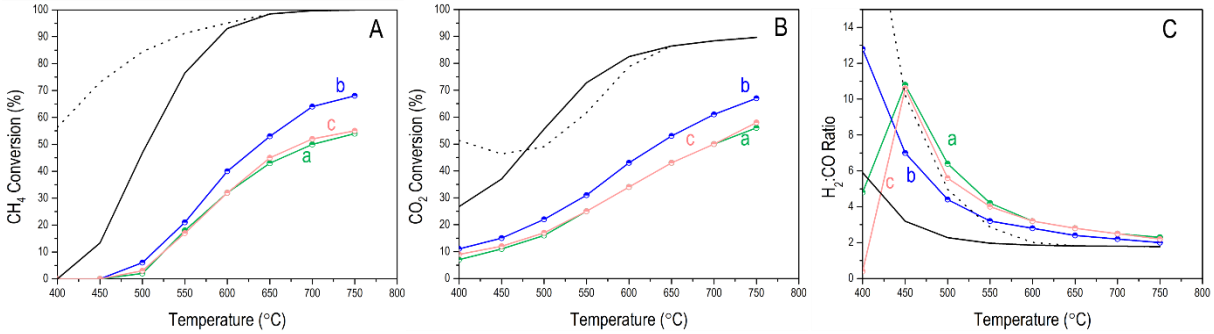

Figure VI-4: (A) CH_4 and (B) CO_2 conversions with (C) H_2:CO ratio as a function of time of: (a) Ni_5-Al_2O_3, (b) Ni_5-Mg_{15}-Al_2O_3, and (c) Ni_5-Mg_{30}-Al_2O_3; black line and black dashed line correspond to thermodynamic values without and with $C_{(s)}$ respectively; Initial feed mixture: CH_4:CO_2:H_2=0.75:1:1.57

temperature (Figure VI-4 A, B), however the CO_2 conversions start at higher values than CH_4 that was always negligible between 400-500 °C. This is due to the presence of H_2 initially in the feed that blocks CH_4 conversion by favoring the CO_2 methanation reaction consuming CO_2 to produce CH_4 and H_2O (hydrogen consumption exceeds the production from hydrocarbon reforming). The main dry reforming reaction dominates then in the high temperature region (550-750 °C) showing consumption of both CH_4 and CO_2 (hydrogen formation from methane balances the oxidation of H_2 by CO_2).

Performing the test over 48 h time on stream (Figure VI-5), all 3 catalysts deactivate slowly through time with the following increasing order of stability: Ni_5-Al_2O_3<Ni_5-Mg_{30}-Al_2O_3<Ni_5-Mg_{15}-Al_2O_3. CO_2 conversion was higher for all catalysts than CH_4 conversion unlike thermodynamics, because the addition of H_2 promotes the RWGS [324], however the H_2:CO ratio did not decrease a lot. This could be due to a competitive side reactions effect

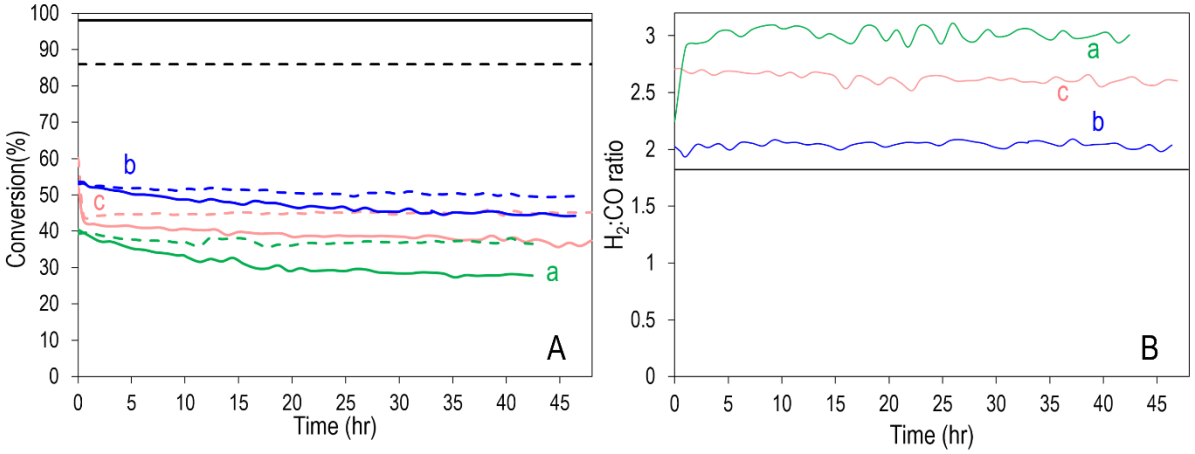

Figure VI-5: (A) CH_4 and (B) CO_2 conversions with (C) H_2:CO ratio as a function of time of: (a) Ni_5-Al_2O_3, (b) Ni_5-Mg_{15}-Al_2O_3, and (c) Ni_5-Mg_{30}-Al_2O_3; black line and black dashed line correspond to thermodynamic values of CH_4 and CO_2 conversions, respectively; Initial feed mixture: CH_4:CO_2:H_2=0.75:1:1.57 (T= 650 °C)

between RWGS and CH_4 decomposition [328]. Moreover, it has been mentioned in other studies [329,330] that the presence of additional amount of H_2 to the reaction can prevent the surface of metal Ni crystallite from deactivation by reacting with carbon deposits formed by CH_4 dissociation. This is true in the case of Ni_5-Mg_{15}-Al_2O_3. The presence of both H_2 and moderate amount of Mg leads to an equilibrium between methane adsorption, dissociation, diffusion and desorption of hydrogen, with CO_2 chemisorption and activation. This equilibrium induces higher CH_4 and CO_2 conversions in Ni_5-Mg_{15}-Al_2O_3 with sustained stability because the carbon formed are removed from two sides reaching a syngas mixture of H_2:CO ratio around 2 close to the expected value.

On the other hand, when higher amount of Mg (Ni_5-Mg_{30}-Al_2O_3) is present, the number of basic sites becomes excessive that the adsorbed CO_2 could cover some of the Ni active sites of the catalyst and desorption from the active sites become difficult due to the strong alkaline sites among the framework of the catalysts. As a result, CH_4 and CO_2 conversions are restrained from further increase, decreasing stability [172]. In Ni_5-Al_2O_3, the presence of an excess of H_2 is not sufficient to cast the carbon formed, and thus it was the least stable acquiring the highest H_2:CO ratio of around 2.8.

VI.3.3. Effect of CO addition to CH_4 and CO_2 feed stream

Adding CO to the reactants blocked the conversion of CH_4 and CO_2 at low temperatures (< 500 °C, Figure VI-6) due to the inhibition of the main dry reforming reaction. Dry reforming of methane is favored at high temperatures contributing to higher values of CH_4 conversions compared to CO_2 conversions since CO_2 is present in excess and will act as an oxidant with a positive effect on CH_4 conversion. H_2 and CO are the major products at high temperatures, but the simultaneous occurrence of the reverse reduction of CO_2 by H_2 (RWGS reaction) and reforming of methane to CO make its production predominant achieving low values of H_2:CO ratios.

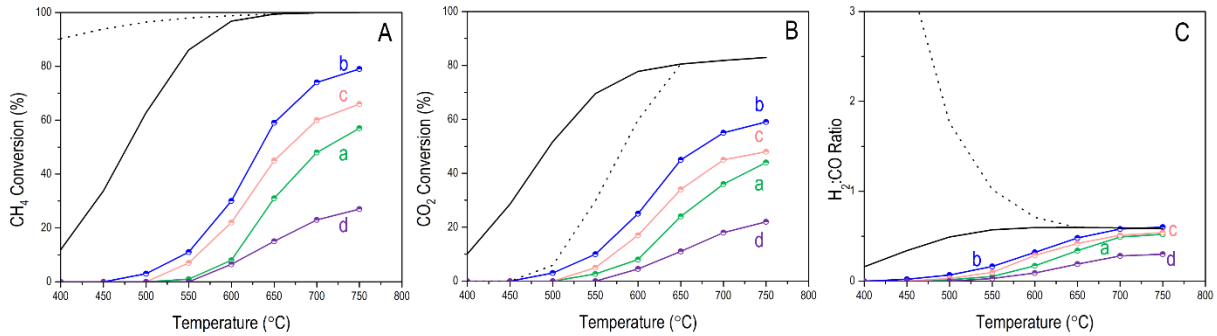

Figure VI-6: (A) CH_4 and (B) CO_2 conversions with (C) H_2:CO ratio as a function of time of: (a) Ni_5-Al_2O_3, (b) Ni_5-Mg_{15}-Al_2O_3, (c) Ni_5-Mg_{30}-Al_2O_3, and Ni_5-Mg_{50}-Al_2O_3; black line and black dashed line correspond to thermodynamic values without and with $C_{(s)}$ respectively; Initial feed mixture: CH_4:CO_2:CO=0.75:1:0.85

As for the stability of the studied materials, Ni_5-Mg_{15}-Al_2O_3 proved again to be the most stable catalyst (Figure VI-7). The higher Mg content catalysts (Ni_5-Mg_{30}-Al_2O_3, Ni_5-Mg_{50}-Al_2O_3) create an excess number of basic sites with more CO_2 adsorbed, leading to occurrence of RWGS producing CO and H_2O and decreasing the H_2:CO ratio.

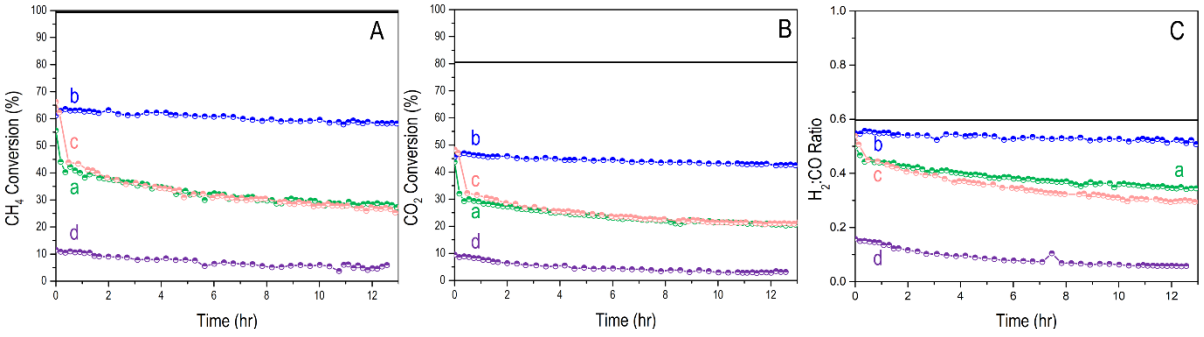

Figure VI-7: (A) CH_4 and (B) CO_2 conversions with (C) H_2:CO ratio as a function of time of: (a) Ni_5-Al_2O_3, (b) Ni_5-Mg_{15}-Al_2O_3, (c) Ni_5-Mg_{30}-Al_2O_3, and Ni_5-Mg_{50}-Al_2O_3; black line corresponds to thermodynamic values without $C_{(s)}$; Initial feed mixture: CH_4:CO_2:CO=0.75:1:0.85 (T= 650 °C)

VI.3.4. Effect of H_2 and CO addition to CH_4 and CO_2 feed stream

The light off curves of a model pyrolysis product mixture are presented in Figure VI-8. The results are somehow a combination of the three previous cases. CO_2 conversions start at lower temperature than that of CH_4 due to the presence of H_2 that stimulates the CO_2 methanation reaction. As the temperature is increased, both conversions are enhanced reflecting the appearance of the main dry reforming of methane reaction. The trend of these conversions resemble the free-carbon thermodynamic curves and the H_2:CO ratio fluctuates around 1.2-1.3.

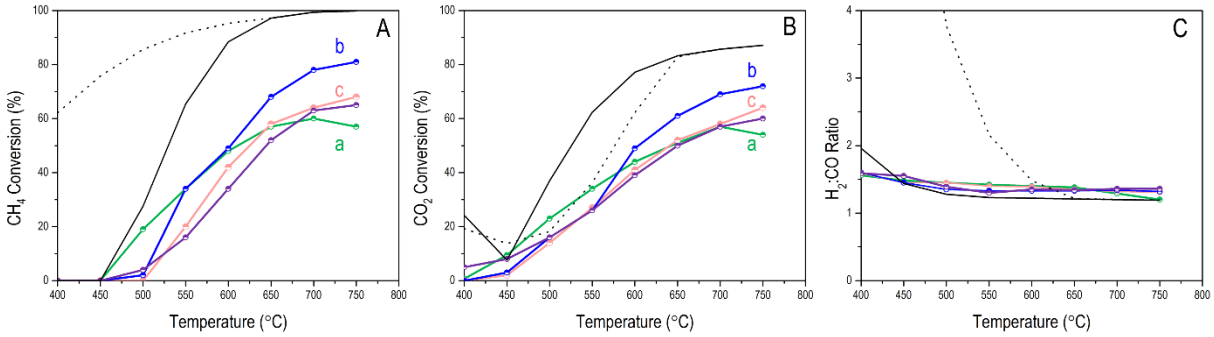

Figure VI-8: (A) CH_4 and (B) CO_2 conversions with (C) H_2:CO ratio as a function of time of: (a) Ni_5-Al_2O_3, (b) Ni_5-Mg_{15}-Al_2O_3, (c) Ni_5-Mg_{30}-Al_2O_3, and Ni_5-Mg_{50}-Al_2O_3; black line and black dashed line correspond to thermodynamic values without and with $C_{(s)}$ respectively; Initial feed mixture: CH_4:CO_2:H_2:CO=0.75:1:1.57:0.85

Concerning the stability of the mesoporous Ni_5-Mg_y-Al_2O_3 materials, Ni_5-Mg_{15}-Al_2O_3 seems to be the most stable with the highest activity through time (Figure VI-9). The other materials face small deactivation (CH_4 conversion loss as follows: 3% in Ni_5-Al_2O_3, 2 % in Ni_5-Mg_{30}-Al_2O_3, and 6% in Ni_5-Mg_{50}-Al_2O_3). This means that the prepared sample (Ni_5-Mg_{15}-

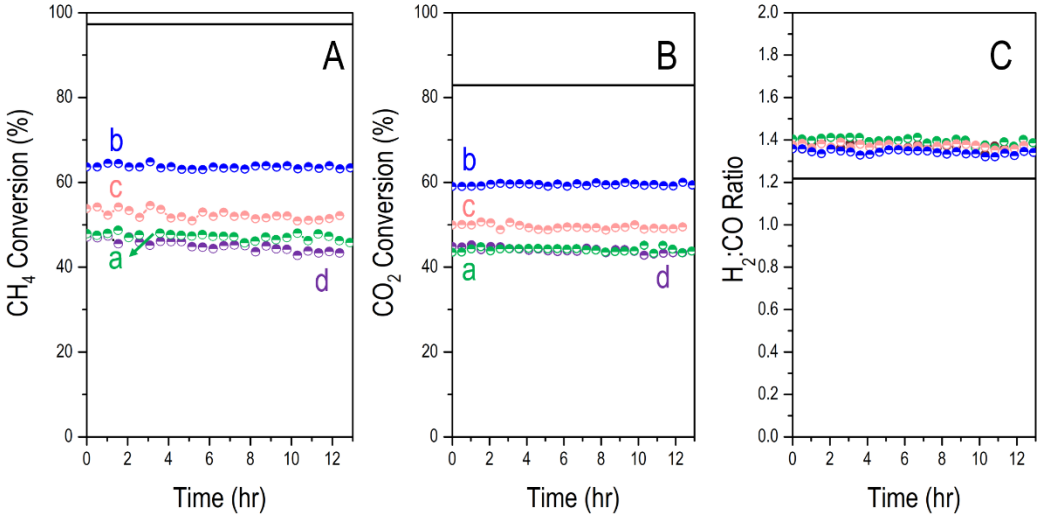

Figure VI-9: (A) CH_4 and (B) CO_2 conversions with (C) H_2:CO ratio as a function of time of: (a) Ni_5-Al_2O_3, (b) Ni_5-Mg_{15}-Al_2O_3, (c) Ni_5-Mg_{30}-Al_2O_3, and (d) Ni_5-Mg_{50}-Al_2O_3; black line corresponds to thermodynamic values without $C_{(s)}$; Initial feed mixture: CH_4:CO_2:H_2:CO=0.75:1:1.57:0.85 (T= 650 °C)

Al_2O_3) is capable to withstand the harsh dry reforming conditions imposed by the complex pyrolysis products. This will be further confirmed by the physicochemical comparison of the spent catalysts presented in the next paragraph.

Spent Ni_5-Al_2O_3, Ni_5-Mg_{15}-Al_2O_3, and Ni_5-Mg_{50}-Al_2O_3 catalysts are characterized by XRD, TEM, TGA and Raman spectroscopy. Regarding TEM microscopy, Figure VI-10 shows that the materials tested are affected to a great extent by the complex dry reforming reaction. Ni_5-Al_2O_3 revealed sintering by showing large particle sizes of nickel and deposition of carbon nanotubes (Figure VI-10 A, A'). The Ni^0 average particle size was increased from 4.5 nm in its reduced state to 11 nm after reforming. Ni_5-Mg_{15}-Al_2O_3 that exhibited the best catalytic performance preserves its textural and structural properties showing no carbon deposition over the support with a small nickel nanoparticles of 4 nm (Figure VI-10 B, B'). Ni_5-Mg_{50}-Al_2O_3 catalyst (Figure VI-10 C, C') does not show carbon nanotubes on its surface, but it faces a high degree of sintering increasing the reduced metallic Ni^0 from 7.7 nm (reduced form) to 15 nm after test. The average Ni^0 particle size of the spent materials were in good trend agreement with XRD measurements with smaller values than those estimated by TEM: 8 nm for Ni_5-Al_2O_3, below detection limit (< 4 nm) for Ni_5-Mg_{15}-Al_2O_3 and 9.3 nm for Ni_5-Mg_{50}-Al_2O_3.

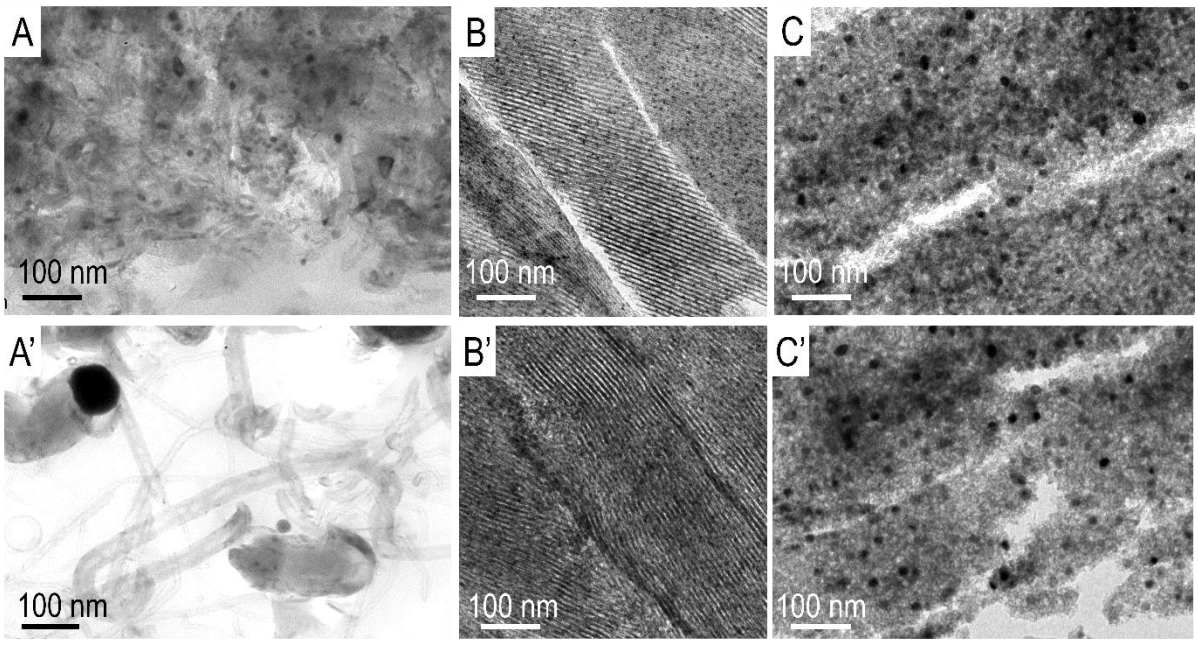

Figure VI-10: TEM images of spent (A, A') Ni_5-Al_2O_3, (B, B') Ni_5-Mg_{15}-Al_2O_3, and (C, C') Ni_5-Mg_{50}-Al_2O_3.

The presence of carbon on spent catalysts is confirmed by TGA analysis as well as to the D and G bands visible by Raman spectroscopy (Figure VI-11). Regarding the TGA analysis,

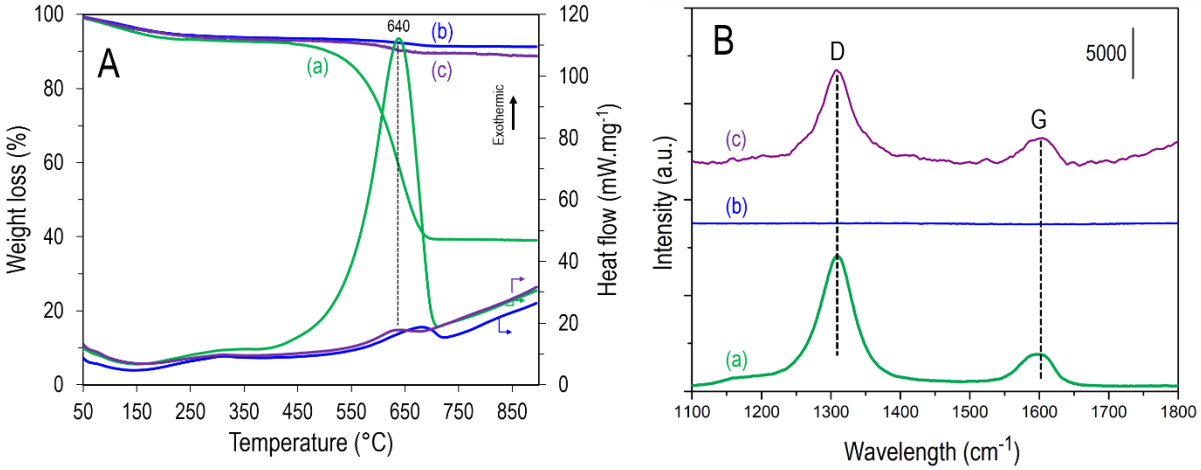

Figure VI-11: (A) TGA profiles (at the top) associated to heat flow signals (at the bottom) and (B) Raman spectroscopy signals of the spent (a) Ni_5-Al_2O_3, (b) Ni_5-Mg_{15}-Al_2O_3, and (c) Ni_5-Mg_{50}-Al_2O_3.

all spent catalysts depict a small decrease in weight (around 9-10 %) at temperatures below 150 °C attributed to desorption of water from the alumina support. An additional loss in weight is noticed at a temperature of 640 °C indicating carbon oxidation with matching exothermic peak. This loss is more important in the case of Ni_5-Al_2O_3 catalyst (40 %) than Ni_5-Mg_{15}-Al_2O_3 (2 %) and Ni_5-Mg_{50}-Al_2O_3 (6 %). As for the Raman spectroscopy, the two main bands (D and G) are typical of the doubly degenerated phonon mode of C atoms in the sp2 carbon networks with high degree of symmetry and of order (graphitic carbon, G-band, 1600 cm^{-1}), and of a disordered structural mode of carbon species (D-band, 1300 cm^{-1}). The intensity ratio between these two bands can be used as an indicator of the crystalline degree and of the presence of defects in the carbon species; the smaller the ratio (<1) the higher the structural order. Here, both Ni_5-Al_2O_3 and Ni_5-Mg_{50}-Al_2O_3 have a ratio significantly higher than 1 (4.77 and 4.15 respectively) which indicates the disordered character of the carbon deposits, in line with the occurrence of carbon nanotubes observed on Ni_5-Al_2O_3 by electron microscopy. Note that the intensities of the two bands are higher in Ni_5-Al_2O_3 than in Ni_5-Mg_{50}-Al_2O_3 in good agreement with TGA results. The absence of any band in Ni_5-Mg_{15}-Al_2O_3 confirms the absence or the presence of a negligible amount of carbon nanotubes not detectible by Raman spectroscopy contributing to a fluorescence background.

VI.4. Conclusion

As a conclusion of this chapter, it is evident that alteration of the initial DR feed mixture influences the products behavior and the selectivity of the reaction. Briefly, a CH_4:CO_2 ratio of 0.75:1 has a positive effect on the reaction due to CH_4 present as limiting reactant, and thus the

more CO_2 available helps in oxidizing carbon formed during reaction. Adding H_2 to the feed blocks CH_4 conversions at low temperatures to direct CO_2 methanation instead. In such condition, DR is dominated at elevated temperatures, but the presence of high H_2 amount shows occurrence of RWGS. The H_2:CO ratio achieved in this case was around 2. When CO is initially added to CO_2 and CH_4 no side reaction takes place at low reaction temperatures (<400 °C), but its presence retards conversions of CH_4 and CO_2 for DRM. The selectivity achieved in this case is as low as H_2:CO of 0.5. The complex model mixture (CH_4, CO_2, H_2, CO) is a combination of the above mentioned mixtures with a selectivity of H_2:CO of 1.3.

Results also revealed that Ni_5-Mg_{15}-Al_2O_3, similar to the case of standard dry reforming of methane (CH_4:CO_2 = 1:1), had the best catalytic performance among all the other tested materials. This confirms the importance of high order mesoporous structure and the presence of an optimum amount of basic modifier to highly disperse nickel particles restricting sintering and carbon formation. Thus, Ni_5-Mg_{15}-Al_2O_3 proved to be a good candidate in reforming of complex and realistic mixtures with a great stability for a long period of time (50 hrs).

General conclusion and perspectives

Despite the enormous studies tackled on dry reforming of methane reaction, this reaction still faces obstructions regarding the utilized catalysts. The problems encountered are mainly related to the sintering of nickel active sites or/and to the formation of carbon species deactivating the catalyst and hindering DRM reaction.

In this work, stable and selective Ni-based alumina material were designed by taking into consideration different key factors: 1) Simultaneous addition of Ni precursors within the synthesis of Al_2O_3 support, 2) mutation in the shape of the alumina support for better trapping and confinement of nickel nanoparticles inside the support structure (pores/walls) preventing sintering, and 3) modification of the material basicity by adding MgO as a basic dopant to enhance reactivity by annealing coke deposition

First, Ni_5-Mg_y-Al_2O_3 ordered mesoporous catalysts were synthesized combining the three aforementioned approaches. Mg loading was varied between 0 and 26 wt%. Ni_5-Mg_{15}-Al_2O_3 with intermediate Mg content (7 wt%) has the best catalytic performances with as superior activity and stability among all the other Mg amounts. This was explained by several combined features: i) the high, homogenous and simultaneous dispersion of both Ni and Mg species, ii) the high surface area and ordered channels for Al_2O_3 support and iii) the enhancement of material basicity that accelerates CO_2 chemisorption reducing the activation energy. Further increment of Mg loading (15-26 wt%) has negative catalytic response due to a strong MgO segregation in the material that disturbs the structure and pores ordering, and strongly affects Ni dispersion.

Second, and inspired by approaches one and two, a deep explanation was given about the benefit of using metal-organic framework (MIL-53(Al)) as a sacrificial nickel precursor host to highly disperse nickel nanoparticles within a porous γ-Al_2O_3 lamellar phase. Indeed, Ni_5-$Al_2O_{3\ MIL\text{-}53}$ synthesized by impregnation of Ni on the MOF prior to calcination resulted in high surface area, with superior dispersion and uniformity of nickel nanoparticles leading to high activity, selectivity and stability in DRM. Under similar test conditions, this new material was even better than $Ni_5@Al_2O_{3\ MIL\text{-}53}$ and traditional $Ni_5@Al_2O_{3\ COM}$ prepared by conventional nickel impregnation over preformed alumina supports that acquired larger nickel nanoparticles with eventually lower dispersion.

Third, the application of Ni_5-Mg_y-Al_2O_3 and Ni_x-$Al_2O_{3\ MIL\text{-}53}$ catalysts was extended to CO_2 methanation reaction where their behavior was as outstanding as in dry reforming of methane. This proves the efficiency of these materials to be applied in versatile energy applications ranging from low to high reaction temperatures. Ni_5-Mg_y-Al_2O_3 catalyst (Ni_5-Mg_{15}-Al_2O_3 specifically) showed also good resistance in dry reforming of pyrolysis gaseous products towards sintering and carbon formation. This further highlights on the capability of the synthesized materials to withstand and operate in realistic conditions.

As for the perspectives, starting first with the materials synthesis, it could be a good idea to work on following same strategies but with cheaper and more "eco-friendly" templates. In the case of one-pot mesoporous Ni_x-Mg_y-Al_2O_3 P123 commercial organic surfactant was used and is applied commonly to many mesoporous materials of Al_2O_3 and silica. But it was recently revealed to have poor biodegradability and toxic to several biological organisms at high concentrations in addition to its high relative cost. The trend should be towards using more environmentally friendly surfactants derived from renewable sources. For instance, chitosan polymers, derived from the shell of crustaceans such as shrimps and crabs, can be used. A basic trials on using such template in the following thesis was tried but it yielded to poorly ordered mesoporouss material. So the parameters of synthesis are suggested to be optimized. In the MOF case for example, the terephtalic acid used in the synthesis produce can be obtained from PET (polyethylene terephthalate) that is an industrially important waste stream and consists of more than 85% of terephtalic acid. Moreover, PET hydrolysis can be achieved at 200 °C in water, which is close to the synthesis conditions of MIL-53(Al). This idea took a part in my PhD work (training of an Italian masters student as internship in the frame of SOL-CARE project) where MIL-53(Al) was successfully synthesized by in-situ/ex-situ generation of linkers from PET hydrolysis. The obtained MIL-53(Al) followed later the same strategy as the seen samples and was impregnated with Ni and calcined.

For industrial application, even though the catalysts used in this work showed very good activity and stability, they need to be further tested at high pressures and for longer period of time (more than two weeks). It is also important to obtain kinetic and mechanistic information to design any reactor and predict products flow rate of the scaled-up operation. A fair part of the kinetics and mechanistic aspects are exploited on mesoporous Ni_5-Al_2O_3 catalyst but they still need to be optimized and applied on the other materials for comparison.

Appendix

Table: Recent development in the synthesis of Ni-Al_2O_3 catalysts in DRM

Ref.	Ni amount (wt%)	Type of Al_2O_3	Ni insertion	Ni (nm)	Ni^s (nm)	Test conditions	$X(CH_4)_i$	$X(CO_2)_i$	$X(CH_4)_f$	$X(CO_2)_f$	H_2:CO	Deactivation reason
[71]	26	Commercial α	W.I.	n.m.	n.m.	n.m.	n.m.	n.m.	n.m.	n.m.	n.m.	Filamentous $C_{(s)}$
[73]	20	Commercial	W.I.	n.m.	n.m.	Fixed bed (h:400 mm, d=14mm),750 °C, 9 h	45	n.m.	25	n.m.	n.m.	$C_{(s)}$
[74]	15	Commercial	W.I.	n.m.	n.m.	Tubular U-shaped, 300 mg, 650 °C, 10 h, 45 $L.g^{-1}.h^{-1}$	40	50	30	45	n.m.	$C_{(s)}$
[75]	26	Commercial α	I.W.I.	n.m.	n.m.	Tubular U-shaped	n.m.	n.m.	n.m.	n.m.	n.m.	n.m.
[64]	10	Commercial	I.W.I.	4	n.m.	Fixed bed (d:9 mm), 200 mg, 800°C, 50h, 48 $L.g^{-1}.h^{-1}$	80	85	50	65	0.8	$C_{(s)}$
[72]	8	Commercial γ	EDF	12	n.m.	Fixed bed, 750 °C, 120 $L.g^{-1}.h^{-1}$	14.5	32	n.m.	n.m.	0.4	$C_{(s)}$
[76]	10	Commercial	electrospinning	6.5	n.m.	Fixed bed (d:8 mm), 100 mg, 700 °C, 300 min, 48 $L.g^{-1}.h^{-1}$	55	82	50	80	0.8	$C_{(s)}$
[77]	12	Al precursor	EISA	15	n.m.	Fixed bed, 50 mg, , 800 °C, 80 h, 72 $L.g^{-1}.h^{-1}$	90	90	88	88	n.m.	$C_{(s)}$
[78]	20	Al precursor	aerogel	9	20	Quartz, (d:18 mm), 200 mg, 800 °C, 30 h	95	95	90	90	n.m.	Amorphous $C_{(s)}$ and S
[79]	10	Al precursor	combustion	4.6	16.8	Fixed bed, 100 mg, 700 °C, 24 h	40	52	35	47	n.m.	Whiskers $C_{(s)}$ and S
[80]	10	Meso-Al_2O_3	One-pot	11	15	Fixed bed, 100 mg, , 800 °C, 500 min, 52 $L.g^{-1}.h^{-1}$	62	75	52	62	0.78	Nanotubes $C_{(s)}$
[81]	10	Al precursor	2-step hydrothermal	7	n.m.	100 mg, , 800 °C, 50 h, 21 $L.g^{-1}.h^{-1}$	95	90	95	90	0.92	Amorphous $C_{(s)}$
[83]	35	γ nanoflakes	Hydrothermal	5.5	8.5	Fixed bed quartz, 100 mg, , 800 °C, 50 h	82	n.m.	80	n.m.	0.90	Nanotubes $C_{(s)}$
[84]	10	Nanosheets γ	I.W.I.	6.7	7	Quartz (d=8mm), 100 mg, 700 °C, 300 min, 48 $L.g^{-1}.h^{-1}$	55	n.m.	55	n.m.	n.m.	-
[86]	10	Nanosheets	Hydrothermal	12	14	Quartz (d=8mm), 100 mg, 800 °C, 100 h, 108 $L.g^{-1}.h^{-1}$	95	94	90	92	0.95	35% $C_{(s)}$
[87]	5	Meso-Al_2O_3	Hydrolysis deposition	5.5	20	Fixed bed s.s.(d= 6 mm), 500 mg, , 800 °C, 10 h, 14.4 $L.g^{-1}.h^{-1}$	92	97	90	92	0.85	$C_{(s)}$ and S
[88]	10	Al precursor	I.W.I.	14	15	Fixed bed Quartz (d=8mm), 100 mg, 700 °C, 100 h, 15$L.g^{-1}.h^{-1}$	80	80	78	78	0.8	Graphitic $C_{(s)}$

References

[1] S. Shafiee, E. Topal, When will fossil fuel reserves be diminished?, Energy Policy. 37 (2009) 181–189.

[2] B. Petroleum, BP statistical review of world energy, 2018.

[3] N. Abas, A. Kalair, N. Khan, Review of fossil fuels and future energy technologies, Futures. 69 (2015) 31–49.

[4] A.C. Marques, J.A. Fuinhas, D.A. Pereira, Have fossil fuels been substituted by renewables? An empirical assessment for 10 European countries, Energy Policy. 116 (2018) 257–265.

[5] OPEC, 2017 OPEC World Oil Outlook, 2017.

[6] X.Y. Wei, Z.M. Zong, X. Fan, Z.K. Li, Coal-based products and their uses, Coal Prod. Process. Technol. (2015) 383–412.

[7] J. Lavoie, F.G. Labiano, Review on dry reforming of methane , a potentially more environmentally-friendly approach to the increasing natural gas exploitation, Front. Chem. 2 (2014) 1–17.

[8] A. Demirbas, The importance of natural gas as a World fuel, Energy Sources, Part B Econ. Plan. Policy. 1 (2006) 413–420.

[9] V. Esen, B. Oral, Natural gas reserve/production ratio in Russia, Iran, Qatar and Turkmenistan: A political and economic perspective, Energy Policy. 93 (2016) 101–109.

[10] M. Mathur, The carbon climax:End of hydrocarbon legacy-A decade of metamorphosis and rapid change, n.d.

[11] IEA, IEA, 2019. Short Term Energy Outlook. Organization for Economic cooperation and development, International energy agency, Paris and Washington Dc, (n.d.).

[12] T. Peebles, Development of Hubbert's Peak Oil Theory and Analysis of its Continued Validity for U.S. Crude Oil Production, 2017.

[13] K.S. Deffeyes, Hubbert's peak: the impending world oil shortage (New Edition), Princeton University Press, 2008.

[14] U. Oemar, Y. Kathiraser, M.L. Ang, K. Hidajat, S. Kawi, Catalytic Biomass Gasification to Syngas over Highly Dispersed Lanthanum-Doped Nickel on SBA-15, ChemCatChem. 7 (2015) 3376–3385.

[15] P. Riemer, Green house gas mitigation technologies, an overview of the CO2 capture, storage and future activities of the IEA Greenhouse Gas R&D programme, Energy Convers. Manag. 37 (1996) 665–670.

[16] I.P. on C.C. (IPCC), Carbon Dioxide Emissions Factor, Kg CO2 per MWh, (n.d.).

[17] M.A. Scibioh, B. Viswanathan, CO 2 Conversion—Relevance and Importance, Carbon Dioxide to Chem. Fuels. (2018) 1–22.

[18] K.L. Smith, J. Wiley, United States Patent (19 FIG-2, (1994).

[19] K.C.C. G.G. Liversidge J.F. Bishop, D.A. Czekai, United States Patent (19) 54, 96 (1980) 62–66.

[20] S.B. Idso, K.E. Idso, Effects of atmospheric CO2 enrichment on plant constituents related to animal and human health, Environ. Exp. Bot. 45 (2001) 179–199.

[21] L.H. Ziska, P.R. Epstein, W.H. Schlesinger, Rising CO2, climate change, and public health: Exploring the links to plant biology, Environ. Health Perspect. 117 (2009) 155–158.

[22] B. Elberling, J. Søndergaard, L.A. Jensen, L.B. Schmidt, B.U. Hansen, G. Asmund, T. Balić-Zunić, J. Hollesen, S. Hanson, P.E. Jansson, T. Friborg, Arctic vegetation damage by winter-generated coal mining pollution released upon thawing, Environ. Sci. Technol. 41 (2007) 2407–2413.

[23] G. Independent, E. Analyst, 4 The Importance of Methane, (2013) 1–6.

[24] B. DESSUS, Global Warming: the Significance of Methane, Unpubl. (2008) 1–7. http://global-chance.org/IMG/pdf/CH4march2008.pdf.

[25] T. Real, B. Line, N. Goal, W. Being, I. Hand, P. Education, Part 7, 91 (2014).

[26] N. Myers, Tropical Deforestation and Climatic Change, 2009.

[27] U.S.E.P. Agency, Overview of greenhouse gases, (n.d.).

[28] G. Centi, E.A. Quadrelli, S. Perathoner, Catalysis for CO2 conversion: A key technology for rapid introduction of renewable energy in the value chain of chemical industries, Energy Environ. Sci. 6 (2013) 1711–1731.

[29] N. Kumar, M. Shojaee, J.J. Spivey, Catalytic bi-reforming of methane: From greenhouse gases to syngas, Curr. Opin. Chem. Eng. 9 (2015) 8–15.

[30] S. Kawi, Y. Kathiraser, J. Ni, U. Oemar, Z. Li, E.T. Saw, Progress in Synthesis of Highly Active and Stable Nickel-Based Catalysts for Carbon Dioxide Reforming of Methane, ChemSusChem. 8 (2015) 3556–3575.

[31] R. Rauch, J. Hrbek, H. Hofbauer, Biomass Gasification for Synthesis Gas Production and Applications of the Syngas, Adv. Bioenergy Sustain. Chall. 3 (2015) 73–91.

[32] C.J. Liu, J. Ye, J. Jiang, Y. Pan, Progresses in the preparation of coke resistant Ni-based catalyst for steam and CO 2 reforming of methane, ChemCatChem. 3 (2011) 529–541.

[33] B. Abdullah, N.A. Abd Ghani, D.V.N. Vo, Recent advances in dry reforming of methane over Ni-based catalysts, J. Clean. Prod. 162 (2017) 170–185.

[34] M. Lyubovsky, S. Roychoudhury, R. LaPierre, Catalytic partial “oxidation of methane to syngas” at elevated pressures, Catal. Letters. 99 (2005) 113–117.

[35] K. Supat, K. Supat, S. Chavadej, S. Chavadej, L.L. Lobban, L.L. Lobban, R.G. Mallinson, R.G. Mallinson, Combined Steam Reforming and Partial Oxidation of Methane to Synthesis Gas under Electrical Discharge, Ind. Eng. Chem. (Analytical Ed. (2003) 1654–1661.

[36] R. Dębek, M. Motak, T. Grzybek, M. Galvez, P. Da Costa, A Short Review on the Catalytic Activity of Hydrotalcite-Derived Materials for Dry Reforming of Methane, Catalysts. 7 (2017)

32.

[37] Z. Bian, S. Das, M.H. Wai, P. Hongmanorom, S. Kawi, A Review on Bimetallic Nickel-Based Catalysts for CO 2 Reforming of Methane, ChemPhysChem. 18 (2017) 3117–3134.

[38] G.A. Olah, A. Goeppert, M. Czaun, T. Mathew, R.B. May, G.K.S. Prakash, Single Step Bi-reforming and Oxidative Bi-reforming of Methane (Natural Gas) with Steam and Carbon Dioxide to Metgas (CO-2H<inf>2</inf>) for Methanol Synthesis: Self-Sufficient Effective and Exclusive Oxygenation of Methane to Methanol with Oxygen, J. Am. Chem. Soc. 137 (2015) 8720–8729.

[39] M.K. Nikoo, N.A.S. Amin, Thermodynamic analysis of carbon dioxide reforming of methane in view of solid carbon formation, Fuel Process. Technol. 92 (2011) 678–691.

[40] A.E. Castro Luna, M.E. Iriarte, Carbon dioxide reforming of methane over a metal modified Ni-Al2O3 catalyst, Appl. Catal. A Gen. 343 (2008) 10–15.

[41] N.A.K. Aramouni, J.G. Touma, B.A. Tarboush, J. Zeaiter, M.N. Ahmad, Catalyst design for dry reforming of methane: Analysis review, Renew. Sustain. Energy Rev. 82 (2018) 2570–2585.

[42] W.J. Jang, J.O. Shim, H.M. Kim, S.Y. Yoo, H.S. Roh, A review on dry reforming of methane in aspect of catalytic properties, Catal. Today. (2018) 0–1.

[43] G. Zhang, J. Liu, Y. Xu, Y. Sun, A review of CH4–CO2 reforming to synthesis gas over Ni-based catalysts in recent years (2010–2017), Int. J. Hydrogen Energy. 43 (2018) 15030–15054.

[44] S. Singh, R. Kumar, H.D. Setiabudi, S. Nanda, D.V.N. Vo, Advanced synthesis strategies of mesoporous SBA-15 supported catalysts for catalytic reforming applications: A state-of-the-art review, Appl. Catal. A Gen. 559 (2018) 57–74.

[45] H. Seo, Recent Scientific Progress on Developing Supported Ni Catalysts for Dry (CO2) Reforming of Methane, Catalysts. 8 (2018) 110.

[46] D. Pakhare, J. Spivey, A review of dry (CO2) reforming of methane over noble metal catalysts, Chem. Soc. Rev. 43 (2014) 7813–7837.

[47] I. V. Yentekakis, G. Goula, M. Hatzisymeon, I. Betsi-Argyropoulou, G. Botzolaki, K. Kousi, D.I. Kondarides, M.J. Taylor, C.M.A. Parlett, A. Osatiashtiani, G. Kyriakou, J.P. Holgado, R.M. Lambert, Effect of support oxygen storage capacity on the catalytic performance of Rh nanoparticles for CO2 reforming of methane, Appl. Catal. B Environ. 243 (2019) 490–501.

[48] S.C.P. Maina, A.D. Ballarini, J.I. Vilella, S.R. de Miguel, Study of the performance and stability in the dry reforming of methane of doped alumina supported iridium catalysts, Catal. Today. (2018) 1–14.

[49] C. Fernández, N. Miranda, X. García, P. Eloy, P. Ruiz, A. Gordon, R. Jiménez, Insights into dynamic surface processes occurring in Rh supported on Zr-grafted γ-Al2O3 during dry reforming of methane, Appl. Catal. B Environ. 156–157 (2014) 202–212.

[50] M. Ocsachoque, J. Bengoa, D. Gazzoli, M.G. González, Role of CeO2 in Rh/α-Al2O3

Catalysts for CO2 Reforming of Methane, Catal. Letters. 141 (2011) 1643–1650.

[51] A. Ballarini, F. Basile, P. Benito, I. Bersani, G. Fornasari, S. De Miguel, S.C.P. Maina, J. Vilella, A. Vaccari, O.A. Scelza, Platinum supported on alkaline and alkaline earth metal-doped alumina as catalysts for dry reforming and partial oxidation of methane, Appl. Catal. A Gen. 433–434 (2012) 1–11.

[52] M. Ghelamallah, P. Granger, Impact of barium and lanthanum incorporation to supported Pt and Rh on α-Al 2O 3 in the dry reforming of methane, Fuel. 97 (2012) 269–276.

[53] C. Shi, P. Zhang, Role of MgO over γ-Al2O3-supported Pd catalysts for carbon dioxide reforming of methane, Appl. Catal. B Environ. 170–171 (2015) 43–52.

[54] M. A. Álvarez, L.F. Bobadilla, V. Garcilaso, M.A. Centeno, J.A. Odriozola, CO2 reforming of methane over Ni-Ru supported catalysts: On the nature of active sites by operando DRIFTS study, J. CO2 Util. 24 (2018) 509–515.

[55] J.H. Park, S. Yeo, T.J. Kang, I. Heo, K.Y. Lee, T.S. Chang, Enhanced stability of Co catalysts supported on phosphorus-modified Al2O3 for dry reforming of CH4, Fuel. 212 (2018) 77–87.

[56] Horváth, K. Baán, E. Varga, A. Oszkó, Vágó, M. Törő, A. Erdőhelyi, Dry reforming of CH4on Co/Al2O3catalysts reduced at different temperatures, Catal. Today. 281 (2017) 233–240.

[57] P. Li, J. Li, Q. Zhu, L. Cui, H. Li, Effect of granulation on the activity and stability of a Co-Al 2O3 aerogel catalyst in a fluidized-bed reactor for CH4-CO2 reforming, RSC Adv. 3 (2013) 8939–8946.

[58] S. Zeng, L. Zhang, X. Zhang, Y. Wang, H. Pan, H. Su, Modification effect of natural mixed rare earths on Co/γ-Al 2O 3 catalysts for CH 4/CO 2 reforming to synthesis gas, Int. J. Hydrogen Energy. 37 (2012) 9994–10001.

[59] J.H. Park, S. Yeo, T.S. Chang, Effect of supports on the performance of Co-based catalysts in methane dry reforming, J. CO2 Util. 26 (2018) 465–475.

[60] H.Y. Wang, E. Ruckenstein, Carbon dioxide reforming of methane to synthesis gas over supported rhodium catalysts: The effect of support, Appl. Catal. A Gen. 204 (2000) 143–152.

[61] S. Yokota, K. Okumura, M. Niwa, Support effect of metal oxide on Rh catalysts in the CH4-CO2reforming reaction, Catal. Letters. 84 (2002) 131–133.

[62] E. Ruckenstein, Y.H. Hu, Role of support in CO2 reforming of CH4 to syngas over Ni catalysts, J. Catal. 162 (1996) 230–238.

[63] Z. Rong-Jun, X. Guo-fu, L. Ming-Feng, N. Hong, L. Da-Dong, Effect of support on the performance of Ni-based catalyst in dry reforming, J. Fuel Chem. Technol. 43 (2015) 1359–1365.

[64] Y. Xu, X. Du, J. Li, P. Wang, J. Zhu, F. Ge, J. Zhou, M. Song, W. Zhu, A comparison of Al2O3 and SiO2 supported Ni-based catalysts in their performance for the dry reforming of methane, J. Fuel Chem. Technol. 47 (2019) 199–208.

[65] K. Jabbour, N. El Hassan, A. Davidson, S. Casale, P. Massiani, Factors affecting the long-term

stability of mesoporous nickel-based catalysts in combined steam and dry reforming of methane, Catal. Sci. Technol. 6 (2016) 4616–4631.

[66] M. Argyle, C. Bartholomew, Heterogeneous Catalyst Deactivation and Regeneration: A Review, Catalysts. 5 (2015) 145–269.

[67] J. Rostrup-Nielsen, L.J. Christiansen, Concepts in syngas manufacture, Imperial college press, London, 2011.

[68] X. Chen, A.R. Tadd, J.W. Schwank, Carbon deposited on Ni/Ce{single bond}Zr{single bond}O isooctane autothermal reforming catalysts, J. Catal. 251 (2007) 374–387.

[69] J. Guo, H. Lou, X. Zheng, The deposition of coke from methane on a Ni/MgAl2O4 catalyst, Carbon N. Y. 45 (2007) 1314–1321.

[70] J.Z. Luo, Z.L. Yu, C.F. Ng, C.T. Au, CO2/CH4 Reforming over Ni–La2O3/5A: An Investigation on Carbon Deposition and Reaction Steps, J. Catal. 194 (2000) 198–210.

[71] A.R. McFarlane, I.P. Silverwood, R. Warringham, E.L. Norris, R.M. Ormerod, C.D. Frost, S.F. Parker, D. Lennon, The application of inelastic neutron scattering to investigate the “dry” reforming of methane over an alumina-supported nickel catalyst operating under conditions where filamentous carbon formation is prevalent, RSC Adv. 3 (2013) 16577–16589.

[72] M.A. Goula, N.D. Charisiou, K.N. Papageridis, A. Delimitis, E. Pachatouridou, E.F. Iliopoulou, Nickel on alumina catalysts for the production of hydrogen rich mixtures via the biogas dry reforming reaction: Influence of the synthesis method, Int. J. Hydrogen Energy. 40 (2015) 9183–9200.

[73] M. Fu, W. Qi, Q. Xu, S. Zhang, Y. Yan, Hydrogen production from bio-oil model compounds dry (CO 2) reforming over Ni/Al 2 O 3 catalyst, Int. J. Hydrogen Energy. 41 (2016) 1494–1501.

[74] C.A. Schwengber, F.A. Da Silva, R.A. Schaffner, N.R.C. Fernandes-Machado, R.J. Ferracin, V.R. Bach, H.J. Alves, Methane dry reforming using Ni/Al2O3 catalysts: Evaluation of the effects of temperature, space velocity and reaction time, J. Environ. Chem. Eng. 4 (2016) 3688–3695.

[75] I.P. Silverwood, N.G. Hamilton, J.Z. Staniforth, C.J. Laycock, S.F. Parker, R.M. Ormerod, D. Lennon, Persistent species formed during the carbon dioxide reforming of methane over a nickel-alumina catalyst, Catal. Today. 155 (2010) 319–325.

[76] L. Liu, S. Wang, Y. Guo, B. Wang, P. Rukundo, S. Wen, Z. jun Wang, Synthesis of a highly dispersed Ni/Al 2 O 3 catalyst with enhanced catalytic performance for CO 2 reforming of methane by an electrospinning method, Int. J. Hydrogen Energy. 41 (2016) 17361–17369.

[77] X. Wang, C. Peng, H. Peng, W. Liu, X. Xu, X. Wang, C. Li, W. Zhou, Methane Dry Reforming over Coke-Resistant Mesoporous Ni-Al2O3 Catalysts Prepared by Methane Dry Reforming over Coke-Resistant Mesoporous Ni-Al 2 O 3 Catalysts Prepared by Evaporation-Induced Self- Assembly Method, ChemCatChem. 7 (2016) 3753–3762.

[78] Z. Jiang, X. Liao, Y. Zhao, Comparative study of the dry reforming of methane on fluidised aerogel and xerogel Ni / Al 2 O 3 catalysts, App. Petrochem Res. 3 (2013) 91–99.

[79] Y.S. Noh, E.-H. Yang, S.S. Lim, K.-Y. Lee, S.W. Kim, D.J. Moon, Nickel Supported on Mesoporous Alumina for Dry Reforming of Methane: Combustion Method, J. Nanosci. Nanotechnol. 17 (2017) 2545–2549.

[80] J. Newnham, K. Mantri, M.H. Amin, J. Tardio, S.K. Bhargava, Highly stable and active Ni-mesoporous alumina catalysts for dry reforming of methane, Int. J. Hydrogen Energy. 37 (2012) 1454–1464.

[81] L. Zhang, Y. Zhang, An active and stable Ni/Al2O3 nanosheet catalyst for dry reforming of CH4, RSC Adv. 5 (2015) 62173–62178.

[82] N. Wang, Z. Xu, J. Deng, K. Shen, X. Yu, W. Qian, One-pot Synthesis of Ordered Mesoporous NiCeAl Oxide Catalysts and a Study of Their Performance in Methane Dry Reforming, ChemCatChem. 6 (2014) 1470–1480.

[83] Q. Zhang, T. Wu, P. Zhang, R. Qi, R. Huang, X. Song, L. Gao, Facile synthesis of hollow hierarchical Ni/γ-Al2O3 nanocomposites for methane dry reforming catalysis, RSC Adv. 4 (2014) 51184–51193.

[84] J. Sun, S. Wang, Y. Guo, M. Li, H. Zou, Z. jun Wang, Carbon dioxide reforming of methane over nanostructured Ni/Al2O3 catalysts, Catal. Commun. 104 (2018) 53–56.

[85] P. Littlewood, S. Liu, E. Weitz, T.J. Marks, P.C. Stair, Ni-Alumina Dry Reforming Catalysts: Atomic Layer Deposition and the Issue of Ni Aluminate, Catal. Today. (Submitted (2018).

[86] W.Y. Kim, Y.H. Lee, H. Park, Y.H. Choi, M.H. Lee, J.S. Lee, Coke tolerance of Ni/Al2O3 nanosheet catalyst for dry reforming of methane, Catal. Sci. Technol. 6 (2016) 2060–2064.

[87] W. Mo, F. Ma, Y. Liu, J. Liu, M. Zhong, A. Nulahong, Preparation of porous Al 2 O 3 by template method and its application in Ni-based catalyst for CH 4 /CO 2 reforming to produce syngas, Int. J. Hydrogen Energy. 40 (2015) 16147–16158.

[88] L. Xu, H. Zhao, H. Song, L. Chou, Ordered mesoporous alumina supported nickel based catalysts for carbon dioxide reforming of methane, Int. J. Hydrogen Energy. 37 (2012) 7497–7511.

[89] M. Garcia-Dieguez, I.S. Pieta, M.C. Herrera, M.A. Larrubia, L.J. Alemany, Nanostructured Pt- and Ni-based catalysts for CO 2 -reforming of methane, J. Catal. 270 (2010) 136–145.

[90] R. Mu, Q. Fu, H. Liu, D. Tan, R. Zhai, X. Bao, Applied Surface Science Reversible surface structural changes in Pt-based bimetallic nanoparticles during oxidation and reduction cycles, Appl. Surf. Sci. 255 (2009) 7296–7301.

[91] C.A. Menning, J.G. Chen, Regenerating Pt – 3d – Pt model electrocatalysts through oxidation – reduction cycles monitored at atmospheric pressure, J. Power Sources. 195 (2010) 3140–3144.

[92] C.A. Menning, J.G. Chen, Thermodynamics and kinetics of oxygen- induced segregation of metals in and bimetallic structures, J. Chem. Phys. 128 (2008) 164704.

[93] C.A. Menning, J.G. Chen, General trend for adsorbate-induced segregation of subsurface metal atoms in bimetallic surfaces, J. Chem. Phys. 130 (2009) 174709.

[94] S.I. Deckers, S. Offerhaus, F.H.P.M. Habraken, W.F. Van Der Weg, Initial growth and surface alloy formation of Pt on Ni (111), Surf. Sci. 237 (1990) 203–212.

[95] L. Li, L. Zhou, S. Ould-chikh, D.H. Anjum, M.B. Kanoun, J. Scaranto, M.N. Hedhili, S. Khalid, P. V. Laveille, L. D'Souza, A. Clo, J.-M. Basset, Controlled Surface Segregation Leads to Efficient Coke- Resistant Nickel / Platinum Bimetallic Catalysts for the Dry Reforming of Methane, ChemCatChem. 6900 (2015) 819–829.

[96] S. Ozkara-Aydinoglu, A.E. Aksoylu, CO_2 reforming of methane over $PtNi/Al_2O_3$ catalysts : Effects of catalyst composition , and water and oxygen addition to the feed, Int. J. Hydrogen Energy. 6 (2010) 2950–2959.

[97] E.G. Mahoney, J.M. Pusel, S.M. Stagg-williams, S. Faraji, The effects of Pt addition to supported Ni catalysts on dry (CO_2) reforming of methane to syngas, J. CO2 Util. 6 (2014) 40–44.

[98] M. Ocsachoque, F. Pompeo, G. Gonzalez, Rh–Ni/CeO2–Al2O3 catalysts for methane dry reforming, Catal. Today. 172 (2011) 226–231.

[99] A. Al-fatesh, S. Kumar, G.S. Kanade, H. Atia, A.H. Fakeeha, A.A. Ibrahim, A.M. El-toni, N.K. Labhasetwar, ScienceDirect Rh promoted and ZrO2/Al2O3 supported Ni/Co based catalysts : High activity for CO2 reforming , steam CO2 reforming and oxy CO2 reforming of CH4, Int. J. Hydrogen Energy. 43 (2018) 12069–12080.

[100] I. Luisetto, C. Sarno, D. De Felicis, F. Basoli, C. Battocchio, S. Tuti, S. Licoccia, E. Di, Ni supported on γ -Al 2 O 3 promoted by Ru for the dry reforming of methane in packed and monolithic reactors, Fuel Process. Technol. 158 (2017) 130–140.

[101] L. Foppa, M. Silaghi, K. Larmier, A. Comas-vives, Intrinsic reactivity of Ni , Pd and Pt surfaces in dry reforming and competitive reactions : Insights from first principles calculations and microkinetic modeling simulations, J. Catal. 343 (2016) 196–207.

[102] Q. Ma, J. Sun, X. Gao, J. Zhang, T. Zhao, Y. Yoneyama, N. Tsubaki, Catalysis Science & Technology bimetallic Pd – Ni catalysts for methane dry, Catal. Sci. Technol. 6 (2016) 6542–6550.

[103] T.D. Gould, M.M. Montemore, A.M. Lubers, L.D. Ellis, A.W. Weimer, J.L. Falconer, J.W. Medlin, General Enhanced dry reforming of methane on Ni and Ni-Pt catalysts synthesized by atomic layer deposition, "Applied Catal. A, Gen. 492 (2015) 107–116.

[104] S.Y. Foo, C.K. Cheng, T. Nguyen, A.A. Adesina, Evaluation of lanthanide-group promoters on Co –Ni/Al2O3 catalysts for CH4 dry reforming, "Journal Mol. Catal. A, Chem. 344 (2011) 28–36.

[105] S. Mehdi, S. Mohammad, Hydrogen production via CO2 -reforming of methane over Cu and Co doped Ni/Al2O3 nanocatalyst : impregnation versus sol – gel method and effect of process

conditions and promoter, J. Sol-Gel Sci. Technol. 67 (2013) 601–617.

[106] M.J. Illa, M.C. Roma, D.S. Jose, Low metal content Co and Ni alumina supported catalysts for the CO 2 reforming of methane, Int. J. Hydrogen Energy. 8 (2013) 0–9.

[107] X. Liao, R. Gerdts, S.F. Parker, L. Chi, Y. Zhao, M. Hill, J. Guo, O. Jones, Z. Jiang, An in-depth understanding of the bimetallic effects and coked carbon species on an active bimetallic Ni(Co)/Al2O3 dry reforming catalyst, Phys. Chem. Chem. Phys. 18 (2016) 17311–17319.

[108] X. Huang, C. Ji, C. Wang, F. Xiao, N. Zhao, N. Sun, W. Wei, Y. Sun, Ordered mesoporous CoO-NiO-Al2O3 bimetallic catalysts with dual confinement effects for CO2 reforming of CH4, Catal. Today. 281 (2017) 241–249.

[109] J. Horlyck, C. Lawrey, E.C. Lovell, R. Amal, J. Scott, Elucidating the impact of Ni and Co loading on the selectivity of bimetallic NiCo catalysts for dry reforming of methane, Chem. Eng. J. 352 (2018) 572–580.

[110] T. Ji, S. Singh, O. Omoregbe, L. Giang, N. Huu, H. Phuc, D.N. Vo, Hydrogen production from CH 4 dry reforming over bimetallic NiCo/Al2O3 catalyst, J. Energy Inst. 91 (2018) 683–694.

[111] V.M. Gonzalez-delacruz, R. Pere, F. Ternero, J.P. Holgado, A. Caballero, In Situ XAS Study of Synergic Effects on NiCo/ZrO 2 Methane Reforming Catalysts, J. Phys. Chem. C. 116 (2012) 2919–2926.

[112] W. Tu, M. Ghoussoub, C.V. Singh, Y.C. Chin, Consequences of Surface Oxophilicity of Ni , Ni-Co , and Co Clusters on Methane Activation, J. Am. Chem. Soc. 139 (2017) 6928–6945.

[113] A. Al-Fatesh, Suppression of carbon formation in CH4–CO2reforming by addition of Sr into bimetallic Ni–Co/γ-Al2O3catalyst, J. King Saud Univ. - Eng. Sci. 27 (2015) 101–107.

[114] I.H. Son, S.J. Lee, I.Y. Song, W.S. Jeon, I. Jung, D.J. Yun, D.W. Jeong, J.O. Shim, W.J. Jang, H.S. Roh, Study on coke formation over Ni/γ-Al2O3, Co-Ni/γ-Al2O3, and Mg-Co-Ni/γ-Al 2O3 catalysts for carbon dioxide reforming of methane, Fuel. 136 (2014) 194–200.

[115] G. Zhang, Y. Wang, X. Li, Y. Bai, L. Zheng, L. Wu, X. Han, Effect of Gd Promoter on the Structure and Catalytic Performance of Mesoporous Ni/Al 2 O 3 -CeO 2 in Dry Reforming of Methane, Ind. Eng. Chem. Res. 57 (2018) 17076–17085.

[116] N.D. Charisiou, G. Siakavelas, K.N. Papageridis, A. Baklavaridis, L. Tzounis, D.G. Avraam, M.A. Goula, Syngas production via the biogas dry reforming reaction over nickel supported on modified with CeO2 and/or La2O3 alumina catalysts, J. Nat. Gas Sci. Eng. 31 (2016) 164–183.

[117] R. Yang, C. Xing, C. Lv, L. Shi, N. Tsubaki, Promotional effect of La2O3 and CeO2 on Ni/γ-Al2O3 catalysts for CO2 reforming of CH4, Appl. Catal. A Gen. 385 (2010) 92–100.

[118] S. Khajeh Talkhoncheh, M. Haghighi, N. Jodeiri, S. Aghamohammadi, Hydrogen production over ternary supported Ni/Al2O3-clinoptilolite-CeO2 nanocatalyst via CH4/CO2 reforming: Influence of support composition, J. Nat. Gas Sci. Eng. 46 (2017) 699–709.

[119] W. Chen, G. Zhao, Q. Xue, L. Chen, Y. Lu, High carbon-resistance Ni/CeAlO3-Al2O3 catalyst for CH4/CO2 reforming, Appl. Catal. B Environ. 136–137 (2013) 260–268.

[120] Y. Ramezani, F. Meshkani, M. Rezaei, Promotional effect of Mg in trimetallic nickel-manganese-magnesium nanocrystalline catalysts in CO2 reforming of methane, Int. J. Hydrogen Energy. 43 (2018) 22347–22356.

[121] S.R. Yahyavi, M. Haghighi, S. Shafiei, M. Abdollahifar, F. Rahmani, Ultrasound-assisted synthesis and physicochemical characterization of Ni-Co/Al2O3-MgO nanocatalysts enhanced by different amounts of MgO used for CH4/CO2 reforming, Energy Convers. Manag. 97 (2015) 273–281.

[122] M. Abdollahifar, M. Haghighi, A.A. Babaluo, S.K. Talkhoncheh, Sono-synthesis and characterization of bimetallic Ni-Co/Al2O3-MgO nanocatalyst: Effects of metal content on catalytic properties and activity for hydrogen production via CO2 reforming of CH4, Ultrason. Sonochem. 31 (2016) 173–183.

[123] N.A. Abd Ghani, A. Azapour, S.A.F. Syed Muhammad, N. Mohamed Ramli, D.-V.N. Vo, B. Abdullah, Dry reforming of methane for syngas production over Ni–Co-supported Al2O3–MgO catalysts, Appl. Petrochemical Res. 8 (2018) 263–270.

[124] S. Mahboob, M. Haghighi, F. Rahmani, Sonochemically preparation and characterization of bimetallic Ni-Co/Al2O3-ZrO2 nanocatalyst: Effects of ultrasound irradiation time and power on catalytic properties and activity in dry reforming of CH4, Ultrason. Sonochem. 38 (2017) 38–49.

[125] M. Sharifi, M. Haghighi, F. Rahmani, S. Karimipour, Syngas production via dry reforming of CH4 over Co- and Cu-promoted Ni/Al2O3-ZrO2 nanocatalysts synthesized via sequential impregnation and sol-gel methods, J. Nat. Gas Sci. Eng. 21 (2014) 993–1004.

[126] N. Rahemi, M. Haghighi, A.A. Babaluo, M.F. Jafari, S. Allahyari, The effect of the calcination temperature on the physicochemical properties and catalytic activity in the dry reforming of methane over a Ni-Co/Al2O3-ZrO2 nanocatalyst prepared by a hybrid impregnation-plasma method, Catal. Sci. Technol. 3 (2013) 3183–3191.

[127] E. Akbari, S.M. Alavi, M. Rezaei, CeO2 Promoted Ni-MgO-Al2O3 nanocatalysts for carbon dioxide reforming of methane, J. CO2 Util. 24 (2018) 128–138.

[128] E.C. Faria, R.C.R. Neto, R.C. Colman, F.B. Noronha, Hydrogen production through CO2 reforming of methane over Ni/CeZrO2/Al2O3 catalysts, Catal. Today. 228 (2014) 138–144.

[129] N.D. Charisiou, A. Iordanidis, K. Polychronopoulou, I. V Yentekakis, M.A. Goula, Studying the stability of Ni supported on modified with CeO 2 alumina catalysts for the biogas dry reforming reaction, Mater. Today Proc. 5 (2018) 27607–27616.

[130] R. Chein, W. Fung, ScienceDirect Syngas production via dry reforming of methane over CeO 2 modified Ni / Al 2 O 3 catalysts, Int. J. Hydrogen Energy. (2019) 1–13.

[131] S. Aghamohammadi, M. Haghighi, M. Maleki, Sequential impregnation vs . sol-gel synthesized Ni / Al 2 O 3 -CeO 2 nanocatalyst for dry reforming of methane : Effect of synthesis method and support promotion, Mol. Catal. 431 (2017) 39–48.

[132] S. Jamal, H. Rad, M. Haghighi, A. Alizadeh, F. Rahmani, N. Rahemi, Sol-gel vs . impregnation preparation of MgO and CeO 2 doped Ni / Al 2 O 3 nanocatalysts used in dry reforming of methane : Effect of process conditions , synthesis method and support composition, Int. J. Hydrogen Energy. 41 (2016) 5335–5350.

[133] N. Laosiripojana, S. Assabumrungrat, Catalytic dry reforming of methane over high surface area ceria, Appl. Catal. B Environ. 60 (2005) 107–116.

[134] N. Wang, K. Shen, L. Huang, X. Yu, W. Qian, W. Chu, Facile Route for Synthesizing Ordered Mesoporous Ni − Ce − Al Oxide Materials and Their Catalytic Performance for Methane Dry Reforming to Hydrogen and Syngas, ACS Catal. 3 (2013) 1638–1651.

[135] N. Rahemi, M. Haghighi, A. Akbar, M. Fallah, P. Estifaee, Synthesis and physicochemical characterizations of Ni/Al 2O3–ZrO2 nanocatalyst prepared via impregnation method and treated with non-thermal plasma for CO 2 reforming of CH4, J. Ind. Eng. Chem. 19 (2013) 1566–1576.

[136] S.A. Shin, Y. Su, G. Hoon, J. In, H. Tae, Dry reforming of methane over Ni / ZrO2-Al2O3 catalysts : Effect of preparation methods, J. Taiwan Inst. Chem. Eng. 90 (2018) 25–32.

[137] S.O. Soloviev, A.Y. Kapran, S.N. Orlyk, E. V Gubareni, Carbon dioxide reforming of methane on monolithic Ni/Al 2O3-based catalysts, J. Nat. Gas Chem. 20 (2011) 184–190.

[138] M. Hassan, S. Putla, S.B. Abd, S.K. Bhargava, Understanding the role of lanthanide promoters on the structure – activity of nanosized Ni/□ -Al2O3 catalysts in carbon dioxide reforming of methane, "Applied Catal. A, Gen. 492 (2015) 160–168.

[139] A.S. Al-fatesh, M.A. Naeem, A.H. Fakeeha, A.E. Abasaeed, Role of La2O3 as Promoter and Support in Ni/Û-Al2O3 Catalysts for Dry Reforming of Methane, Chinese J. Chem. Eng. 22 (2014) 28–37.

[140] N. Pegios, V. Bliznuk, J.M. Schneider, R. Palkovits, K. Simeonov, Comparative study on La-promoted methane dry reforming – spray drying for enhanced nickel dispersion and strong metal – support interactions, RSC Adv. 8 (2018) 606–618.

[141] N.D. Charisiou, L. Tzounis, V. Sebastian, S.J. Hinder, M.A. Baker, K. Polychronopoulou, Investigating the correlation between deactivation and the carbon deposited on the surface of Ni/Al2O3 and Ni/La2O3 -Al 2O3 catalysts during the biogas reforming reaction, Appl. Surf. Sci. 474 (2019) 42–56.

[142] F.R. Shamskar, F. Meshkani, M. Rezaei, Preparation and characterization of ultrasound-assisted co-precipitated nanocrystalline La- , Ce- , Zr – promoted Ni-Al2O3 catalysts for dry reforming reaction, J. CO2 Util. 22 (2017) 124–134.

[143] C. Jiménez-González, Z. Boukha, B. De Rivas, J.J. Delgado, M.Á. Cauqui, J.R. González-Velasco, J.I. Gutiérrez-Ortiz, R. López-Fonseca, Structural characterisation of Ni/alumina reforming catalysts activated at high temperatures, Appl. Catal. A Gen. 466 (2013) 9–20.

[144] F. Guo, J. Xu, W. Chu, CO 2 reforming of methane over Mn promoted Ni / Al 2 O 3 catalyst

treated by N 2 glow discharge plasma, Catal. Today. 256 (2015) 124–129.

[145] C.J. Chem, A.H. Fakeeha, M.A. Naeem, W.U. Khan, A.E. Abasaeed, A.S. Al-fatesh, A.S. Al-fatesh, Reforming of Methane by CO2 over Bimetallic Ni-Mn / γ- Al2O3 Catalyst, Chinese J. Chem. Phys. 27 (2014) 214–220.

[146] P. Tan, Z. Gao, C. Shen, Y. Du, X. Li, W. Huang, Ni-Mg-Al solid basic layered double oxide catalysts prepared using surfactant-assisted coprecipitation method for CO<inf>2</inf> reforming of CH4, Chinese J. Catal. 35 (2014) 1955–1971.

[147] Z. Alipour, M. Rezaei, F. Meshkani, Effect of Ni loadings on the activity and coke formation of MgO-modified Ni/Al2O3 nanocatalyst in dry reforming of methane, J. Energy Chem. 23 (2014) 633–638.

[148] J.-E. Min, Y.-J. Lee, H.-G. Park, C. Zhang, K.-W. Jun, Carbon dioxide reforming of methane on Ni–MgO–Al2O3 catalysts prepared by sol–gel method: Effects of Mg/Al ratios, J. Ind. Eng. Chem. 26 (2014) 375–383.

[149] M.C. Herrera, I.S. Pieta, M.A. Larrubia, L.J. Alemany, NiBa catalysts for CO2-reforming of methane, CATCOM. 11 (2010) 1133–1136.

[150] A. Ranjbar, M. Rezaei, Dry reforming reaction over nickel catalysts supported on nanocrystalline calcium aluminates with different CaO /Al2O3 ratios, J. Nat. Gas Chem. 21 (2012) 178–183.

[151] Z. Alipour, M. Rezaei, F. Meshkani, Effect of alkaline earth promoters (MgO, CaO, and BaO) on the activity and coke formation of Ni catalysts supported on nanocrystalline Al2O3 in dry reforming of methane, J. Ind. Eng. Chem. 20 (2014) 2858–2863.

[152] Z. Alipour, M. Rezaei, F. Meshkani, Effects of support modifiers on the catalytic performance of Ni/Al 2O3 catalyst in CO2 reforming of methane, Fuel. 129 (2014) 197–203.

[153] E. Ruckenstein, Y.H. Hu, Carbon dioxide reforming of methane over nickel/alkaline earth metal oxide catalysts, Appl. Catal. A, Gen. 133 (1995) 149–161. [154] Y.H. Hu, Solid-solution catalysts for CO2 reforming of methane, Catal. Today. 148 (2009) 206–211.

[155] M. Thommes, K. Kaneko, A. V. Neimark, J.P. Olivier, F. Rodriguez-Reinoso, J. Rouquerol, K.S.W. Sing, Physisorption of gases, with special reference to the evaluation of surface area and pore size distribution (IUPAC Technical Report), Pure Appl. Chem. 87 (2015) 1051–1069.

[156] S. Storck, H. Bretinger, W.F. Maier, Characterization of micro- and mesoporous solids by physisorption methods and pore-size analysis, Appl. Catal. 174 (1998) 137–146.

[157] H.S. Kaufman, I. Fankuchen, X-ray diffraction, Anal. Chem. 21 (1949) 24–29.

[158] Z.W. Chen, W.M. Gibson, H. Huang, High Definition X-Ray Fluorescence: Principles and Techniques, X-Ray Opt. Instrum. 2008 (2008) 1–10.

[159] S. Bals, B. Kabius, M. Haider, V. Radmilovic, C. Kisielowski, Annular dark field imaging in a TEM, Solid State Commun. 130 (2004) 675–680.

[160] J. Wang, N. Lu, J. Pablo Oviedo, X. Peng, G. Lian, M.J. Kim, Aberration Corrected High

Angle Annular Dark Field (HAADF) Scanning Transmission Electron Microscopy (STEM) and In Situ Transmission Electron Microscopy (TEM) Study of Transition Metal Dichalcogenides (TMDs), Microsc. Microanal. 21 (2016) 431–432.

[161] A. Knop-Gericke, X-ray Photoelectron Spectroscopy. An Introduction to Principles and Practices. By Paul van der Heide., Angew. Chemie Int. Ed. 51 (2012) 9218–9218.

[162] G.S. Bumbrah, R.M. Sharma, Raman spectroscopy – Basic principle, instrumentation and selected applications for the characterization of drugs of abuse, Egypt. J. Forensic Sci. 6 (2016) 209–215.

[163] P.A. Webb, Introduction to Chemical Adsorption Analytical Techniques and their Applications to Catalysis, MIC Tech. Publ. (2003) 1–12. http://www.micromeritics.com/Repository/Files/intro_to_chemical_adsorption.pdf.

[164] T. Schaaf, J. Grünig, M.R. Schuster, T. Rothenfluh, A. Orth, Methanation of CO2 - storage of renewable energy in a gas distribution system, Energy. Sustain. Soc. 4 (2014) 2.

[165] A. Catarina Faria, C. V. Miguel, L.M. Madeira, Thermodynamic analysis of the CO2 methanation reaction with in situ water removal for biogas upgrading, J. CO2 Util. 26 (2018)

[166] J. Gao, Y. Wang, Y. Ping, D. Hu, G. Xu, F. Gu, F. Su, A thermodynamic analysis of methanation reactions of carbon oxides for the production of synthetic natural gas, RSC Adv. 2 (2012) 2358–2368.

[167] L. Zhang, Q. Zhang, Y. Liu, Y. Zhang, Dry reforming of methane over Ni/MgO-Al 2 O 3 catalysts prepared by two-step hydrothermal method, Appl. Surf. Sci. 389 (2016) 25–33.

[168] H.S. Roh, K.W. Jun, Carbon dioxide reforming of methane over Ni catalysts supported on Al 2O3 modified with La2O3, MgO, and CaO, Catal. Surv. from Asia. 12 (2008) 239–252.

[169] N.D. Charisiou, A. Baklavaridis, V.G. Papadakis, M.A. Goula, Synthesis gas production via the biogas reforming reaction over Ni/MgO-Al2O3 and Ni/CaO-Al2O3 catalysts, Waste Biomass Valorization. 7 (2016) 725–736.

[170] H. Arbag, Effect of impregnation sequence of Mg on performance of mesoporous alumina supported Ni catalyst in dry reforming of methane, Int. J. Hydrogen Energy. 43 (2018) 6561–

[171] E. Akbari, S.M. Alavi, M. Rezaei, Synthesis gas production over highly active and stable nanostructured NiMgOAl2O3 catalysts in dry reforming of methane: Effects of Ni contents, Fuel. 194 (2017) 171–179.

[172] Y. Zhan, J. Han, Z. Bao, B. Cao, Y. Li, J. Street, F. Yu, Biogas reforming of carbon dioxide to syngas production over Ni-Mg-Al catalysts, Mol. Catal. 436 (2017) 248–258.

[173] Z. Hou, T. Yashima, Meso-porous Ni/Mg/Al catalysts for methane reforming with CO2, Appl. Catal. A Gen. 261 (2004) 205–209.

[174] L. Xu, H. Song, L. Chou, Ordered mesoporous MgO-Al2O3 composite oxides supported Ni based catalysts for CO2 reforming of CH4 : Effects of basic modifier and mesopore structure, Int. J. Hydrogen Energy. 38 (2013) 7307–7325.

[175] R. Dębek, M.E. Galvez, F. Launay, M. Motak, T. Grzybek, P. Da Costa, Low temperature dry methane reforming over Ce, Zr and CeZr promoted Ni–Mg–Al hydrotalcite-derived catalysts, Int. J. Hydrogen Energy. 41 (2016) 11616–11623.

[176] A. Vallezi Paladino, E. Assaf, J. Assaf, Hydrotalcites derived catalysts for syngas production from biogas reforming: Effect of nickel and cerium load, Catal. Today. 289 (2017) 78–88.

[177] J. Abdelsadek, M. Sehailia, D. Halliche, V.M. Gonzalez-Delacruz, J.P. Holgado, K. Bachari, A. Caballero, O. Cherifi, In-situ hydrogasification/regeneration of NiAl-hydrotalcite derived catalyst in the reaction of CO2 reforming of methane: A versatile approach to catalyst recycling, J. CO2 Util. 14 (2016) 98–105.

[178] B. Rego de Vasconcelos, D. Pham Minh, N. Lyczko, T.S. Phan, P. Sharrock, A. Nzihou, Upgrading greenhouse gases (methane and carbon dioxide) into syngas using nickel-based catalysts, Fuel. 226 (2018) 195–203.

[179] W. Cai, J. Yu, C. Anand, A. Vinu, M. Jaroniec, Facile synthesis of ordered mesoporous alumina and alumina-supported metal oxides with tailored adsorption and framework properties, Chem. Mater. 23 (2011) 1147–1157.

[180] S.M. Morris, P.F. Fulvio, M. Jaroniec, Ordered mesoporous alumina-supported metal oxides, J. Am. Chem. Soc. 130 (2008) 15210–15216.

[181] Q. Yuan, A.-X. Yin, C. Luo, L.-D. Sun, Y.-W. Zhang, W.-T. Duan, H.-C. Liu, C.-H. Yan, Facile Synthesis for Ordered Mesoporous γ-Aluminas with High Thermal Stability, J. Am. Chem. Soc. 130 (2008) 3465–3472.

[182] L. Xu, H. Song, L. Chou, One-Pot Synthesis of Ordered Mesoporous NiO−CaO−Al2O3 Composite Oxides for Catalyzing CO2 Reforming of CH4, ACS Catal. 2 (2012) 1331–1342.

[183] V. Meynen, P. Cool, E.F. Vansant, Verified syntheses of mesoporous materials, Microporous Mesoporous Mater. 125 (2009) 170–223.

[184] A. Grosman, C. Ortega, Capillary condensation in porous materials. Hysteresis and interaction mechanism without pore blocking/percolation process, Langmuir. 24 (2008) 3977–3986.

[185] L. Karam, S. Casale, H. El Zakhem, N. El Hassan, Tuning the properties of nickel nanoparticles inside SBA-15 mesopores for enhanced stability in methane reforming, J. CO2 Util. 17 (2017) 119–124.

[186] C.T. Kresge, M.E. Leonowicz, W.J. Roth, J.C. Vartuli, J.S. Beck, Ordered mesoporous molecular sieves synthesized by a liquid-crystal template mechanism, Nature. 359 (1992) 710–712.

[187] S. Erdem, B. Erdem, R.M. ??ks??zo??lu, A. ????tak, Effect of calcination temperature on the structural and magnetic properties of Ni/SBA-15 nanocomposite, J. Porous Mater. 22 (2015) 689–698.

[188] D. Pan, Z. Dong, M. He, W. Chen, S. Chen, F. Yu, B. Fan, X. Cui, R. Li, Structural and surface properties of highly ordered mesoporous magnesium-aluminium composite oxides derived

from facile synthesis, Mater. Chem. Phys. 186 (2017) 574–583.

[189] N. Wang, X. Yu, K. Shen, W. Chu, W. Qian, Synthesis, characterization and catalytic performance of MgO-coated Ni/SBA-15 catalysts for methane dry reforming to syngas and hydrogen, Int. J. Hydrogen Energy. 38 (2013) 9718–9731.

[190] Y.L. Wei, Y.M. Wang, J.H. Zhu, Z.Y. Wu, In-Situ Coating of SBA-15 with MgO: Direct Synthesis of Mesoporous Solid Bases from Strong Acidic Systems, Adv. Mater. 15 (2003) 1943–1945.

[191] D. Li, Y. Nakagawa, K. Tomishige, Methane reforming to synthesis gas over Ni catalysts modified with noble metals, Appl. Catal. A Gen. 408 (2011) 1–24.

[192] J.A.C. Dias, J.M. Assaf, Influence of calcium content in Ni/CaO/Al2O3 catalysts for CO2-reforming of methane, Catal. Today. 85 (2003) 59–68.

[193] J.-E. Min, Y.-J. Lee, H.-G. Park, C. Zhang, K.-W. Jun, Carbon dioxide reforming of methane on Ni–MgO–Al2O3 catalysts prepared by sol–gel method: Effects of Mg/Al ratios, J. Ind. Eng. Chem. 26 (2015) 375–383.

[194] Q. Liu, S. Wang, G. Zhao, H. Yang, M. Yuan, X. An, H. Zhou, Y. Qiao, Y. Tian, CO2 methanation over ordered mesoporous NiRu-doped CaO-Al2O3 nanocomposites with enhanced catalytic performance, Int. J. Hydrogen Energy. 43 (2018) 239–250.

[195] Ş. Özkara-Aydınoğlu, A. Erhan Aksoylu, A comparative study on the kinetics of carbon dioxide reforming of methane over Pt–Ni/Al2O3 catalyst: Effect of Pt/Ni Ratio, Chem. Eng. J. 215–216 (2013) 542–549.

[196] L. Zhang, X. Wang, C. Chen, X. Zou, W. Ding, X. Lu, Dry reforming of methane to syngas over lanthanum-modified mesoporous nickel aluminate/Γ-alumina nanocomposites by one-pot synthesis, Int. J. Hydrogen Energy. 42 (2017) 11333–11345.

[197] A.A. Lemonidou, I.A. Vasalos, Carbon dioxide reforming of methane over 5 wt.% Ni/CaO-Al2O3catalyst, Appl. Catal. A Gen. 228 (2002) 227–235. [198] A. Guerrero-Ruiz, I. Rodriguez-Ramos, P. Ferreira-Aparicio, Comparative study at low and medium reaction temperatures of syngas production by methane reforming with carbon dioxide over silica and alumina supported catalysts, Appl. Catal. A Gen. 170 (1998) 177–187.

[199] S. Wang, M. Lu, S. Wang, G.Q.M. Lu, A Comprehensive Study on Carbon Dioxide Reforming of Methane over Ni/γ-Al2O3 Catalysts, Ind. Eng. Chem. Res. 38 (1999) 2615–2625.

[200] A. Nandini, K.K. Pant, S.C. Dhingra, Kinetic study of the catalytic carbon dioxide reforming of methane to synthesis gas over Ni-K/CeO2-Al2O3 catalyst, Appl. Catal. A Gen. 308 (2006) 119–127.

[201] U. Oemar, Y. Kathiraser, L. Mo, X.K. Ho, S. Kawi, CO2 reforming of methane over highly active La-promoted Ni supported on SBA-15 catalysts: mechanism and kinetic modelling, Catal. Sci. Technol. 6 (2016) 1173–1186.

[202] Y. Kathiraser, U. Oemar, E.T. Saw, Z. Li, S. Kawi, Kinetic and mechanistic aspects for CO2

reforming of methane over Ni based catalysts, Chem. Eng. J. 278 (2015) 62–78.

[203] S. Wang, G.Q. Lu, A comprehensive study on carbon dioxide reforming of methane over Ni/γ-Al2O3 catalysts, Ind. Eng. Chem. Res. 38 (1999) 2615–2625.

[204] Ş. Özkara-Aydinoğlu, A. Erhan Aksoylu, A comparative study on the kinetics of carbon dioxide reforming of methane over Pt-Ni/Al2O3 catalyst: Effect of Pt/Ni Ratio, Chem. Eng. J. 215–216 (2013) 542–549.

[205] Y.R. Lee, J. Kim, W.S. Ahn, Synthesis of metal-organic frameworks: A mini review, Korean J. Chem. Eng. 30 (2013) 1667–1680.

[206] N. Stock, S. Biswas, Synthesis of Metal-Organic Frameworks (MOFs): Routes to Various MOF topologies, morphologies, and composites, Chem. Rev. 112 (2011) 933–969.

[207] H. Zhao, H. Song, L. Xu, L. Chou, Isobutane dehydrogenation over the mesoporous Cr2O 3/Al2O3 catalysts synthesized from a metal-organic framework MIL-101, Appl. Catal. A Gen. 456 (2013) 188–196.

[208] D. Yuan, J. Chen, S. Tan, N. Xia, Y. Liu, Worm-like mesoporous carbon synthesized from metal-organic coordination polymers for supercapacitors, Electrochem. Commun. 11 (2009) 1191–1194.

[209] X. Yan, N. Lu, B. Fan, J. Bao, D. Pan, M. Wang, R. Li, Synthesis of mesoporous and tetragonal zirconia with inherited morphology from metal-organic frameworks, CrystEngComm. 17 (2015) 6426–6433.

[210] Y. Lü, W. Zhan, Y. He, Y. Wang, X. Kong, Q. Kuang, Z. Xie, L. Zheng, MOF-templated synthesis of porous Co3O4 concave nanocubes with high specific surface area and their gas sensing properties, ACS Appl. Mater. Interfaces. 6 (2014) 4186–4195.

[211] Z. Li, Y.N. Wu, J. Li, Y. Zhang, X. Zou, F. Li, The metal-organic framework mil-53(AL) constructed from multiple metal sources: Alumina, aluminum hydroxide, and boehmite, Chem. - A Eur. J. 21 (2015) 6913–6920.

[212] S.H. Lo, D. Senthil Raja, C.W. Chen, Y.H. Kang, J.J. Chen, C.H. Lin, Waste polyethylene terephthalate (PET) materials as sustainable precursors for the synthesis of nanoporous MOFs, MIL-47, MIL-53(Cr, Al, Ga) and MIL-101(Cr), Dalt. Trans. 45 (2016) 9565–9573.

[213] Y. Zhou, J. Long, Y. Li, Ni-based catalysts derived from a metal-organic framework for selective oxidation of alkanes, Chinese J. Catal. 37 (2016) 955–962.

[214] Y. Yang, Y. Zhang, C.J. Sun, X. Li, W. Zhang, X. Ma, Y. Ren, X. Zhang, Heterobimetallic metal-organic framework as a precursor to prepare a nickel/nanoporous carbon composite catalyst for 4-nitrophenol reduction, ChemCatChem. 6 (2014) 3084–3090.

[215] M.S. Wu, W.H. Hsu, Nickel nanoparticles embedded in partially graphitic porous carbon fabricated by direct carbonization of nickel-organic framework for high-performance supercapacitors, J. Power Sources. 274 (2015) 1055–1062.

[216] R. Li, X. Ren, X. Feng, X. Li, C. Hu, B. Wang, A highly stable metal- and nitrogen-doped

nanocomposite derived from Zn/Ni-ZIF-8 capable of CO 2 capture and separation, Chem. Commun. 50 (2014) 6894–6897.

[217] T. Wang, Q. Zhou, X. Wang, J. Zheng, X. Li, MOF-derived surface modified Ni nanoparticles as an efficient catalyst for the hydrogen evolution reaction, J. Mater. Chem. A. 3 (2015) 16435–16439.

[218] Y. Wang, S. Sang, W. Zhu, L. Gao, G. Xiao, CuNi@C catalysts with high activity derived from metal-organic frameworks precursor for conversion of furfural to cyclopentanone, Chem. Eng. J. 299 (2016) 104–111.

[219] Y. Yang, F. Yang, H. Hu, S. Lee, Y. Wang, H. Zhao, D. Zeng, B. Zhou, S. Hao, Dilute NiO/carbon nanofiber composites derived from metal organic framework fibers as electrode materials for supercapacitors, Chem. Eng. J. 307 (2017) 583–592.

[220] I.A. Khan, Y. Qian, A. Badshah, M.A. Nadeem, D. Zhao, Highly Porous Carbon Derived from MOF-5 as a Support of ORR Electrocatalysts for Fuel Cells, ACS Appl. Mater. Interfaces. 8 (2016) 17268–17275.

[221] L. Peng, J. Zhang, Z. Xue, B. Han, J. Li, G. Yang, Large-pore mesoporous Mn3O4 crystals derived from metal-organic frameworks, Chem. Commun. 49 (2013) 11695–11697.

[222] T. Wang, L. Shi, J. Tang, V. Malgras, S. Asahina, G. Liu, H. Zhang, X. Meng, K. Chang, J. He, O. Terasaki, Y. Yamauchi, J. Ye, A Co3O4-embedded porous ZnO rhombic dodecahedron prepared using zeolitic imidazolate frameworks as precursors for CO2 photoreduction, Nanoscale. 8 (2016) 6712–6720.

[223] L. Zheng, X. Li, W. Du, D. Shi, W. Ning, X. Lu, Z. Hou, Metal-organic framework derived Cu/ZnO catalysts for continuous hydrogenolysis of glycerol, Appl. Catal. B Environ. 203 (2017) 146–153.

[224] K. Khaletskaya, A. Pougin, R. Medishetty, C. Rösler, C. Wiktor, J. Strunk, R.A. Fischer, Fabrication of Gold/Titania Photocatalyst for CO2 Reduction Based on Pyrolytic Conversion of the Metal-Organic Framework NH2-MIL-125(Ti) Loaded with Gold Nanoparticles, Chem. Mater. 27 (2015) 7248–7257.

[225] M. Derakhshani, A. Hashamzadeh, M.M. Amini, High surface area mesoporous alumina nanosheets and nanorolls from an aluminum based metal organic framework, Ceram. Int. 42 (2016) 17742–17748.

[226] D. Liu, F. Dai, X. Li, J. Liang, Y. Liu, C. Liu, A non-template approach to fabricate mesoporous alumina with predefined morphology by solid-state transformation of Al-based metal-organic frameworks, RSC Adv. 5 (2015) 15182–15186.

[227] D. Liu, F. Dai, H. Liu, Y. Liu, C. Liu, An investigation of the transformation of Al-based metal-organic frameworks to mesoporous Al2O3 with core-shell and nanoporous structure, Mater. Lett. 139 (2015) 7–11.

[228] Y. Liu, S. Liu, Z. Yue, Mesoporous alumina nanosheets and nanorolls derived from

topologically identical Al-based MOFs, RSC Adv. 5 (2015) 31742–31745.

[229] V.I. Isaeva, A.L. Tarasov, V. V. Chernyshev, L.M. Kustov, Control of morphology and size of microporous framework MIL-53(Al) crystals by synthesis procedure, Mendeleev Commun. 25 (2015) 466–467.

[230] T. Loiseau, C. Serre, C. Huguenard, G. Fink, F. Taulelle, M. Henry, T. Bataille, G. Férey, A Rationale for the Large Breathing of the Porous Aluminum Terephthalate (MIL-53) Upon Hydration, Chem. - A Eur. J. 10 (2004) 1373–1382.

[231] J.O. Hsieh, K.J. Balkus, J.P. Ferraris, I.H. Musselman, MIL-53 frameworks in mixed-matrix membranes, Microporous Mesoporous Mater. 196 (2014) 165–174.

[232] P. Horcajada, P. Horcajada, C. Serre, C. Serre, G. Maurin, G. Maurin, N. a Ramsahye, N. a Ramsahye, F. Balas, M. Vallet-Regí, M. Sebban, F. Taulelle, G. Férey, Flexible Porous Metal-Organic Frameworks for a Controlled Drug Delivery, J. Am. Chem. Soc. 130 (2008) 6774–6780.

[233] S. Hu, M. Liu, K. Li, C. Song, G. Zhang, X. Guo, Surfactant-assisted synthesis of hierarchical NH2-MIL-125 for the removal of organic dyes, RSC Adv. 7 (2017) 581–587.

[234] S. Yuvaraj, F.Y. Lin, T.H. Chang, C.T. Yeh, Thermal decomposition of metal nitrates in air and hydrogen environments, J. Phys. Chem. B. 107 (2003) 1044–1047.

[235] S.M. Pourmortazavi, S.G. Hosseini, M. Rahimi-Nasrabadi, S.S. Hajimirsadeghi, H. Momenian, Effect of nitrate content on thermal decomposition of nitrocellulose, J. Hazard. Mater. 162 (2009) 1141–1144.

[236] L. Pino, C. Italiano, A. Vita, M. Laganà, V. Recupero, Ce 0.70 La 0.20 Ni 0.10 O 2-Δ catalyst for methane dry reforming: Influence of reduction temperature on the catalytic activity and stability, Appl. Catal. B Environ. 218 (2017) 779–792.

[237] I. Luisetto, S. Tuti, C. Romano, M. Boaro, E. Di Bartolomeo, Dry reforming of methane over Ni supported on doped CeO 2 : New insight on the role of dopants for CO 2 activation, J. CO2 Util. 30 (2019) 63–78.

[238] L. Zhou, L. Li, N. Wei, J. Li, J.M. Basset, Effect of NiAl2O4 Formation on Ni/Al2O3 Stability during Dry Reforming of Methane, ChemCatChem. 7 (2015) 2508–2516.

[239] R. Benrabaa, A. Barama, H. Boukhlouf, J. Guerrero-Caballero, A. Rubbens, E. Bordes-Richard, A. Löfberg, R.N. Vannier, Physico-chemical properties and syngas production via dry reforming of methane over NiAl2O4catalyst, Int. J. Hydrogen Energy. 42 (2017) 12989–12996.

[240] H. Drobná, M. Kout, A. Sołtysek, V.M. González-Delacruz, A. Caballero, L. Čapek, Analysis of Ni species formed on zeolites, mesoporous silica and alumina supports and their catalytic behavior in the dry reforming of methane, React. Kinet. Mech. Catal. 121 (2017) 255–274.

[241] A.R.J.M. Mattos, S.H. Probst, J.C. Afonso, M. Schmal, Hydrogenation of 2-ethyl-hexen-2-al on Ni/Al2O3catalysts, J. Braz. Chem. Soc. 15 (2004) 760–766.

[242] M. Shah, S. Das, A.K. Nayak, P. Mondal, A. Bordoloi, Smart designing of metal-support interface for imperishable dry reforming catalyst, Appl. Catal. A Gen. 556 (2018) 137–154.

[243] H. Long, T. Shi, H. Hu, S. Jiang, S. Xi, Z. Tang, Growth of Hierarchal Mesoporous NiO Nanosheets on Carbon Cloth as Binder-free Anodes for High-performance Flexible Lithium-ion Batteries, Sci. Rep. 4 (2014) 7413.

[244] K. Jabbour, P. Massiani, A. Davidson, S. Casale, N. El Hassan, Ordered mesoporous "one-pot" synthesized Ni-Mg (Ca)-Al 2 O 3 as effective and remarkably stable catalysts for combined steam and dry reforming of methane (CSDRM)., Appl. Catal. B Environ. 201 (2017) 527–542.

[245] L. Li, Z. Shang, Z. Xiao, L. Wang, X. Liang, G. Liu, Steam reforming of n-dodecane over mesoporous alumina supported nickel catalysts: Effects of metal-support interaction on nickel catalysts, Int. J. Hydrogen Energy. 44 (2019) 6965–6977.

[246] S. Dama, S.R. Ghodke, R. Bobade, H.R. Gurav, S. Chilukuri, Active and durable alkaline earth metal substituted perovskite catalysts for dry reforming of methane, Appl. Catal. B Environ. 224 (2018) 146–158.

[247] E. le Saché, L. Pastor-Pérez, D. Watson, A. Sepúlveda-Escribano, T.R. Reina, Ni stabilised on inorganic complex structures: superior catalysts for chemical CO 2 recycling via dry reforming of methane, Appl. Catal. B Environ. 236 (2018) 458–465.

[248] S. Rönsch, J. Schneider, S. Matthischke, M. Schlüter, M. Götz, J. Lefebvre, P. Prabhakaran, S. Bajohr, Review on methanation – From fundamentals to current projects, Fuel. 166 (2016) 276–296.

[249] K. Stangeland, D. Kalai, H. Li, Z. Yu, CO2Methanation: The Effect of Catalysts and Reaction Conditions, Energy Procedia. 105 (2017) 2022–2027.

[250] M. Specht, F. Baumgart, B. Feigl, V. Frick, B. Stürmer, U. Zuberbühler, M. Sterner, G. Waldstein, Storing bioenergy and renewable electricity in the natural gas grid, FVEE AEE Top. 2009. (2009) 69–78.

[251] S. Wang, G.Q. Lu, G.J. Millar, Carbon dioxide reforming of methane to produce synthesis gas over metal-supported catalysts: State of the art, Energy and Fuels. 10 (1996) 896–904.

[252] J. Gao, Q. Liu, F. Gu, B. Liu, Z. Zhong, F. Su, Recent advances in methanation catalysts for the production of synthetic natural gas, RSC Adv. 5 (2015) 22759–22776.

[253] X. Guo, A. Traitangwong, M. Hu, C. Zuo, V. Meeyoo, Z. Peng, C. Li, Carbon Dioxide Methanation over Nickel-Based Catalysts Supported on Various Mesoporous Material, Energy and Fuels. 32 (2018) 3681–3689.

[254] P. Riani, G. Garbarino, M.A. Lucchini, F. Canepa, G. Busca, Unsupported versus alumina-supported Ni nanoparticles as catalysts for steam/ethanol conversion and CO 2 methanation, J. Mol. Catal. A Chem. 383–384 (2014) 10–16.

[255] B. Mutz, A. Gänzler, M. Nachtegaal, O. Müller, R. Frahm, W. Kleist, J.-D. Grunwaldt, Surface Oxidation of Supported Ni Particles and Its Impact on the Catalytic Performance during

Dynamically Operated Methanation of CO2, Catalysts. 7 (2017) 279.

[256] W. Yang, Y. Feng, W. Chu, Promotion Effect of CaO Modification on Mesoporous Al2O3-Supported Ni Catalysts for CO2 Methanation, Int. J. Chem. Eng. (2016) 2041821.

[257] C. Liang, X. Hu, T. Wei, P. Jia, Z. Zhang, D. Dong, S. Zhang, Q. Liu, G. Hu, Methanation of CO 2 over Ni/Al 2 O 3 modified with alkaline earth metals: Impacts of oxygen vacancies on catalytic activity, Int. J. Hydrogen Energy. 44 (2019) 8197–8213.

[258] G. Garbarino, C. Wang, T. Cavattoni, E. Finocchio, P. Riani, M. Flytzani-Stephanopoulos, G. Busca, A study of Ni/La-Al 2 O 3 catalysts: A competitive system for CO 2 methanation, Appl. Catal. B Environ. (2019) 286–297.

[259] S. He, C. Li, H. Chen, D. Su, B. Zhang, X. Cao, B. Wang, M. Wei, D.G. Evans, X. Duan, A surface defect-promoted Ni nanocatalyst with simultaneously enhanced activity and stability, Chem. Mater. 25 (2013) 1040–1046.

[260] A. Aljishi, G. Veilleux, J.A.H. Lalinde, J. Kopyscinski, The effect of synthesis parameters on ordered mesoporous nickel alumina catalyst for CO2 methanation, Appl. Catal. A Gen. 549 (2018) 263–272.

[261] F. Song, Q. Zhong, Y. Yu, M. Shi, Y. Wu, J. Hu, Y. Song, Obtaining well-dispersed Ni/Al2O3 catalyst for CO2 methanation with a microwave-assisted method, Int. J. Hydrogen Energy. 42 (2017) 4174–4183.

[262] W.A. Wan Abu Bakar, R. Ali, N.S. Mohammad, The effect of noble metals on catalytic methanation reaction over supported Mn/Ni oxide based catalysts, Arab. J. Chem. 8 (2015) 632–643.

[263] R. Lippi, S.C. Howard, H. Barron, C.D. Easton, I.C. Madsen, L.J. Waddington, C. Vogt, M.R. Hill, C.J. Sumby, C.J. Doonan, D.F. Kennedy, Highly active catalyst for CO2 methanation derived from a metal organic framework template, J. Mater. Chem. A. 5 (2017) 12990–12997.

[264] H. Jiang, Q. Gao, S. Wang, Y. Chen, M. Zhang, The synergistic effect of Pd NPs and UiO-66 for enhanced activity of carbon dioxide methanation, J. CO2 Util. 31 (2019) 167–172.

[265] M. Mihet, G. Blanita, M. Dan, L. Barbu-Tudoran, M.D. Lazar, Pt/UiO-66 Nanocomposites as Catalysts for CO_2 Methanation Process, J. Nanosci. Nanotechnol. 19 (2019) 3187–3196.

[266] W. Li, A. Zhang, X. Jiang, C. Chen, Z. Liu, C. Song, X. Guo, Low Temperature CO2 Methanation: ZIF-67-Derived Co-Based Porous Carbon Catalysts with Controlled Crystal Morphology and Size, Acs Sustain. Chem. Eng. 5 (2017) 7824–7831.

[267] W. Zhen, B. Li, G. Lu, J. Ma, Enhancing catalytic activity and stability for CO2 methanation on Ni@MOF-5 via control of active species dispersion, Chem. Commun. 51 (2015) 1728–1731.

[268] W. Zhen, F. Gao, B. Tian, P. Ding, Y. Deng, Z. Li, H. Gao, G. Lu, Enhancing activity for carbon dioxide methanation by encapsulating (111) facet Ni particle in metal–organic frameworks at low temperature, J. Catal. 348 (2017) 200–211.

[269] M.C. Bacariza, I. Graça, J.M. Lopes, C. Henriques, Enhanced activity of CO2 hydrogenation to CH4 over Ni based zeolites through the optimization of the Si/Al ratio, Microporous Mesoporous Mater. 267 (2018) 9–19.

[270] M.C. Bacariza, I. Graça, J.M. Lopes, C. Henriques, Ni-Ce/Zeolites for CO2 Hydrogenation to CH4: Effect of the Metal Incorporation Order, ChemCatChem. 10 (2018) 2773–2781.

[271] L. Karam, N. El Hassan, Advantages of mesoporous silica based catalysts in methane reforming by CO 2 from kinetic perspective, J. Environ. Chem. Eng. 6 (2018) 4289–4297.

[272] R. Delmelle, R.B. Duarte, T. Franken, D. Burnat, L. Holzer, A. Borgschulte, A. Heel, Development of improved nickel catalysts for sorption enhanced CO2 methanation, Int. J. Hydrogen Energy. 41 (2016) 20185–20191.

[273] A. Borgschulte, N. Gallandat, B. Probst, R. Suter, E. Callini, D. Ferri, Y. Arroyo, R. Erni, H. Geerlings, A. Züttel, Sorption enhanced CO2 methanation, Phys. Chem. Chem. Phys. 15 (2013) 9620–9625.

[274] S. Walspurger, G.D. Elzinga, J.W. Dijkstra, M. Saric, W.G. Haije, Sorption enhanced methanation for substitute natural gas production: Experimental results and thermodynamic considerations, Chem. Eng. J. 242 (2014) 379–386.

[275] M.A.A. Aziz, A.A. Jalil, S. Triwahyono, M.W.A. Saad, CO2 methanation over Ni-promoted mesostructured silica nanoparticles: Influence of Ni loading and water vapor on activity and response surface methodology studies, Chem. Eng. J. 260 (2015) 757–764.

[276] F. Ocampo, Développement de catalyseurs pour la réaction de méthanation du dioxyde de carbone, University of Strasbourg, 2011.

[277] H.X. Yang, Q.F. Dong, X.H. Hu, X.P. Ai, S.X. Li, Preparation and characterization of LiNiO2 synthesized from Ni(OH)2 and LiOH·H2O, J. Power Sources. 79 (1999) 256–261.

[278] A. Borgschulte, E. Callini, N. Stadie, Y. Arroyo, M.D. Rossell, R. Erni, H. Geerlings, A. Züttel, D. Ferri, Manipulating the reaction path of the CO2 hydrogenation reaction in molecular sieves, Catal. Sci. Technol. 5 (2015) 4613–4621.

[279] C.M. Mfoumou, S. Mignard, T. Belin, The preferential adsorption sites of H2O on adsorption sites of CO2 at low temperature onto NaX and BaX zeolites, Adsorpt. Sci. Technol. (2018) 0263617418762494.

[280] M.C. Bacariza, M. Biset-Peiró, I. Graça, J. Guilera, J. Morante, J.M. Lopes, T. Andreu, C. Henriques, DBD plasma-assisted CO2 methanation using zeolite-based catalysts: Structure composition-reactivity approach and effect of Ce as promoter, J. CO2 Util. 26 (2018) 202–211.

[281] H.Y. Kim, H.M. Lee, J.-N. Park, Bifunctional Mechanism of CO2 Methanation on Pd-MgO/SiO2 Catalyst: Independent Roles of MgO and Pd on CO2 Methanation, J. Phys. Chem. C. 114 (2010) 7128–7131.

[282] Q. Liu, B. Bian, J. Fan, J. Yang, Cobalt doped Ni based ordered mesoporous catalysts for CO2 methanation with enhanced catalytic performance, Int. J. Hydrogen Energy. 43 (2018) 4893–

4901.

[283] C.-S. Chen, C.S. Budi, H.-C. Wu, D. Saikia, H.-M. Kao, Size-Tunable Ni Nanoparticles Supported on Surface-Modified, Cage-Type Mesoporous Silica as Highly Active Catalysts for CO2 Hydrogenation, ACS Catal. 7 (2017) 8367–8381.

[284] L. Xu, H. Yang, M. Chen, F. Wang, D. Nie, L. Qi, X. Lian, H. Chen, M. Wu, CO2 methanation over Ca doped ordered mesoporous Ni-Al composite oxide catalysts: The promoting effect of basic modifier, J. CO2 Util. 21 (2017) 200–210.

[285] L. Xu, F. Wang, M. Chen, J. Zhang, K. Yuan, L. Wang, K. Wu, G. Xu, W. Chen, CO2 methanation over a Ni based ordered mesoporous catalyst for the production of synthetic natural gas, Rsc Adv. 6 (2016) 28489–28499.

[286] L. Xu, F. Wang, M. Chen, H. Yang, D. Nie, L. Qi, X. Lian, Alkaline-promoted Ni based ordered mesoporous catalysts with enhanced low-temperature catalytic activity toward CO_2 methanation, RSC Adv. 7 (2017) 18199–18210.

[287] M.C. Bacariza, I. Graça, S.S. Bebiano, J.M. Lopes, C. Henriques, Magnesium as Promoter of CO2 Methanation on Ni-Based USY Zeolites, Energy & Fuels. 31 (2017) 9776–9789.

[288] D. Hu, J. Gao, Y. Ping, L. Jia, P. Gunawan, Z. Zhong, G. Xu, F. Gu, F. Su, Enhanced Investigation of CO Methanation over Ni/Al2O3 Catalysts for Synthetic Natural Gas Production, Ind. Eng. Chem. Res. 51 (2012) 4875–4886.

[289] J. Guo, H. Lou, H. Zhao, X. Zheng, Improvement of stability of out-layer MgAl2O4 spinel for a Ni/MgAl2O4/Al2O3 catalyst in dry reforming of methane, React. Kinet. Catal. Lett. 84 (2005) 93–100.

[290] A. Westermann, B. Azambre, M.C. Bacariza, I. Graça, M.F. Ribeiro, J.M. Lopes, C. Henriques, Insight into CO2 methanation mechanism over NiUSY zeolites: An operando IR study, Appl. Catal. B Environ. 174–175 (2015) 120–125.

[291] P.A.U. Aldana, F. Ocampo, K. Kobl, B. Louis, F. Thibault-Starzyk, M. Daturi, P. Bazin, S. Thomas, A.C. Roger, Catalytic CO2 valorization into CH4 on Ni-based ceria-zirconia. Reaction mechanism by operando IR spectroscopy, Catal. Today. 215 (2013) 201–207.

[292] J.-N. Park, E.W. McFarland, A highly dispersed Pd–Mg/SiO2 catalyst active for methanation of CO2, J. Catal. 266 (2009) 92–97.

[293] M.C. Bacariza, I. Graça, S.S. Bebiano, J.M. Lopes, C. Henriques, Micro- and mesoporous supports for CO2 methanation catalysts: A comparison between SBA-15, MCM-41 and USY zeolite, Chem. Eng. Sci. 175 (2018) 72–83.

[294] H.C. Wu, Y.C. Chang, J.H. Wu, J.H. Lin, I.K. Lin, C.S. Chen, Methanation of CO2 and reverse water gas shift reactions on Ni/SiO2 catalysts: the influence of particle size on selectivity and reaction pathway, Catal. Sci. Technol. 5 (2015) 4154–4163.

[295] L. Xu, F. Wang, M. Chen, D. Nie, X. Lian, Z. Lu, H. Chen, K. Zhang, P. Ge, CO2 methanation over rare earth doped Ni based mesoporous catalysts with intensified low-temperature activity,

Int. J. Hydrogen Energy. 42 (2017) 15523–15539.

[296] X. Fang, C. Peng, H. Peng, W. Liu, X. Xu, X. Wang, C. Li, W. Zhou, Methane Dry Reforming over Coke-Resistant Mesoporous Ni-Al2O3Catalysts Prepared by Evaporation-Induced Self-Assembly Method, ChemCatChem. 7 (2015) 3753–3762.

[297] X. Ning, Y. Lu, H. Fu, H. Wan, Z. Xu, S. Zheng, Template-Mediated Ni(II) Dispersion in Mesoporous SiO2for Preparation of Highly Dispersed Ni Catalysts: Influence of Template Type, ACS Appl. Mater. Interfaces. 9 (2017) 19335–19344.

[298] M. Pirouzmand, B. Nikzad-Kojanag, S.A. Hosseini-Yazdi, Catalytic capture of CO2 with template-containing Zn/MCM-41 and its transformation to solid carbonate, J. Braz. Chem. Soc. 27 (2016) 2354–2360.

[299] M.C. Bacariza, R. Bértolo, I. Graça, J.M. Lopes, C. Henriques, The effect of the compensating cation on the catalytic performances of Ni/USY zeolites towards CO2 methanation, J. CO2 Util. 21 (2017) 280–291.

[300] M.C. Bacariza, I. Graça, A. Westermann, M.F. Ribeiro, J.M. Lopes, C. Henriques, CO2 Hydrogenation Over Ni-Based Zeolites: Effect of Catalysts Preparation and Pre-reduction Conditions on Methanation Performance, Top. Catal. 59 (2015) 314–325.

[301] I. Graça, L. V. González, M.C. Bacariza, A. Fernandes, C. Henriques, J.M. Lopes, M.F. Ribeiro, CO2 hydrogenation into CH4 on NiHNaUSY zeolites, Appl. Catal. B Environ. 147 (2014) 101–110.

[302] H. Liu, H. Wang, J. Shen, Y. Sun, Z. Liu, Preparation, characterization and activities of the nano-sized Ni/SBA-15 catalyst for producing COx-free hydrogen from ammonia, Appl. Catal. A Gen. 337 (2008) 138–147.

[303] H. Drobná, M. Kout, A. Sołtysek, V.M. González-Delacruz, A. Caballero, L. Čapek, Analysis of Ni species formed on zeolites, mesoporous silica and alumina supports and their catalytic behavior in the dry reforming of methane, React. Kinet. Mech. Catal. 121 (2017) 255–274.

[304] L. Espinosa-Alonso, K.P. de Jong, B.M. Weckhuysen, Effect of the Nickel Precursor on the Impregnation and Drying of γ-Al2O3 Catalyst Bodies: A UV−vis and IR Microspectroscopic Study, J. Phys. Chem. C. 112 (2008) 7201–7209.

[305] K. Zhao, W. Wang, Z. Li, Highly efficient Ni/ZrO2 catalysts prepared via combustion method for CO2 methanation, J. Co2 Util. 16 (2016) 236–244.

[306] G. Du, S. Lim, Y. Yang, C. Wang, L. Pfefferle, G.L. Haller, Methanation of carbon dioxide on Ni-incorporated MCM-41 catalysts: The influence of catalyst pretreatment and study of steady-state reaction, J. Catal. 249 (2007) 370–379.

[307] G. Garbarino, P. Riani, L. Magistri, G. Busca, A study of the methanation of carbon dioxide on Ni/Al2O3 catalysts at atmospheric pressure, Int. J. Hydrogen Energy. 39 (2014) 11557–11565.

[308] S. Yilmaz, H. Selim, A review on the methods for biomass to energy conversion systems design, Renew. Sustain. Energy Rev. 25 (2013) 420–430.

[309] P. McKendry, Energy production from biomass (part 2): conversion technologies, Bioresour. Technol. 83 (2002) 47–54.

[310] S. Sharma, R. Meena, A. Sharma, P. kumar Goyal, Biomass Conversion Technologies for Renewable Energy and Fuels: A Review Note., IOSR J. Mech. Civ. Eng. 11 (2014) 28–35.

[311] A. V Bridgwater, G.V.C. Peacocke, <2000-Fast pyrolysis processes for biomass 被引1124次.pdf>, 4 (2000).

[312] P. Chen, Q. Xie, M. Addy, W. Zhou, Y. Liu, Y. Wang, Y. Cheng, K. Li, R. Ruan, Utilization of municipal solid and liquid wastes for bioenergy and bioproducts production, Bioresour. Technol. 215 (2016) 163–172.

[313] M.A. Hossain, J. Jewaratnam, P. Ganesan, Prospect of hydrogen production from oil palm biomass by thermochemical process – A review, Int. J. Hydrogen Energy. 41 (2016) 16637–16655.

[314] B. Li, H. Yang, L. Wei, J. Shao, X. Wang, H. Chen, Absorption-enhanced steam gasification of biomass for hydrogen production: Effects of calcium-based absorbents and NiO-based catalysts on corn stalk pyrolysis-gasification, Int. J. Hydrogen Energy. 42 (2017) 5840–5848.

[315] S. Sobek, S. Werle, Solar pyrolysis of waste biomass: Part 1 reactor design, Renew. Energy. 143 (2019) 1939–1948.

[316] N. Couto, V. Silva, A. Rouboa, Municipal solid waste gasification in semi-industrial conditions using air-CO2 mixtures, Energy. 104 (2016) 42–52.

[317] S.L. Wu, J.H. Kuo, M.Y. Wey, Thermal degradation of waste plastics in a two-stage pyrolysis-catalysis reactor over core-shell type catalyst, J. Anal. Appl. Pyrolysis. (2019) 104641.

[318] Y. Zhang, J. Huang, P.T. Williams, Fe-Ni-MCM-41 Catalysts for Hydrogen-Rich Syngas Production from Waste Plastics by Pyrolysis-Catalytic Steam Reforming, Energy and Fuels. 31 (2017) 8497–8504.

[319] N. Wang, D. Chen, U. Arena, P. He, Hot char-catalytic reforming of volatiles from MSW pyrolysis, Appl. Energy. 191 (2017) 111–124.

[320] J.M. Saad, P.T. Williams, Pyrolysis-Catalytic-Dry Reforming of Waste Plastics and Mixed Waste Plastics for Syngas Production, Energy and Fuels. 30 (2016) 3198–3204.

[321] K. Kawamoto, B. Lu, Gasification and reforming of biomass and waste samples by means of a novel catalyst, J. Mater. Cycles Waste Manag. 18 (2016) 646–654.

[322] Y. Zhang, C. Wu, M.A. Nahil, P. Williams, Pyrolysis-catalytic reforming/gasification of waste tires for production of carbon nanotubes and hydrogen, Energy and Fuels. 29 (2015) 3328–3334.

[323] H. Hiblot, I. Ziegler-Devin, R. Fournet, P.A. Glaude, Steam reforming of methane in a synthesis gas from biomass gasification, Int. J. Hydrogen Energy. 41 (2016) 18329–18338.

[324] L. Liu, Q. Wang, J. Song, X. Yang, Y. Sun, Dry reforming of model biomass pyrolysis products to syngas by dielectric barrier discharge plasma, Int. J. Hydrogen Energy. 43 (2018)

10281–10293.

[325] A.L. Karemore, P.D. Vaidya, R. Sinha, P. Chugh, On the dry and mixed reforming of methane over Ni/Al2O3 ??? Influence of reaction variables on syngas production, Int. J. Hydrogen Energy. 41 (2016) 22963–22975.

[326] A. Serrano-Lotina, L. Daza, Influence of the operating parameters over dry reforming of methane to syngas, Int. J. Hydrogen Energy. 39 (2014) 4089–4094.

[327] M. Jafarbegloo, A. Tarlani, A.W. Mesbah, S. Sahebdelfar, Thermodynamic analysis of carbon dioxide reforming of methane and its practical relevance, Int. J. Hydrogen Energy. 40 (2015) 2445–2451.

[328] A. Behroozsarand, A.N. Pour, Modeling of microreactor for methane dry reforming: Comparison of Langmuir-Hinshelwood kinetic and microkinetic models, J. Nat. Gas Sci. Eng. 20 (2014) 99–108.

[329] W. Gac, A. Denis, T. Borowiecki, L. Kepiński, Methane decomposition over Ni-MgO-Al2O3 catalysts, Appl. Catal. A Gen. 357 (2009) 236–243.

[330] J.I. Villacampa, C. Royo, E. Romeo, J.A. Montoya, P. Del Angel, A. Monzon, Catalytic decomposition of methane over Ni-Al2O3 coprecipitated catalysts: Reaction and regeneration studies, Appl. Catal. A Gen. 252 (2003) 363–383.

List of figures

List of tables

Journal Publications

1. Tuning the properties of nickel nanoparticles inside SBA-15 mesopores for enhanced stability in methane reforming, L. Karam, S. Casale, H. El Zakhem, N. El Hassan, J. CO_2 Util. 17 (2017) 119-124. *doi.org/10.1016 /j.jcou.2016.12.002*

2. Effect of pore geometry of mesoporous supports on catalytic performances in methane reforming, J. Tannous; L. Karam; M.N. Kaydouh; H. El Zakhem; N. El Hassan; S. Casale, International Conference on Energy, Power, Petroleum and Petrochemical Engineering (2018). *doi.org/10.1051/matecconf/201817101003*

3. Advantages of mesoporous silica based catalysts in methane reforming by CO_2 from kinetic perspective, L. Karam, N. El Hassan, J. Environ. Chem. Eng. 6 (2018) 4289-4297. *doi.org/10.1016/j.jece.2018.06.031*

4. Porous nickel-alumina derived from metal-organic framework (MIL-53): a new approach to achieve active and stable catalysts in methane dry reforming, L. Karam, J. Reboul, S. Casale, P. Massiani, N. El Hassan, *under revision*

5. Comprehensive study on the effect of magnesium loading over Nickel-ordered mesoporous alumina in dry reforming of methane, L. Karam, P. Massiani, N. El Hassan, *under preparation*

6. Mesoporous nickel-alumina catalysts derived from MIL-53(Al) metal organic framework: a new path for achieving promising activity for CO_2 methanation, L. Karam, M.C. Bacariza, J.M. Lopes, C. Henriques, J. Reboul, N. El Hassan, P. Massiani, *under preparation*

Conferences (* attended as presenting author)

1. Reforming kinetics over highly dispersed nickel nanoparticles supported on mesoporous silica prepared by a facile method, L. Karam*, N. El Hassan, LIRA Program, (December 2016, Beirut, Lebanon), Poster

2. Dry reforming of methane over porous alumina materials derived from metal organic framework, L. Karam*, J. Reboul, N. El Hassan, P. Massiani, Premier congres français des MOFs, COFs et polymeres poreux (May 2018, Paris, France), Poster

3. Reforming of waste gasification products to syngas on nickel-magnesium mesoporous alumina catalysts, L. Karam*; N. El Hassan; P. Massiani, Groupe d'etude en catalyse-GECAT, (May 2018, Trégunc, France), Poster

4. Promotion of mesoporous nickel-alumina based catalysts by magnesium addition for reforming of waste gasification products, L. Karam*; N. El Hassan; F. Launay; P. Massiani, International symposium on heterogeneous catalysis, (August 2018, Sofia, Bulgaria), **Oral**

5. Advanced Catalytic Materials with Well-Defined Nanostructures for Energy & Fuel, L. Karam*; J. Reboul; S. Casale; N. El Hassan; P. Massiani; ACS National Meeting & Exposition, (August 2018, Boston, USA), **Oral**

6. Mesoporous Ni-Al_2O_3 derived from metal organic framework: A promising catalyst for CO_2 methanation, L. Karam*, J. Reboul, M.C. Bacariza, J.M. Lopes, C. Henriques, N. El Hassan, P. Massiani, EuropaCat (August 2019, Aachen, Germany), Poster

Abstract :

Dry reforming of methane is a process that converts CH_4 and CO_2 gases, emitted from burning of fossil fuels or decomposition of biomass, into syngas gaseous mixture of H_2:CO ratio equal to 1. Ni based catalysts proved to be suitable candidates for the reaction due to their good activity, wider availability and lower cost than noble-based materials. However, these catalysts still face sintering of Ni active phase and coke deposition decreasing the catalytic stability. In this thesis we developed two different synthesis routes of mesoporous Ni-Al_2O_3 based catalysts that can occlude Ni inside the pores achieving high activity and stability in reforming. A set of complimentary physicochemical techniques was systematically applied to thoroughly investigate the materials properties at all steps of preparation and activation. The first approach embraced synthesis of mesoporous Ni-Mg-Al_2O_3 materials by one-pot strategy. Results demonstrated that 7 wt% Mg (optimum loading) based sample contribute to high and homogenous Ni dispersion with simultaneous excellent Mg repartition, preserving ordered mesoporous Al_2O_3 walls. The good structural and textural characteristics in addition to the enhance basicity reinforce activity and stability. The second method involved synthesizing new mesoporous Ni-Al_2O_3 materials using metal-organic framework as sacrificial template. This procedure results in small Ni^0 nanoparticles homogeneously dispersed and stabilized within the high surface area support resisting sintering and inhibiting carbon nanotubes formation during reforming reaction. Based on catalytic tests completed by thermodynamics calculations, the synthesized materials proved to be efficient not only for dry reforming of methane, but also for CO_2 methanation reaction and dry reforming of waste pyrolysis products.

Keywords: methane reforming, CO_2 methanation, nickel nanoparticles, mesoporous Al_2O_3, metal-organic framework